PHYSIK-DEPARTMENT

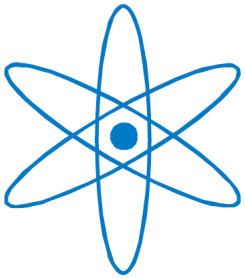

Detection of Supernova Neutrinos in the Liquid-Scintillator Experiment LENA

Dissertation
von

Jürgen Michael Albrecht Winter

TECHNISCHE UNIVERSITÄT
MÜNCHEN

Technische Universität München
Physik-Department
Lehrstuhl für Experimentalphysik und Astroteilchenphysik
Univ.-Prof. Dr. Stefan Schönert

Detection of Supernova Neutrinos in the Liquid-Scintillator Experiment LENA

Jürgen Michael Albrecht Winter

Vollständiger Abdruck der von der Fakultät für Physik der Technischen Universität München zur Erlangung des akademischen Grades eines

Doktors der Naturwissenschaften (Dr. rer. nat.)

genehmigten Dissertation.

Vorsitzender:		Univ.-Prof. Dr. Alejandro Ibarra
Prüfer der Dissertation:	1.	Univ.-Prof. Dr. Lothar Oberauer
	2.	Univ.-Prof. Dr. Laura Fabbietti

Die Dissertation wurde am 12.12.2013 bei der Technischen Universität München eingereicht und durch die Fakultät für Physik am 25.02.2014 angenommen.

Abstract

The LENA project (**L**ow-**E**nergy **N**eutrino **A**stronomy) is a planned large-volume liquid-scintillator detector. The good energy resolution, low-energy threshold, and its large mass allow to perform real-time spectroscopy of low-energy neutrinos with high statistics. This is especially beneficial for the observation of rare events such as a galactic core-collapse supernova.

In a liquid scintillator, interactions by different particle types cause different scintillation light pulse shapes. They can be used to identify proton recoils induced by neutrino-proton scattering from supernova neutrinos or by cosmogenic knock-out neutrons. In order to evaluate the performance of the detector, a precise characterization of the liquid scintillator is necessary.

In the course of this work, an experiment has been set up at the Maier-Leibnitz-Laboratorium in Garching in order to determine the pulse shape of proton and electron recoils in different liquid-scintillator mixtures. Neutrons produced via ^{11}B(p,n)^{11}C or an americium-beryllium source were used to induce proton recoils. Compton scattering of simultaneously emitted γs provided information on the electron recoils. A time-of-flight measurement allows for an easy identification of neutron and γ induced events and thus effective background reduction. The tail-to-total and the Gatti method are used in order to determine the energy-dependent discrimination power of proton and electron recoils in liquid scintillator. Combining both methods, a proton recoil identification efficiency of $(99.70 \pm 0.05)\%$ can be achieved between 1-1.5 MeV, while suppessing 99% of the γ induced recoils for the probable liquid scintillator mixture for LENA, *linear alkylbenzene* (LAB) as solvent and 3 g/ℓ *2,5-diphenyloxazole* (PPO) and 20 mg/ℓ *1,4-bis-(o-methylstyryl)-benzole* (bisMSB) as fluors. Moreover, the decay constants τ_i and the respective amplitudes n_i are determined for various liquid scintillator mixtures. It can be observed that the decay times decrease with increasing PPO content and decrease with the addition of non-scintillating solvent.

The detection of supernova neutrinos is a major goal for LENA. In this thesis, the expected time-resolved visible energy spectra for the six most important detection channels are evaluated using the supernova neutrino emission predicted by a model from the Garching group. For a supernova at a distance of 10 kPc, about 6000 events are expected within 10 s, mostly in the inverse β decay channel. Due to the small degeneracy of the mean neutrino energies, the determination of the neutrino mass hierarchy with the help of the H- and L-resonance in the supernova is difficult. Neutrinos emitted in the late burning phases of the supernova progenitor provide an early warning signal for an upcoming supernova of at

least a few hours. While for oxygen burning LENA is sensitive up to about 1 kPc, silicon burning can be observed even up to several kPc. For Betelgeuse, a red giant and thus a candidate for a galactic core-collapse supernova, ∼10,000 cpd are expected towards the end of its lifetime via $\nu - e$ scattering and the inverse β decay.

Zusammenfassung

Das geplante Großexperiment zur Neutrino-Detektion LENA (**L**ow-**E**nergy **N**eutrino **A**stronomy) setzt Flüssigszintillator als Detektor-Material ein. Seine gute Energieauflösung, seine Möglichkeit zur Messung niedriger Energien und seine große Masse ermöglichen die Spektroskopie von niederenergetischen Neutrinos mit hohen Zählraten. Dies ist besonders für die Beobachtung von seltenen Ereignissen von Vorteil, wie zum Beispiel einer galaktischen Kernkollaps-Supernova.

Wechselwirkungen von verschiedenen Teilchenarten führen in Flüssigszintillatoren zu unterschiedlichen Szintillationslichtprofilen. Dies kann zur Identifikation von Protonen-Rückstößen verwendet werden, die von der Streuung von Supernova-Neutrinos an Protonen oder von kosmogen erzeugten Neutronen herrühren. Hierfür ist eine genaue Charakterisierung des Flüssigszintillators notwendig.

Ein Experiment zur Bestimmung der Pulsform von Protonen- und Elektronenrückstößen in verschiedenen Flüssigszintillatormischungen wurde am Maier-Leibnitz-Laboratorium in Garching aufgebaut. Für die Erzeugung der Protonenrückstöße wurden Neutronen verwendet, die einerseits mittels eines gepulsten ^{11}B Strahls via ^{11}B(p,n)^{11}C und andererseits durch eine Americium-Beryllium Quelle erzeugt wurden. Compton-Streuung von gleichzeitig erzeugter Gammastrahlung liefert Informationen zu Elektronenrückstößen. Die Messung der Flugzeit erlaubt eine einfache Identifikation der durch Neutronen und Gammateilchen induzierten Ereignisse und damit eine effektive Verringerung des Untergrunds. Das 'Tail-to-total' und das 'Gatti'-Kriterium werden eingesetzt, um die energieabhängige Diskriminierung von Protonen- und Elektronenrückstößen in Flüssigszintillator zu untersuchen.

Für die wahrscheinliche Szintillatormischung für LENA, *Lineares Alkylbenzol* (LAB) als Lösungsmittel mit 3 g/ℓ *2,5-Diphenyloxazol* (PPO) und 20 mg/ℓ *1,4-bis-(o-Methylstyryl)-benzol* (bisMSB) als Fluoreszenzmittel, können durch die Kombination beider Kriterien $(99.70 \pm 0.05)\%$ der Protonenrückstöße zwischen 1-1.5 MeV identifiziert werden bei gleichzeitiger Unterdrückung von γ-induzierten Rückstößen von 99%. Des Weiteren wurden Abklingzeiten und -amplituden für zahlreiche Szintillatoren bestimmt.

Die Beobachtung von Supernova-Neutrinos ist eines der Hauptziele von LENA. Auf Basis von Simulationsdaten zur Neutrinoemmision der Garchinger Gruppe wurden die zeitaufgelösten Energiespektren der sechs wichtigsten Messkanäle ermittelt. Für eine Supernova in einem Abstand von 10 kPc werden ungefähr 6000 Ereignisse in 10 s erwartet, die meisten davon über den inversen β-Zerfall. Aufgrund der kleinen Unterschiede der mittleren Neutrinoenergien ist die Bestimmung der Massenhierarchie der Neutrinos mittels H- und

L-Resonanz in der Supernova schwierig.
Neutrinos, die in den letzten Brennphasen des Vorläufersterns der Supernova abgestrahlt werden, kündigen eine Explosion um mindestens einige Stunden im Voraus an. Für Neutrinos der Sauerstoff-Brennphase ist LENA bis zu 1 kPc sensitiv, für solche von der Silizium-Fusion sogar mehrere Kiloparsec. Für Beteigeuze, ein roter Riese und damit ein möglicher Supernova-Kandidat, können am Ende seiner Lebenszeit bis zu 10.000 Ereignisse über den inversen β-Zerfall gemessen werden.

Contents

Chapter 1

Introduction

In the past decades, neutrinos have gained increasing attention from both particle physics, astrophysics, and even geophysics. While the neutrino has already been postulated by Wolfgang Pauli in 1930 [1], it took until 1956 to confirm its existence experimentally by Reines and Cowan [2]. A milestone in the field of neutrino physics was the solar neutrino experiment by Davis [3]. Detecting neutrinos originating from the solar hydrogen fusion, it was the first experiment to use neutrinos as a probe for otherwise hidden processes. At the same time, the observed neutrino deficit was the inspiration for the concept of neutrino oscillations, a window to physics beyond the standard model of particle physics (SM).

A large variety of experiments has been dedicated to neutrino oscillations and the determination of neutrino mixing parameters. Evidence for neutrino oscillation, solving the solar neutrino problem, has been adduced by the SNO experiment [4], supported by measurements of GALLEX/GNO [5, 6], SAGE [7], and Super-Kamiokande [8]. Moreover, oscillation of atmospheric neutrinos has been proven by Super-Kamiokande [9]. Accelerator neutrino experiments like K2K [10] and MINOS [11] further investigated atmospheric mixing. The last unknown mixing angle θ_{13} has been determined lately with great precision by the three reactor disappearance experiments Daya Bay [12], Reno [13], and Double Chooz [14].

Nevertheless, some neutrino properties still remain unknown and motivate new experiments. Most fundamentally, the particle nature of the neutrino, Majorana or Dirac particle, is unknown. It is in the focus of neutrinoless double-β decay searches GERDA [15] and CUORICINO [16]. Moreover, the absolute mass of the neutrinos is unknown, motivating direct neutrino mass experiments like KATRIN [17]. Neutrino mass hierarchy and CP-violating phase δ_{CP} are in the focus of long-baseline neutrino beam experiments [18]. The possibility to use LENA as a far detector is discussed in chapter 2. Information on the neutrino mass hierarchy could also be provided by supernova (SN) neutrinos.

As neutrinos are uncharged particles, they are unaffected by electromagnetic fields and pinpoint to their origin. Moreover, neutrinos are only weakly-interacting and are thus hardly affected by matter. Therefore, they serve as messengers from the interior of optically opaque objects, such as the sun, supernovae (SNe) or the earth. In this thesis, the focus is on the planned large-volume liquid-scintillator detector LENA (**L**ow-**E**nergy **N**eutrino **A**stronomy) [19] and its detection capabilities for SN neutrinos. In order to separate the different interaction channels via pulse shape analysis, the characteristics of the liquid scintillator (LS) has to be examined.

Since neutrino flavor oscillations have a large influence on the spectra of the SN neutrinos, they are discussed in detailed in the first part of this chapter. In the second part, the evolution of a massive star is presented, starting from hydrogen fusion up to a possible core-collapse. Here, the focus is on the neutrino emission in the various phases. The design and the physics program of the LENA project is presented in chapter 2. As the characterization of organic LS is a major part of this thesis, a thorough introduction to its properties is given in chapter 3. In chapter 4, the experimental setup of the neutron scattering experiment is presented, followed by the discrimination of neutron and γ-induced recoil events via pulse shape analysis for different LS mixtures in chapter 5. Moreover, the energy-dependent decay times and amplitudes of both event types are determined. Finally, chapter 6 evaluates the the neutrino signal from a galactic core-collapse SN in the LENA experiment.

1.1 Neutrinos in the standard model

In the *standard model of particle physics* (SM), all fermions are classified in three generations or flavors [20, 21]. The left-handed leptons are ordered in weak-isospin doublets and consist of a charged lepton and the corresponding neutrino:

$$\begin{pmatrix} \nu_e \\ e \end{pmatrix}_L, \begin{pmatrix} \nu_\mu \\ \mu \end{pmatrix}_L, \begin{pmatrix} \nu_\tau \\ \tau \end{pmatrix}_L . \tag{1.1}$$

While the neutrinos have a weak isospin component $T_3 = \frac{1}{2}$, for the charged leptons $T_3 = -\frac{1}{2}$. In consequence of the Goldhaber experiment [21], neutrinos are assumed to be massless and right-handed neutrinos do not exist in the SM. Therefore, the right-handed leptons (and quarks) are weak-isospin singlets. For anti-particles, the doublets are right-handed.

Leptons and quarks are subject to weak interaction, mediated by the gauge bosons Z^0 (M_Z = 91 GeV) and $W^\pm$ (M_W= 80 GeV) [20]. Due to the high masses of the gauge bosons, the range of the weak interaction and thus the cross-sections for low-energy neutrinos are small, $\leq 10^{-40}\,\mathrm{cm}^{-2}$. The exchange of Z^0 and $W^\pm$ is referred to as *neutral current* (NC) and *charged current* (CC) interaction, respectively. In weak interactions, weak isospin and

flavor are conserved. Z^0 and $W^\pm$ exclusively couple to left-handed particles and right-handed anti-particles, which means that the weak interaction violates parity maximally. While CC interactions change the particle within a doublet, the NC interaction does not alter the weak isospin.

1.2 Neutrino oscillations in vacuum

Neutrino oscillation is a phenomenon beyond the SM, since it violates lepton family number conservation and requires massive neutrinos. As stated before, the SM comprises three neutrino flavors[1]: $|\nu_\alpha\rangle$ (α=e,μ,τ), also referred to as flavor eigenstates. In general, these flavor eigenstates do not coincide with the eigenstates of the free Hamiltonian, called mass eigenstates $|\nu_j\rangle$ (j=1,2,3), that possess a defined mass. The transformation between these two bases is described by the *Pontecorvo-Maki-Nakagawa-Sakata* (PMNS) matrix [23]:

$$|\nu_\alpha\rangle = \sum_j U_{\alpha j} \, |\nu_j\rangle \, , \tag{1.2}$$

$$|\nu_j\rangle = \sum_\alpha U^*_{\alpha j} \, |\nu_\alpha\rangle \, . \tag{1.3}$$

$U_{\alpha j}$ represents the elements of the PMNS matrix. The unitary matrix can be parametrized in the following way:

$$\begin{aligned} U &= \begin{pmatrix} 1 & 0 & 0 \\ 0 & c_{23} & s_{23} \\ 0 & -s_{23} & c_{23} \end{pmatrix} \begin{pmatrix} c_{13} & 0 & s_{13}e^{-i\delta} \\ 0 & 1 & 0 \\ -s_{13}e^{i\delta} & 0 & c_{13} \end{pmatrix} \begin{pmatrix} c_{12} & s_{12} & 0 \\ -s_{12} & c_{12} & 0 \\ 0 & 0 & 1 \end{pmatrix} \\ &= \begin{pmatrix} U_{e1} & U_{e2} & U_{e3} \\ U_{\mu 1} & U_{\mu 2} & U_{\mu 3} \\ U_{\tau 1} & U_{\tau 2} & U_{\tau 3} \end{pmatrix} . \end{aligned} \tag{1.4}$$

s_{jk} and c_{jk} (j,k=1,2,3) stand for $\sin(\theta_{jk})$ and $\cos(\theta_{jk})$, respectively, with the rotation mixing angles θ_{jk} and δ for a possible CP-violating Dirac phase. In case the neutrino is a Majorana particle, two additional phases have to be considered.

The mass eigenstates $|\nu_j\rangle$ describe stationary states that evolve in time according to the Schrödinger equation[2]:

$$|\nu_j(t)\rangle = \exp(-iE_j t) \, |\nu_j\rangle \, , \tag{1.5}$$

[1]The so-called reactor antineutrino anomaly (RAA) indicates neutrino oscillations into a fourth, sterile neutrinos [22]. While the decay of the Z^0 boson clearly indicates three neutrino flavors [20], it still leaves a possibility for neutrinos that interact in a non-standard way.

[2]For simplicity, here and in the following natural units are used: $c = \hbar = 1$.

where E_j is the neutrino energy of the respective mass state. As for relativistic particles $p = |\vec{p}_j| \gg m_j$ and $p \approx E$,

$$E_j = \sqrt{p^2 + m_j^2} \simeq p + \frac{m_j^2}{2p} \simeq E + \frac{m_j^2}{2E}. \tag{1.6}$$

Now, consider a neutrino produced in weak interaction with an arbitrary flavor α. At the time t=0, this flavor can be expressed in the system of the mass eigenstate basis as

$$|\nu_\alpha\rangle = |\nu(t=0)\rangle = \sum_j U_{\alpha j} \, |\nu_j\rangle \, . \tag{1.7}$$

Using 1.5 and 1.3, the wave function at time t can be written as

$$|\nu(t)\rangle = \sum_{j,\beta} U_{\alpha j} U^*_{\beta j} \, \exp(-i(E + \frac{m_j^2}{2E})t) \, |\nu_\beta\rangle \, . \tag{1.8}$$

The probability that a neutrino changes its flavor from α to β, can be calculated to

$$\begin{aligned} P_{\alpha\beta} &= |\langle \nu_\beta | \nu(t) \rangle \, |^2 \\ &= \Big| \sum_j U_{\alpha j} U^*_{\beta j} \, \exp(-i(E + \frac{m_j^2}{2E})t) \Big|^2 \\ &= \sum_{j,k} U_{\alpha j} U^*_{\beta j} U^*_{\alpha k} U_{\beta k} \exp(-i \frac{\Delta m^2_{jk}}{2E} t). \end{aligned} \tag{1.9}$$

with $\Delta m^2_{jk} = m_j^2 - m_k^2$, which is in general non-zero. Obviously, neutrino oscillations only occur for non-degenerate masses.

In the simple case of two flavors (denoted ν_e and ν_μ here), one mass square difference Δm^2 and one mixing angle θ suffice to describe the system. eq. (1.9) simplifies to

$$P_{e\mu} = \sin^2 2\theta \, \sin^2 \left(\frac{\Delta m^2 t}{4E} \right), \tag{1.10}$$

$$= \sin^2 2\theta \, \sin^2 \left(\frac{\pi z}{l_{osc}} \right) \tag{1.11}$$

where

$$l_{osc} = \frac{4\pi E}{\Delta m^2} = 2.48 \cdot 10^7 \, \mathrm{cm} \left(\frac{E}{\mathrm{MeV}} \right) \left(\frac{10^{-5} \, \mathrm{eV}^2}{\Delta m^2} \right) \tag{1.12}$$

is called the oscillation length in vacuum. As the neutrinos almost travel at the speed of light $t \approx z$.

The current best values for the mixing angles θ_{jk} and the mass square differences Δm^2_{jk} are shown in table 1.1. The unknown sign of Δm^2_{23} leaves two possibilities of mass hierarchies of the neutrino mass eigenstates: the so-called *normal* ($m_3 > m_2 > m_1$) (NH) and *inverted* ($m_2 > m_1 > m_3$) hierarchy (IH).

parameter	best fit ($\pm 1\sigma$)
Δm^2_{21} (solar) $[10^{-5}\text{eV}^2]$	7.50 ± 0.20
$\lvert\Delta m^2_{32}\rvert$ (atmospheric) $[10^{-3}\text{eV}^2]$	$2.32^{+0.12}_{-0.08}$
$\sin^2 2\theta_{12}$	0.857 ± 0.024
$\sin^2 2\theta_{23}$	> 0.95
$\sin^2 2\theta_{13}$	0.098 ± 0.013

Table 1.1: Neutrino mass square differences and mixing angles [20].

1.3 Neutrino oscillations in matter

If neutrinos propagate in matter instead of vacuum, their oscillation behavior changes due to the interaction of electron neutrinos with the electrons present in matter. Neutrino oscillations in matter were investigated first by Wolfenstein [24]. If the matter density is constant, the situation is essentially like in the vacuum case, yet with different mixing angles. In case of a varying matter density a resonance effect can occur, which is able to enhance the transition probability maximally. This resonance has been discovered by Mikheyev and Smirnov [25], and is referred to as Mikheyev-Smirnov-Wolfenstein (MSW) effect. The MSW effect plays an important role for solar neutrinos and moreover, for supernova neutrinos.

1.3.1 Constant matter density

The interaction with matter can be considered in the oscillation formalism with the introduction of an effective potential to the equation of motion [26]

$$i\nabla \left|\nu_\alpha\right\rangle = \left(A + \frac{UM^2U^\dagger}{2E}\right)\left|\nu_\alpha\right\rangle, \tag{1.13}$$

where $A = \sqrt{2}G_F n_e$ with the Fermi constant G_F and the electron density n_e. The additional potential for nu_e and $\bar{\nu}_e$ is due to charged current interactions with electrons. Neutral current interactions with electrons, neutrons, and protons are equal for all neutrino flavors. These contributions only add a term proportional to the unity matrix, resulting in a change of phase that has no impact on oscillations.

In a simple case of only two neutrino flavors, it is easier to understand the effect of matter on the oscillations. In a straightforward way, the equation of motion for mass eigenstates in matter can be written according to the two-flavor case in vacuum:

$$i\nabla \begin{pmatrix} \nu_e \\ \nu_\mu \end{pmatrix} = \frac{\Delta m_m^2}{4E} \begin{pmatrix} -\cos 2\theta_m & \sin 2\theta_m \\ \sin 2\theta_m & \cos 2\theta_m \end{pmatrix} \begin{pmatrix} \nu_e \\ \nu_\mu \end{pmatrix}, \tag{1.14}$$

again neglecting terms proportional to the identity matrix. The angle θ_m is the mixing angle representing the matter case. The modified parameters for the matter case are related to the parameters in vacuum:

$$\sin 2\theta_m = \frac{\sin 2\theta}{\sqrt{(\xi - \cos 2\theta)^2 + \sin^2 2\theta}} \tag{1.15}$$

and

$$\Delta m_m^2 = \Delta m^2 \sqrt{(\xi - \cos 2\theta)^2 + \sin^2 2\theta}. \tag{1.16}$$

The dimensionless density parameter ξ is equal to

$$\begin{aligned} \xi &= \frac{2\sqrt{2} G_F n_e E}{\Delta m^2} \\ &= 1.53 \cdot 10^{-2} \left(\frac{n_e}{\mathrm{gcm}^{-3}}\right) \left(\frac{E}{\mathrm{MeV}}\right) \left(\frac{10^{-5}\,\mathrm{eV}^2}{\Delta m^2}\right). \end{aligned} \tag{1.17}$$

In analogy to the oscillation length in vacuum (eq. (1.12)), the oscillation length in matter is defined as

$$l_{osc,m} \equiv \frac{4\pi E}{\Delta m_m^2} = \frac{\sin 2\theta_m}{\sin 2\theta} l_{osc}. \tag{1.18}$$

For $\xi = \cos 2\theta$ the angle of maximum mixing in matter $\theta_m = \frac{\pi}{4}$ is obtained. This case of maximum flavor conversion is called resonance. The resonance density ρ_{res} can be derived from eq. (1.17) and is

$$\rho_{res} = 1.3 \cdot 10^2\,\mathrm{g\,cm}^{-3} \cos 2\theta \left(\frac{0.5}{n_e}\right) \left(\frac{\mathrm{MeV}}{E}\right) \left(\frac{\Delta m^2}{10^{-5}\mathrm{eV}^2}\right). \tag{1.19}$$

At the resonance density, the mass square difference (1.16) is minimal, and the mixing is maximum.

As expected in case of vacuum, θ_m is equal to the vacuum mixing angle θ. On the other side, for densities much higher than ρ_{res}, the matter mixing angle θ_m approaches $\frac{\pi}{2}$. As one can see from eq. (1.2), this means that mixing is suppressed and the flavor eigenstate $|\nu_e\rangle$ coincides with the heaviest mass eigenstate. This has to be considered for SN neutrinos, as they are produced at densities $\geq 10^{10}\,\mathrm{gcm}^{-3}$.

In the anti-neutrino sector, the potential enters negatively into eq. 1.13. Therefore, the effective mass of the anti-electron neutrinos is smaller than for $\bar{\nu}_x$. At densities $\rho \gg \rho_{res}$, the eigenstate $|\bar{\nu}_e\rangle$ is equal to the lightest mass eigenstate.

1.3.2 Varying matter density

In case of a varying matter density, θ_m and thus U are position dependent. Recapitulating eq. (1.14), assuming a propagation in z-direction, and changing the basis yields

$$i\frac{\partial}{\partial z}\begin{pmatrix}\nu_{1,m}\\ \nu_{2,m}\end{pmatrix} = \begin{pmatrix} -\frac{\Delta m_m^2}{2E} & -i\frac{\partial\theta_m}{\partial z} \\ i\frac{\partial\theta_m}{\partial z} & \frac{\Delta m_m^2}{2E}\end{pmatrix}\begin{pmatrix}\nu_{1,m}\\ \nu_{2,m}\end{pmatrix}. \tag{1.20}$$

Obviously, even the mass eigenstates mix for an inhomogeneous density. If the matrix is approximately diagonal, meaning

$$\left|\frac{\partial\theta_m}{\partial z}\right| \ll \frac{\Delta m_m^2}{2E}, \tag{1.21}$$

the mass eigenstates will not mix. Both ν_1 and ν_2 will remain the same as before the point of resonance. This is called *adiabatic* resonance. On the other hand, if condition (1.21) is not fulfilled, mixing occurs, called *non-adiabatic* resonance. The mixing is maximum for large $\frac{\partial\theta_m}{\partial z}$, around the resonance point defined in eq. (1.19). Naturally, the mixing of mass eigenstates also results in an observable oscillation of neutrino flavors.
An adiabaticity parameter γ can be derived from eq. (1.21) [26]

$$\gamma = \frac{\Delta m^2}{E\left|\frac{\partial ln(n_e)}{\partial z}\right|_{res}}\sin 2\theta\tan 2\theta. \tag{1.22}$$

Here, n_e denotes the electron density profile and $\left|\frac{\partial ln(n_e)}{\partial z}\right|_{res}$ its gradient at the point of resonance. An adiabatic resonance occurs, if $\left|\frac{\partial ln(n_e)}{\partial z}\right|_{res}$ is small compared to the oscillation length $l_{osc,m}$. Assuming a density profile $\rho(r) = \rho_0 r^{-n}$, γ becomes [26]

$$\gamma = \frac{1}{2n}\frac{\sin^2 2\theta}{(\cos^2\theta)^{1+1/n}}\left(\frac{\Delta m^2}{E}\right)^{1-1/n}\left(\frac{2\sqrt{2}G_F n_e\rho_0}{m_p}\right)^{1/n}. \tag{1.23}$$

1.3.3 H- and L-resonance

The resonant conversions of neutrinos that can occur within a supernova are called H- and L-resonance (H for high, L for low density). Due to the large mass gap ($\Delta m_{23}^2 \gg \Delta m_{12}^2$) and the smallness of θ_{13}, the oscillations of the original three-neutrino system can be described with the help of two two-neutrino oscillations. The L-resonance is driven by $\Delta m_{12}^2 \approx 8\cdot 10^{-5}\,\mathrm{eV}^2$ and θ_{12} and occurs for neutrinos only, e.g. for solar neutrinos. The H-resonance is driven by $\Delta m_{13}^2 \approx 2\cdot 10^{-3}\,\mathrm{eV}^2$ and θ_{13} and occurs for neutrinos in the

	hierarchy	
	normal	inverted
ν-sector	H,L	L
$\bar{\nu}$-sector	-	H

Table 1.2: Occurrences of H- and L-resonance for ν_e and $\bar{\nu}_e$ for both neutrino mass hierarchies.

case of NH ($m_3 > m_2 > m_1$) and for anti-neutrinos in the case of inverted hierarchy ($m_2 > m_1 > m_3$) (see table 1.2).

According to eq. (1.19) the L- and H-resonance occur at

$$\rho_L \approx (20 - 200)\,\mathrm{g\ cm^{-3}}, \tag{1.24}$$

$$\rho_H \approx (1 - 10) \cdot 10^3\,\mathrm{g\ cm^{-3}}. \tag{1.25}$$

The resonance regions are far from the SN core ($r \lesssim 100\,\mathrm{km} = 1.4 \cdot 10^{-4}\,R_\odot$ [3]), thus it is not expected that the SN dynamics are affected by flavor conversion [26]:

$$R_L \approx 0.1 - 0.2\,R_\odot \tag{1.26}$$

$$R_H \approx 0.05 - 0.1\,R_\odot \tag{1.27}$$

According to eq. (1.23), the adiabaticity depends on the mixing angle involved, the density profile and the neutrino energy. As $\sin^2 2\theta_{12} = 0.857$ (see table 1.1), and assuming a density profile with $n \approx 3$ [27], the L-resonance is perfectly adiabatic for typical SN-ν energies. Due to the large value of $\sin^2 2\theta_{13} = 0.096$, also the H-resonance is adiabatic for all SN neutrino energies, and the adiabaticity parameter $\gamma = 4.7 \cdot 10^3$ for $E = 1\,\mathrm{MeV}$ and $\gamma = 2.2 \cdot 10^2$ for $E = 100\,\mathrm{MeV}$.

The flip probability P at the resonance point is given by the Landau-Zener formula [28]

$$P = \exp\left(-\frac{\pi\gamma}{2}\right), \tag{1.28}$$

such that for adiabatic conditions, i.e. large γ, $P \approx 0$.

Figure 1.1 schematically shows the resonances occurring for the normal neutrino mass hierarchy. In this case both resonances occur in the neutrino sector. For the inverted mass hierarchy the H-resonance occurs in the anti-neutrino sector and the L-resonance in the neutrino sector. As stated before, the flavor eigenstates coincide with the mass eigenstates for extremely high densities as in the SN core. In the case of NH this means that $\nu_e = \nu_{3,m}$ and $\bar{\nu}_e = \bar{\nu}_{1,m}$. For IH, $\nu_e = \nu_{2,m}$ and $\bar{\nu}_e = \bar{\nu}_{3,m}$. In case of adiabatic resonances, the mass eigenstates persist and appear as such on earth.

[3] solar radius $R_\odot = 6.96 \cdot 10^5\,\mathrm{km}$

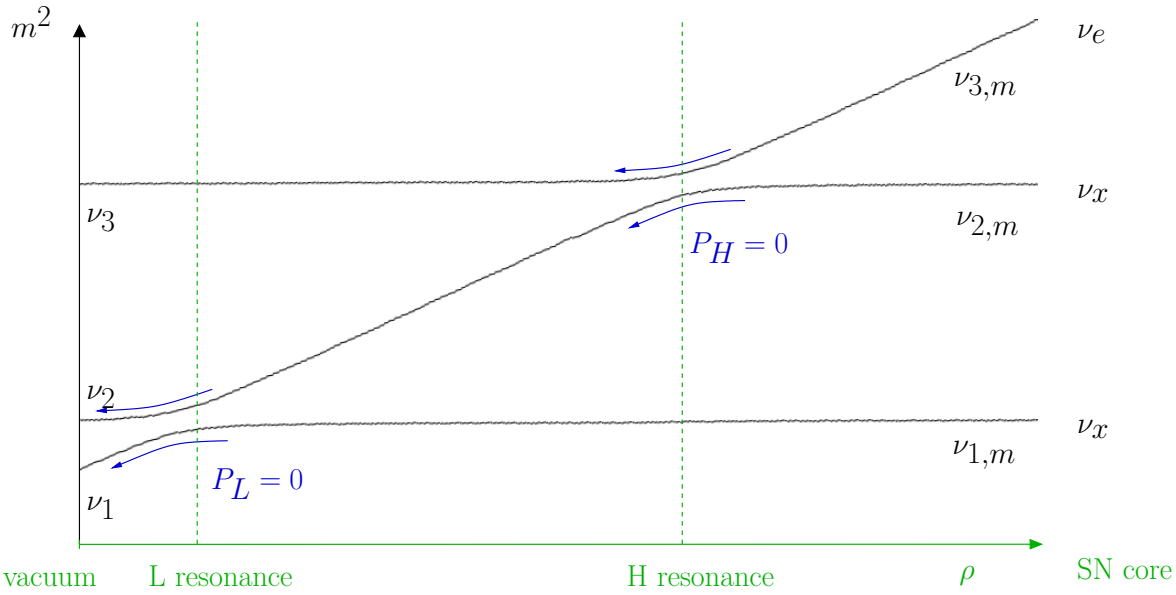

Figure 1.1: In case of NH, both H- and L-resonance occur in the neutrino sector for SN neutrinos. The figure shows the evolution of the effective masses of the neutrino mass eigenstates with respect to the density. In the core, flavor and mass eigenstates coincide. A classification between ν_τ and ν_μ into $\nu_{1,m}$ or $\nu_{2,m}$ is not necessary since both fluxes are equal, f_x. The H-resonance occurs between $\nu_{3,m}$ and $\nu_{2,m}$ for high densities ($\rho_H \approx (1-10) \cdot 10^3\,\mathrm{g\ cm^{-3}}$). The adiabatic L-resonance occurs for low densities ($\rho_L \approx (20-200)\,\mathrm{g\ cm^{-3}}$) between $\nu_{2,m}$ and $\nu_{1,m}$. For adiabatic resonance ($P_{L/H} = 0$) the flavor eigenstates persist, while there is a maximal crossing probability for non-adiabatic resonance ($P_{L/H} = 1$).

For SN neutrinos, the fluxes on earth f_α ($\alpha = e, \bar{e}, x, \bar{x}$) can be calculated depending on the original fluxes f^0_β ($\beta = e, \bar{e}, x$). Here, f_e and $f_{\bar{e}}$ describe the fluxes of ν_e and $\bar{\nu}_e$, respectively. $f_x = f_\mu = f_\tau$ and $f_{\bar{x}} = f_{\bar{\mu}} = f_{\bar{\tau}}$ denote the single fluxes of ν_μ/ν_τ and $\bar{\nu}_\mu/\bar{\nu}_\tau$, respectively. Since ν_x and $\bar{\nu}_x$ are produced thermally in a SN, this differentiation between neutrinos and anti-neutrinos is not made in case of the original flux f^0_x.

With the flip probabilities P_L and P_H for the L- and H-resonance, respectively, the neutrino fluxes on earth assuming NH can be expressed as

$$f_i = a_i f^0_e + (1 - a_i) f^0_x \tag{1.29}$$

where

$$\begin{aligned} a_1 &= P_L P_H, \\ a_2 &= (1 - P_L) P_H, \text{and} \\ a_3 &= 1 - P_H \end{aligned} \tag{1.30}$$

denote the contributions of the original ν_e flux f_e^0 to f_i, the fluxes referring to the mass eigenstates in vacuum. Their coherence is already lost in the outer layers of the exploding star, so that the neutrinos arrive there as incoherent fluxes of the mass eigenstates.

Subsequently follows from neutrino mixing

$$\begin{aligned} f_e &= \sum_i |U_{ei}|^2 f_i \\ &= p f_e^0 + (1-p) f_x^0, \end{aligned} \tag{1.31}$$

where

$$p \equiv |U_{e1}|^2 P_L P_H + |U_{e2}|^2 (1-P_L) P_H + |U_{e3}|^2 (1-P_H) \tag{1.32}$$

is the probability that an electron neutrino produced in the SN is detected as such on earth.

Due to flux conservation,

$$f_\mu + f_\tau = 2 f_x = (1-p) f_e^0 + (1+p) f_x^0. \tag{1.33}$$

Analogously, the fluxes can be calculated for inverted hierarchy. In fact, the substitution $P_H = 1$ in eqs. (1.29), (1.31), and (1.33) yields the correct result for this scenario.

For the anti-neutrino sector, the same calculations lead to

$$f_{\bar{e}} = \bar{p} f_{\bar{e}}^0 + (1-\bar{p}) f_x^0 \tag{1.34}$$

and

$$f_{\bar{\mu}} + f_{\bar{\tau}} = 2 f_{\bar{x}} = (1-\bar{p}) f_{\bar{e}}^0 + (1+\bar{p}) f_x^0 \tag{1.35}$$

where

$$\bar{p} \equiv |U_{e1}|^2 P_H + |U_{e3}|^2 (1-P_H) \tag{1.36}$$

is the probability that an electron anti-neutrino produced in the SN is detected as such on earth.

Inserting all relevant values, the flavor fluxes on earth are composed as shown in 1.2. As both the H- and the L-resonance are fully adiabatic, the flavor contents are determined by the vacuum mixing angles only.

Neutrino sector The mean energy of ν_x produced in SNe are expected to be higher than the mean energy of ν_e (cf. chapter 6). Therefore, oscillations will make the original ν_e spectrum harder, which is beneficial for detection since the cross-sections increase with energy.

In the case of NH, both resonances occur in the neutrino sector and the survival probability p for ν_e is given by $|U_{e3}|^2 = 0.025$. Hence, the major part of the flux f_e observed on earth

is dominated by the ν_x spectrum. On the other side, f_x contains almost all ν_e produced in a SN. Thus, neutrinos from the deleptonization can only be detected in neutral current (NC) channels in this case.

For IH, only the L-resonance occurs in the neutrino sector. Due to the high core density, ν_e coincides with $\nu_{2,m}$. Due to the adiabaticity of the L-resonance, it arrives at the detector as ν_2. Hence, the probability that a ν_e produced in the SN is detected as such is higher than for NH, $\sim 30\%$.

Anti-neutrino sector No resonances occur for the NH in the anti-neutrino sector. Hence, most part of the original flux $f^0_{\bar{e}}$ can be observed as $\bar{\nu}_e$ in a detector, as $|U_{e1}|^2$ is largest.

As the H-resonance is adiabatic, $\bar{\nu}_{3,m}$ and $\bar{\nu}_{1,m}$ do not mix in the IH. Therefore, $f_{\bar{\nu}_3}$ contains the original $f_{\bar{e}}$ flux when reaching earth. As for neutrinos in the NH, the probability to detect an original $\bar{\nu}_e$ as such is very low.

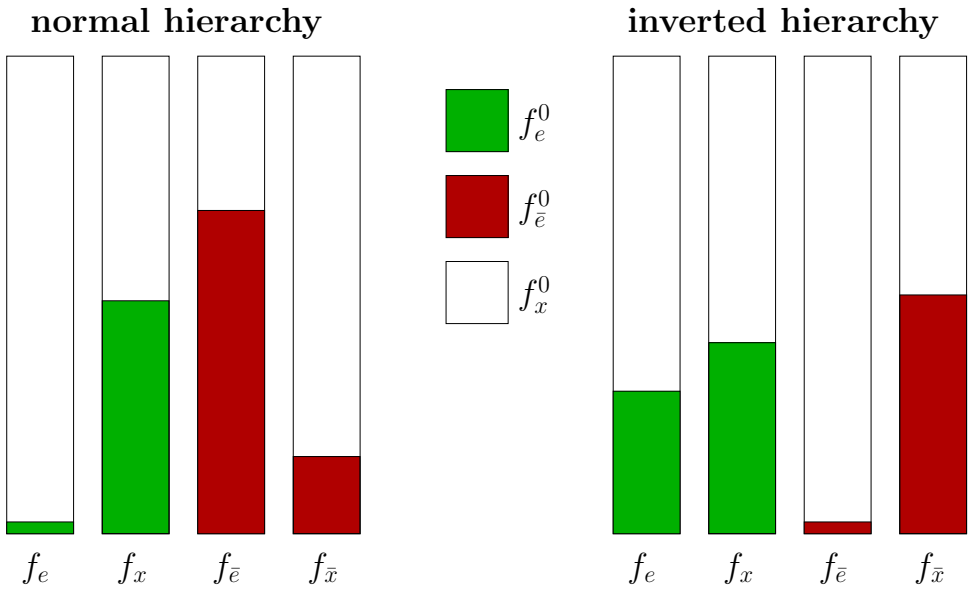

Figure 1.2: Flavor fluxes f on earth in dependency of the original produced fluxes f^0 for both normal and inverted hierarchy in the neutrino and anti-neutrino sector. Due to flux conversation, $f_e + 2f_x = f^0_e + 2f^0_x$ and analogously for anti-neutrinos $f_{\bar{e}} + 2f_{\bar{x}} = f^0_{\bar{e}} + 2f^0_{\bar{x}}$.

1.3.4 Earth matter effect

The so-called *earth matter effect* occurs when neutrinos pass through the earth. Observation or non-observation of the effect can give further information on neutrino oscillation parameters and original fluxes.

The earth effect is usually expressed by the difference between the flux at the surface of the earth f_e and the flux at the detector (on the opposite side of the earth) $f_e^D = \sum_i P_{ei} f_i$, where P_{ei} denotes the probability that a ν_j entering the earth reaches the detector as a ν_e. Rewriting f_i again with the original fluxes f_α^0 (eq. (1.29)) one obtains

$$f_e^D - f_e = (1 - 2P_L)P_H(P_{e2} - |U_{e2}|^2)(f_e^0 - f_x^0), \tag{1.37}$$

where $\sum_i P_{ei} = 1$ and $\sum_i |U_{ei}|^2 = 1$ are used. Due to the low density of the earth ($\rho_E = \mathcal{O}(\text{g cm}^{-3})$) and the smallness of the mixing angle θ_{13}, the term proportional to $(P_{e3} - |U_{e3}|^2)$ is neglected.

Evaluating the factor $(P_{e2} - |U_{e2}|^2)$, assuming a constant density of the earth and two-flavor oscillation finally leads to the expression

$$f_e^D - f_e = (1 - 2P_L)P_H \frac{\xi \sin^2 2\theta_{13}}{(\xi - \cos 2\theta_{13})^2 + \sin^2 2\theta_{13}} \cdot \sin^2\left(\frac{\pi z}{l_{osc,m}}\right)(f_e^0 - f_x^0). \tag{1.38}$$

The expression is also valid for $\bar{\nu}_e$, setting P_L to 1. The dimensionless density parameter ξ is the same as defined in eq. (1.17) and z denotes the distance the neutrino traveled trough the earth. The oscillation length in matter $l_{osc,m}$ is the defined in eq. (1.18) and can be rewritten to

$$l_{osc,m} = 3.1 \cdot 10^2 \,\text{km} \frac{1}{\sqrt{(\xi - \cos 2\theta_{13})^2 + \sin^2 2\theta_{12}}} \left(\frac{E}{10\,\text{MeV}}\right)\left(\frac{8 \cdot 10^{-5}\,\text{eV}^2}{\Delta m_{12}^2}\right). \tag{1.39}$$

From eq. (1.38) the conditions for the appearance of the earth effect can be derived. First, there has to be a difference of the original fluxes f_e^0 and f_x^0. Second, there has to be as well a difference between f_1 and f_2 at earth, while the third generation can be neglected. In eq. (1.38), this is considered by the factor $(1 - 2P_L)P_H$: if $P_H = 0$, $f_1 = f_2 = f_x^0$, and if $P_L = 1/2$, $f_1 = f_2$ have the same mixture of the original spectra of ν_e and ν_x. As the H-resonance is adiabatic, the earth effect can be only observed for neutrinos (anti-neutrinos) for inverted (normal) hierarchy.

With the $\bar{\nu}_e$ capture on protons (cf. section 6.3.1) LENA provides the possibility to investigate the earth effect with high statistics and its good energy resolution.

1.4 Collective neutrino oszillations

In case of very high neutrino densities, an additional potential $A_{\nu\nu}$ due to coherent NC neutrino-neutrino forward scattering has to be considered in the equation of motion (1.13) [29]:

$$A_{\nu\nu} = \sqrt{2} G_F \int d^3q (1 - \hat{p} \cdot \hat{q})(\rho_q - \bar{\rho}_q). \tag{1.40}$$

Here, $\hat{p}$ and $\hat{q}$ denote the unit vectors for the propagation of a test neutrino and the background neutrino, respectively. The neutrino flavor density matrices ρ_q and $\bar{\rho}_q$ are functions of position and time. The additional term introduces nonlinearities that ultimately lead to synchronized neutrino oscillations, i.e. all neutrinos of one flavor oscillate collectively. The collective oscillations occur a few hundred of kilometers above the neutrinosphere.

Collective oscillations are discussed to play a major role for SN neutrinos. However, due to the anisotropy and inhomogeneity of the SN environment and the different energies and momenta of the neutrinos, the complexity is enormous. So far, collective two-flavor neutrino oscillations have been modeled under specific assumptions, such as simple bipolar systems or homogeneous and isotropic neutrino gases and help to understand qualitative features [29]. A characteristic prediction of collective oscillations is the occurrence of one or more so-called *spectral swaps*, i.e. two neutrino spectra are entirely swapped above a given energy [30].

While many effects of the collective neutrino oscillations have been under investigation, many effects still remain unknown. e.g. the influence of anisotropies and inhomogeneities. Moreover, the difference between two- and three-flavor oscillations has to be investigated further. A high-statistics observation of SN neutrino spectra and their time evolution with a large-volume like LENA could be be most advantageous to discover effects due to collective neutrino oscillations.

1.5 Stellar evolution

In its lifetime, a massive star ($M > 8\,M_\odot$) undergoes several fusion phases, described in the following [31]. In general, the ashes of the previous stage are the fuel for the next. Hydrostatic equilibrium is assumed and thus explosive burning stages are neglected. With every fusion stage, a larger variety of nuclei is present and many reactions have to be considered, making modeling more and more complicated. In the late burning stages, neutrino-cooling dominates.

1.5.1 Hydrogen and helium burning

In a star, there are two different possibilities for the hydrogen to helium fusion. First, in the so-called pp chain, protons are gradually fused to helium. In the CNO-cycle, carbon, nitrogen, and oxygen serve as catalyst to produce helium [32]. While the pp energy production dominates in the sun, the CNO cycle is more important in heavier objects.

When the fusion rate drops, the thermal pressure decreases and the core contracts. This leads to an increase of the core temperature and starts the ignition of the next burning stage. The resulting rise in thermal pressure stops the contraction again. This process of alternating nuclear burning and core contraction also happens in the subsequent cycles.

After hydrogen fusion, He burning sets in. Two processes compete:

$$3\alpha \longrightarrow {}^{12}\mathrm{C} \tag{1.41}$$

$${}^{12}\mathrm{C} + \alpha \longrightarrow {}^{16}\mathrm{O} + \gamma \tag{1.42}$$

In general, the first process will be dominant at the beginning of the helium burning phase and the latter towards later times. However, the prominence of the reactions also depend on the star's mass and metallicity. At the end of the He burning, a carbon-oxygen (CO) core has been built up.

Already during the He burning but more importantly in later stages neutron capture (*s-process*) leads to the formation of nuclei other than the fusion products. These neutrons originate from (α,n) reactions or the decay of excited states. Isotopes even heavier than ^{56}Fe can be produced this way, although no more energy can be gained by nuclear fusion as the binding energy per nucleon peaks at this point. However, photo disintegration leads to their re-decay into the iron group. Nevertheless, rather than s-process reactions, only the fusion stages described in the following are important for the energy generation in the star. Usually, the lightest abundant isotope is the fuel for the next fusion phase due to the lower Coulomb barrier.

1.5.2 Late burning stages

The late burning stages comprise carbon, neon, oxygen, and silicon fusion. Gradually, the star's core contracts and its temperature and density increases. Finally, an onion-like shell structure builds up with an iron core from Si burning and surrounding layers from the ashes of the previous fusion stages.

After the He stage, carbon burning starts:

$$^{12}\mathrm{C} + {}^{12}\mathrm{C} \longrightarrow {}^{24}\mathrm{Mg}^* \longrightarrow {}^{23}\mathrm{Mg} + n - 2.62\,\mathrm{MeV} \quad (1.43)$$
$$\longrightarrow {}^{20}\mathrm{Ne} + \alpha + 4.62\,\mathrm{MeV} \quad (1.44)$$
$$\longrightarrow {}^{23}\mathrm{Na} + p + 2.24\,\mathrm{MeV} \quad (1.45)$$

At this stage ($T > 5 \cdot 10^8\,\mathrm{K}$), energy losses due to emission thermal neutrinos start to dominate over radiative diffusion and convection [31]. This is the reason why the core evolution accelerates significantly at this point. From the start of the carbon to the end of the silicon burning phase, it takes only a few thousand years, depending on the mass and metallicity of the star. The duration of the single fusion phases can be seen in table 1.3. The neutrinos are produced thermally in equilibrium with the core plasma. Hence, the rise of the core temperature with each burning stage results in increasing mean neutrino energies and also a higher fraction of $\bar{\nu}_x$. Moreover, as the luminosity increases significantly from carbon to silicon burning, especially the detection of neutrinos from oxygen and silicon burning is of interest.

As a result of the short time scales, the outer hydrogen shell of the star is unaffected by the core dynamics and surface luminosity and temperature do not change until the SN explosion. Therefore, only neutrino observation can shed light on these late burning stages and announce a coming SN. A possibility to use these neutrinos as a warning signal for a SN explosion is elaborated in section 6.5.

fusion stage	t	$\langle E \rangle$ [MeV]	$\nu_e/\bar{\nu}_e$ fraction	L [erg/s]
C	0.03-2.82 ky	0.71	0.425	$7.4 \cdot 10^{39}$
Ne	0.03-0.73 y	0.99	0.398	$1.2 \cdot 10^{43}$
O	0.01-4.77 y	1.13	0.389	$7.4 \cdot 10^{43}$
Si	0.2-18.3 d	1.85	0.363	$3.1 \cdot 10^{45}$

Table 1.3: Duration t, mean neutrino energies $\langle E \rangle$, fraction of emitted ν_e and $\bar{\nu}_e$, and average luminosities L for the last fusion cycles of a massive star [31, 33].

As ^{16}O is a highly-stable double magic nucleus burning of the heavier ^{20}Ne sets in first. The (α,γ) reaction and the inverse photo disintegration of ^{20}Ne form the net reaction

$$^{20}\mathrm{Ne} + {}^{20}\mathrm{Ne} \longrightarrow {}^{16}\mathrm{O} + {}^{24}\mathrm{Mg} + 4.59\,\mathrm{MeV} \quad (1.46)$$

Next, oxygen burning sets in

$$^{16}\mathrm{O} + {}^{16}\mathrm{O} \longrightarrow {}^{32}\mathrm{S}^*, \quad (1.47)$$

which decays mainly via

$$^{32}\mathrm{S}^* \longrightarrow {}^{31}\mathrm{P} + p + 7.68\,\mathrm{MeV}, \text{ and} \quad (1.48)$$
$$^{32}\mathrm{S}^* \longrightarrow {}^{28}\mathrm{Si} + \alpha + 9.59\,\mathrm{MeV}. \quad (1.49)$$

Many secondary reactions take place during oxygen burning. Towards its end, two major groups of nuclei have formed that are in a quasi-equilibrium state: isotopes with a mass number of $A = 24 - 46$ and isotopes from the iron group around $A = 56$.

In the silicon fusion stage, gradual (γ,α) processes lead to a complete disintegration of ^{28}Si into α particles. These αs gradually fuse to nuclei above ^{28}Si to form isotopes of the iron group. Mainly, ^{54}Fe and ^{56}Fe are produced. At the end of nuclear fusion, the star has an onion-shell structure, with an iron core and outer hydrogen and helium layers.

1.6 Core-collapse supernova

As stated before, heavy elements up to iron are produced in the star, steadily increasing the mass of the core. During the lifetime of the star an equilibrium between the gravitational pull and the pressure of the degenerate relativistic electron gas is maintained. However, when the core reaches the Chandrasekhar mass ($\sim 1.4\,M_\odot$), the electron gas can no longer compensate the pressure and the core starts to self-contract. As soon as the density reaches $10^{10}\,\mathrm{gcm}^{-3}$ and $T \sim 10^{13}\,\mathrm{K}$, electron capture (EC) on iron leads to a reduction of the electron gas pressure

$$e^- + {}^{56}\mathrm{Fe} \longrightarrow {}^{56}\mathrm{Mn} + \nu_e. \tag{1.50}$$

Furthermore, the endothermic photo dissociation

$$\gamma + {}^{56}Fe \longrightarrow 12\alpha + 4n - 124\,\mathrm{MeV} \tag{1.51}$$

reduces the thermal pressure as well and the core collapses even more rapidly.

At densities around $10^{12}\,\mathrm{gcm}^{-3}$ in the core, the mean free path of the neutrinos gets in the order of the core radius, due to coherent neutrino-nucleus scattering. Hence, the neutrinos can no longer stream freely outwards. This effect is called *neutrino trapping*: Like photons in the sun, the neutrinos diffuse outwards. The neutrinos are in thermal equilibrium with the environment which reflects in their emission spectra. The surface of the last scattering is dependent on the neutrino flavor and energy as different reactions are involved to different extents. It is widely referred to as *neutrino sphere* analogously to the photosphere of the sun. The energy spectra can be approximated with thermal Fermi-Dirac distributions and are strongly correlated to the conditions around the neutrino sphere. As ν_μ and ν_τ (and $\bar{\nu}_\mu$ and $\bar{\nu}_\tau$) are produced in neutral current (NC) reactions only, since the environment does not allow for μ or τ production in large quantities, they are regarded as one species $\bar{\nu}_x$. For ν_e and $\bar{\nu}_e$, the main contribution for production and opacity arises from the charged current (CC) reactions

$$\nu_e + n \longleftrightarrow p + e^- \tag{1.52}$$

$$\bar{\nu}_e + p \longleftrightarrow n + e^+ \tag{1.53}$$

As the proton to neutron ratio is around 1:3 in the protoneutron star, the opacity is higher for ν_e. Thus, the radius of neutrino sphere for $\bar{\nu}_e$ is larger than for $\bar{\nu}_e$. Therefore, the mean energy of ν_e, $\langle E_e \rangle$, is smaller than the mean energy of $\bar{\nu}_e$, $\langle E_{\bar{e}} \rangle$. Accordingly, $\langle E_x \rangle$ denotes the mean neutrino energy of $\overset{(-)}{\nu}_x$. As $\overset{(-)}{\nu}_x$ couple least to matter, the radius of its neutrino sphere is smallest. As a consequence, a hierarchy $\langle E_e \rangle < \langle E_{\bar{e}} \rangle < \langle E_x \rangle$ is expected. In a more refined picture, this hierarchy does not hold for $\overset{(-)}{\nu}_x$. Several processes are contributing to their production: nucleon-nucleon Bremsstrahlung

$$N + N \longrightarrow N + N + \nu_x + \bar{\nu}_x, \tag{1.54}$$

electron-positron annihilation

$$e^+ e^- \longleftrightarrow \nu_x + \bar{\nu}_x, \tag{1.55}$$

and neutrino-pair annihilation

$$\nu_e + \bar{\nu}_e \longleftrightarrow \nu_x + \bar{\nu}_x. \tag{1.56}$$

Moreover, scattering off nucleons N, electrons or neutrinos has to be considered:

$$\overset{(-)}{\nu}_x + N \longrightarrow \overset{(-)}{\nu}_x + N \tag{1.57}$$

$$\overset{(-)}{\nu}_x + e^- \longrightarrow \overset{(-)}{\nu}_x + e^- \tag{1.58}$$

$$\overset{(-)}{\nu}_x + \nu \longrightarrow \overset{(-)}{\nu}_x + \nu. \tag{1.59}$$

None of the creation or scattering reactions is dominating over the others.

This variety of different processes that freeze out at different radii makes it clear that a precise definition of a neutrino sphere is no longer possible. Therefore, a neutrino number sphere with radius R_n and a transport sphere with radius $R_t > R_n$ is introduced [34, 35]. Inside R_n, ν_x are produced and trapped, outside R_t the neutrinos stream freely. In between, energy loss occurs due to the scattering processes (1.57-1.59), significantly shifting the $\overset{(-)}{\nu}_x$ spectrum to lower energies. As a result, $\langle E_{\bar{e}} \rangle \approx \langle E_x \rangle$.

The core continues to contract adiabatically until it reaches nuclear densities $\mathcal{O}(10^{14}\,\mathrm{gcm}^{-3})$. Now, nuclear repulsive forces start to dominate and the collapse is halted and reversed. The outgoing shock front quickly dissipates its energy via photo dissociation on heavy nuclei and eventually the shock stalls at ∼100-200 km. As a consequence, a large number of ν_e is produced via electron capture $e^- + p \longrightarrow n + \nu_e$ right behind the shock. When the shock reaches the ν_e-sphere, a huge number of ν_e accumulated behind the shock can escape at once. This sudden outburst is known as neutralization or deleptonization burst. This distinct peak in luminosity ($\sim 10^{53}\mathrm{ergs}^{-1}$) lasts for about 20 ns. The ν_e produced in the core are trapped, blocking states for further deleptonization. Therefore, their mean energy rises significantly described with a chemical potential of up to 130 MeV. In the course of the diffusion outwards, these ν_e heat the matter of the progenitor star to ∼15 MeV. This leads to an increased production of thermal $\nu\bar{\nu}$ pairs of all flavors. In the hot post-bounce

core, all other neutrino flavors are produced as stated in reactions (1.53)-(1.56). The protoneutron star continues to cool down via neutrino emission. This *cooling phase* lasts for about 10 s. In the neutron rich environment outside the core, neutron capture of nuclei are suspected to take place producing nuclei heavier than iron. This is referred to as *r-process* (rapid), in contrast to the low s-process described before. Due to the high neutron flux, the production of heavy elements takes places at a very fast time scale [36].

Chapter 2

The LENA detector

Almost one decade has passed since the first proposal of the LENA (**L**ow-**E**nergy **N**eutrino **A**stronomy) experiment in 2005 [37]. Since then, various analyses have been devoted to the detection capabilities of this large liquid-scintillator detector. Major goals are the search for proton decay and the detection of low-energy neutrinos, such as the diffuse supernova background (DSNB) or geoneutrinos [38, 39, 40, 19]. A deeper look into the detector performance at high energies revealed great potential, broadening the physics range to the GeV regime.

In this chapter, the main properties of the LENA detector are outlined. The LENA design is presented in the first section, followed by a discussion about photomultiplier tube (PMT) requirements. The main goals of the physics programme are outline in the last section. As the characterization of liquid scintillator (LS) is a major topic in this thesis, its properties are introduced separately in chapter 3.

2.1 Detector design

A sketch of the LENA detector is shown in figure 2.1. As the attenuation length of typical organic LS is of the order of 10-20 m [19], the concrete tank is of cylindrical shape with r=16 m. Thus, a large target mass can be achieved while maintaining a light yield sufficient for low-energy neutrino detection. The tank height is planned to be 100 m, limited by the cavern size. If located in Pyhäsalmi, Finland, the unisotropic rock stress dictate an elliptical cross section [41]. A minimum rock overburden of 4,000 mwe[1] is desired in order to minimize background from atmospheric muons.

[1] meter water equivalent; the overburden expressed in terms of a water layer that results in the same shielding from cosmic muons.

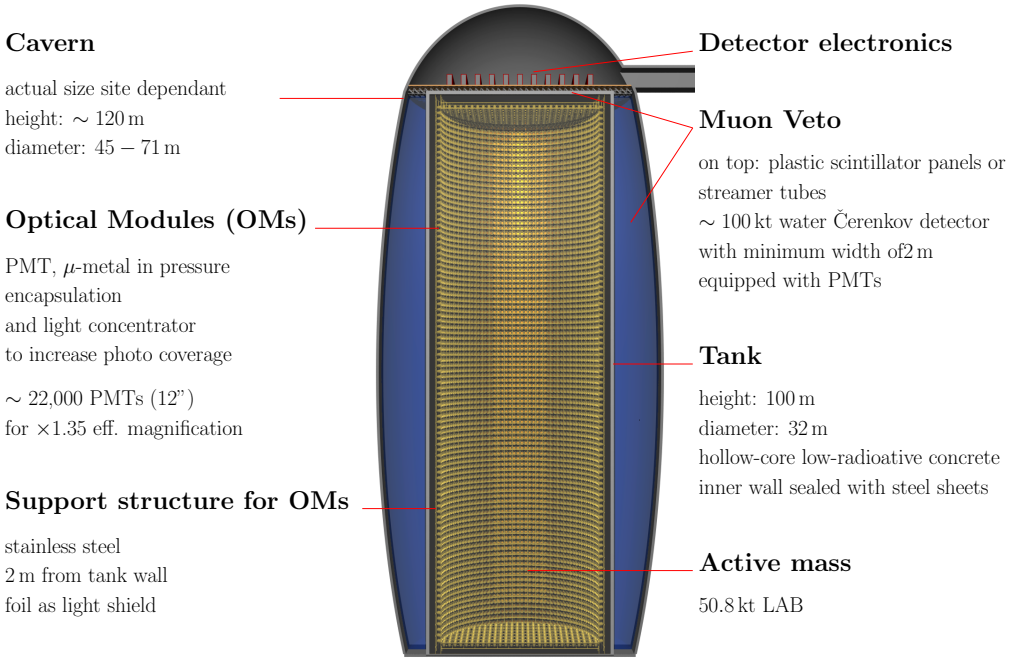

Figure 2.1: Sketch of the LENA detector along with a description of the main components.

The scintillation photons are detected using photomultiplier tubes (PMTs). They are contained in optical modules (OM) along with μ-metal shielding, electronics socket and connector. For pressure resistance, the OMs are each contained in a stainless steel encapsulation with an acrylic window and filled with non-scintillating LAB as buffer. A stainless steel scaffolding 2 m from the tank walls serves as support structure of the OMs. About 30,000 12-inch PMTs are required for an optical coverage of 30%. The possibility to use 8-inch or 11-inch PMTs is discussed as well. Additional light concentrators, increasing the effective collection area by a factor of 1.35, can help to reduce the number of 12-inch PMTs to ∼22,000. A non-reflecting foil is installed at the OM support structure. This way, background light due to the decay of radioactive isotopes from the concrete or the photomultiplier tubes (PMTs) cannot reach the target volume. Moreover, it helps to suppress the convection of these isotopes into the inner volume.

Muon induced neutrons and long-lived cosmogenics cause a dangerous background for low-energy measurements. In order to maintain high detection lifetime, the active muon veto serves to tag muons and help to reconstruct their tracks. The muon veto consists of two parts. First of all, several layers of plastic scintillator panels or streamer tubes are mounted on top of the detector. Secondly, the cavern around the tank is filled with water and equipped with PMTs to detect Čerenkov light. Moreover, this water chamber provides passive shielding against external radiation from surrounding rock, i.e. fast neutrons.

Additionally, layers of plastic scintillator panels are needed to tag muon from top

The zinc and copper mine in Pyhäsalmi, the deepest active mine in Europe, is the favored detector location for LENA. With a depth of 1450 m the muon flux is reduced to $\sim 0.2\,\mathrm{m}^{-2}\mathrm{h}^{-1}$ [42]. Another option is an extension of the existing Laboratoire Souterrain de Modane (LSM) in Fréjus, adjacent to a highway tunnel connecting France and Italy. Both possibilities are discussed within the LAGUNA (Large Apparatus for Grand Unification and Neutrino Astronomy) site study [43].

2.2 Photo sensors and read-out electronics

The performance of the photo sensors used for the scintillation light detection has a major impact on the goals of LENA. While the detection efficiency of photons directly affects energy resolution and threshold, the timing accuracy influences tracking, pulse shape discrimination, and position reconstruction.

Bialkali photomultipliers (PMTs) currently seem to be the most promising choice, as they have proven their qualities and long-term stability in existing experiments like Super-Kamiokande [8] and KamLAND [44]. They feature a maximum photon detection efficiency of ∼20% at 420 nm [45, 46], matching very well with the emission spectrum of liquid scintillators. Moreover, in order to ensure low-background conditions, PMTs made from ultra low-background borosilicate glass are available. Since the goals of LENA extend from low-energy to multi-GeV physics, this requires a large dynamic range of the photo sensors.

Generally, small PMTs are preferred due to a larger dynamic range, smaller transit time spread, and a reduced number of afterpulses. A higher number of sensors also enhances the position reconstruction and tracking capabilities. On the other side, larger PMTs and thus less sensors and electronic channels are more cost-effective. In order to increase the photosensitive area, it is planned to mount light concentrators in front of the PMTs. Moreover, also sensors with an enhanced quantum efficiency ($\geq$25%) are under consideration [45].

Currently, performance tests of various sensor types are under way [47]. Alongside, Monte Carlo (MC) studies are performed in order to understand the impact of the PMTs and light concentrators on the detector performance. Moreover, as the pressure at the bottom of the detector is too high for available PMT series ($\sim$ 11.2 bar), pressure encapsulations are currently being developed, including μ-metal shielding against magnetic fields,light concentrators, voltage divider and buffer [48].

Like the photo sensors, the read-out electronics have to reflect the large spread in the energy range for all LENA goals and be able to cope with SN rates. Moreover, a sub-nanosecond time resolution has to be guaranteed for an ideal performance covering position reconstruc-

tion, pulse shape discrimination and the disentanglement of different event topologies of GeV beam neutrino interactions. A core-collapse of Betelgeuze, a red giant at a distance of only 200 Pc from earth, would trigger about 10^7 events in 10 s in LENA putting strong constraints on the electronics performance.

2.3 Physics program

LENA is a versatile detector, opening a window of measurements stretching from sub-MeV to GeV physics. Apart from the large detector mass, all analyses introduced in the following benefit from the high energy resolution and low energy threshold. The planned lifetime few decades enables to gain sufficient statistics even for weak signals. Moreover, using liquid scintillator as target material offers the possibility to discriminate background efficiently taking advantage of coincidence signals and pulse shape analysis. In the following the main goals of the LENA project are listed, starting at low energies.

2.3.1 Solar neutrinos

At high energies, Kamiokande [49, 50, 8] and SNO [4] have observed this effect detecting ^{8}B neutrinos. The germanium based experiments Gallex/GNO [5, 6] and SAGE [7] have measured the integral flux down to the neutrinos from the pp fusion. The transition between vacuum and matter dominated neutrino oscillations has been explored by Borexino, measuring ^{7}Be, pep, and low-energetic ^{8}B neutrinos [51, 52, 53]. In the near future, Borexino and SNO+ [54] aim at the observation of neutrinos from the CNO cycle and maybe even a real time measurement of pp neutrinos.

source	energy window [MeV]	fiducial mass [kt]	rate [cpd]
pp	> 0.25	30	40
pep	0.8-1.4	30	$2.8 \cdot 10^2$
^{7}Be	> 0.25	35	$1.0 \cdot 10^4$
^{8}B	> 2.8	35	79
CNO	0.8-1.4	30	$1.9 \cdot 10^2$
^{8}B (via ^{13}C channel)	> 2.2	35	2.4

Table 2.1: Estimates for the event rates of solar neutrinos from different H burning processes in LENA in counts per day (cpd). The fiducial volumes have been determined in MC calculation for the γ background [55]

Solar neutrino event rates in the LENA detector for neutrinos from different solar fusion

reactions are shown in table 2.1. In order to suppress mainly γ background from the PMTs, a fiducial volume cut is performed, estimated through MC simulations. Due to the high statistics, especially for ^{7}Be neutrinos, detailed studies of the neutrino spectra and their so far unobserved temporal variations can be performed. As shown in [56], there is a 3σ discovery potential for amplitudes as low as 0.5% for modulations between tens of minutes to $\sim$100 years. Hence, the stability of solar fusion processes can be checked and connections to helioseismic g-modes in the sun's center. Other possible sources for variations are due to changes in the solar matter density, magnetic field, or to the eccentricity of earth's orbit around the sun.

Due to the low energy threshold and the high rate of ^{8}B neutrinos, it is possible to probe the MSW transition region with LENA. Simulations of the ^{8}B spectrum and possible background show that if no upturn of the ν_e survival probability is detected after 5 years, the MSW-LMA prediction could be ruled out by 5σ [57].

2.3.2 Geoneutrinos

Geoneutrinos originate from radioactive elements naturally abundant on earth, namely the β-decay chains of ^{238}U and ^{232}Th, and the decay of ^{40}K. Due to the energy threshold of 2.2 MeV of the inverse β-decay, only the spectra of U and Th can be observed with LENA. Geoneutrinos have already been detected by KamLAND [44, 58] and Borexino [59, 60]. However, only a kton detector like LENA has the capability to acquire the statistics needed to solve the discrepancy between geochemical and geophysical models. According to bulk silicate earth models, which state that the radioactive isotopes are mostly abundant in the mantle and crust, $\mathcal{O}(10^3)$ events per year are expected for LENA. In Pyhäsalmi, the $\bar{\nu}_e$ flux can be determined with a precision of about 10% already after one year, and disentanglement between U and Th contributions is possible. A 10-years campaign would further decrease the error to 2-4%. The detector location in Fréjus is disfavored due to the higher reactor neutrino background, deteriorating the accuracy (4-7 % after 10 years) [19].

Besides reactor neutrinos, cosmogenic radioisotopes such as ^{9}Li and ^{8}He can mimic the inverse β-decay signature. These events can be reduced with the help of temporal and spatial cuts around the muon track to $\sim$1 event per year. Fast neutrons produced in the surrounding rock account for $\sim$ 10 events in the energy region of interest in one year [55]. Another neutron background is originating from the ^{13}C(α,n)^{16}O reaction, where the α particle originates from the decay of ^{210}Po [59, 60]. Assuming a comparable level of radiopurity for LENA, about 10 events per year are expected for this background.

2.3.3 Diffuse supernova neutrino background (DSNB)

The diffuse supernova neutrino background (DSNB) originates from historical core-collapse SN explosions, whereas the contribution from SNe within a redshift of $z \leq 1$ is highest above neutrino energies of 10 MeV [61]. In general, it contains neutrinos of all flavors. In contrast to a single galactic SN detection, the DSNB provides an average neutrino spectrum, giving information on all possible types of core-collapse scenarios.

Due to the large cross-section of the inverse β-decay $\bar{\nu}_e + p \rightarrow n + e^+$, the search for the DSNB focuses on $\bar{\nu}_e$. Moreover, this detection channel has a clearly distinguishable coincidence signal: after a prompt signal from the positron annihilation, the neutron thermalizes and is captured by a proton releasing 2.2 MeV with a delay of $\sim 250\,\mu s$.

The event rate of the DSNB depends on the anti-neutrino spectrum and the cosmic core collapse rate. The best rate limit up to date has been determined by the water-Čerenkov detector Super-Kamiokande to $1.2\,\mathrm{cm}^{-2}\mathrm{s}^{-1}$ above 19.3 MeV [62]. Depending on the neutrino average energy, $\sim$ 5-10 events per year are expected in LENA, about twice as much as in Super-Kamiokande.

Despite the clear coincidence signature of the inverse β-decay, various backgrounds have to be considered due to the expected low rate. Reactor $\bar{\nu}_e$ and atmospheric $\bar{\nu}_e$ cannot be separated from the DSNB signal and therefore constrain the observation window to $\sim$10-25 MeV. Depending on the mean energy of the DSNB neutrinos, 50-100 events are expected in 10 years. A severe background is due to NC interaction of atmospheric neutrinos with ^{12}C, which is about ten times higher than the expected DSNB signal. However, pulse shape analysis can reduce this background to (21.8 $\pm$ 0.4) events per years while reducing the DSNB rate by about 60%. After 10 years of data taking, the DSNB can be detected with more than 3σ significance assuming the expected value of the background rate is known with 5% uncertainty. In case no DSNB signal is found, all current models can be ruled out with 90% C.L. [57].

2.3.4 Supernova neutrinos

A galactic core-collapse supernova (SN) will trigger several 1000-10,000 events within LENA, depending on its luminosity, neutrino average energies, and distance. Several neutral-current (NC) and charge-current (CC) channels offer the possibility to disentangle the neutrino flavors and thus examine the dynamics of the exploding star as well as neutrino oscillation parameters. As it is one main focus of this thesis, the detection of SN neutrinos in LENA will be discussed thoroughly in chapter 6.

2.3.5 Proton decay

Due to its large mass and scheduled long lifetime ≥ 30 y,LENA is perfectly suited for the search for the proton decay. This baryon number violating process is predicted by grand unified theories [63, 64]. In the minimum supersymmetric SU(5) [65], the favored decay mode is

$$p \rightarrow K^+ + \bar{\nu}, \tag{2.1}$$

with an estimated lifetime of $10^{33} - 10^{34}$ years. Subsequently, the kaon will decay after $\tau_{K^+} = 12.8$ ns via $K^+ \rightarrow \mu^+\nu_\mu$ (63.43%) or $K^+ \rightarrow \pi^0\pi^+$ (21.13%). As all processes are two-body decays and the kaon is most likely to decay at rest, all particle energies are fixed. If a proton inside a carbon nucleus decays, its binding energy and its Fermi motion have to be considered. This proton decay channel provides a distinct signature in a liquid scintillator detector like LENA. CC interactions of atmospheric ν_μ pose a severe background, as the final state muon can deposit energies in the expected range of the proton decay. However, they can be rejected if the time resolution of the detector is good enough to disentangle the signal of the K^+ and its decay product. Based on a MC simulation it could be shown that a cut on the risetime leaves an upper limit of 0.05 misidentified muons per year, retaining 65% of the proton decay events [66]. Moreover, CC interactions of atmospheric ν_μ may produce kaons and a final state muon that can mimic the proton decay signal. If the signature of the electron from the μ decay can be identified, these deep inelastic interactions can be discriminated, with a residual background of 0.06 events per year. Considering these background sources and assuming no proton decay event signature within a time span of 10 years, a lifetime limit of $\tau_p > 4 \cdot 10^{34}$ y (90% C.L.) can be deduced [39].

2.3.6 Long-baseline neutrino oscillation

Within in the EU-funded LAGUNA-LBNO (Long Baseline Neutrino Oscillation) study [18], the possibility to use LENA as a far detector for a long-baseline neutrino oscillation experiment is currently being discussed. Through both a neutrino and an antineutrino campaign, the comparison of the disappearance probabilities $\mathrm{P}(\nu_i \rightarrow \nu_j)$ and $\mathrm{P}(\bar{\nu}_i \rightarrow \bar{\nu}_j)$ provides information on the sign of Δm^2_{13}.

Taking advantage of the already existing infrastructure, a probable site for the production of the neutrino beam is CERN. For conventional neutrino beams, at first stage pions and kaons are produced by protons that are directed onto a target [67]. Subsequently these particles decay mostly into muon-flavor neutrinos. By choosing positively/negatively charged kaons or pions with a magnetic horn, ν_μ and $\bar{\nu}_\mu$ can be selected. A conventional beam from CERN to Pyhäsalmi allows to check for the appearance $\nu_\mu \rightarrow \nu_e$. The oscillation maximum for the distance of ~ 2300 km is around 4 GeV; here the difference between NH and IH signal is largest. The measurement of the ν_e appearance probability requires the

discrimination of ν_e and ν_μ CC events or $\bar{\nu}_e$ and $\bar{\nu}_\mu$, respectively. In LENA, this is done via pulse shape analysis. However, NC π^0 production needs to be investigated in order to calculate the sensitivity for this setup. The determination of the CP-violating phase δ_{CP} seems challenging.

Chapter 3

Organic liquid scintillator

Organic liquid scintillator (LS) is a detector target material widely used in particle physics. The power of this technology has been successfully demonstrated in various neutrino experiments like Borexino [68], Double Chooz [14], or KamLAND [44]. It features a low energy-threshold, a good energy resolution, and is easily scalable to large masses. Therefore, liquid-scintillator detectors are particularly suited for detection of low-event rate signals, e.g. solar neutrinos.

As liquid scintillator is the main component of LENA detector, its properties are discussed thoroughly in this chapter. Starting with the scintillation mechanism itself, important scintillator components and the sample preparation for the neutron beam scattering experiment are discussed in the following.

3.1 Scintillation mechanism

When a charged particle passes through a medium, the molecules on its track are ionized or excited due to electromagnetic interactions. In scintillators, some of this deposited energy is released in deexcitation processes, emitting photons in the ultraviolet or visible region. This process is called *luminescence* and its reasons lie within the electronic structure of the molecules. Energy losses due to ionization and non-radiative deexcitation are known as *quenching*.

Organic liquid scintillators consist of hydrocarbons that also contain at least one benzene ring. In this hexagonal structure, the carbon atoms ($1s^2 2s^2 2p^2$) are in sp^2 hybridization. Two orbitals of each atom combine with the orbitals of neighboring carbon atoms to form strong σ-bonds, responsible for the stability of the planar ring. The third sp^2 orbital bonds with a hydrogen atom or the rest of the molecule. The remaining electrons in the p shell

form one delocalized π-orbital. They are loosely bound and emit light in the transition from excited states to the ground state.

Formally, one pair of π-electrons forms one double bond. The relative spin orientation of these electrons is responsible for the single states S_i (anti-parallel) or triplet states T_i (parallel). Both have different energy levels in the order of few eV. Vibrational sub-levels ($\mathcal{O}(0.1\,\mathrm{eV})$) can also be populated. Excitation of the ground state S_0 leads to a population of the singlet states S_i ($i \geq 1$). Both vibrational levels and higher singlet states $S_2, S_3, ..$ lose their energy rapidly ($\mathcal{O}(\mathrm{ps})$) through vibrational relaxation and collision with other molecules, respectively, until finally reaching the S_1 level. The deexcitation from S_1 to the ground state emitting light is known as *fluorescence*. Moreover, this transition can also be non-radiatively (phonons), leading to additional energy losses.

Triplet states are usually not excited directly from the ground state, since this transition is quantum-mechanically forbidden. They can rather be populated by a spin flip $S_1 \rightarrow T_1$, called *inter-system crossing*. Moreover, if a molecule is ionized, the free electron is most likely to recombine forming a triplet state [69]. The deexcitation of $T_1 \rightarrow S_0$ is known as *phosphorescence*. As mentioned, it is forbidden and therefore its lifetime is relatively long ($\mathcal{O}(\mu\mathrm{s})$). However, through collision with other molecules, the triplet state can also reverse the spin flip $T_1 \rightarrow S_1$. Moreover, due to its long lifetime, it is possible that two molecules with triplet states combine creating both a singlet ground and excited state:

$$T_1 + T_1 \rightarrow S_0 + S* \,. \tag{3.1}$$

Since the time scale of the transition $T_1 \rightarrow S_1$ through molecular collisions is large, the emission of fluorescence light is in both cases delayed w.r.t. the direct emission.

In multi-component scintillators, one or more *fluors* are added in order to prevent self-absorption of the solvent. Their purpose is to absorb the fluorescence light emitted by the solvent and shift it to longer wavelength regions where the scintillator is transparent. A detailed description of the multi-component scintillation process can be found in [70]. For the understanding of the system, long-lived triplet states of both solvent and solute can be ignored.

As the concentrations of the fluors are small ($\mathcal{O}(\mathrm{g}/\ell)$), mainly molecules of the solvent are excited when a charged particle crosses the scintillator. As mentioned before, higher excited triplet states and vibrational levels will quickly relax to S_1. However, since the lifetime of the transition $S_1 \rightarrow S_0$ is large ($\mathcal{O}(10\,\mathrm{ns})$), it competes with two other processes. First, the energy can be transferred through collisions to another solvent molecule (*energy hopping*). Secondly, the $S_{1,solute}$ level of the solute can be excited via the dipole-dipole interaction [69, 71]. $S_{1,solute}$ can also be populated when fluorescence photons with $\lambda_{solvent}$ emitted from the solvent are absorbed by the solute.

If no other fluor is present, the excited state of the solute will decay radiatively or non-radiatively to the ground state. As the wavelength of the emitted photos will be longer than

$\lambda_{solvent}$, it is less likely to be absorbed. If a third fluor is added, it is excited analogously to the processes described above.

The light output that is observed after an interaction of a charged particle in the scintillator is a measure for energy deposit that has been transferred in this process. It is an important parameter, as it has direct influence on the energy threshold and the energy resolution of the detector.

3.2 Scintillator properties

3.2.1 Quenching

As stated in section 3.1, there are various processes in the conversion of excitation energy to fluorescence light where energy is dissipated. This happens for example via non-radiative decays or ionization. Therefore, less energy than deposited is measurable in the light output. This effect is referred to as *quenching*. Quenching largely depends on the particle type and the ionization and excitation density. The light output per unit length $\frac{dL}{dx}$ is linked to the energy deposit per unit length $\frac{dE}{dx}$ via the semi-empirical Birk's equation [69]

$$\frac{dL}{dx} = \frac{A\frac{dE}{dx}}{1 + kB\frac{dE}{dx}} \tag{3.2}$$

Here, A denotes the unquenched light output. The relation between $\frac{dE}{dx}$ and the ionization density is described by kB. Both parameters are unique for every scintillator and particle and have to be measured experimentally. The energy deposit per unit length $\frac{dE}{dx}$ can be derived from the Bethe-Bloch equation [21].

The quenching effect is most prominent for small ionization densities, i.e. for low-energy electrons or heavier particles such as protons and αs. At high energies, quenching gets minimal and the light output is proportional to the energy deposit.

A more experimental description of the quenching effect is given by the definition of the quenching factor QF. It relates the visible energy of an energy deposit of one particle type p to another, commonly electrons, since their quenching is negligible at higher energies.

$$QF = \frac{E^{p}_{vis}}{E^{e^-}_{vis}} \tag{3.3}$$

This parameter delivers an effective description of the quenching processes, also taking into account secondary particles whose production is neglected in eq. (3.2).

3.2.2 Scintillation pulse shape

The scintillation pulse shape is the key for understanding the particle identification methods described in chapter 5. This particle discrimination is a very powerful tool for background reduction, e.g. for the DSNB [57]. The time evolution of the number of fluorescence photons $n(t)$ can be described by an exponential decay

$$n(t) = n_0 \cdot exp\left(-\frac{t}{\tau}\right), \tag{3.4}$$

where n_0 is the number of excited states at $t = 0$ that decay radiatively and τ the decay time constant of the process $S_1 \rightarrow S_0$ of the fluor. However, as described above, other exited states and processes also contribute to the scintillation mechanism. They are usually accounted for with additional exponential term to the photon probability density function (PDF):

$$n(t) = \sum_i n_{,i} \cdot exp\left(-\frac{t}{\tau_i}\right). \tag{3.5}$$

Here, $n_{,i}$ denote the amplitudes of the corresponding decay time τ_i. Usually, the fastest process is dominating the photon emission, i.e. $n_1 > n_i, i \geq 2$. Unlike the decay times, the amplitudes depend on $\frac{dE}{dx}$. Therefore the PDF is different for every particle type and can be used to distinguish for example neutron-induced proton recoils from γ-induced electron recoils.

3.2.3 Emission spectra

As noted before, the emission and absorption spectra of the solvent largely overlap [70]. Therefore, one or more fluors are added in order to shift the wavelength to higher regions where the solvent is transparent. As the photons are detected with photomultiplier tubes (PMTs), the spectrum of the emitted photons (maximum $\sim$ 340 nm) have to match the spectral sensitivity of the photo cathode. As it peaks around 350 nm for standard bialkali PMTs with borosilicate window, they offer a good choice.

3.2.4 Attenuation

Attenuation describes both scattering and absorption processes that occur for fluorescence photons propagating through liquid scintillator. In general, these effect are decreasing

with increasing wavelength. Rayleigh scattering in scintillator molecules and absorption(-reemission) processes because of impurities are most dominant. A detailed description of these processes and the determination of absorption and scattering lengths can be found in [61]. The attenuation has a major impact on the detector geometry of large-scale detectors. Absorption processes reduce the number of photons emitted, and thus decrease the effective light yield of an event signal. Consequently, the energy-threshold increases and the energy resolution - proportional to the number of photons - deteriorates. Hence, the diameter of a detector has to be adjusted to the attenuation length.

3.2.5 Radiopurity

In order to maintain a low-energy threshold and suppress possible background sources for low-rate measurements, radioactive impurities in the liquid scintillator have to be minimized. After production of the scintillator, it is exposed to cosmic rays and is also subject to surface contamination in the storage vessel. Therefore, purification plants are necessary. Polar contaminations can be removed with the help of water-extraction. This technique has already been used successfully in the Borexino experiment [52], reaching ultra-pure environments with $\mathcal{O}(10^{-17}\,\mathrm{g/g})$ ^{238}U and $\mathcal{O}(10^{-18}\,\mathrm{g/g})$ for ^{232}Th and ^{40}K. An intrinsic background is originating from ^{14}C β-decay, with an endpoint of 156 keV and a rate dominating all neutrino signals below this value.

3.3 Scintillator Components

Organic liquid scintillator consists of a solvent and an admixture of one or more wavelength shifters, where both are scintillating organic compounds. In this section, the components of the scintillator mixtures investigated under neutron irradiation in chapter 5 are introduced. In the center of interest is the mixture of linear alkylbenzene (LAB) with $3\,g/\ell$ 2,5-Diphenyloxazole (PPO) and $20\,mg/\ell$ 1,4-bis-(o-methylstyryl)-benzole (bisMSB).

3.3.1 Solvents

Linear alkylbenzene (LAB) has first been investigated for the SNO+ R&D [54]. It does not consist of a single compound but is a mixture of alkyl-benzenes with carbon chains of different length. Figure 3.1 shows the chemical structure of one compound.

LAB exhibits a high light yield and long attenuation length of about 20 m [72]. Thanks to its relatively high flash point of 140 ℃, it is uncomplicated in liquid handling. Moreover it is not considered hazardous according to the Hazardous Materials Identification System

(HMIS) rating and is largely biodegradable. Since LAB is industrially produced for the use in detergents, it is easily available and considerably cheap. In table 3.1, the main properties of LAB are listed and the chemical structure of one LAB molecule is shown in figure 3.1. For this study, LAB has been purchased from two different companies, Petresa [73] and Helm [74].

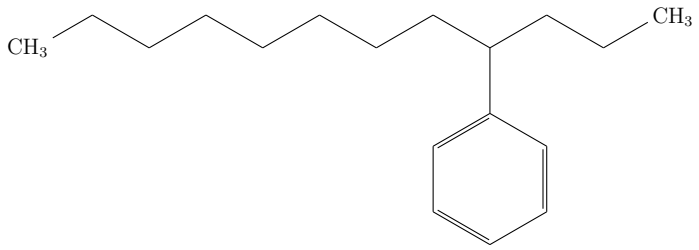

Figure 3.1: Chemical structure of one LAB

short name	**LAB**
solvent name	linear alkylbenzene
chemical formula	$CH_3-(CH_2)_n-CH[C_6H_5]-(CH_2)_m-CH_3$ (n+m=7-10)
density [kg/ℓ]	0.863
flash point [°C]	140
CAS number	67774-74-7
absorption maximum[nm]	260
emission maximum [nm]	283

Table 3.1: Properties of LAB.

A non-scintillating solvent is n-paraffin. It consists of linear hydrocarbons with 10-13 carbon atoms and is also used for the production of LAB itself. It is used as an admixture to LAB in order to increase the number of free protons in the scintillator. This is especially beneficial for the proton decay search and all electron anti-neutrinos detected via the inverse β decay channel. n-Paraffine can also be added to adjust the density of the liquid scintillator in order to minimize buoyancy forces in multi-vessel experiments like Double Chooz [14].

name	**n-Paraffine**
chemical formula	C_nH_{2n+2} (n=10-13)
density [g/cm^3]	0.749
flashpoint [°C]	70
CAS-number	929-018-5

Table 3.2: Properties of n-paraffin.

3.3.2 Fluors

A common primary fluor is *2,5-diphenyloxazole* (PPO), a powder which is added in small quantities of a few g/ℓ. As shown in table 3.3, the absorption maximum is in the emission range of LAB. As is has a relatively small *Stokes* shift of $\sim 60\,\text{nm}$, PPO is usually combined with a secondary wavelength shifter like *1,4-bis-(o-methylstyryl)-benzole* (bisMSB). Its properties are also listed in table 3.3. The function of bis-MSB is to further shift the absorbed light towards longer wavelengths, where the solvent is even more transparent. In order to prevent self-absorption, only few mg/ℓ are dissolved in LAB.

short name	**PPO**	**bisMSB**
fluor	2,5-Diphenyloxazole	1,4-bis-(o-methylstyryl)-benzole
chemical formula	$C_{15}H_{11}NO$	$C_{24}H_{22}$
cas number	92-71-7	13280-61-0
company	Perkin-Elmer [75]	Perkin-Elmer [75]
absorption wavelength [nm]	303	345
emission wavelength [nm]	365	420

Table 3.3: Properties of PPO and bisMSB.

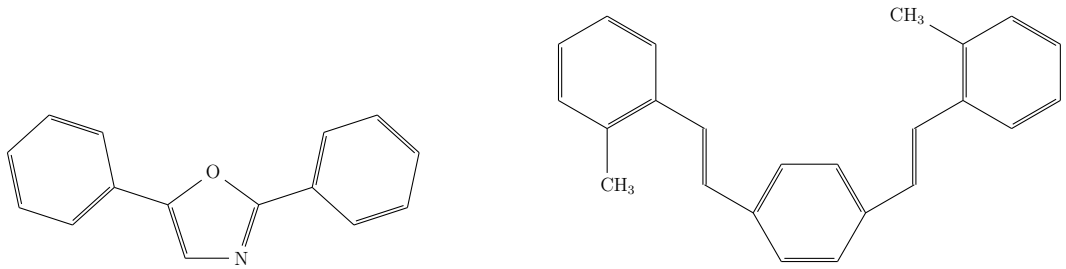

(a) **(b)**

Figure 3.2: Chemical structure of (a) PPO and (b) bisMSB

3.4 Sample Preparation

All scintillator mixtures mentioned in table 3.4 have been prepared in the laboratory in Garching. In order to minimize the risk of oxygen-induced degradation, all samples have been purged with nitrogen before storing it in a cool and dark place. The filling of the scintillator into the container for the neutron scattering experiment is done in glove bags under nitrogen atmosphere. Here, the oxygen level is kept lower than 1%, checked with a small oxygen monitor [76]. The scintillator preparation of the oxidated samples is described in [77]. They have been in contact to air for different amounts of time, after which they have been stored in a glass vessel with a nitrogen blanket on top.

Table 3.4 list all LS mixtures used in the neutron beam experiment described in chapter 4 and and analyzed in chapter 5. The favored LENA mixture, LAB + 3 g/ℓ PPO + 20m g/ℓ bisMSB, is in the center of attention. LAB from the providers Helm [74] and Petresa [73] has been under investigation as well as aged samples. In all mixtures, 2,5-diphenyloxazole (PPO) and 1,4-bis-(o-methylstyryl)-benzole (bis-MSB) from Perkin-Elmer [75] are used in varying concentrations.

short	solvent 1 (provider)	solvent 2 (provider)	PPO	bis-MSB	comment
LH3	LAB (Helm)		3 g/ℓ	20 mg/ℓ	LENA standard
LH3*	LAB (Helm)		3 g/ℓ	20 mg/ℓ	LH3 used in reproducibility test
LH10	LAB (Helm)		10 g/ℓ	20 mg/ℓ	
LP	LAB (Petresa)		3 g/ℓ	20 mg/ℓ	(F1 from [77])
LP1d	LAB (Petresa)		3 g/ℓ	20 mg/ℓ	24 h aged (F3 from [77])
LPmax	LAB (Petresa)		3 g/ℓ	20 mg/ℓ	35 d aged (F7 from [77])
DCMV	51.6% LAB (Petresa/Helm)	48.4% n-paraffin (CBR)	2 g/ℓ	20 mg/ℓ	Double Chooz muon veto scintillator [78]
L50	50% LAB (Helm)	50% n-paraffin (CBR)	3 g/ℓ	20 mg/ℓ	

Table 3.4: List of all organic liquid scintillators investigated in the beamtime in August 2012. As main solvent, linear alkyl benzene (LAB) from the providers Helm [74] and Petresa [73] is used. In the case of DCMV, the LAB (Petresa) is used for the master solution and LAB (Helm) for dilution. The non-scintillating n-paraffin from the company CBR [79] helps to adjust the density of the scintillator. Moreover, an admixture increases the number of protons in the LS, which is beneficial for the inverse beta decay channel. In all mixtures, 2,5-diphenyloxazole (PPO) and 1,4-bis-(o-methylstyryl)-benzole (bis-MSB) from Perkin-Elmer [75] are used in varying concentrations. A detailed description of the preparation of the samples LP, LP1d, and LPmax can be found in [77], along with the characterization of their optical properties.

Chapter 4

Neutron Scattering Experiment at Maier-Leibniz-Laboratorium

The characterization of a liquid scintillator (LS) is crucial for the estimation of the potential of future LS detectors such as LENA [80]. Little is known of parameters like energy quenching and pulse shape of proton recoils. Experimentally, these recoils can be induced by neutron irradiation. Lighter and charged particles are more likely to excite the electrons of the scintillator, while heavier particles would loose most of their energy reacting with the carbon nuclei.

There are two major experimental methods for the determination of proton recoil quenching factors and pulse shape. One option is the use of neutron sources such as AmBe or ^{252}Cf [81]. Their energies reach up to about 10 MeV, which is in the region of interest for low-energy neutrino physics. A more sophisticated approach is provided by neutron production in (p,n)-reactions at accelerators. Given a pulsed beam, it has the advantage that neutrons are easy to tag with the help the *time-of-flight* (ToF) technique.

In this chapter, the experimental setup of the neutron scattering experiment is introduced, hosted at the Maier-Leibniz-Laboratorium (MLL) in Garching. The accelerator facility is described in the first section in detail, starting from the ion source and ending at the neutron production in the hydrogen cell. In the second section, the scintillator detector unit is presented, including electronics and the data acquisition system. A special focus is set on the description of the time-of-flight method which is central to the experiment. In the last two sections, data handling, calibration, and validation are discussed.

4.1 The MLL accelerator lab

The Maier-Leibniz-Laboratorium (MLL) in Garching is the host of a tandem accelerator. With its maximum voltage of 2 × 15 MV it is well-suited for the study of processes in an organic liquid scintillator in the MeV regime. It has already been used in former quenching factor studies of proton recoil events in organic liquid scintillators [78, 82]. In order to measure the pulse shape of proton recoils as well, the experiment has been continuously improved. Most importantly, the electronics and the data acquisition system have been upgraded and the size of the scintillator sample enlarged in order to improve statistics. The beamtimes for the experiments described in this work have been shared with the quenching factor measurements done for the direct dark-matter search experiment CRESST [83, 84, 85, 86].

A floor plan of the MLL is depicted in 4.1. In the following, the experimental setup will be described starting at the ion source and following the accelerator beam line up to the hydrogen cell.

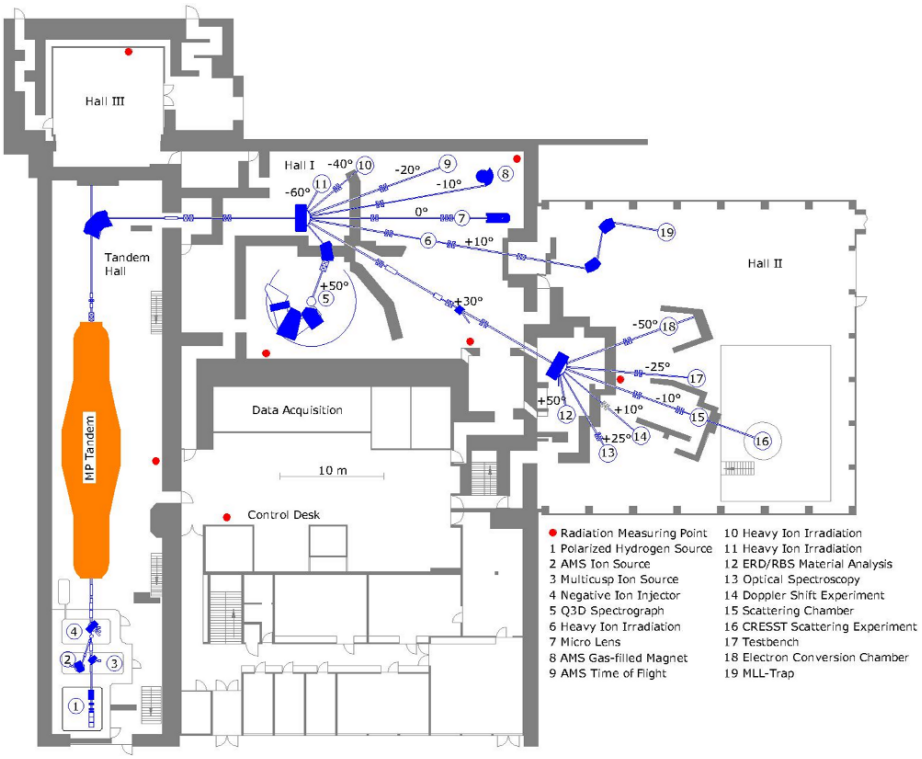

Figure 4.1: Floor plan, beam lines, and experimental sites of the Maier-Leibniz-Laboratorium in Garching. The negative boron ions are generated at (4) and guided through the Van-de-Graaff accelerator tank to the CRESST scattering facility (16), where the LS detector unit is placed as well [87].

4.1.1 Ion source

In order to benefit from the full potential of the tandem accelerator, negative ions have to be generated first. This can be done with a variety of elements in the negative ion injector. In the case presented here, a solid, cone-shaped boron source is used. Heating a solid caesium sample and with the help of an ionizer at $\sim 1400\,℃$, Cs^+ ions are obtained. These Cs^+ ions are accelerated onto the source, knocking out ^{11}B atoms. Due to the heater, a thin layer of neutral Cs atoms also settles on surface of the boron sample. Because of their higher electronegativity, the boron atoms are likely to pick up the outermost electron from the caesium, creating negatively charged ^{11}B ions which are then preaccelerated by the extraction voltage and progress to the chopper.

4.1.2 Pulsing

In order to perform a time-of-flight measurement a pulsed beam is necessary. This is done with the help of the low-energy chopper and the adjacent buncher [88]. The performance of these elements, i.e. the pulse width and rate, directly influences the accuracy of the experiment.

The low-energy chopper works like an electromagnetic steerer common at accelerators. A total number of five AC coupled capacitors deflect the beam, while only a small aperture allows the beam to pass. The frequency of the pulsing can be adjusted to $2.5\,\mathrm{MHz}/2^i$ ($i \in \mathbb{N}$), whereas i is commonly referred to as *Untersetzung*. During most runs, the chopper was adjusted such that $i = 3$, i.e. the time difference between two subsequent ion bunches was $\sim 3.3\,\mu s$. In this beamtime, the Untersetzung could not be decreased further than three, as the decay times of the $CaWO_2$ crystals of the parallel running CRESST quenching factor measurement are already in the regime of $\mathcal{O}(\mu s)$.

The task of the buncher is to compress the pulses coming from the chopper. It consists of beam-enclosing tubes to which a saw-tooth voltage is applied, approximated by the superposition of 5 and 10 MHz AC sine voltages. As a result, ions in the onset of the pulse are decelerated while ions in the tail are accelerated, making the final bunch more compact. For this purpose, amplitude and phase of the buncher voltage must be adjusted appropriately with respect to the chopper. At best, the pulse width can be adjusted between 2-3 ns.

As described, the buncher voltage is synchronous to the ^{11}B ion pulses. Therefore, a logic signal is diverged here in order to get the timing information needed for the time-of-flight measurement.

4.1.3 Accelerator and ion beam guidance

After chopper and buncher, the ions are guided to the tandem van-de-Graaff accelerator tank. This linear accelerator takes advantage of the applied voltage twice. The negatively charged ions pass the potential for a first time until they arrive at the stripper foil in the middle of the tank. This thin carbon foil strips off electrons, producing positively charged ions. Then, these ions are accelerated a second time towards the end of the tank.

In the following 90 degrees magnet, a specific energy and degree of ionization can be filtered. In our case, $^{11}B^{5+}$ ions with an energy of 61.5 MeV (6× $\sim$ 10.2 MV potential difference) are selected. The monoenergetic pulsed beam is then guided towards the experimental site, focused by several quadrupole magnets.

4.1.4 Gaseous hydrogen target

At the end of the beam line is a gaseous hydrogen target. It is contained in a small cylindrical cell with 1 cm in diameter and 3 cm long, operated at a pressure of about 2 bar. Here, the neutrons are produced via [89]

$$^{11}\mathrm{B} + p \rightarrow {}^{11}\mathrm{C} + n \tag{4.1}$$

A thin molybdenum foil ($\sim$ 5 μm) separates the cell from the vacuum of the beam line. Ions that pass the cell without interaction are stopped by a gold beam stop at the end of the cell. As shown in [90], the low-energy neutron background produced in ^{197}Au is comparably small.

In order to gain a high yield and high neutron energy while avoiding inelastic scattering, an ^{11}B energy of 55.4 MeV is chosen [89]. Accounting for the average energy losses in both the Mo window (4.9 MeV) and the H_2 target (1.3 MeV) [84], the initial beam energy thus translates to 61.5 MeV. As stated before, this corresponds to a nominal accelerator voltage of 10.2 MV.

Synchronously to the neutrons, Bremsstrahlung is produced by the ^{11}B ions in the H_2 cell. These γ-rays play a crucial role for the time-of-flight measurement, as explained in more detail in section 4.3.1.

4.2 Liquid-scintillator scattering experiment

4.2.1 Liquid-scintillator detector unit

The LS detector unit consists of two main parts: the container for the liquid scintillator and a photomultiplier tube (PMT) to collect the emitted photons. A photograph and cross-section can be seen in figure 4.2. It has been designed together with V. Zimmer [91] and modeled by a workshop.

The unit is designed such that it meets best the requirements of a beamtime experiment. It is important that the scintillator container can be changed fast and easily. As beamtimes are limited to 7-10 days, only a highly effective use of the facility allows to characterize a great variety of different scintillator mixtures. For this reason, two identical containers have been manufactured in the workshop. Hence, a new sample can be prepared while the other container is still mounted acquiring taking data. The filling procedure is described chapter 3. Moreover, the detector unit is quite handy and thus easily movable. This allows to measure neutron induced recoils at different angles with respect to the beam line. In this way different maximum neutron energies are accessible which is beneficial for the determination of the proton recoil quenching factors.

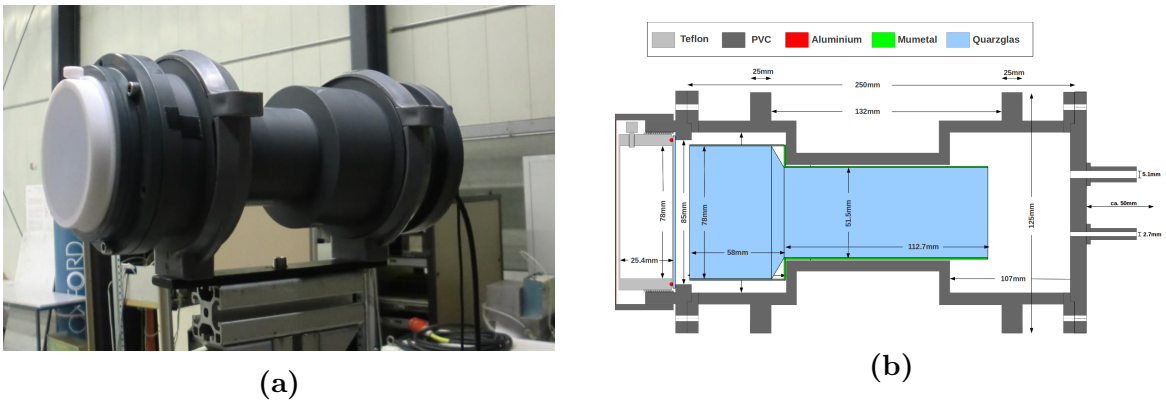

(a) (b)

Figure 4.2: Photograph (a) and cross-section (b) of the LS detector unit. For the picture, the aluminum lid has been removed in order to see the polytetrafluoroethylene (PTFE) cell. The detector unit has been customized by the workshop in order guarantee light-tightness. Towards the photo cathode, the PTFE container can be easily attached. Since PTFE is not perfectly light-tight, a thin aluminum sheet is put atop. On the other side, towards the multiplier base, feed-throughs for HV and signal cable also ensure light-tightness.

The scintillator container is made of polytetrafluoroethylene (PTFE), as this material is chemically inert to the organic liquid scintillator (cf. fig. 4.3 (a)). Reflecting very well photons around 430 nm [92], it also increases the photon collection efficiency. The container

has a cylindrical shape, featuring one open side for a window. The diameter is chosen such that it matches the diameter of the photomultiplier (PMT) which is 3 inches. The height is $\sim$ 2.5 cm, thus about 150 ml of scintillator material is needed. The bottom of the PTFE container is very thin, in order to minimize neutron scattering within the material. Therefore, a thin aluminum lid is put over it to guarantee light-tightness. On the rim of the PTFE cell, a small hole has been drilled. It is used to fill the detector and can be sealed with a Teflon screw.

A threaded rim allows to attach the PTFE part to the polyvinyl chloride (PVC) flange. A window is fixed between these two components. It is made of quartz glass in order to minimize the photon absorption around 430 nm. With the PVC flange, the LS cell can be attached to the PMT holder. Several screws ensure light-tightness, stability, and reproducibility. Between the PMT cathode and the quartz glass, there is a small air gap of a few millimeters.

(a) **(b)**

Figure 4.3: PTFE LS cell (a) and permalloy (b). Both have been customized in the workshop to meet the dimensions of the photo multiplier. Teflon has been chosen for the cell as it is inert towards liquid scintillators and features a high reflectivity around 430 nm. The mu metal was installed to compensate for magnetic fields.

The PMT (type ETEL 9822 KB [93]) is held by a customized PVC housing which also serves as a light barrier. A point-welded thin mu metal has been manufactured in order to minimize the magnetic field influence on the PMT performance (cf. fig. 4.3 (b)). Before installation, it has been tempered under hydrogen atmosphere at over 1000℃ at the Vakuumschmelze Hanau [94]. The PMT is operated at 1790 V, which is at the minimum specified for this type, in order to ensure linearity throughout the whole energy range. The calibration of the detector confirms this behavior as shown in fig. 5.12 in chapter 5. The small time jitter of 2.2 ns specified enables a good pulse-shape resolution and time-of-flight determination accuracy.

All different parts flanged or put together are further sealed with black tape. Finally, the whole detector unit is kept under black felt during measurements.

4.2.2 Experimental setup

A top view of the experimental setup can be seen in figure 4.4. In order to have access to different (maximum) neutron energies, the detector unit was mounted on an Item rail [95]. In total eight different positions were marked, between 2.8°and 30.9°, cf. table 4.1. In order to determine the respective neutron energies, the distance from each position to the hydrogen cell has been measured with a laser distance meter [96]. Up to position 6, the line of sight is blocked by the cryostat of the CRESST scattering facility. Hence, triangulation is used to calculate the distance, giving rather large errors.

The wide range of incident neutron energies allows to determine the energy-dependent quenching factor for proton recoils in a simple way. Since only the shoulders of the proton recoil spectra have to be fitted. In figure 4.5, the dependency of the incident neutron energy E_{tof} is shown as a function of the angle to the beam axis. The kinematic model qualitatively fits to the measured data. As can be seen, larger angles offer a larger spectrum of incident neutron energies. Hence, a wider energy range for the determination of the quenching factors can be used.

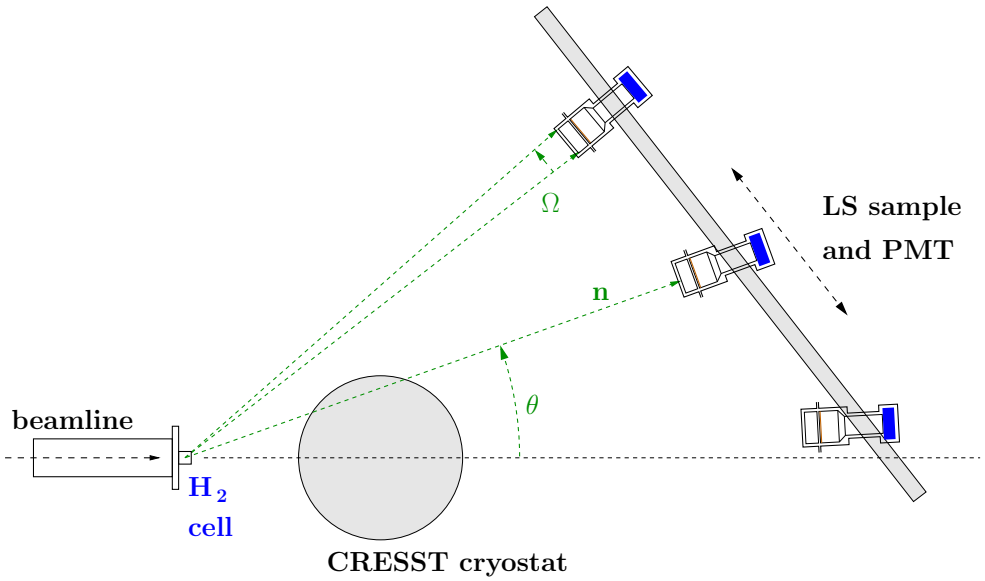

Figure 4.4: Sketch of the detector setup at the Maier-Leibniz-Laboratorium in Garching. The $^{11}B^{5+}$ ions enter from the left, producing neutrons in the hydrogen target. The detector unit is mounted movable onto an Item rail [95], such that the angle θ relative to the beam axis can be easily changed. In this way, recoil spectra can be recorded for different maximum neutron energies. Since the beamtime was shared with the CRESST experiment, the LS detector was shadowed by their cryostat for most positions.

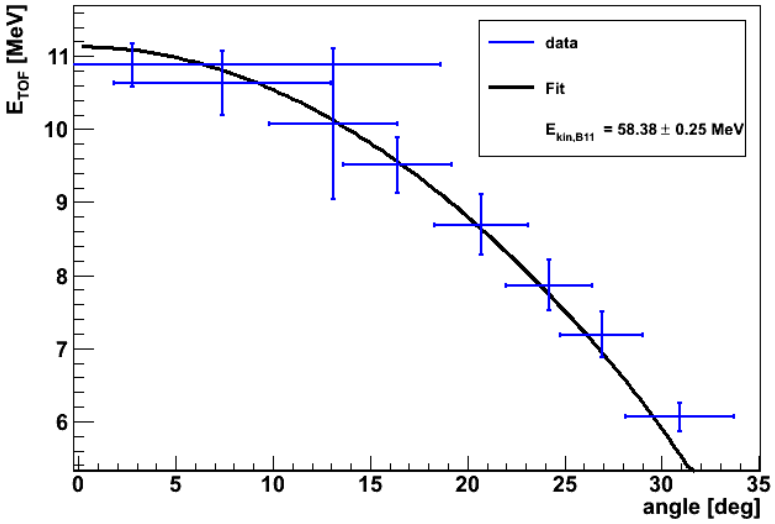

Figure 4.5: Maximal neutron energies for all positions, derived from the time of flight and distance according to Eq. (A.7) and fitted with kinematically expected dependency according to Eq. (A.4).

position	d [cm]	ϑ [deg]	$t_{n,calib}$ [ns]	E_{tof} [MeV]
0	327.6 ± 3.8	2.8 ± 15.8	72.4 ± 2.5	10.9 ± 0.5
1	296.1 ± 3.4	7.4 ± 5.6	66.2 ± 2.8	10.6 ± 0.6
2	267.9 ± 3.1	13.1 ± 3.3	61.5 ± 4.6	10.1 ± 1.0
3	254.6 ± 2.9	16.4 ± 2.8	60.1 ± 2.8	9.5 ± 0.6
4	240.3 ± 2.7	20.7 ± 2.4	59.3 ± 3.2	8.7 ± 0.6
5	231.3 ± 2.7	24.2 ± 2.2	60.0 ± 3.2	7.9 ± 0.6
6	224.9 ± 2.6	26.9 ± 2.1	61.0 ± 3.4	7.2 ± 0.6
7	216.9 ± 2.6	30.9 ± 2.8	64.0 ± 3.4	6.1 ± 0.4

Table 4.1: Distance d of the center of the hydrogen cell to the LS container center for each position, along with the respective angle ϑ with respect to the beam axis, the calibrated neutron time of flight $t_{n,calib}$ (cf. eq. (4.3)) and corresponding neutron energy E_{tof} (cf. eq. (4.4)).

4.3 Data acquisition

4.3.1 Time-of-flight technique

For the success of the scattering experiment, i.e. the determination of the quenching factor (see Eq. (3.3)), it is vital to know the energy of the incident neutrons. This information is reconstructed by measuring the difference in time between the neutron production in the hydrogen cell and the neutron scattering in the liquid-scintillator container. This method is widely referred to as the *time-of-flight* technique. In order to take advantage of this technique, a pulsed beam is necessary. The pulse width of 2-3 ns directly translates into the accuracy of the neutron energy determination. Therefore, in order to reconstruct the neutron energy at a high precision, enough data has to be collected. This is shown in the time-of-flight spectrum fig. 4.6a, where a neutron peak as well as a γ peak from Bremsstrahlung for the scintillator LAB (Helm) + $3g/\ell$ PPO + $20mg/\ell$ bisMSB (LH3, cf. table 3.4) can be observed.

As it is not possible to have a timing signal of the neutron production in the hydrogen cell, the neutron time-of-flight has to be reconstructed in a more complex way. As described in the following section 4.3.2, this is reflected in the electronic coincidence logic.

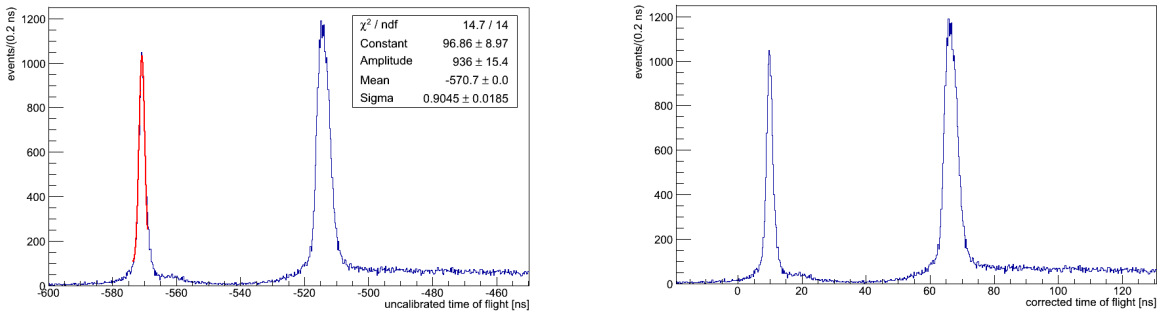

(a) **(b)**

Figure 4.6: (a) shows the uncalibrated, while (b) shows the calibrated time-of-flight spectrum for the scintillator LAB (Helm) + $3g/\ell$ PPO + $20mg/\ell$ bisMSB at position 1. Both the early γ peak and the neutron peak are very distinct. The tail of the neutron peak originates from slower neutrons, scattered in the surrounding. A Gaussian fit including background is performed in (a) in order to obtain the mean γ time of flight t_γ. The same is done for the neutron peak to get t_n. Finally, (a) can be converted to (b) via Eq. 4.3.

4.3.2 Electronics

A schematic diagram of the NIM-based[1] electronics can be seen in fig. 4.7. As there is no timing information from the neutron production, one has to take advantage of the logic signal provided by the buncher. As stated in section 4.1.2, the buncher signal is synchronous to the $^{11}B^{5+}$ bunches. However, there is an unknown time shift with respect to the neutron production at the H_2 cell. It is quite unlikely that a buncher signal and a coincident neutron scattering signal from the scintillator unit emerge from the very same bunch. However, connecting two different bunches in a coincidence constitutes no problem as long as the pulse rate and thus the time shift is stable. Therefore, the coincidence can be designed even such that a buncher pulse coming *after* the PMT pulse triggers the data acquisition, as shown in fig. 4.8.

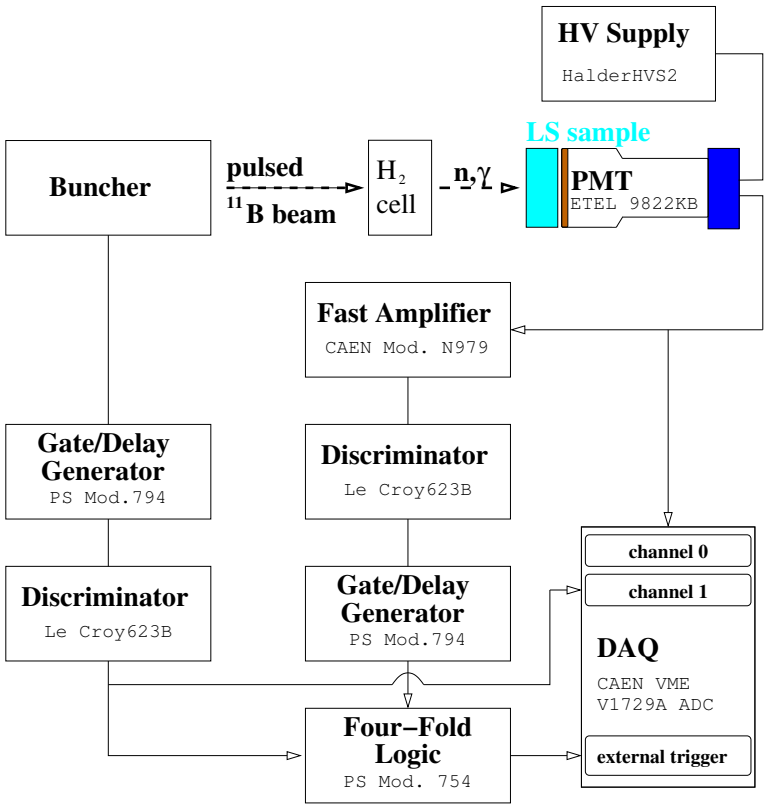

Figure 4.7: NIM-based electronics of the the coincidence measurement. Analog and digital signals are depicted with solid arrows, particles with dashed arrows. In order to obtain a coincidence between the buncher and the PMT signal, gate and delay units are necessary. The working principle of the trigger can be seen in fig. 4.8. While the trigger signal of the PMT is amplified by a factor of 10 in order to lower the threshold, the original signal is stored.

[1]Nuclear Instrumentation Module

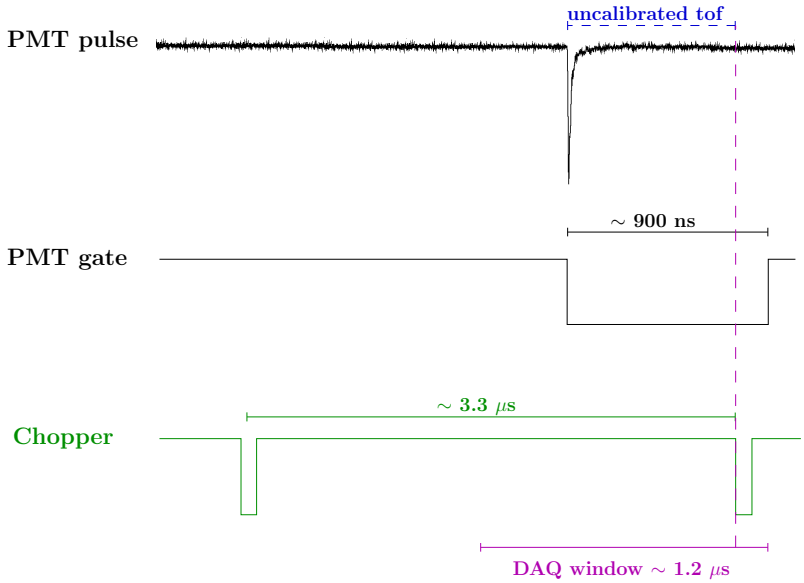

Figure 4.8: Working principle of the external trigger of the data acquisition. If a pulse is recorded in the LS cell, a gate generator opens window of ~ 900 ns. Its length has been determined experimentally and is well-suited to record both γ and neutron peaks in the time-of-flight spectrum for all detector positions. If a buncher signal arrives within this time window, the data acquisition is triggered.

In a voltage divider, the PMT signal is divided into a trigger and a signal branch, fed directly and unaltered into the analog-to-digital converter (ADC). After a tenfold amplification and discrimination, the signal is used to open a gate of about 900 ns. The buncher signal is delayed to make sure that the γ and neutron peak lie well within the acquisition window for all detector positions. Finally, the signals are merged in the logic AND-gate in order to create the trigger. Both the PMT and the buncher signal are recorded in order to reconstruct the particles' time of flight, which is more precise than using the trigger time.

The signals are recorded with a 14-bit CAEN V1729 switched-capacitor ADC [97] covering voltages between -1 and 1 V. It features a maximum sampling rate of 2 GS/s with an acquisition window of almost 1.3 μs.

All PMT and chopper pulses are fully stored in ROOT tree format [98]. Moreover, the VME electronics have been programmed such that several pulse features are computed online [2]. This allows to check data consistency already during data acquisition. Parameters such as the baseline and its errors and pulse height are stored. As a more precise measure for the energy deposit in the scintillator, the integral of the pulse is calculated:

$$charge = \int_{t0}^{t1} P(t)dt, \tag{4.2}$$

[2] in cooperation with D. Hellgartner and V. Zimmer

where $P(t)$ stands for the recorded PMT pulse. The integration start time $t0$ is defined as the time when the pulse first reaches 10% of the pulse height. Similarly, the integration end time is calculated. Since the time resolution of the ADC is 0.5 ns, linear interpolation is applied. Note that this start time is also used for the calculation of the time of flight.

Once triggered, both PMT and chopper channel are recorded. These two signals are used to reconstruct the time-of-flight spectrum offline. As noted above, the start time of the pulse is defined to be at 10% of the pulse maximum. Collecting all coincident scattering events leads to the time-of-flight spectrum. Thanks to the coincidence, the time difference between γ and neutron recoil events is already known. As the distance from the LS detector cell to the hydrogen cell has been measured, the calibrated neutron time of flight $t_{n,calib}$ can be determined with the help of the information from the γ peak:

$$t_{n,calib} = t_n - t_\gamma + d/c \tag{4.3}$$

Here t_n and t_γ denote the uncorrected time of flight, determined with Gaussian fits to the respective peaks. The distance d divided by the speed of light c corrects for the γ time of flight. A corrected tof spectrum can be seen in fig. 4.6b. The incident neutron energy can be calculated to

$$E_{tof} = \left(\left(1 - \left(\frac{d}{ct_{n,calib}} \right)^2 \right)^{-\frac{1}{2}} - 1 \right) m_n c^2 \tag{4.4}$$

Figure 4.9 shows the time-of-flight energy E_{tof} spectrum for a neutron peak for LH3 at position 0. It can be modeled very well with a normal distribution, taking into account the γ background with an exponential function, too.

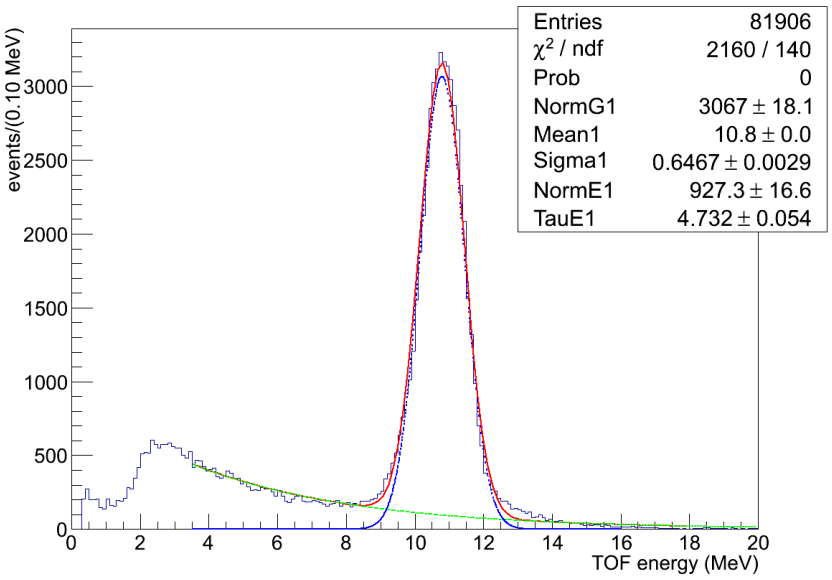

Figure 4.9: Energy spectrum of a neutron peak for the scintillator LH3 at position 0. With the help of a Gaussian fit, the mean incident neutron energy can be determined. The exponential background is due to γs.

Chapter 5

Particle identification

In the following chapter, the particle identification analysis of the neutron scattering experiments at the Maier-Leibniz-Laboratorium is presented. Various scintillator mixtures are characterized under both neutron beam and americium-beryllium (AmBe) source irradiation. As detector calibration and data validation are very important, they are discussed in detail. Afterwards, it is shown how the standard pulses for γ and neutron induced events are generated. The *Gatti* and *Tail-to-Total* (T2T) method are introduced and their efficiencies evaluated. Finally, the pulse shape parameters are determined with the help of fits.

5.1 Liquid-scintillator mixtures

In the course of the beamtime, several different organic liquid-scintillator (LS) mixtures have been studied. Main focus lies on the designated LS for the LENA experiment: linear alkylbenzene (LAB) as solvent and $3\,\mathrm{g}/\ell$ 2,5-diphenyl-oxazole (PPO) and $20\,\mathrm{mg}/\ell$ 1,4-bis-(o-methylstyryl)-benzene (bisMSB) as wavelength shifters. Information on the characteristics of the single compounds can be found in chapter 3. A list of all mixtures investigated in the beamtime in August 2012 is shown in table 5.1.

LAB from two different providers, Helm [74] and Petresa [73], is investigated in order to check for possible quality differences. Moreover, the admixture of non-scintillating n-paraffin is of interest. It is sometimes added to adjust the density of the LS mixture in order to minimize buoyancy forces in multi-vessel experiments like e.g. in the Double Chooz experiment [14]. While the light yield of the LS decreases adding n-paraffin (see chapter 3), the total number of free protons increases. Hence, the event rate of $\bar{\nu}_e$ detected via the inverse beta decay channel rises. The scintillator of the muon veto of the Double

short	solvent 1 (provider)	solvent 2 (provider)	PPO	bis-MSB	comment
LH3	LAB (Helm)		3 g/ℓ	20 mg/ℓ	LENA standard
LH3*	LAB (Helm)		3 g/ℓ	20 mg/ℓ	LH3 used in reproducibility test
LH10	LAB (Helm)		10 g/ℓ	20 mg/ℓ	
LP	LAB (Petresa)		3 g/ℓ	20 mg/ℓ	(F1 from [77])
LP1d	LAB (Petresa)		3 g/ℓ	20 mg/ℓ	24 h aged (F3 from [77])
LPmax	LAB (Petresa)		3 g/ℓ	20 mg/ℓ	35 d aged (F7 from [77])
DCMV	51.6% LAB (Petresa/Helm)	48.4% n-paraffin (CBR)	2 g/ℓ	20 mg/ℓ	Double Chooz muon veto scintillator [78]
L50	50% LAB (Helm)	50% n-paraffin (CBR)	3 g/ℓ	20 mg/ℓ	

Table 5.1: List of all organic liquid scintillators investigated in the beamtime in August 2012.

Chooz experiment (DCMV) has also been measured in the course of the beamtime, mainly in order to measure its proton recoil quenching factor. Nevertheless, it also offers a good comparison with respect to pulse shape discrimination.

A check for degradation effects due to oxidation is provided by the LS mixtures LP, LP1d, and LPmax. The preparation of these samples is explained in detail in [77], along with the characterization of their optical properties. In order to induce oxidation, the LS mixtures were exposed to air for one day (LP1d) and 35 days (LPmax) respectively. Finally, the samples were covered with nitrogen in order to stop the oxidation process.

Table 5.2 gives an overview of the detector positions used for data acquisition under neutron beam irradiation or each LS mixture. In order to be able to determine the quenching factor in a wide energy range, every LS sample was at least measured at a position at a small, medium, and large angle. Table 5.3 shows the calibration measurements for all LS mixtures. For ^{22}Na, data was taken with a higher threshold as well in order to specifically select the Compton edge of the 1.2 MeV decay γs. The AmBe source can be used for calibration and pulse shape discrimination purposes. As the priority lay on to record data with the pulsed neutron source, not every scintillator mixture was subject to irradiation from the AmBe source. All neutron beam and calibration source data for each LS mixture was acquired using the identical sample. An exception is the LH3* sample that is used to check the reproducibility of the system.

LS mixture	P 0	P 1	P 2	P 3	P 4	P 5	P 6	P 7
ϑ [deg]	2.8 ± 15.8	7.4 ± 5.6	13.1 ± 3.3	16.4 ± 2.8	20.7 ± 2.4	24.2 ± 2.2	26.9 ± 2.1	30.9 ± 2.8
LH3	×	×	×	×	×	×	×	×
LH10		×			×			×
LP		×			×			×
LPmax		×			×			×
DCMV	×	×	×	×	×	×	×	×
L50	×		×	×	×	×	×	×

Table 5.2: Scintillator samples and detector positions P0-P7 for data acquisition under neutron beam irradiation during the beamtime in August 2012. Every sample was at least measured at small, medium and large angles in order have a wide range of (maximum) proton recoil energies.

source type	Cs137	Na22		welding	AmBe	
energy threshold		low	high	rods	low	high
LH3	×	×	×	×	×	×
LH3*	×	×	×	×	×	×
LH10	×	×	×	×	×	×
DCMV	×	×	×	×	×	×
L50	×	×	×	×	×	×
LP	×	×	×	×		
LPmax	×	×	×	×	×	×
LP1d	×	×	×	×	×	×

Table 5.3: Runs that were recorded under irradiation of radioactive sources for different scintillator samples. The γ sources ^{137}Cs, ^{22}Na, and the welding rods are used for detector calibration and for linearity testing. For the same reasons, the γ and neutron emitting americium-beryllium source is also used to check the γ/n pulse shape discrimination. All source runs were taken during the beamtime with exactly the same sample used for the beam runs. As the priority was to record data with the pulsed neutron beam, not every scintillator mixture was subject to AmBe irradiation. LH3* refers to a reproducibility test at the end of the beamtime with the scintillator mixture LH3, however with a newly filled cell.

5.2 Data handling

Before starting with the particle identification analysis, the data has to be validated, filtered, and selected. The validation already starts during data acquisition, when the time-of-flight (ToF) spectrum, the proton recoil spectrum, and the event rate are monitored.

5.2.1 Pulse Reconstruction

In figure 5.1, an inverted photo multiplier (PMT) pulse recorded by the data acquisition system (DAQ) is shown in order to illustrate the raw pulse parameters used in the following section. The height of the *baseline* and its error are determined in a region well before the pulse onset. The *pulse height* denotes the difference between the baseline and the maximum of the pulse. The *pulse onset time* or *start time* is defined as the time when the pulse reaches 10% of the pulse height and is used for the measurement of the particles' time of flight. In order to have a more precise measure for the energy than the pulse height, the *charge* variable is introduced. It is calculated by the integral of the pulse between the start time and the time when the pulse falls below 10% of the pulse height.

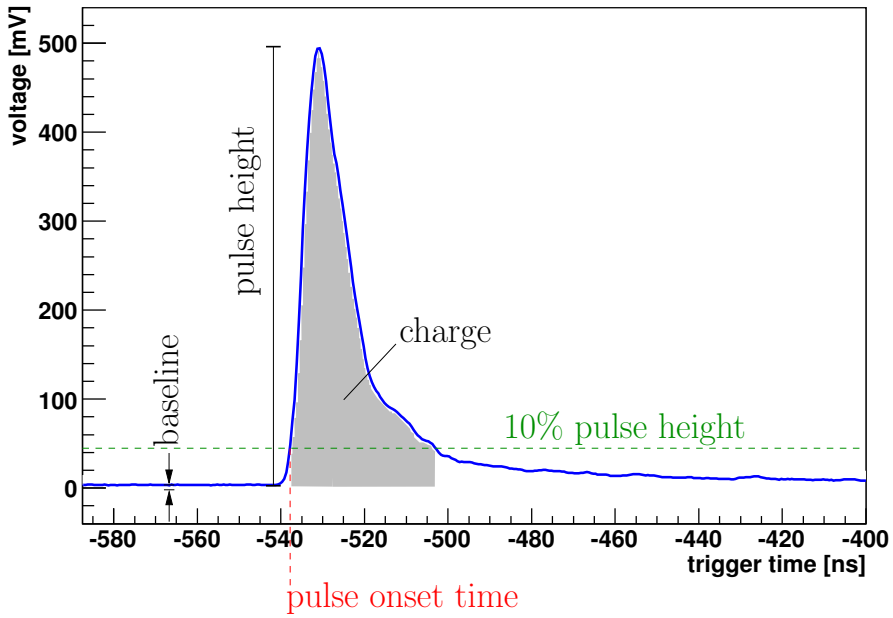

Figure 5.1: (Inverted) PMT voltage signal illustrating the definition of pulse parameters used in this thesis.

5.2.2 Data selection

The goal of the data selection is to obtain clean samples of γ and neutron induced scattering events in the LS sample, rejecting time periods with no ^{11}B beam, background, and 'strange' events such as double pulses. The selection of the data for beam runs is carried out in two basic steps.

First, the beam run quality is checked by monitoring the rate of events belonging to the neutron peak. These events are selected via a Gaussian fit to the ToF spectrum, with events in the region $\pm 1\sigma$ around the fit maximum being accepted. Saturated pulses and background noise are rejected from the data by a cut on the pulse height. If the rate drops below 2/3 of the mean rate, events are cut off from the data sample. The cut has been determined by visually validating the temporal behavior of the neutron peak rate. An example for the stability of the rate can be seen in fig. 5.2. Reasons for drops are manifold, i.e. small beam-off times due to maintenance, changes in pulsing, or even sparks within the accelerator tank. In average around 10% of the events are rejected, depending on the scintillator mixture.

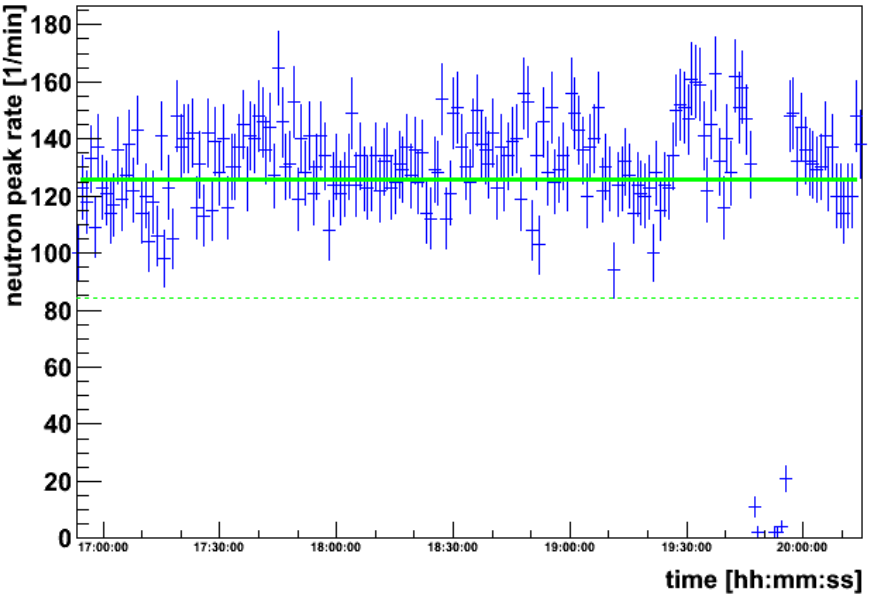

Figure 5.2: Neutron peak rate monitor for a run with LAB (Helm) $+3g/\ell$ PPO $+20mg/\ell$ bisMSB where the detector was at position 5 ($\sim 24°$). The solid green line depicts the value of a fit with a single constant p_0, the dashed green line the cut at $\frac{2}{3}p_0$. The rate is stable except for a short period of 10 minutes when no beam was present.

In average, the neutron peak rate varies between 1-3 Hz, while the total event rate in

the scintillator sample ranges from 6 Hz to 14 Hz, increasing towards larger angles (see fig. 5.3a). As one can see in fig. 5.3b, the relative neutron rate slightly decreases with increasing angle.

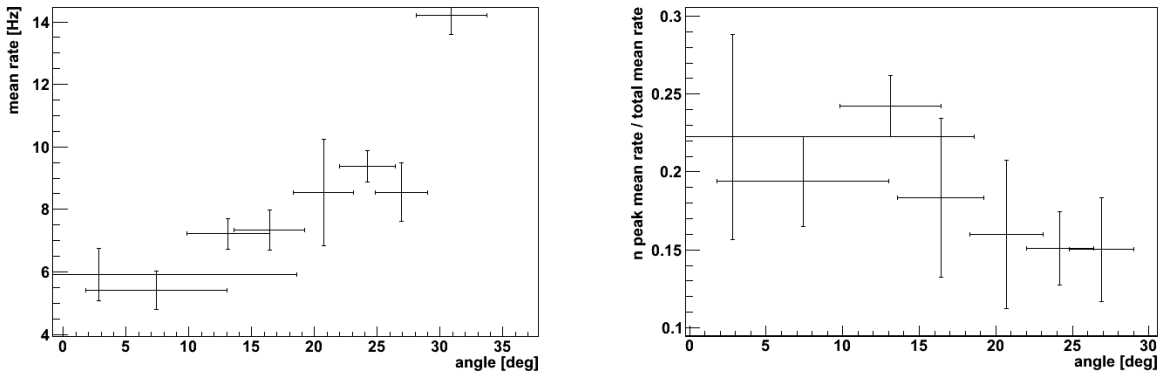

(a) **(b)**

Figure 5.3: Angular dependence of mean rate (a) and ratio of the neutron peak rate to the mean rate (b) combining all beam runs for all LS mixtures and positions.

In a second step, the quality of the pulses that passed the first filter is checked. The cut variables are

- charge-to-height ratio
- baseline stability
- risetime
- pre pulses
- double pulses

Both charge-to-height ratio, baseline, and risetime distributions are fitted with a normal distribution. Events within 2σ of the mean value are accepted. Moreover, algorithms filter pre and double pulses from the data samples. For higher energies, these cuts are minimal, each leaving $\sim 99\%$ of the residual events after the first filter for LAB (Helm) $+ 3g/\ell$ PPO $+ 20mg/\ell$ bisMSB (see fig. 5.4). Less than $\sim 6\%$ of the events are lost due to beam issues tagged by neutron peak rate stability monitoring.

While the first two steps' main purpose is to reduce background, the disentanglement of γ and neutron induced recoil events requires further cuts. First, taking advantage of the ToF technique, it is possible to identify any event within the γ and neutron peaks with the respective particle. However, the neutron sample is still interspersed with γs and vice

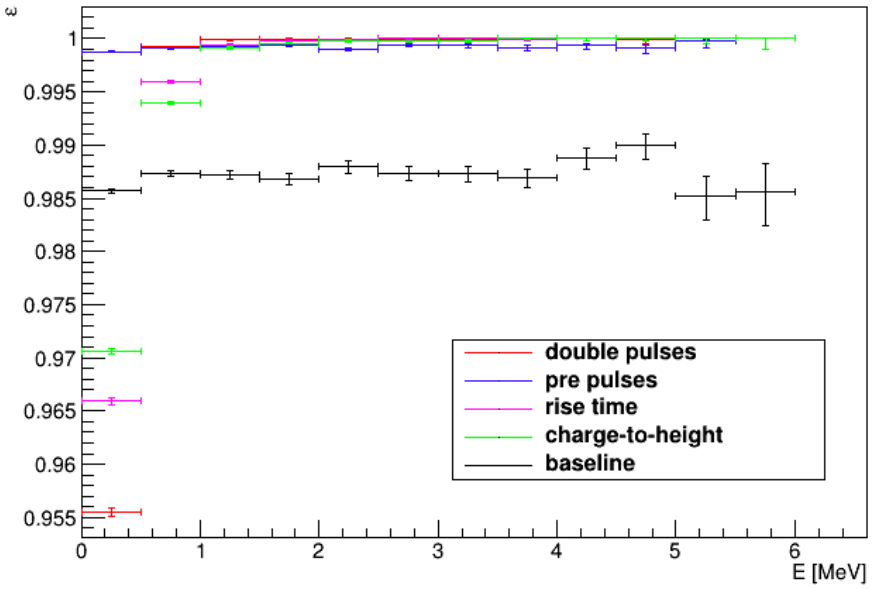

Figure 5.4: Energy-dependent cut efficiencies ε for different filters for LH3 taking into account runs at all positions.

versa, as can be cross-checked with the Gatti method (see e.g. Figure 5.14). Approximately 6% of all events can be assigned to as γs and $\sim$ 34% as neutrons. Their energy spectrum can be seen in fig. 5.5. The cross-check with the help of the Gatti method shows (see section 5.3.2) that the residual contamination is highest for energies below 1 MeV.

As described in section 5.3, pulse shape discrimination via the Gatti or the T2T method can be applied to disentangle different event types. Details on both algorithms can be found there, upon application of these discrimination techniques, one obtains even cleaner γ and neutron induced recoil data samples. In this thesis, only γs and neutrons with a 90% confidence level (C.L.) for both criteria are accepted. Naturally, this further decreases the number of events, as depicted in fig. 5.5 for LH3. The cut on the pulse shape criteria further reduces the number for both recoil event types by $\sim$ 70%. In average, the efficiency now decreases to about $\sim$ 5% for γ's and $\sim$ 25% for neutrons (fig. 5.7).

In case of the runs with the AmBe source, the neutron and γ induced recoil event samples are purely based on the T2T pulse shape discrimination and the filters described in the second step. A cut on the Gatti parameter would be possible if one uses the information on the pulse shape from the beam runs. However, this information cross-transfer would clearly undermine the comparison between the pulse shape from beam and source runs.

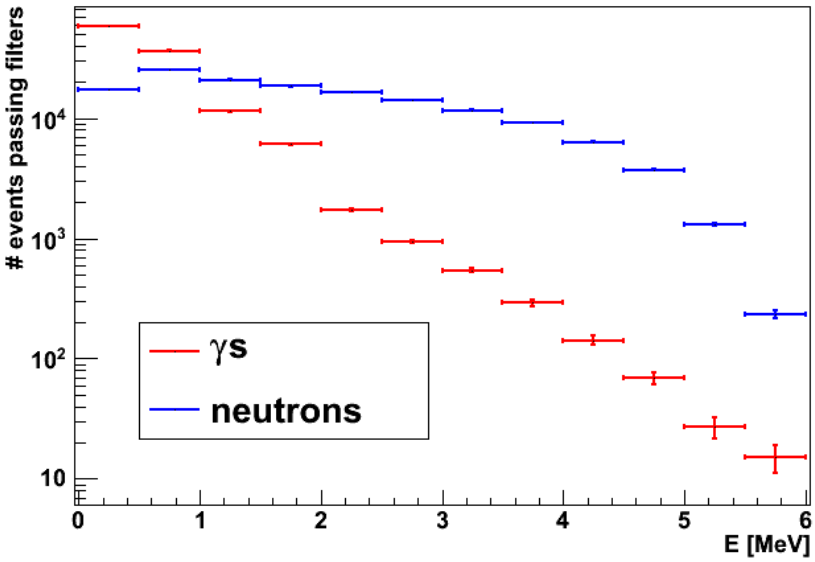

Figure 5.5: Total number of γ and neutron induced recoil events in LH3, summed over all positions and after the 2 standard cuts described and ToF peaks to identify γs and neutrons. While the neutrons are abundant up to 6 MeV, the number of γs drops rapidly.

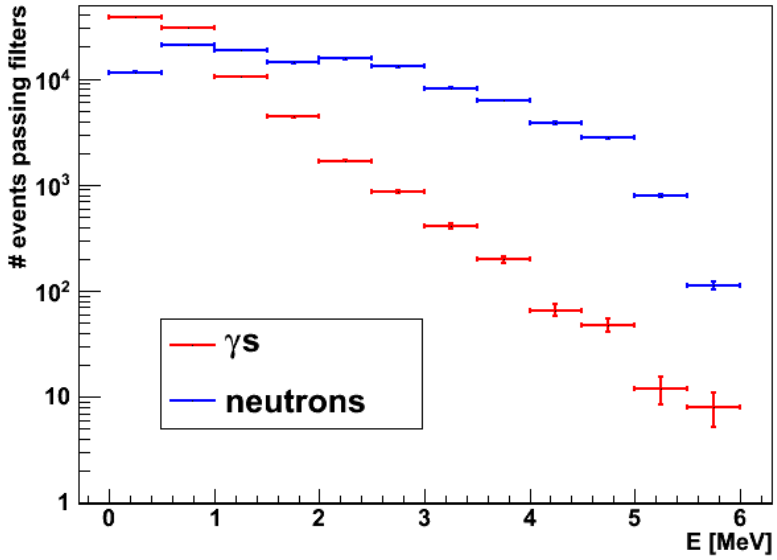

Figure 5.6: As fig. 5.5, yet further including a cut on the Gatti and T2T criteria. A γ/neutron induced recoil event was identified if it exceeded 90% C.L. for both the Gatti and the T2T probability.

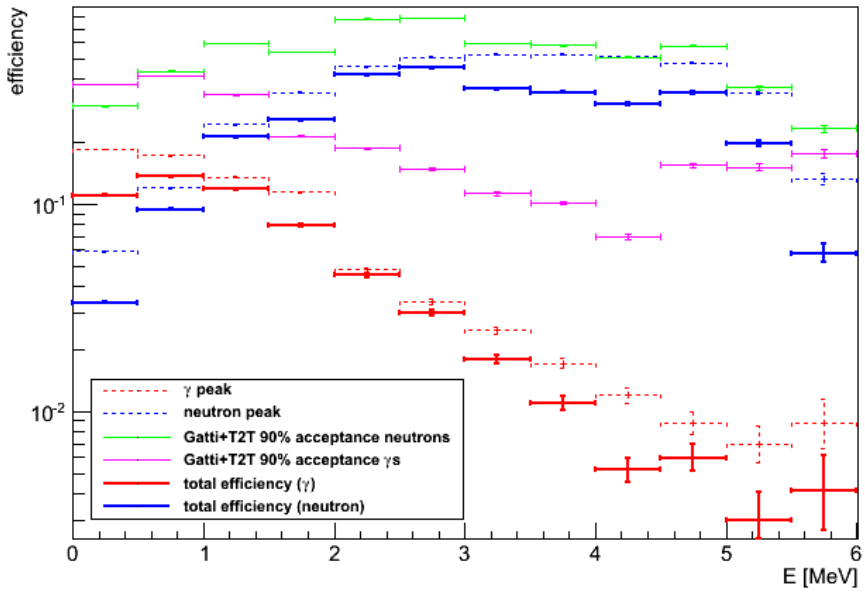

Figure 5.7: Efficiencies for γs and neutrons cutting on each peak, on 90% C.L. Gatti and T2T probability, and both criteria combined for LH3.

	parameter	efficiency
standard cuts	rise time	0.985 ± 0.002
	charge/height ratio	0.986 ± 0.002
	pre pulses	0.999 ± 0.002
	double pulses	0.982 ± 0.002
	baseline	0.987 ± 0.002
Gatti + T2T 90% C.L.	neutron type	0.440 ± 0.0009
	γ type	0.336 ± 0.0007
cut on ToF peaks	γ peak	0.146 ± 0.0004
	neutron peak	0.181 ± 0.0005
total (without Gatti + T2T cut)	γ	0.171 ± 0.0005
	neutron	0.137 ± 0.0004
total with Gatti + T2T cut	γ	0.137 ± 0.0004
	neutron	0.102 ± 0.0004

Table 5.4: Single and combined efficiencies for all cuts applied for all LH3 data between 0-6 MeV. Efficiencies for the other scintillator mixtures investigated are comparable. They are listed in table 5.4

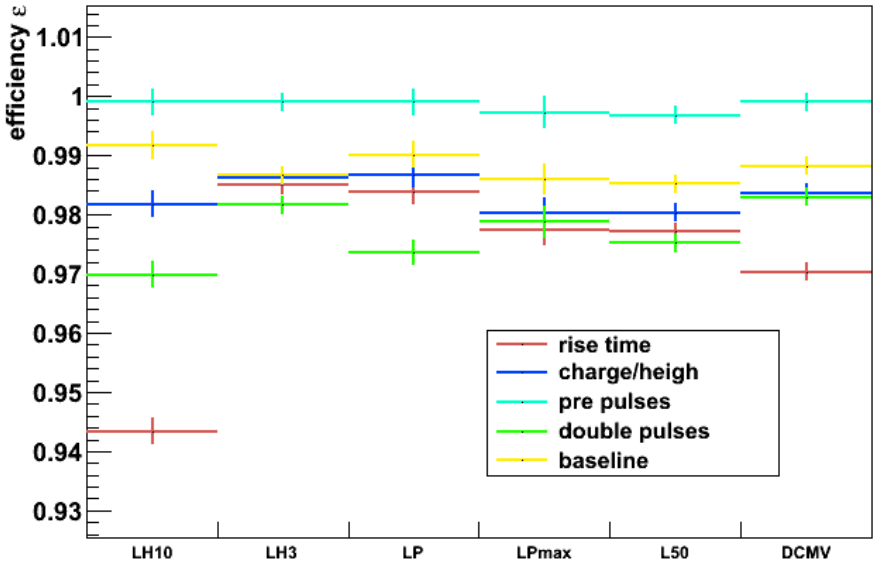

(a)

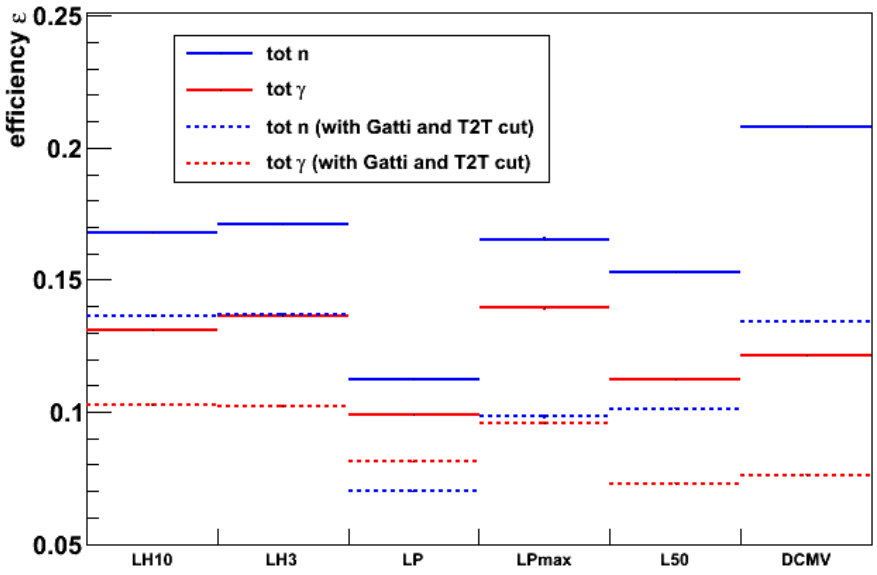

(b)

Figure 5.8: Comparison of the cut efficiencies ε for all LS mixtures under neutron beam irradiation, (a) for pulse shape parameter cuts and (b) their combined efficiency with and without additional Gatti and T2T particle identification.

5.2.3 Calibration

For the detector calibration various γ sources have been used, as listed in table 5.5. The sources cover well the energy region of interest for neutron scattering. Moreover, the calibration provides a good check for the linearity of the detector. The calibrations have been performed during the beamtime for each scintillator mixture.

A non-standard source used for calibration are WT-40 welding rods. They are made of tungsten and have a fraction of 5% ThO_2 and are used for high-temperature welding [99]. Each rod has a length of 175 mm, a diameter of 8 mm, and a weight of about 160 g. At the end of the ^{232}Th decay chain, the β^- decay from ^{208}Tl to ^{208}Pb is accompanied with the emission of a 2.61 MeV γ used for calibration. With the help of Germanium spectroscopy, the activity of this decay has been determined to be 38.5 ± 8.4 kBq/kg. The whole spectrum can be seen in fig. 5.9. For calibration, a collection of ten welding rods is used. The ^{241}AmBe source emits both neutrons and γs, which makes it suitable for particle discrimination analyses. Moreover, the highest γ energy at 4.43 MeV serves very well for calibration purposes.

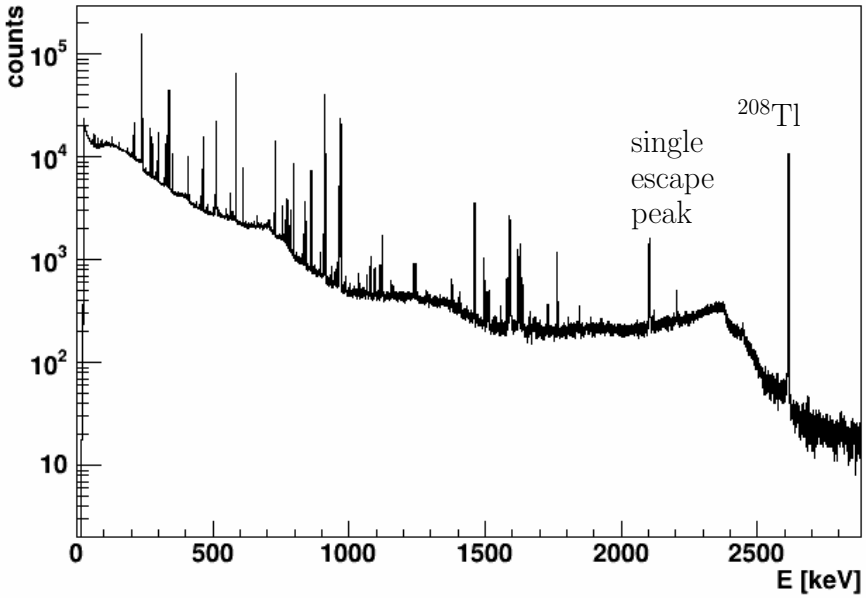

Figure 5.9: Spectrum of one welding rod measured with an HPGe detector in the underground laboratory 2 in Garching [100]. Only the Compton edge of the ^{208}Tl γ peak is used to calibrate the LS detector due to background at lower energies.

In the LS detector, the monoenergetic γs undergo Compton scattering resulting in a Compton spectrum smeared with the energy resolution of the system. However, dedicated Monte Carlo studies with GEANT4 [101] showed that multiple scattering has to be taken into

source	decay	Energy [keV]	E_{CE} [keV]
^{137}Cs	$^{137}\text{Cs} \longrightarrow {}^{137}\text{Ba} + e^- + \bar{\nu}_e + \gamma$	661.63	477.31
^{22}Na	$^{22}\text{Na} \longrightarrow {}^{22}\text{Ne} + e^+ + \nu_e + \gamma$	1274.53	1061.70
	$e^+ + e^- \longrightarrow 2\gamma$	511.00	340.66
welding rod	$^{208}\text{Tl} \longrightarrow {}^{208}\text{Pb} + e^- + \bar{\nu}_e + \gamma$	2610.66	2377.94
AmBe	$^{9}\text{Be} + \alpha \longrightarrow {}^{12}\text{C}^* + \text{n}$ $^{12}\text{C}^* \longrightarrow {}^{12}\text{C} + \gamma$	4432.98	4191.93

Table 5.5: List of all sources with their respective γ lines and the observed Compton edge energy E_{CE}.

consideration as well, particularly at higher energies [82]. On this basis, a more precise calibration procedure has been developed that is also used in this thesis [91]. This method has been validated with a coincidence experiment of the LS detector with a HPGe diode ([82]).

Despite the paramagnetic shielding, a small energy deviation of a few percent has been observed for varying positions. This is checked with the help of ^{22}Na source calibrations at each detector position [91].

In order to reconstruct the correct Compton edge, the energy deposition in the LS cell is simulated in a first step. This is depicted by the green line in figures 5.10 (a)-(e) [91]. The vertical red line shows the Compton edge energy E_{CE} scaled to the units of *charge*. In the simulated spectra, a large fraction of events appears above E_{CE} due to multiple scattering. These events, smeared with the detector's energy resolution, contribute significantly to the shape of the edge and thus have to be considered in the reconstruction of the Compton energy.

In order to reproduce the measured data, the energy deposition spectrum has to be convoluted with the detector resolution function N_{det}, approximated by

$$N_{det}(E;\mu,\sigma) = \frac{1}{\sqrt{2\pi\sigma^2(E)}} \cdot exp\left(-\frac{\mu^2(E)}{2\sigma^2(E)}\right). \tag{5.1}$$

Here, $\mu(E) = E \cdot A$ is the expected number of photons created at energy E and scale parameter A introduced in order to link the DAQ variable *charge* with the actual energy. The energy resolution is given by $\sigma(E) = r \cdot \sqrt{A \cdot E}$, where r links the resolution to the number of photons. The effect of γ quenching is neglected in the fit. This does not alter the result if the energy deposit is high enough and as long as the fit is performed locally around the Compton edge.

The probability density function (PDF) is built up by numerical convolution of the energy

deposit with the detector resolution N_{det}. Finally, a maximum-likelihood fit to the data is performed using the MINUIT package of the ROOT framework [102]. The red curves in fig. 5.10 (a)-(d) and fig. 5.11 represent the best fit. The fit parameters A and r are denoted by *ScaleParameter* and *ResParameter*, respectively. A constant background is also accounted for, yet shows to be small. The reconstructed Compton edge charge Q_{CE} is now given by

$$Q_{CE} = E_{CE} \cdot A, \tag{5.2}$$

with the Compton edge energy E_{CE}.

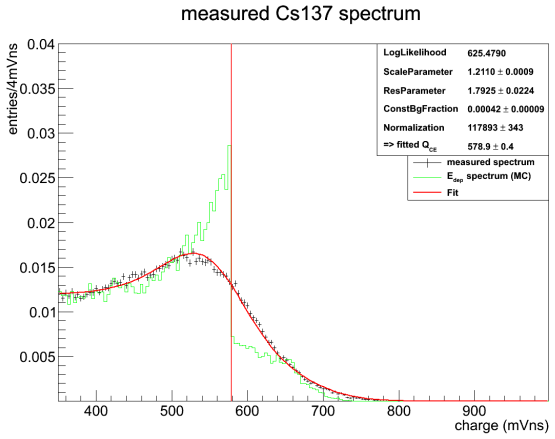

(a) ^{137}Cs 661 keV line

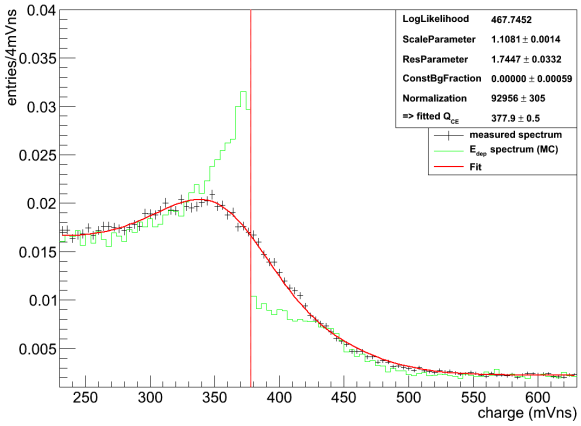

(b) ^{22}Na 511 keV line

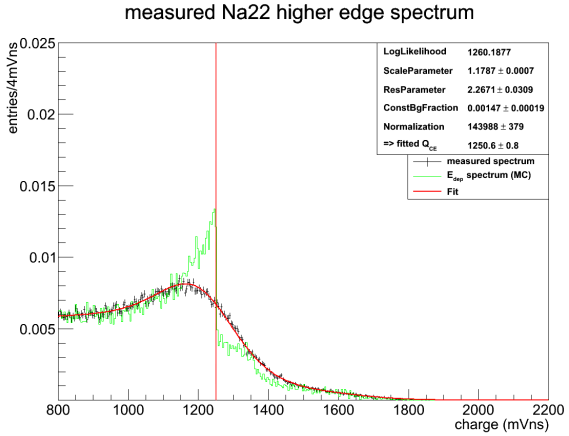

(c) ^{22}Na 1274.5 keV line

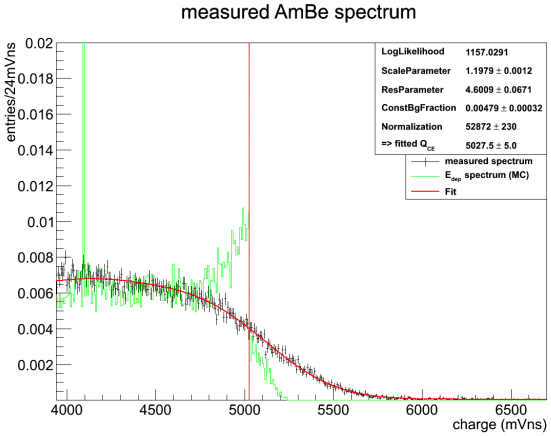

(d) AmBe (^{12}C* 4.43 MeV line)

Figure 5.10: Fitted Compton edges for all sources used for the detector calibration for LH3. In order to find the correct Compton edge, the energy deposition has been simulated with GEANT4 [101], depicted by the green spectra. The likelihood fits are shown in red and the reconstructed Compton edge is indicated by the vertical red line [91].

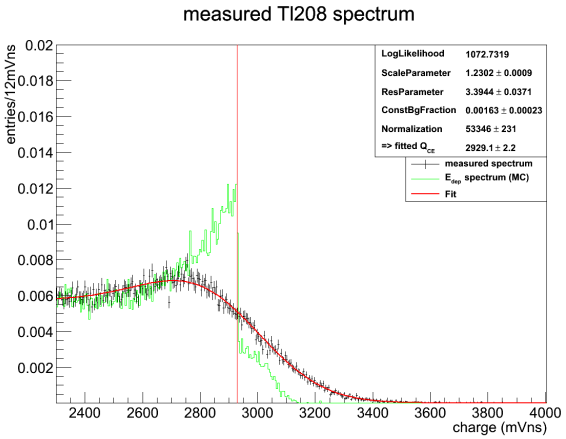

Figure 5.11: Fitted Compton edge of the welding rods (^{208}Tl 2.61 MeV line) for LH3

In fig. 5.12, all fits of all monoenergetic γ lines are brought together, providing the energy calibration. In order to link the visible energy with the *charge* variable, a linear fit is performed:

$$E_{vis} = p_0 + p_1 \cdot charge \tag{5.3}$$

The fit shows that linearity over the whole energy range is well-given. All other LS mixtures showed this linear behavior. The fit parameters p_0, p_1 are listed in table 5.6 for all LS mixtures. The energy threshold for all LS under investigation is between 200-300 keV .

LS	p_0 [MeV]	p_1 [MeV/mV/ns]
LH3	0.03389 ± 0.00658	$7.96 \cdot 10^{-4} \pm 1.3 \cdot 10^{-5}$
LH10	0.05773 ± 0.00616	$9.62 \cdot 10^{-4} \pm 1.6 \cdot 10^{-5}$
LP	0.04019 ± 0.00761	$9.23 \cdot 10^{-4} \pm 1.8 \cdot 10^{-5}$
LP1d	0.05097 ± 0.00633	$9.65 \cdot 10^{-4} \pm 1.6 \cdot 10^{-5}$
LPmax	0.05124 ± 0.00631	$9.47 \cdot 10^{-4} \pm 1.6 \cdot 10^{-5}$
L50	0.04793 ± 0.00636	$9.66 \cdot 10^{-4} \pm 1.6 \cdot 10^{-5}$
DCMV	0.03094 ± 0.00675	$9.17 \cdot 10^{-4} \pm 1.6 \cdot 10^{-5}$

Table 5.6: Calibration fit parameters for all LS mixtures, assuming a linear dependency $E_{vis} = p_0 + p_1 \cdot charge$ [91].

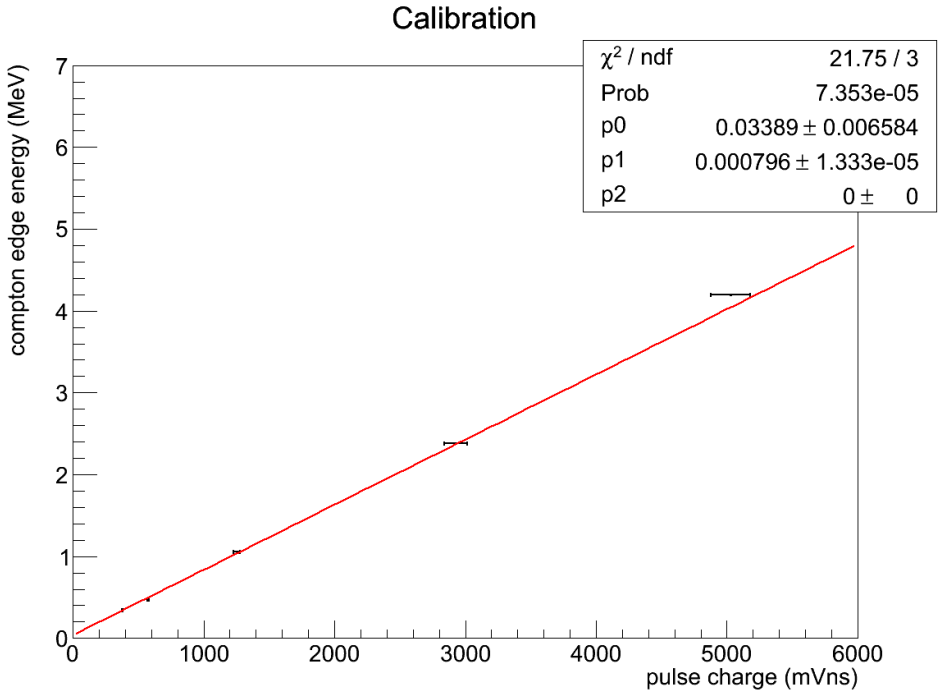

Figure 5.12: Calibration data and linear fit for LH3 [91].

5.3 Pulse shape analysis

The pulse shape discrimination with the help of the tail-to-total (T2T) or the Gatti method is a powerful tool to disentangle different particle types interacting with liquid scintillator. The reason lies within the different ionization densities leading to different decay amplitudes for the same decay time constants (cf. fig. 5.16). Pulse-shape discrimination is a widely-used technique in particle physics and one of the key methods to identify background. For example, it helps to tag cosmogenic neutrons produced in the detectors themselves or the surrounding rock [55].

As the Gatti technique requires the knowledge of the standard pulse shape of γ and neutron induced recoil events, their construction is presented first. Both the Gatti and the T2T pulse shape discrimination method are introduced afterwards.

5.3.1 Standard pulses

The construction of standard pulses is a necessary requirement for the calculation of the Gatti parameter introduced in section 5.3.2. Moreover, it provides one possibility to obtain the pulse shape parameters as presented in section 5.4.

There are two main steps in the construction of standard pulses, as shown in fig. 5.13. First, γ and neutron induced recoil events are separated with the help of the ToF technique. In a second step, Gatti and T2T criteria are used to further refine the standard pulses. In order to obtain the standard pulse for neutrons and γ recoil events in the different scintillator mixtures, the single pulses passing the several filters have been averaged. Maximizing statistics, this is done taking advantage of all data acquired in all positions. Standard pulses have been derived for three different data sets: (SP1) neutron beam data with ToF cut, (SP2) like SP1 with additional cuts on Gatti and T2T distributions, and (SPA) AmBe data with T2T cut.

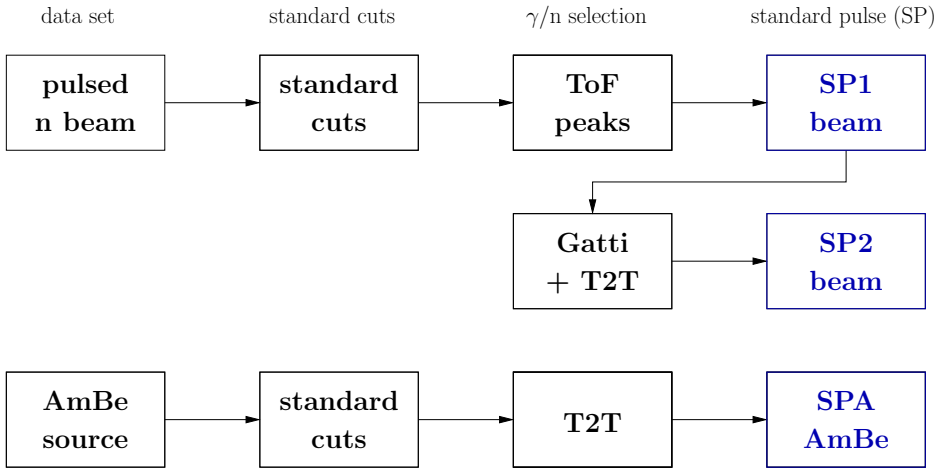

Figure 5.13: Analysis steps for the construction of standard pulses from neutron beam and AmBe source data.

Neutron and γ recoil event samples are selected using the ToF spectra for each position. Both peaks are fitted with Gaussian distributions, accepting the interval of $\pm 2\sigma$ around the maxima (cf. fig. 4.6b). Events within the γ/neutron peak are identified as γ/neutron induced recoil events. The residual peak contaminations are around 10% (see fig. 5.14), checked with the help of the Gatti method. As one can see in fig. 5.14, the γ contamination in the neutron peak is spread over all energies. This is the result of inelastic neutron interactions with the detector material and surrounding producing γs. On the other side, the neutron contamination of the γ peak is low-energetic. This is due to the fact that the Gatti distributions highly overlap at low energies, leading to particle mis-identifications. The γ and neutron induced recoils in the tails of the ToF peaks cause a lower energy deposit in the scintillator as well. This hints that those particle have been scattered in the surrounding before producing a signal in the LS detector.

In order to evaluate the energy dependency, standard pulses are built in 0.5 MeV intervals between 0 and 6 MeV visible energy (calibrated according to eq. 5.3) Towards higher energies, both γ and neutron spectra drop significantly to few entries (see fig. 5.5).

The selection cuts in order to obtain γ and neutron recoil event samples are described in

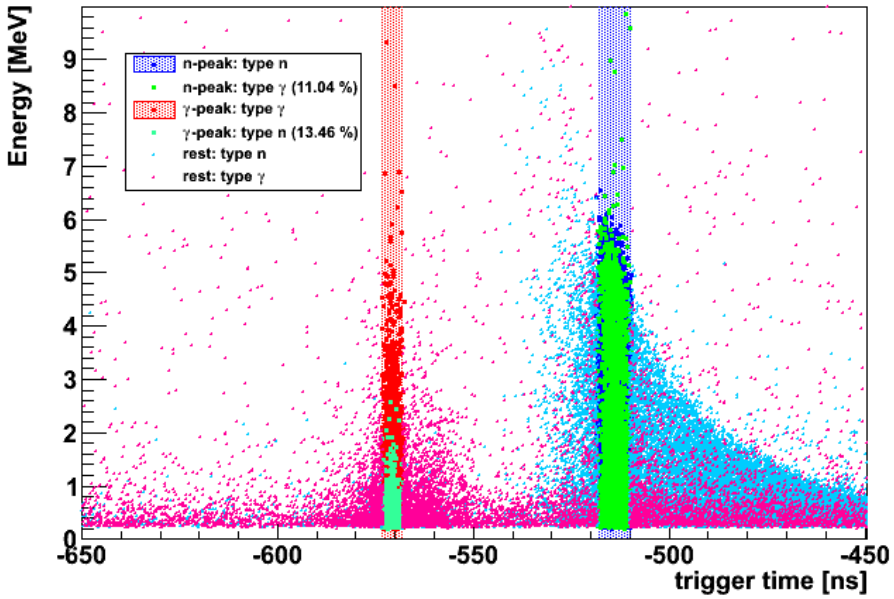

(a)

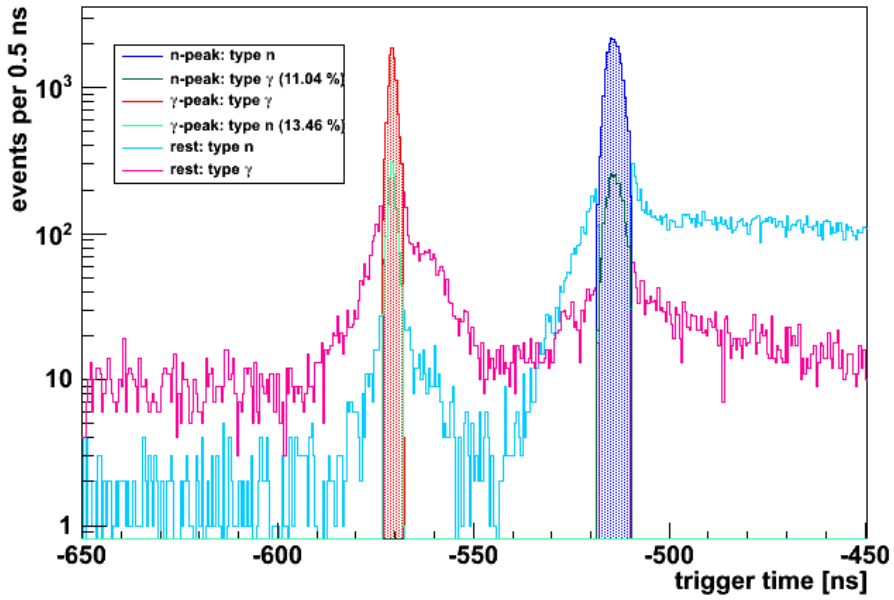

(b)

Figure 5.14: (a) Uncalibrated time of flight versus energy scatter plot and (b) its projection for LH3 at position 1. The accepted $\pm 2\sigma$ intervals around the peaks are indicated by the shaded regions. Moreover, particles are tagged as γ or neutron type with the help of the Gatti parameter (see section 5.3.2), using γ and neutron type pulses averaged between 0-5 MeV, respectively. The residual contaminations in the peak regions are around 10% each.

section 5.2.2: After cuts on the pulse shape and neutron peak rate stability, only events from the respective peaks in the ToF spectrum are selected. Finally, all pulses passing those filters are summed in a 2-d scatter plot. They are adjusted in time such that their steepest slope coincides at $t = 0\,\text{ns}$ and are normalized to the *charge* variable. An example for LH3 between 2-2.5 MeV can be seen in figure 5.15. The color is a measure for the number of entries in each bin. On the top right, a fit of a slice is shown.

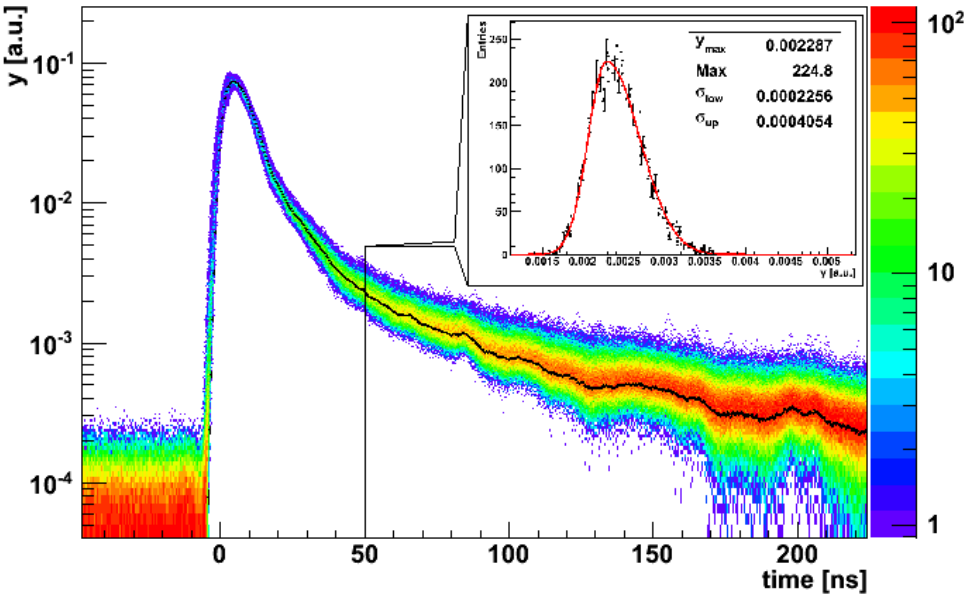

Figure 5.15: Scatter plot overlaying all sampled pulses passing the selection cuts for γ induced event in the scintillator LH3 between 2-2.5 MeV. The color code represents the number of entries in each bin. The black line shows the best fit value of y_{max} according to eq. (5.4). On the top right, an exemplary fit of the y-projection at $t = 50\,\text{ns}$ is shown.

Next, in every 0.5 ns time bin a likelihood fit is performed with an asymmetric normal distribution:

$$G_{asym}(y) = \begin{cases} N_{max} \cdot exp\left(-\frac{(y-y_{max})^2}{2\sigma_1^2}\right) & \text{for } y < y_{max} \\ N_{max} \cdot exp\left(-\frac{(y-y_{max})^2}{2\sigma_2^2}\right) & \text{else,} \end{cases} \tag{5.4}$$

where y is the pulse height in arbitrary units. At the maximum y_{max} the function is continuous and differentiable. The asymmetry accounts for the timing uncertainties of the summation of single pulses described above.

Standard pulses for γ and neutron induced events in LH3 are shown in figure 5.16. As one can see, both types of events can be clearly distinguished, especially in the tail, as expected. As the rise time is an intrinsic experimental parameter, it does not differ for γ and neutron event types. The error bars are given by the fit error of y_{max}.

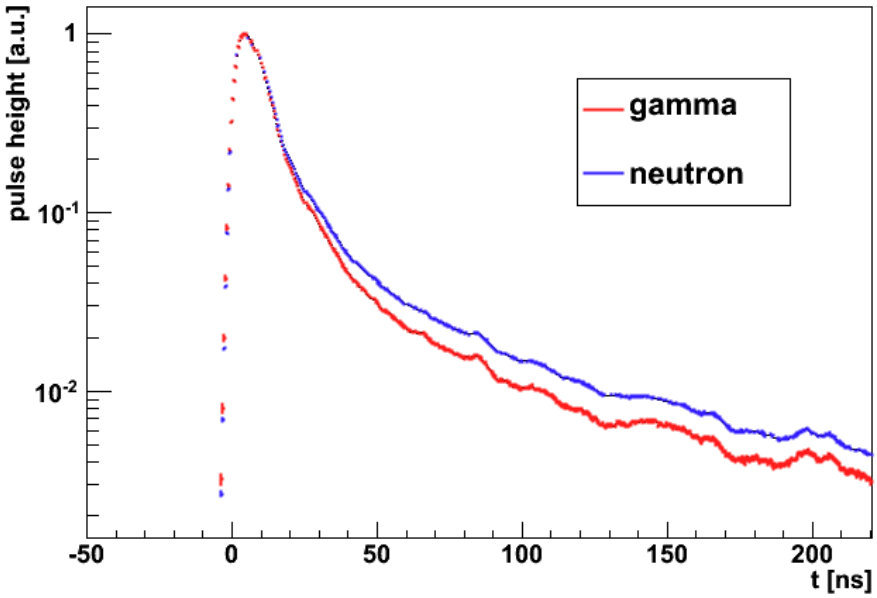

Figure 5.16: Standard pulses for γ (red) and neutron (blue) induced events in LH3. The error bars are given by the fit error of the maximum y_{max} (see eq. 5.4). Both pulse maxima are normalized to 1 in order to emphasize the difference of the decay amplitudes.

A second iteration of standard pulses (SP2) can be made with the help of the Gatti and T2T methods described in the following sections. For this purpose, only such events are accepted that are within 90% C.L. of the Gatti and T2T probability for the respective event type. In addition, standard pulses were constructed from the AmBe data alone (SPA). Here, γ and neutron induced events are separated via the T2T method only. All three different standard pulses are compared in figure 5.17. Notably, both sets of recoil types are clearly distinct. The application of the Gatti and T2T cuts mainly has an effect on the neutron pulse shape. At low energies, where γ-type event contamination in the neutron peak is highest (see fig. 5.14) it is most prominent. Therefore, the standard pulses after the cut feature a more prominent tail.

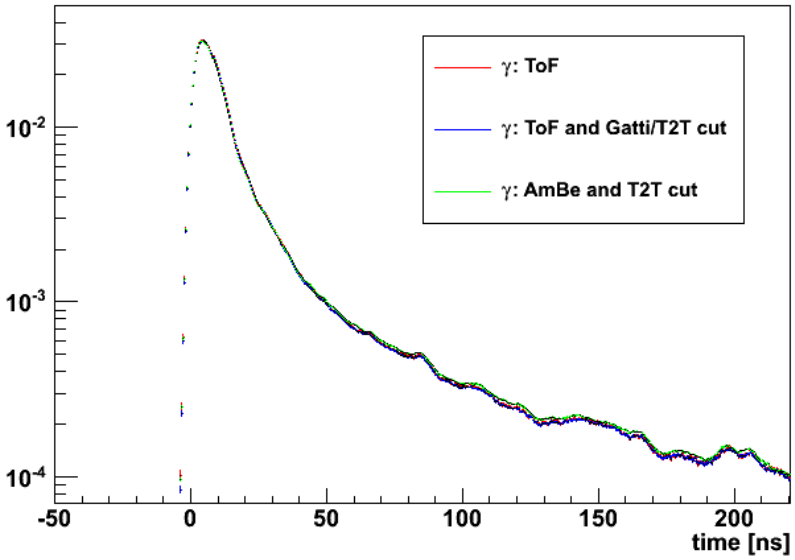

(a) standard pulses for γ induced events

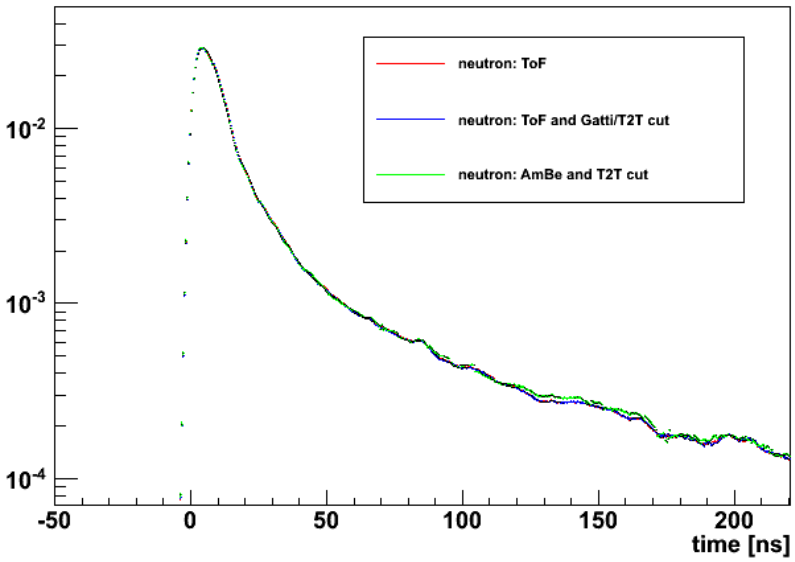

(b) standard pulses for neutron induced events

Figure 5.17: Comparison of standard pulses of γ and neutron induced events from three different data sets for LH3 between 2-2.5 MeV. First, only the information on the time of flight is used to disentangle the recoil types. In a more refined analysis, additionally only events with a 90% Gatti and T2T probability are accepted. Lastly, the T2T method was used in order to separate γ and neutron type events in AmBe source runs. Besides small variations due to electronic noise, all event types show good agreement and γ and neutron events are clearly distinguishable.

5.3.2 Pulse-shape discrimination via Gatti method

The Gatti method for pulse shape discrimination has been developed by E. Gatti in the late 1950s [103]. It is usually more accurate since it takes into account the information of every time bin rather the integral used in the T2T method. A comparison of both methods can be found in [104].

The Gatti parameter G of a time pulse function $P(t)$ is defined as

$$G = \sum_{i=0}^{N_{bins}} w_i \cdot P_i. \tag{5.5}$$

where the sum loops over all bins N_{bins} of $P(t)$ with a width of $\Delta t = 0.5\,\text{ns}$. Accordingly, P_i denotes the value of the pulse $P(t)$ in the ith bin and w_i the value of the weight function $w(t)$, with

$$w_i = \frac{n_i - \gamma_i}{n_i + \gamma_i}. \tag{5.6}$$

Here, $n(t)$ and $\gamma(t)$ denote the standard pulses for neutron and γ induced events, respectively. Their integral is normalized to 1, so n_i and γ_i can be interpreted as the photon emission probability in the time interval $t \in (i \cdot \Delta t, (i+1) \cdot \Delta t)$. If $P(t)$ originates from a γ-type recoil, bins with $\gamma(t) > n(t)$ (and thus $w(t) < 0$), are weighted more, resulting in a negative Gatti parameter G. On the other hand, neutron induced events are connected with positive G. As the integration time is finite, the Gatti distribution will not be perfectly symmetrical around $G = 0$. This can be seen in figure 5.19 (a).

As mentioned, the Gatti technique requires the knowledge of the standard pulse time profiles for both particle types. As these are not known a priori, a two-step approach is taken in order to determine the discrimination efficiency of the method. First, γ and neutron peak are used to build up both types of standard pulses. Those pulse profiles are then used to calculate the Gatti parameter on an event-by-event basis. In a second instance, this information is further used to build up new and more refined standard pulses, which again are used as input to compute the Gatti parameter once more. Finally, the discrimination power of the Gatti method can be evaluated.

As the standard pulses are constructed for 0.5 MeV intervals, the discrimination of the Gatti technique is evaluated using these intervals as well. Figure 5.18 shows the relation between energy and the Gatti parameter G for ToF peak events. Events in the neutron peak are shown in blue, γ peak events in red. While at low energies both distributions overlap, the discrimination improves towards higher energies. A profile can be seen in figure 5.19 (a), made for LH3 at position 0 between 0-0.5 MeV. In this case, only events within $\pm 2\sigma$ of the ToF peaks are selected.

The disentanglement of γ and neutron-type events is done with the help of two subsequent

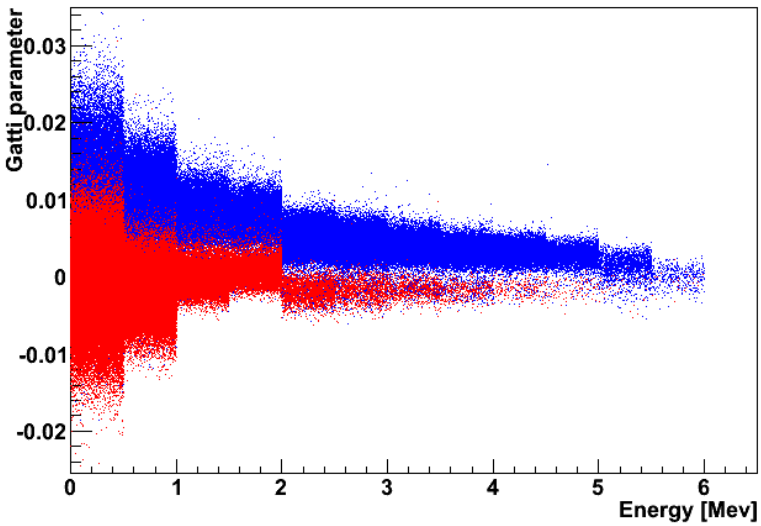

Figure 5.18: Scatter plot of the Gatti parameter G versus the energy for LH3. Events from the neutron peak are shown in blue and γ peak events in red. Both types of events can be clearly distinguished. The step-like structure is due to the evaluation of the Gatti parameter in 0.5 MeV intervals, as given by the standard pulses.

fits. First, selecting the γ and neutron peak in the ToF spectrum, one obtains two separate Gatti distributions. Both are fitted with Gaussian functions $G_{npeak,0}$ and $G_{\gamma peak,0}$. However, since there is a large contamination of the neutron peak by γ-type events, this contamination can also be found in its respective Gatti distribution. Therefore, a second fit with the sum of two Gaussians $G_\gamma + G_n$ is performed. Here, all data without the ToF peak cuts are used and thus statistics are not as limited at high energies. The results from the first fits are used as start parameters of the second fit, which shows to be most stable. The second fit can be used as long as there are only two types of particle interactions and thus only two peaks appear in the Gatti spectrum. A check is given by the χ^2/ndf values of the second fit, which improve significantly compared to the fit of the neutron peak alone.

Knowing both distributions G_γ and G_n now enables to calculate the probability of a γ-like event:

$$p_\gamma = \frac{N_\gamma}{N_\gamma + N_n} \tag{5.7}$$

Here, N_γ and N_n denote the normalized functions of G_γ and G_n, respectively. Figure 5.19b shows p_γ as a function of the Gatti parameter. The steepness of the transition region is a measure for the particle discrimination power. Accordingly, the probability that an event is from a neutron induced recoil is $p_n = 1 - p_\gamma$.

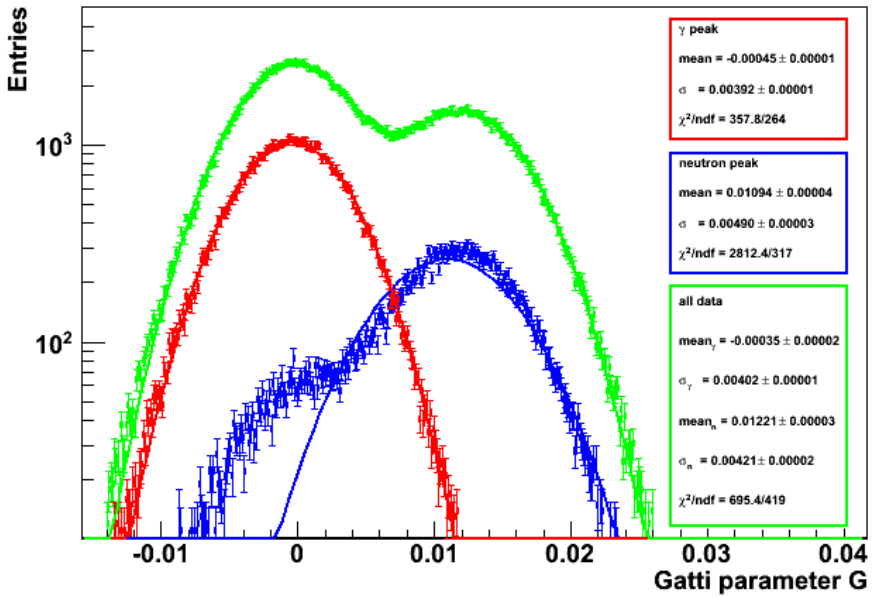

(a)

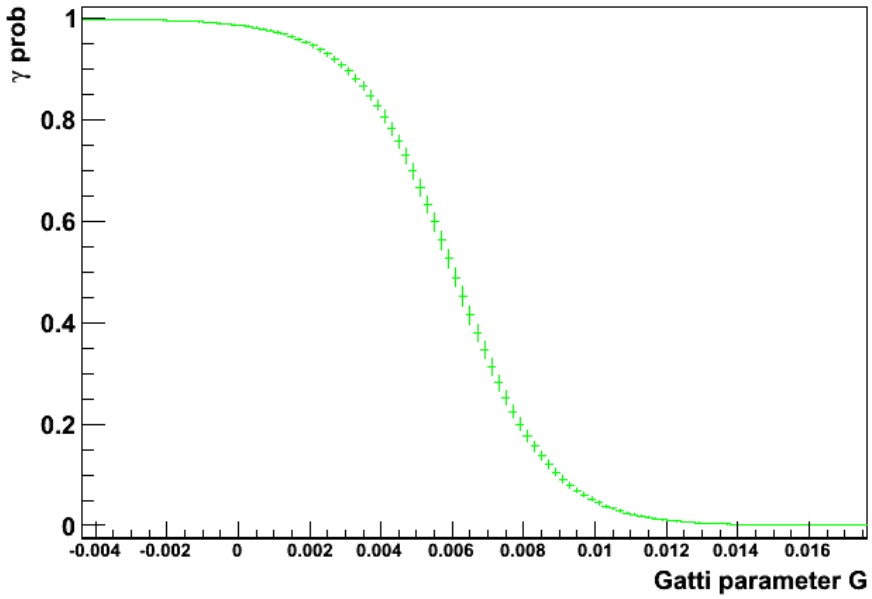

(b)

Figure 5.19: (a) Gatti distribution for LH3 between 0-0.5 MeV and (b) the resulting γ probability as a function of the Gatti parameter G. The Gatti distributions of the ToF peaks and their respective fits are shown in red for the γ and blue for the neutron peak. Due to the large amount of γ induced recoils in the neutron peak, the fit is distorted. Therefore, a second fit is performed on all data (green), using the previous results as input.

In order to express the discrimination more quantitatively, the efficiency

$$\varepsilon_n = \int_g^\infty N_n(G)dG \tag{5.8}$$

is calculated. It is the fraction of neutron-induced events that are in the range $G \in [g, \infty]$. In other words, it is the efficiency to tag n-type events above a given cut parameter g. Thus, the respective residual probability r_γ that γ-type events can be found in $[g, \infty]$ is

$$r_\gamma = \int_g^\infty N_\gamma(G)dG. \tag{5.9}$$

Varying the cut parameter g, the correlation between ε_n and r_γ can be displayed. It is shown in figure 5.20 for different energy intervals for LH3. Naturally, the residual γ contamination cannot be maximized without decreasing the neutron efficiency at the same time. The discrimination power peaks around 3 MeV, which is due to statistics and the smaller difference of the γ and neutron standard pulses at higher energies.

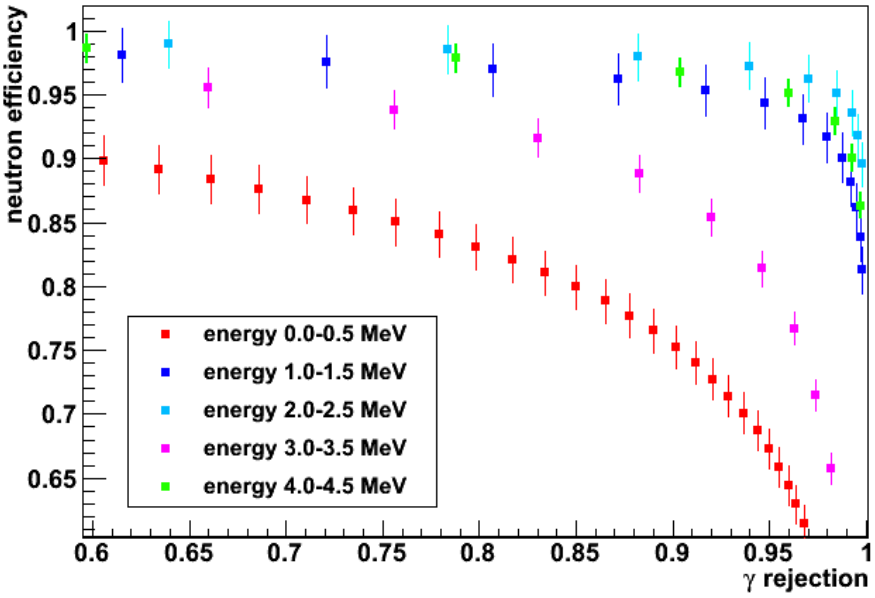

Figure 5.20: Neutron efficiency ε_n versus γ rejection r_γ for LH3 considering data from all detector positions. The errors of the fit parameters of G_n are propagated through the integral in order to obtain the displayed error bars.

In order to be able to compare all neutron tagging efficiencies more easily, all ε_n are taken at a γ rejection of 90%. In figure 5.21, the efficiencies for the different data samples are shown. First, the beam data is used to calculate ε_n for SP1 and SP2. These results are

compared to the neutron efficiency for SPA. As expected, the efficiency rises with increasing energy in all three cases. Already above 1 MeV, the neutron efficiency exceeds 95% for LH3. Moreover, both beam and source data coincide within the error bars. As both data sets are completely independent, this ascertains the behavior of ε_n as a function of the energy. At high energies, low statistics limit the fit quality. All other scintillator mixtures show a similar behavior.

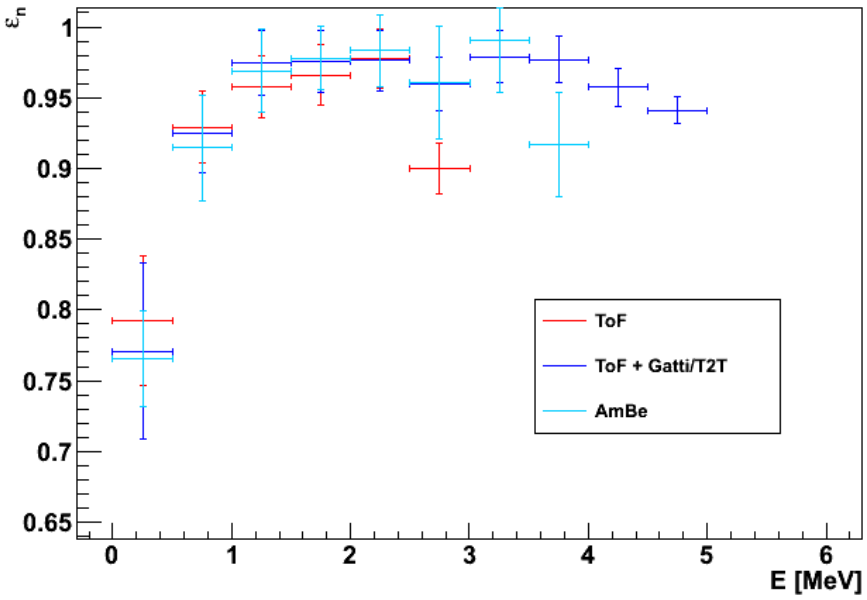

Figure 5.21: Energy dependency of the neutron tagging efficiency ε_n at 90% γ rejection for LH3. The three data sets represent the three types of standard pulses introduced in section 5.3.1: SP1 (red), SP2 (blue), and SPA (turquoise).

In figure 5.22, the neutron efficiency is compared for all scintillator mixtures under neutron irradiation. Here, the Gatti parameter of each pulse is computed with the standard pulses derived from the ToF peaks including cuts on Gatti and T2T parameters. Throughout the energy range, a clear hierarchy is visible: the discrimination power of DCMV and L50 is lowest. This is due to the high content of non-scintillating n-paraffin resulting in a lower light yield. The lower neutron efficiency of LPmax compared to LP3 shows the effect of degradation, which leads to a lower light yield as well. The difference between LH3 and LP3 can only be caused by impurities from production and handling processes. However, the effect is quite small since the error bars well overlap. Adding more PPO further improves the discrimination capabilities, as the LH10 data proofs.

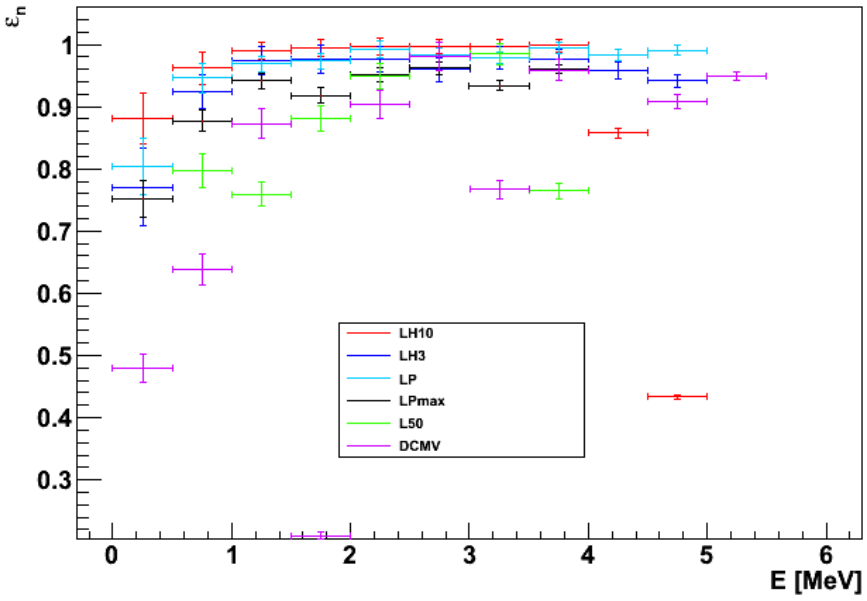

Figure 5.22: Comparison of the neutron efficiency ε_n of the Gatti method for different scintillator mixtures using the standard pulses SP2.

5.3.3 Particle discrimination via the tail-to-total method

The tail-to-total (T2T) pulse shape discrimination technique has been and still is widely used in particle physics. It is a straight forward method and can be easily implemented into data handling. Here however, we take a closer look in order to optimize the separation power of this method.

The T2T discrimination technique directly takes advantage of the differing pulse shape for γ and neutron induced recoil events (fig. 5.16), i.e. the difference in amplitude of the slowest decay constant. The T2T parameter tt is defined as

$$tt = \frac{\int_{t_{start}}^{\infty} P(t)}{\int_{-\infty}^{\infty} P(t)}, \tag{5.10}$$

where P(t) describes the pulse shape in time. As the pulse is only recorded in a finite time window, tt is calculated as

$$tt = \frac{\int_{t_{start}}^{t_{stop}} P(t)}{\int_{t_0}^{t_{stop}} P(t)}. \tag{5.11}$$

where $t_{stop} = 220\,\text{ns}$ and $t_0 = -20\,\text{ns}$, well in the baseline. The steepest slope of each pulse is set to $t = 0$ (see figure 5.23). In order to optimize the discrimination power of the

T2T method, the parameter t_{start} was varied for each scintillator in 1 MeV energy intervals up to 6 MeV. Again, the cuts described above on the pulse shape parameters are made. However, no selection of the peaks in the ToF spectrum is done. For each integration start parameter t_{start}, tt is calculated event-by-event according to eq. (5.11). As the tail of neutron induced recoils is longer, their T2T ratio is larger and the peaks can be assigned to each event type. Both peaks are fitted with a Gaussian function (see fig. 5.24).

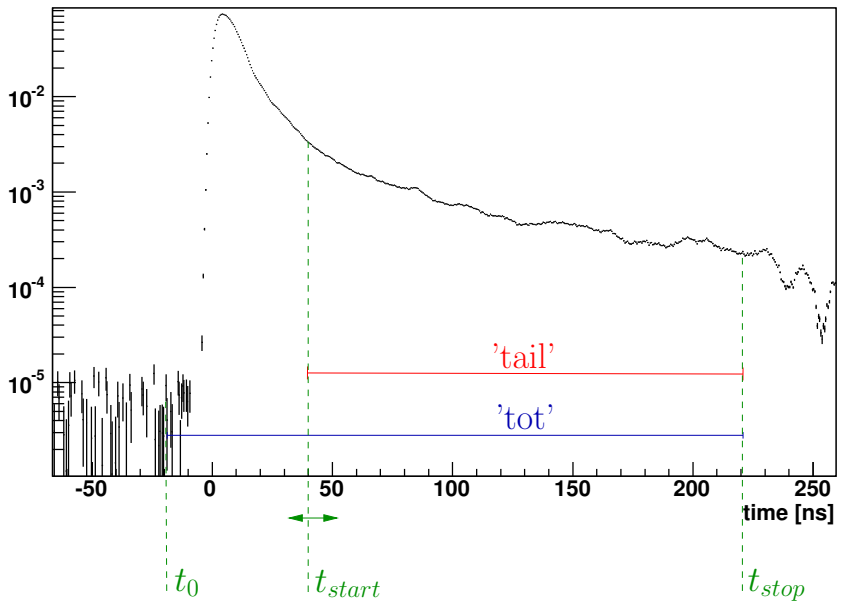

Figure 5.23: Integration limits for the determination of the T2T parameter. While $t_0 = -20$ ns and $t_{stop} = 220$ ns are fixed, t_{start} is varied in order to optimize discrimination.

After normalization, the discrimination power is computed by two means. First with the help of a *factor of merit* D, which weighs the difference of the fit maxima with their combined widths:

$$D = \frac{tt_{max,n} - tt_{max,\gamma}}{\sqrt{\sigma_n^2 + \sigma_\gamma^2}}, \tag{5.12}$$

where $tt_{max,n}$ and $tt_{max,\gamma}$ refer to the T2T value of the maxima of the respective Gaussian fits and σ_n and σ_γ their respective widths.

Secondly, also based on the fit, the residual γ recoil event contamination is calculated while accepting 90% of the neutron recoils events. Both parameters show a comparable behavior varying t_{start} (fig. 5.25). As one can see the slope between $\sim 30 - 50$ ns is very small. This means that the pulse shape discrimination power varies minimally in that region. Taking a look at figure 5.26, one can see a good agreement of both parameters. Moreover, no energy dependency can be observed. The combination of both energy-averaged mean values is shown for all scintillator mixtures subject to beam runs in fig. 5.27. The error is estimated

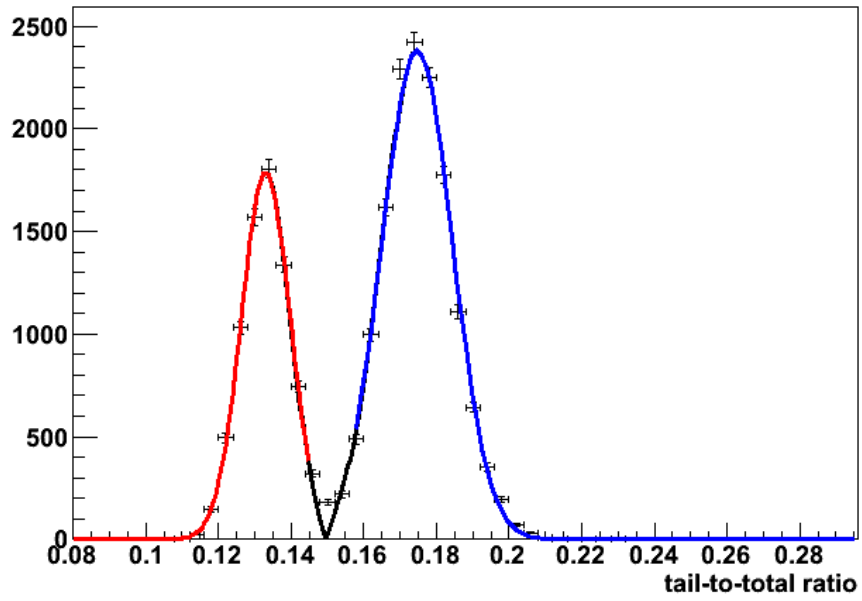

Figure 5.24: T2T distribution for LH3 between 1-2 MeV. The integration start time is $t_{start} = 40$ ns.

by the root-mean-square errors. Despite some differences, the error bars are too large to give an ideal scintillator-specific t_{start}. Also having in mind the weak dependency on the variation of the integration start time in fig. 5.25, t_{start} is set to 40 ns for all scintillators in the following analysis.

The discrimination efficiency of the T2T method is derived analogously to the Gatti technique. With the start time set to 40 ns, the T2T parameter is calculated on an event-by-event basis. One can already see in fig. 5.28 that γ and neutron induced events can be clearly discriminated above 1 MeV.

Again, the scatter plot is cut into 0.5 MeV slices and their projections fitted as shown in figure 5.29 for LH3 between 0.5-1 MeV. First, the T2T distributions of both ToF peaks are fitted separately. Their results are used as input parameters for a fit of the sum of two Gaussians. As explained for the Gatti method in section 5.3.2, this routine accounts for the high γ contamination on the neutron peak and the fit stability.

After normalization, the neutron efficiency and residual γ contamination can be calculated according to equations (5.8) and (5.9). Like before, a residual contamination of γ induced events of 10% is chosen in order to determine the neutron tagging efficiency ε_n. The energy dependency of this parameter is shown in figure 5.30 for LH3 for neutron beam and AmBe source data. Both independent data sets feature the same dependency, exceeding 90% efficiency above 1 MeV.

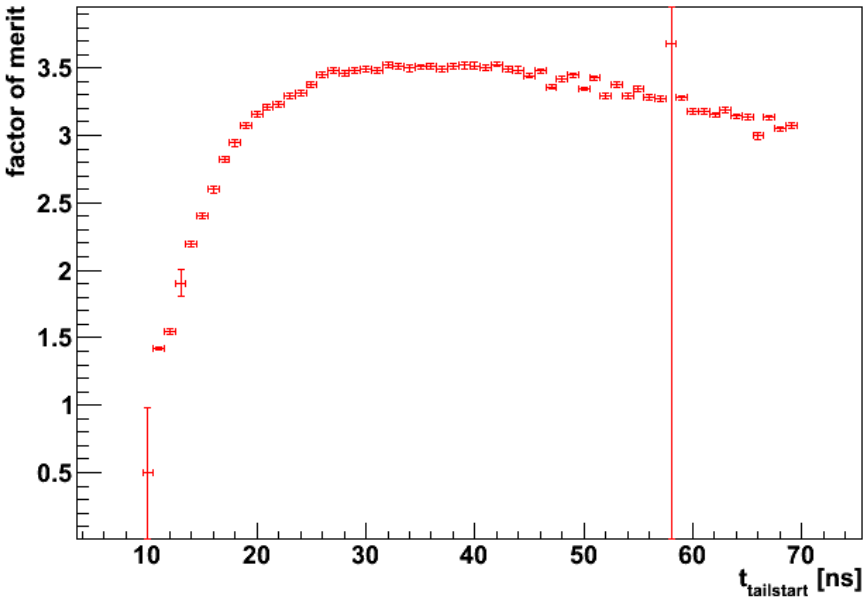

(a)

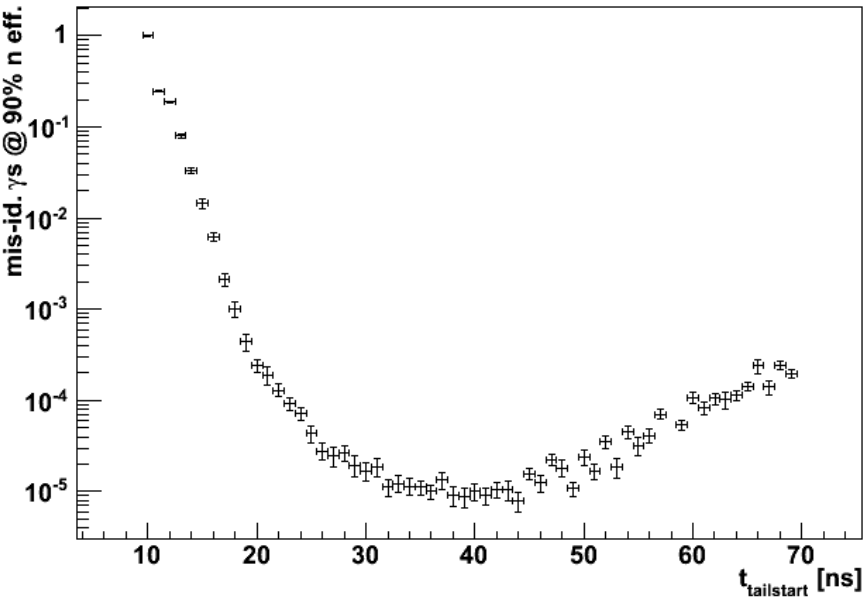

(b)

Figure 5.25: Finding the pulse integration start time for an ideal T2T pulse shape discrimination, using (a) the maximum of the factor of merit D and (b) the minimum of the residual γ contamination at 90% neutron efficiency. Both plots refer to LH3 in the energy region of 1-2 MeV. Both extrema coincide around 40 ns. Clearly, the flatness of the distributions and the error bars allow for start time variations between 30-50 ns without great effect on the discrimination power between γ and neutron induced recoil events.

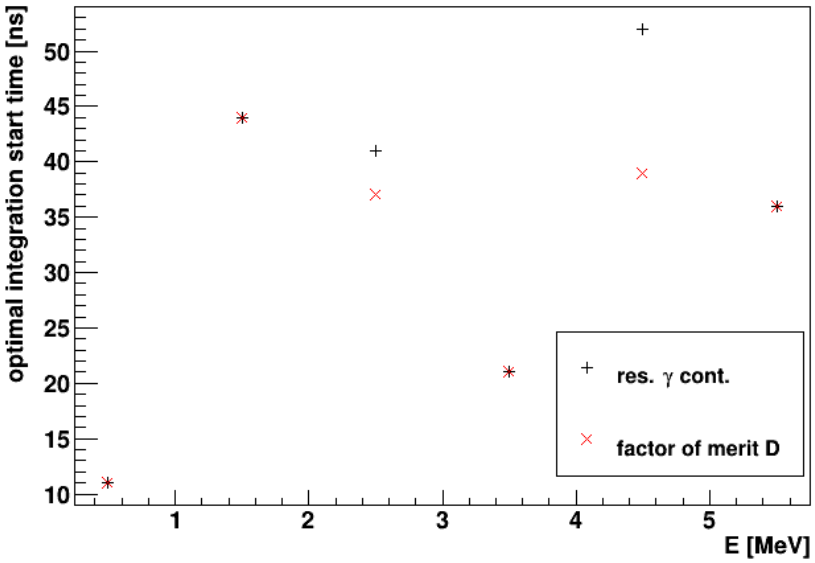

Figure 5.26: Energy dependency of the factor of merit D and the residual γ contamination for LH3. Both methods result in similar values. All optimized integration start time values spread between 30-50 ns, resembling the flatness of the distributions in this region.

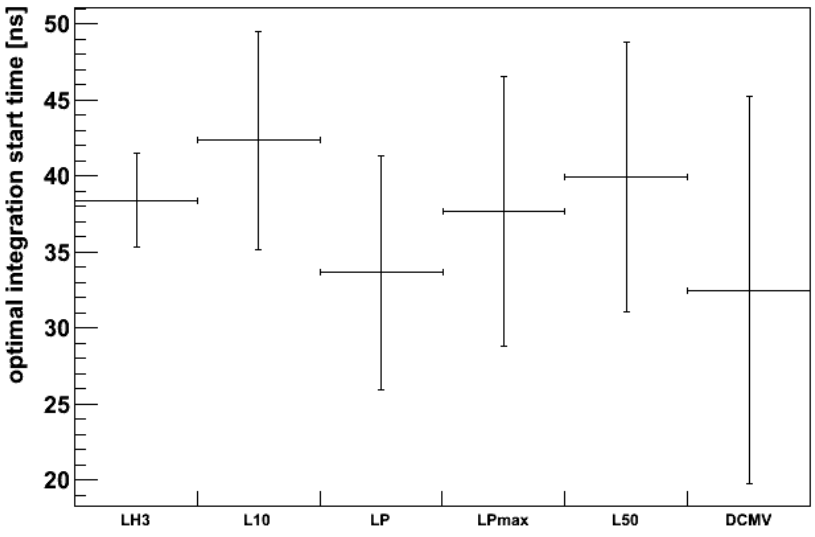

Figure 5.27: Ideal integration start time parameter t_{start} for the different investigated LS mixtures. As all values fit well within the error bars, the integration start time for the T2T analysis is set to 40 ns.

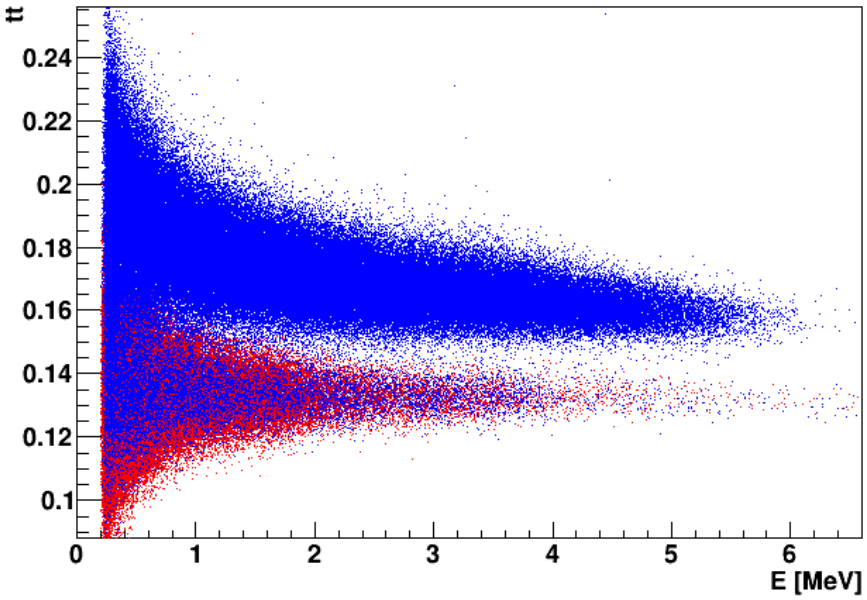

Figure 5.28: Scatter plot of tt versus visible energy for LH3 for events in the γ (red) and neutron ToF peak (blue). Obviously, both event types can be distinguished well above 1 MeV.

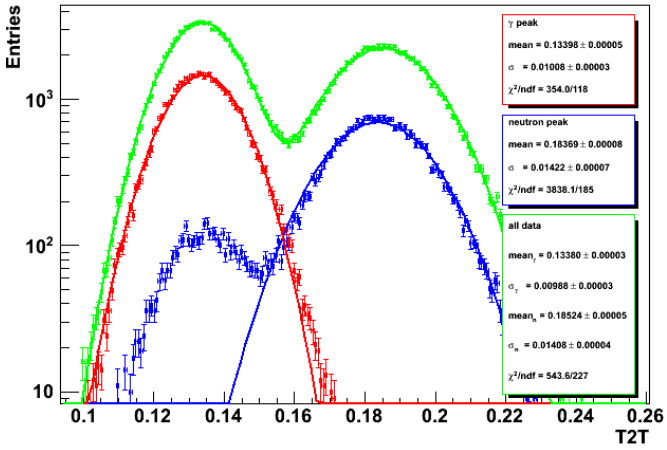

Figure 5.29: Fits of the T2T distributions between 0.5-1 MeV for LH3. The results from the fit of the γ (red) and neutron ToF peak (blue) are used as input parameters for a combined fit (green).

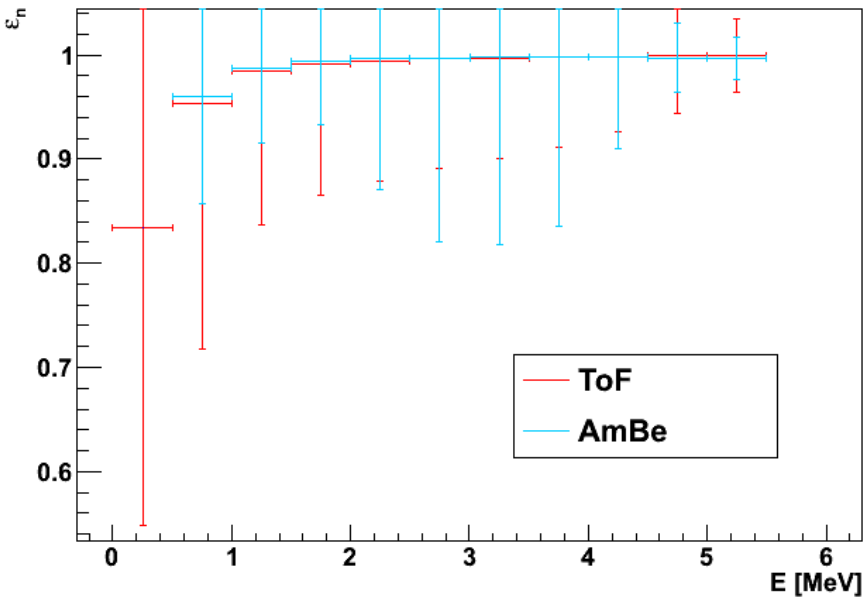

Figure 5.30: Neutron tagging efficiency ε_n for a rejection of γ-type events of 90%. Both data from the neutron beam (red) and from the AmBe source (blue) are shown for LH3. Both sources yield almost identical values.

A comparison of the various scintillator mixtures can be seen in figure 5.31. The hierarchy of the scintillator mixtures appears like in the Gatti analysis, depending on the light yield.

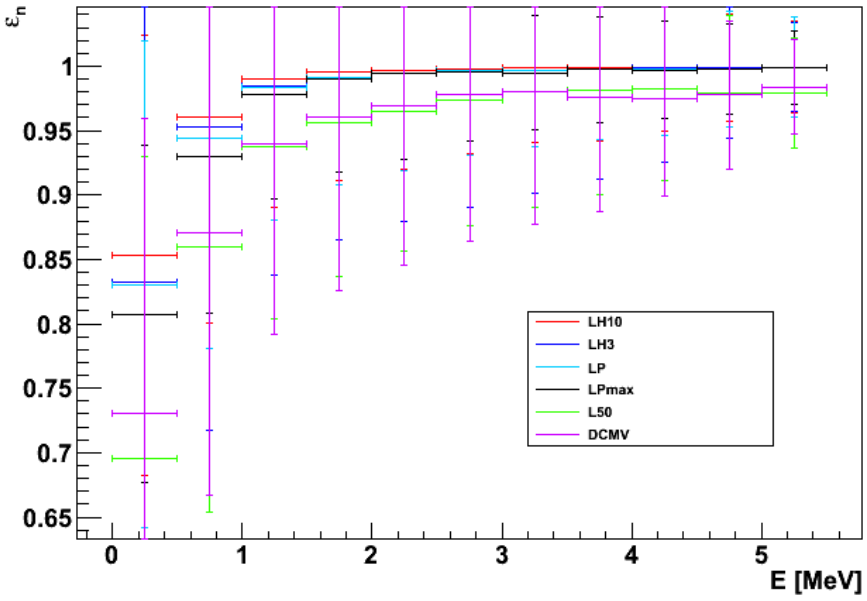

Figure 5.31: Neutron tagging efficiency ε_n for rejection of γ-type events of 90% for all scintillator mixtures under neutron irradiation. Within error bars, all mixtures show the same behavior.

5.3.4 Comparison of Gatti and T2T method

Although the Gatti and the T2T pulse shape discrimination method appear similar, some differences can be seen by comparison of figures 5.22 and 5.31. A common feature is the hierarchy of the scintillators. In both analyses, the same order appears: DCMV and L50 show the lowest discrimination power, both containing a large amount of non-scintillating n-paraffin in the mixture. The small difference in PPO concentration ($2\,\mathrm{g}/\ell$ vs. $3\,\mathrm{g}/\ell$) does not reflect in the plots. Moreover the neutron efficiencies of LP and LH3, only differing in the provider company of the LAB, coincides within error bars. However, the aged LPmax sample shows a systematical loss in discrimination power. In both analyses, L10 displays the best ability to distinguish γ and neutron induced events.

While the fits work very well in the T2T analysis and values for ε_n are obtained up to over 5 MeV for all scintillators, the Gatti method is more instable. This is due to the fact that the pulses contain electronic noise which makes it impossible to evaluate the weight function until the pulse vanishes in the background. Therefore, the peaks are less distinct at high energies. Moreover, the Gatti method is more sensitive to the lower statistics at high energies than the T2T method. It requires larger event numbers for the construction of standard pulses, passing various filters. Nevertheless, the Gatti method shows its strength at low energies where statistics is significantly larger, yielding higher ε_n and smaller error

bars.

Therefore, both methods are combined in order to obtain the ideal values for the discrimination power. Figure 5.32 shows a scatter plot of the Gatti versus the T2T parameter for LH3 between 1-1.5 MeV. The ellipsoidal shape hints that both parameters are correlated. Nevertheless, a combination can still improve the discrimination power. This is done by an estimate. The two-dimensional structure is approximated by the product of the two fits of the 1-d projections. Like before, each fit combines two normal distributions. Along a line perpendicular to the connection of the two peak maxima both distributions are separated. Shifting this cut line parallely, the final γ rejection is adjusted. The neutron efficiency is given by the integral of the neutron peak. The results from the combined analysis can be seen in table 5.7, along with the results from the Gatti and T2T analysis, are shown between 1-1.5 MeV. Neutron efficiencies of more than 99% for all scintillator mixtures show the superb quality of organic liquid scintillators for particle identification via pulse shape analysis above 1 MeV. In table 5.8, ε_n is shown in dependency of the γ rejection. Only minimal differences between the LS without n-paraffin can be observed. For L50 and DCMV, about 5% of the proton recoils cannot be identified. Below 0.5 MeV, the differences between the various LS is more distinct (cf. table 5.9). While the difference between LH3 and LP is minimal, the aged sample LPmax shows a clear decline in efficiency. However, the addition of non-scintillating mineral oil gives even worse discrimination, retaining only about two thirds of the proton recoils.

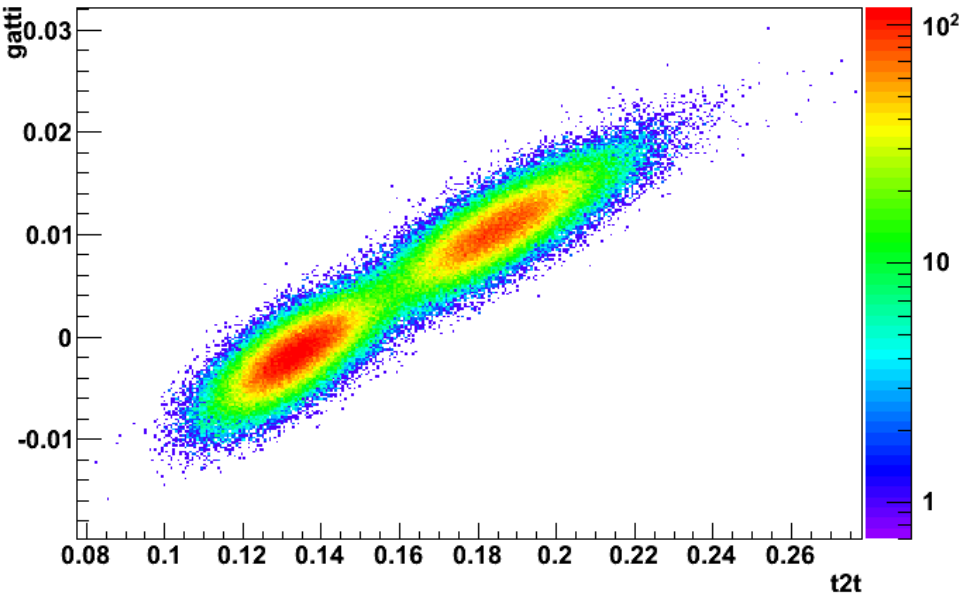

Figure 5.32: Scatter plot of Gatti parameter versus T2T for LH3 for energies between 1-1.5 MeV.

LS	Gatti	T2T	combined analysis
L10	0.990 ± 0.014	0.990 ± 0.099	0.9999^{+8e-06}_{-6e-06}
LH3	0.975 ± 0.022	0.983 ± 0.148	0.9998^{+2e-05}_{-3e-05}
LP	0.968 ± 0.013	0.983 ± 0.103	0.9997^{+1e-05}_{-1e-05}
LPmax	0.941 ± 0.012	0.978 ± 0.081	0.9994^{+5e-05}_{-7e-05}
LP1d		0.978 ± 0.087	
L50	0.759 ± 0.019	0.938 ± 0.134	$0.9931^{+0.0001}_{-0.0001}$
DCMV	0.873 ± 0.024	0.940 ± 0.148	$0.9949^{+0.0001}_{-0.0002}$

Table 5.7: Neutron efficiencies at 90% γ rejection for all scintillator mixtures for energies between 1-1.5 MeV. All values refer to beam data, except for LP1d. The Gatti method is based in the standard pulses SP2.

LS	1-1.5 MeV		
	$\varepsilon_n(90\%)$	$\varepsilon_n(95\%)$	$\varepsilon_n(99\%)$
L10	0.9999^{+6e-6}_{-8e-6}	0.9998^{+1e-5}_{-2e-5}	$0.9982^{+0.0003}_{-0.0003}$
LH3	0.9998^{+2e-5}_{-3e-5}	$0.9991^{+0.0004}_{-0.0004}$	$0.9970^{+0.0005}_{-0.0005}$
LP	0.9997^{+1e-5}_{-1-e5}	0.9991^{+3e-5}_{-3e-5}	$0.9940^{+0.0005}_{-0.0006}$
LPmax	0.9994^{+5e-5}_{-7e-5}	0.9986^{+4e-5}_{-8e-5}	$0.9934^{+0.0003}_{-0.0007}$
L50	$0.9931^{+0.0001}_{-0.0001}$	$0.9857^{+0.0005}_{-0.0005}$	$0.9523^{+0.0028}_{-0.0070}$
DCMV	$0.9949^{+0.0001}_{-0.0002}$	$0.9889^{+0.0004}_{-0.0008}$	$0.9633^{+0.0011}_{-0.0028}$

Table 5.8: Neutron efficiencies depending on the γ rejection (90%,95%, and 99%) for all scintillator mixtures for energies between 1-1.5 MeV.

LS	0-0.5 MeV		
	$\varepsilon_n(90\%)$	$\varepsilon_n(95\%)$	$\varepsilon_n(99\%)$
L10	$0.9712^{+0.0011}_{-0.0015}$	$0.9490^{+0.0012}_{-0.0006}$	$0.8596^{+0.0026}_{-0.0102}$
LH3	$0.9663^{+0.0008}_{-0.0008}$	$0.9391^{+0.0014}_{-0.0014}$	$0.8438^{+0.0027}_{-0.0106}$
LP	$0.9655^{+0.0004}_{-0.0004}$	$0.9338^{+0.0015}_{-0.0036}$	$0.8322^{+0.0058}_{-0.0100}$
LPmax	$0.9444^{+0.0011}_{-0.0017}$	$0.9047^{+0.0026}_{-0.0043}$	$0.7861^{+0.0030}_{-0.0133}$
L50	$0.8799^{+0.0009}_{-0.0009}$	$0.8147^{+0.0037}_{-0.0004}$	$0.6479^{+0.0112}_{-0.0095}$
DCMV	$0.8972^{+0.0016}_{-0.0032}$	$0.8408^{+0.0011}_{-0.0043}$	$0.6858^{+0.0112}_{-0.0095}$

Table 5.9: Neutron efficiencies depending on the γ rejection (90%,95%, and 99%) for all scintillator mixtures for energies between 0-0.5 MeV.

5.4 Determination of scintillation pulse parameters

The determination of the scintillation pulse parameters can not only help to understand the process of scintillation (cf. chapter 3) [70], but is also necessary as an input for detector Monte Carlo studies for LENA. By simulating interactions of different particle types using their respective decay characteristics, the particle discrimination power can be evaluated and background studies performed [55].

5.4.1 Fit of standard pulses

As described in chapter 3, several de-excitation processes are involved in the photon emission in liquid scintillators. Its time profile can be described by the sum of several exponentials. Amplifying these photons with a photo multiplier smears this decay due to its intrinsic Gaussian time jitter. Hence, the probability density function (PDF) $P(t)$ can be described as the convolution of the sum of decays with a Gaussian:

$$\begin{aligned} P(t) &= \sum_{i=1}^{N} \left(n_i \cdot exp\left(-\frac{t-t_0}{\tau_i} \right) \Big|_{t>t_0} \right) \otimes \left(\frac{1}{\sqrt{2\pi\sigma^2}} exp\left(-\frac{t^2}{2\sigma^2} \right) \right) \\ &= \sum_{i=1}^{N} n_i \cdot \left(exp\left(-\frac{t-t_0}{\tau_i} \right) \Big|_{t>t_0} \otimes \frac{1}{\sqrt{2\pi\sigma^2}} exp\left(-\frac{t^2}{2\sigma^2} \right) \right) \\ &= \sum_{i=1}^{N} n_i P_i(t) \end{aligned} \tag{5.13}$$

Here, n_i denotes the amplitude of each decay time τ_i and N the number of decay constants. In this thesis, the pulse is modeled using three decay constants. The width σ of the Gaussian accounts for the bunch width of the ^{11}B ions. In order to have an optimized resolution, the width of the ion bunches should be as small as possible. The onset of the unconvoluted pulse is denoted by t_0.

The integral of the convolution expressed as

$$P_i(t) = \frac{1}{2\tau_i} \cdot exp\left(\frac{2 \cdot t_0 + \sigma^2 \tau_i^{-1} - 2t}{2\tau_i} \right) \cdot Erfc\left(\frac{t_0 + \sigma^2 \tau_i^{-1} - t}{\sqrt{2}\sigma} \right), \tag{5.14}$$

with the complementary error function

$$\begin{aligned} Erfc(x) &= 1 - Erf(x) \\ &= 1 - \frac{2}{\sqrt{\pi}} \int_x^{\infty} e^{-t^2} dt \end{aligned} \tag{5.15}$$

which is implemented in the ROOT function library [98].

Figure 5.33 shows the fit applied to an standard pulse for LH3 between 2-2.5 MeV. The dotted green lines show the fraction of each decay component to the total, red pulse. As the fit consists of the sum of three identical functions, the assignment of τ_1, τ_2, and τ_3 is arbitrary. It was reordered before the following analyses, such that τ_1 corresponds to the fastest and τ_3 to the slowest decay time.

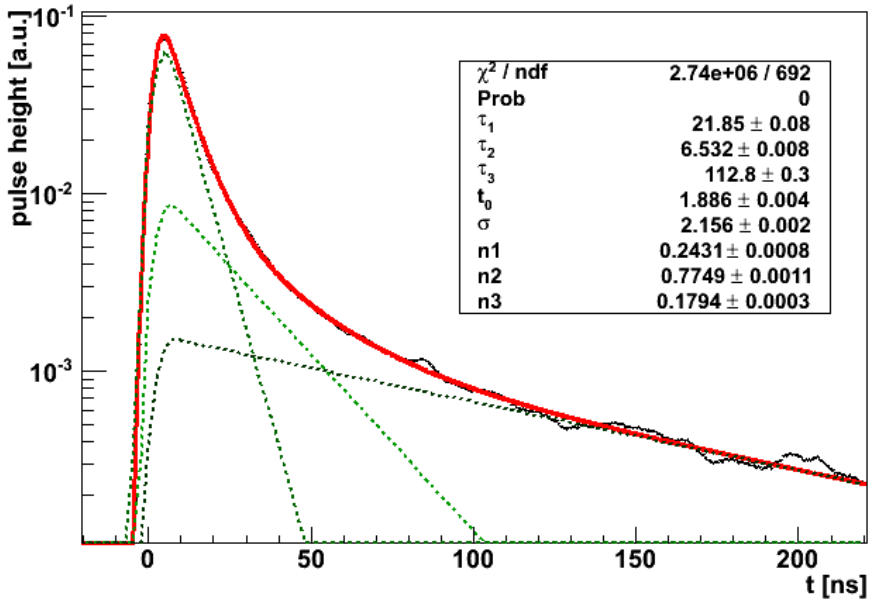

Figure 5.33: Pulse profile of a standard pulse for γ recoil events for LH3 between 2-2.5 MeV fitted using eq. (5.13).

As standard pulses have been calculated for each 0.5 MeV interval between 0-6 MeV, the energy dependency of the PDF parameters can now be checked. In the following, this is done for LH3. All other LS mixtures show a similar behavior. For both γ and neutron induced events, the energy dependency of the decay constants is shown in figure 5.34, the decay amplitudes in figure 5.35. Both $\tau_{\gamma,i}$ and $\tau_{n,i}$ match very well. Apart from a slight rise towards low energies, the decay times are constant over the whole energy range. Hence, the decay constants are scintillator-intrinsic properties. The decay amplitudes $n_{i,\gamma}$ and $n_{i,n}$ are clearly distinct (cf. fig. 5.35). While $n_{\gamma,1} > n_{n,1}$, it is the other way round for the second and third decay component. A slight energy dependency can be observed as well: around 3 MeV, n_1 shows a minimum and n_3 is at its maximum. Figure 5.36 shows the energy dependency of the time resolution σ for LH3.

The averaged values along with their statistical root-mean-square error is shown in table 5.10 for three different categories, originating from the three different standard pulse types described before: ToF peaks (SP1), ToF peaks with Gatti/T2T cut (SP2), and AmBe source with T2T cut (SPA). The values for the energy-averaged pulse types match well

within the given statistical errors. Indeed it is most notably that the completely independent AmBe data gives almost the same results for the amplitudes. The decay amplitudes seem to be systematically lower, yet still within the error bars.

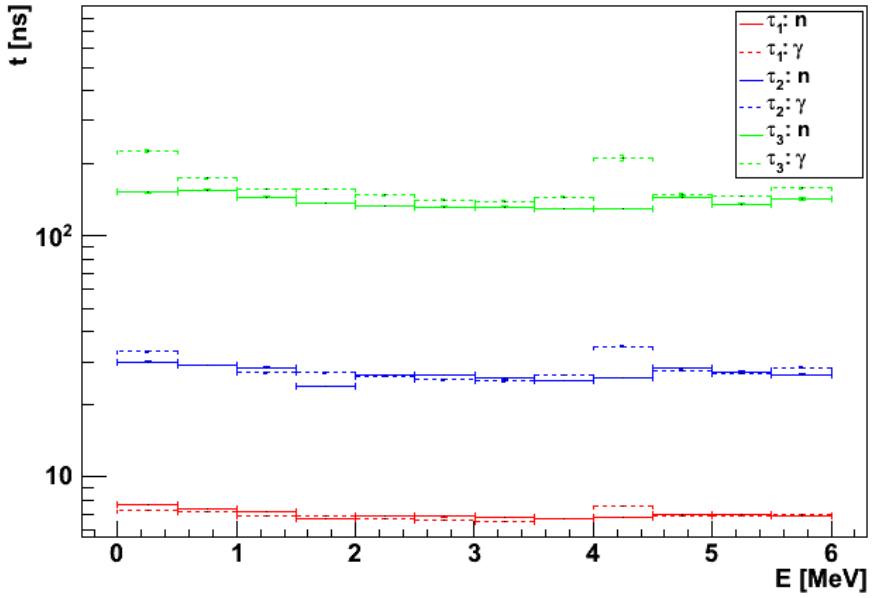

Figure 5.34: Energy dependency of the fitted decay time constants τ_i for γ (dashed lines) and neutron (solid lines) induced recoil events in LH3. Both $\tau_{\gamma,i}$ and $\tau_{n,i}$ match very well. Apart from a slight rise towards low energies, the decay times are constant over the energy range.

5.4.2 Estimation of systematical errors

The estimation of systematical errors is done through a Monte-Carlo study. Using the best fit values $\tau_{i,MC}$ and $n_{i,MC}$ as pulse shape parameters (cf. tables 5.13,5.14,5.15,5.16), 10,000 pulses are simulated for each scintillator mixture. Afterwards, the pulses are fitted with the PDF in eq. (5.13). The systematical errors are calculated via the differences between the MC truth $\tau_{i,MC}, n_{i,MC}$ and the edges of the regions accepting 68.3% of all events. An example is shown in figure 5.37 for τ_3; all other parameters have a less asymmetric distribution.

Another possibility for the estimation of the systematical errors is given by the LH3* measurement: at the end of the beamtime, the LS cell was filled once more with the scintillator mixture LH3 and exposed to the AmBe source. Therefore, the fit values for the AmBe source for LH3 and LH3* give an estimate for the systematical error of the experiment. Table 5.11 compares all fit parameters for LH3 and LH3*. The systematical

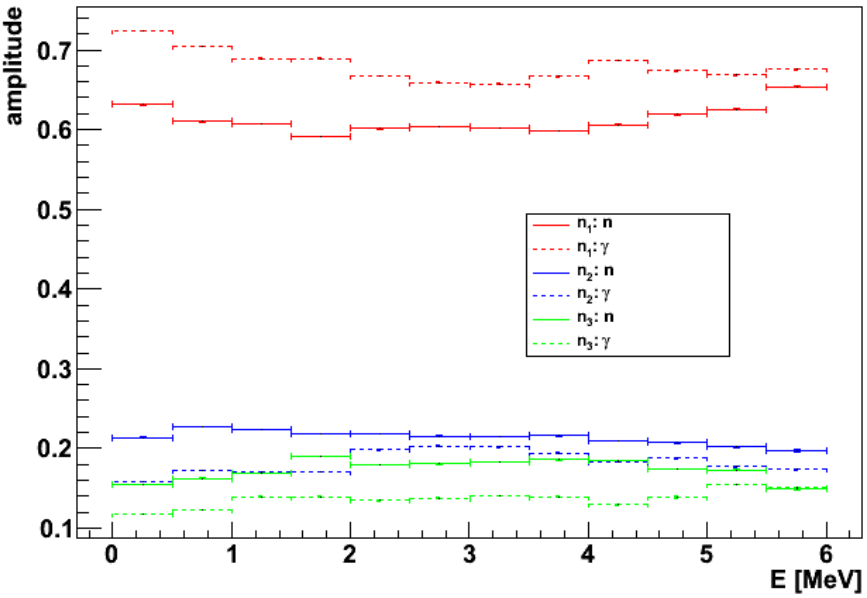

Figure 5.35: Energy dependency of the fitted decay amplitudes n_i for γ (dashed lines) and neutron (solid lines) induced recoil events in LH3.

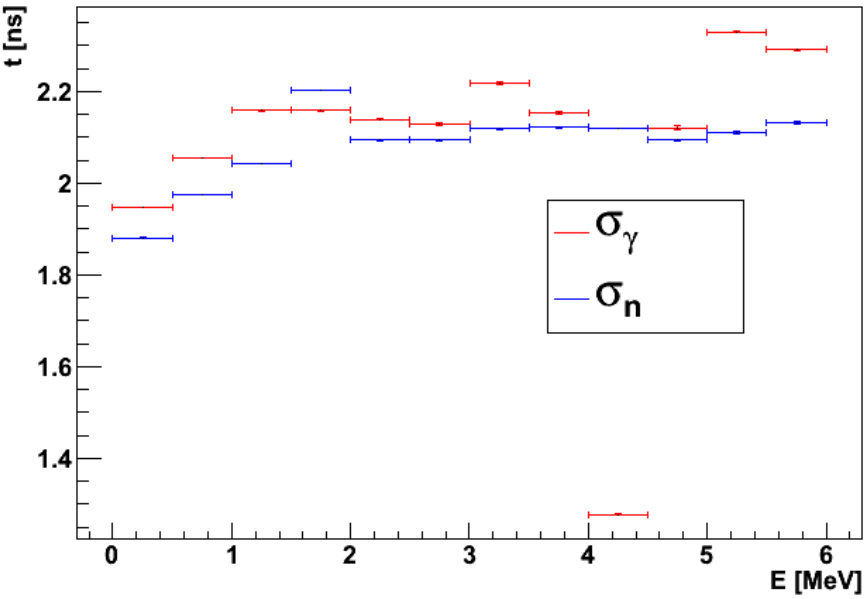

Figure 5.36: Energy dependency of the fitted Gaussian smearing σ for γ (red) and neutron (blue) induced recoil events in LH3.

fit parameter	recoil type	SP1	SP2	SPA
τ_1 [ns]	γ	6.8 ± 0.2	7.0 ± 0.3	6.8 ± 0.2
	n	7.0 ± 0.2	7.0 ± 0.3	6.9 ± 0.2
τ_2 [ns]	γ	26.5 ± 2.2	28.1 ± 2.9	27.0 ± 1.0
	n	27.3 ± 1.5	26.9 ± 1.7	25.5 ± 1.8
τ_3 [ns]	γ	152.3 ± 22.0	162.1 ± 26.6	147.9 ± 6.1
	n	140.8 ± 10.4	138.8 ± 8.3	131.3 ± 14.8
n_1	γ	0.67 ± 0.02	0.68 ± 0.02	0.67 ± 0.02
	n	0.61 ± 0.01	0.61 ± 0.02	0.59 ± 0.01
n_2	γ	0.19 ± 0.01	0.18 ± 0.01	0.19 ± 0.01
	n	0.21 ± 0.01	0.21 ± 0.01	0.22 ± 0.01
n_3	γ	0.14 ± 0.01	0.13 ± 0.01	0.15 ± 0.01
	n	0.18 ± 0.01	0.17 ± 0.01	0.19 ± 0.01
σ [ns]	γ	2.2 ± 0.1	2.1 ± 0.3	2.2 ± 0.1
	n	2.1 ± 0.1	2.1 ± 0.1	2.1 ± 0.1
t_0 [ns]	γ	1.8 ± 0.1	1.8 ± 0.1	1.7 ± 0.1
	n	1.7 ± 0.1	1.7 ± 0.0	1.7 ± 0.0

Table 5.10: Comparison of the energy-averaged fit results for LH3 for the different standards pulses SP1, SP2, and SPA (cf. fig. 5.13).

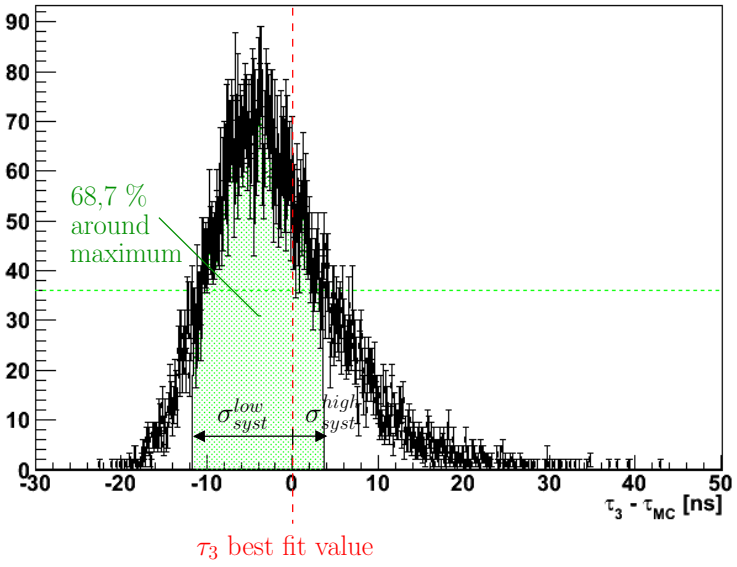

Figure 5.37: Distribution of the different $\tau_3 - \tau_{3,MC}$ from fits to MC generated pulses with input parameters from table 5.10. As the peak is asymmetric and shifted, the systematic errors are asymmetric as well.

error is most conservatively chosen to be the difference between the fit values. σ_{syst} is larger for γ than for neutron recoil events, reflecting the wider spread of results also apparent in table 5.10. The systematical errors match very well the numbers estimated using the MC simulations for LH3. Therefore, the systematical errors of the fit are used for all scintillator mixtures. They are shown in table B.12.

fit parameter	recoil type	LH3	LH3*	$\sigma_{syst,AmBe}$	$\sigma_{syst,MC}$
$\tau_1\,[ns]$	n	6.89 ± 0.22	6.84 ± 0.29	0.05	$^{+0.17}_{-0.17}$
	γ	6.84 ± 0.16	6.30 ± 1.66	0.53	$^{+0.17}_{-0.17}$
$\tau_2\,[ns]$	n	25.49 ± 1.80	24.86 ± 2.20	0.63	$^{+1.98}_{-2.08}$
	γ	27.00 ± 1.05	24.65 ± 5.97	2.35	$^{+1.56}_{-2.23}$
$\tau_3\,[ns]$	n	131.29 ± 14.76	126.63 ± 13.46	4.66	$^{+3.61}_{-11.68}$
	γ	147.87 ± 6.05	136.92 ± 31.86	10.95	$^{+3.61}_{-14.59}$
n_1	n	0.586 ± 0.007	0.586 ± 0.014	0.0004	$^{+0.025}_{-0.023}$
	γ	0.665 ± 0.019	0.608 ± 0.176	0.056	$^{+0.039}_{-0.029}$
n_2	n	0.222 ± 0.009	0.228 ± 0.011	0.006	$^{+0.07}_{-0.013}$
	γ	0.189 ± 0.012	0.235 ± 0.130	0.045	$^{+0.031}_{-0.021}$
n_3	n	0.191 ± 0.012	0.186 ± 0.013	0.006	$^{+0.019}_{-0.025}$
	γ	0.146 ± 0.014	0.157 ± 0.048	0.011	$^{+0.017}_{-0.021}$
$\sigma\,[ns]$	n	1.69 ± 0.04	1.77 ± 0.11	0.07	$^{+0.03}_{-0.03}$
	γ	1.72 ± 0.11	1.80 ± 0.24	0.08	$^{+0.02}_{-0.01}$
$t_0\,[ns]$	n	2.07 ± 0.10	2.09 ± 0.10	0.01	$^{+0.035}_{-0.031}$
	γ	2.15 ± 0.10	2.16 ± 0.10	0.002	$^{+0.025}_{-0.021}$

Table 5.11: Comparison of fit result parameters for the determination of systematical errors. Both samples consisted of the same LS mixture and filling procedures were equal. LH3 data was taken at the beginning and the LH3* data at the end of the beamtime.

5.4.3 Single pulse fit

Another approach to obtain the pulse shape parameters using the PDF in eq. (5.13) is given by fitting every single pulse instead of using standard pulses. This is done again for positions and LS mixtures under neutron beam irradiation. The cuts presented in section 5.2.2 are applied as well. For the analysis of the decay constants τ_i, t_0 no restrictive cuts on the peaks have to be performed as these parameters are independent of the event type.

Therefore, statistics is higher and a wider energy range can be investigated. This works best for the first decay constant τ_1, which is shown in the scatter plot fig. 5.38. The broad distribution at low-energies indicate that the pulse reconstruction of small pulses is problematic.

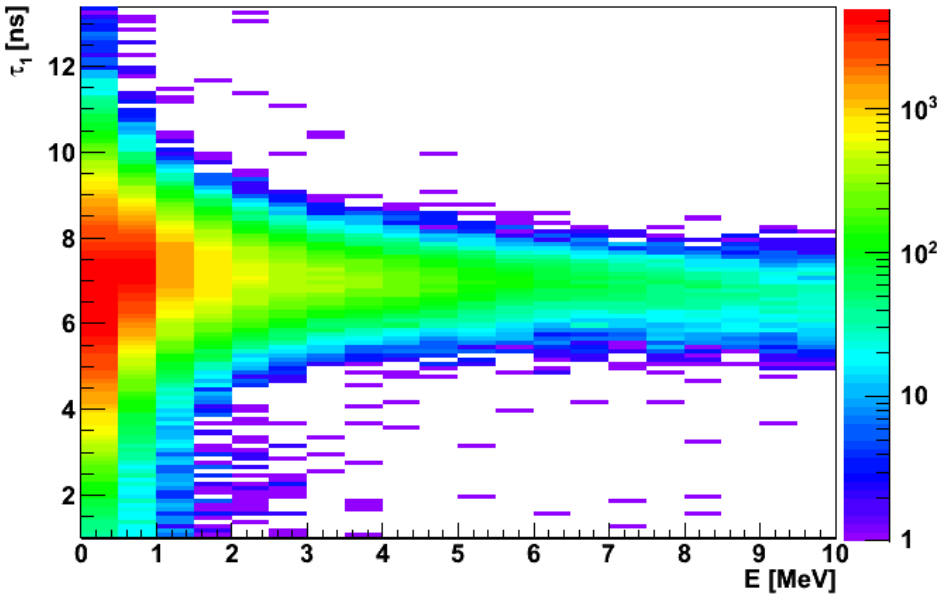

Figure 5.38: Scatter plot of the fit parameter τ_1 for all filtered events for LH3 under neutron beam irradiation. No cut on the ToF peaks is performed.

However, not all parameters are so easily accessible. For example, the three-component PDF also allows for a two-component fit with two identical decay times. Therefore, a three-dimensional Gaussian function is fitted to a 3-d histogram for both decay constants and amplitudes. In the latter case, γ and neutron induced recoils are identified with the help of the ToF peaks. Moreover, a background cut at 2 MeV is necessary to get rid of badly fitted low-energy pulses forming a uniform background. The projections of $n_{i,n}$ are shown in figure 5.39. The best fit values are marked with an asterisk. Although the fit with the Gaussian distributions does not account for the correlations between the fit parameters, it identifies the maximum reliably and gives a cross-check for the fit results of the standard pulses. In table 5.12 the results of the singe pulse fit parameters for all scintillators under neutron beam conditions are collected.

LS	parameter	$i = 1$	$i = 2$	$i = 3$
L10	$n_{\gamma,i}$	0.541 ± 0.140	0.262 ± 0.047	0.197 ± 0.032
	$n_{n,i}$	0.487 ± 0.077	0.265 ± 0.037	0.248 ± 0.036
	τ_i	2.86 ± 4.99	11.48 ± 99.87	201.03 ± 63.58
LH3	$n_{\gamma,i}$	0.670 ± 0.066	0.164 ± 0.051	0.165 ± 0.026
	$n_{n,i}$	0.608 ± 0.088	0.193 ± 0.040	0.198 ± 0.032
	τ_i	7.00 ± 0.37	23.39 ± 2.96	111.10 ± 12.58
LP3	$n_{\gamma,i}$	0.630 ± 0.115	0.189 ± 0.039	0.181 ± 0.049
	$n_{n,i}$	0.558 ± 0.126	0.213 ± 0.036	0.229 ± 0.036
	τ_i	6.94 ± 0.50	22.48 ± 3.67	120.02 ± 16.43
LPmax	$n_{\gamma,i}$			
	$n_{n,i}$	0.550 ± 0.000	0.210 ± 0.030	0.240 ± 0.030
	τ_i	6.91 ± 0.41	21.12 ± 3.16	99.42 ± 0.26
DCMV	$n_{\gamma,i}$			
	$n_{n,i}$	0.653 ± 0.074	0.171 ± 0.051	0.175 ± 0.035
	τ_i	8.92 ± 0.47	26.97 ± 4.46	108.40 ± 13.97

Table 5.12: Fit results for decay amplitude and constant from 3-d Gaussian fit to the fit parameters obtained from the single pulse fits. For the fit of the decay amplitudes, no particle type is selected. In case of the decay constants, the peaks from the ToF spectra are used to select γ and neutron induced events. If no numbers are given, the fit did not converge.

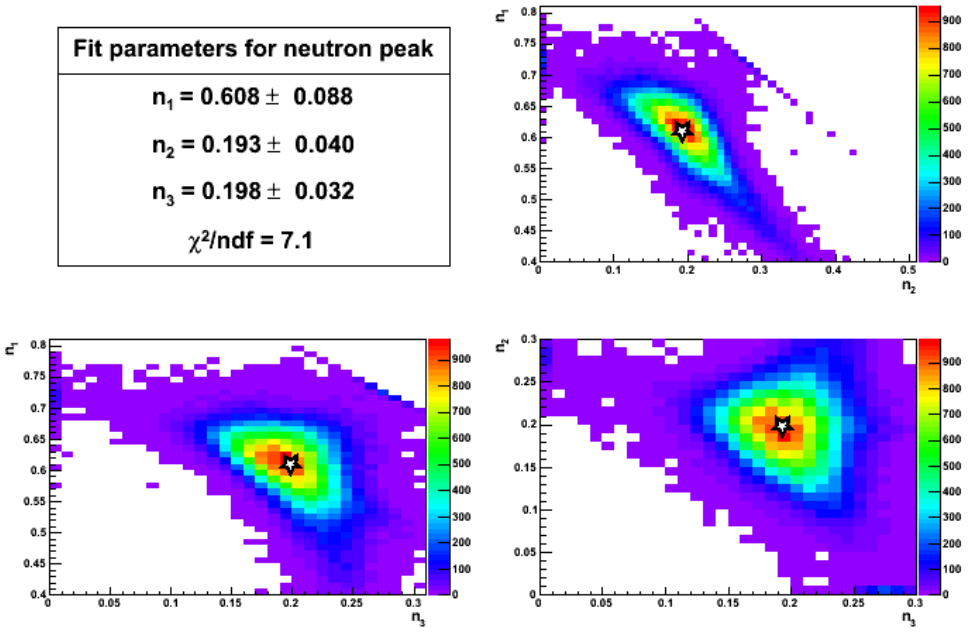

Figure 5.39: Projections of the 3-d scatter plot and best fit value of the decay amplitudes n_i for neutrons between 2-10 MeV for LH3.

5.4.4 Results

Table 5.13 summarizes all results from the fit of the standard pulses for LH3. The total result is a combination of three standard pulse fits: (1) SP2, (2) SPA for LH3, and (3) SPA for LH3*. Since the decay times for γ and neutron induced recoil events are found to be similar, they are combined. Analogously, the combined values for the other scintillator mixtures are calculated from the previously derived standard pulses. The final fit parameter values are shown in tables 5.14-5.16. The fit results of each data set can be found in the appendices B.5-B.10. The results from the single pulse fit are not used in the calculations of the decay amplitudes, as not all 3-d fits converge well. This is due to the correlations between the parameters that are not not taken into account by the spherical symmetrical fit model. Consequently, neither the decay constants obtained from the single pulse fits are considered in the final result. However, they serve as a good cross-check of the standard pulse analysis (see B.5-B.10). Except for the slowest decay constant, the single pulse fit confirms the results of the standard pulse fits.

Figures 5.40, 5.41, and 5.42 are a graphical summary of all combined results, including statistical and systematical errors. Overall, the third component seems to have the largest impact on the pulse shape discrimination (cf. table 5.9).

parameter	recoil type	LH3 SP2	LH3 SPA	LH3* SPA	Total $\pm\sigma_{stat}\ \pm\sigma_{syst}$
τ_1 [ns]	n	7.0 ± 0.3	6.9 ± 0.2	6.9 ± 0.2	6.9 ± 0.1 ± 0.2
	γ	6.9 ± 0.2	6.8 ± 0.2	6.0 ± 2.0	
τ_2 [ns]	n	26.9 ± 2.0	25.5 ± 2.0	25.6 ± 1.8	$26.4 \pm 0.8\ ^{+2.0}_{-2.2}$
	γ	27.4 ± 2.5	26.8 ± 1.2	23.8 ± 7.1	
τ_3 [ns]	n	139.1 ± 9.2	126.0 ± 15.0	126.0 ± 13.4	$141.0 \pm 4.3\ ^{+3.6}_{-14.6}$
	γ	160.4 ± 26.6	146.1 ± 5.9	132.7 ± 38.3	
n_1	n	0.606 ± 0.011	0.586 ± 0.007	0.590 ± 0.008	$0.591 \pm 0.006\ ^{+0.043}_{-0.027}$
	γ	0.682 ± 0.022	0.669 ± 0.022	0.586 ± 0.213	$0.676 \pm 0.016\ ^{+0.039}_{-0.031}$
n_2	n	0.219 ± 0.005	0.227 ± 0.006	0.232 ± 0.005	$0.222 \pm 0.004\ ^{+0.070}_{-0.019}$
	γ	0.184 ± 0.016	0.193 ± 0.014	0.256 ± 0.155	$0.189 \pm 0.010\ ^{+0.031}_{-0.021}$
n_3	n	0.176 ± 0.012	0.187 ± 0.009	0.179 ± 0.008	$0.183 \pm 0.007\ ^{+0.021}_{-0.025}$
	γ	0.134 ± 0.008	0.138 ± 0.009	0.157 ± 0.058	$0.136 \pm 0.006\ ^{+0.017}_{-0.025}$

Table 5.13: Fit results of the pulse decay constants and amplitudes for LH3. The total result in the last column is a combination of the fit result of the different standard pulses given in columns 3-5.

LH10	mean	σ_{stat}	σ_{syst}
τ_1 [ns]	5.0	±0.1	$^{+0.3}_{-0.2}$
τ_2 [ns]	20.4	±0.4	$^{+1.0}_{-0.8}$
τ_3 [ns]	111.1	±1.4	$^{+2.6}_{-7.2}$
$n_{1,n}$	0.477	±0.010	$^{+0.073}_{0.015}$
$n_{1,\gamma}$	0.536	±0.017	$^{+0.025}_{-0.021}$
$n_{2,n}$	0.285	±0.004	$^{+0.053}_{0.009}$
$n_{2,\gamma}$	0.288	±0.008	$^{+0.021}_{-0.023}$
$n_{3,n}$	0.241	±0.009	$^{+0.043}_{0.005}$
$n_{3,\gamma}$	0.175	±0.009	$^{+0.009}_{-0.013}$

(a)

LP	mean	σ_{stat}	σ_{syst}
τ_1 [ns]	6.9	±0.2	$^{+0.5}_{-0.4}$
τ_2 [ns]	26.6	±1.7	$^{+3.9}_{-1.6}$
τ_3 [ns]	142.9	±9.8	$^{+20.4}_{-17.2}$
$n_{1,n}$	0.574	±0.015	$^{+0.021}_{-0.015}$
$n_{1,\gamma}$	0.653	±0.029	$^{+0.033}_{-0.005}$
$n_{2,n}$	0.231	±0.004	$^{+0.015}_{-0.015}$
$n_{2,\gamma}$	0.202	±0.016	$^{+0.011}_{-0.043}$
$n_{3,n}$	0.195	±0.017	$^{+0.019}_{-0.027}$
$n_{3,\gamma}$	0.145	±0.013	$^{+0.005}_{-0.099}$

(b)

Table 5.14: Final fit results of the pulse decay constants and amplitudes for (a) LH10 and (b) LP.

LP1d	mean	σ_{stat}	σ_{syst}
τ_1 [ns]	6.8	± 0.1	$^{+0.2}_{-0.2}$
τ_2 [ns]	24.9	$\pm$ 0.4	$^{+1.3}_{-1.7}$
τ_3 [ns]	138.5	$\pm$ 2.7	$^{+4.4}_{-11.4}$
$n_{1,n}$	0.590	± 0.022	$^{+0.011}_{-0.045}$
$n_{1,\gamma}$	0.665	± 0.020	$^{+0.029}_{-0.031}$
$n_{2,n}$	0.246	± 0.006	$^{+0.011}_{-0.027}$
$n_{2,\gamma}$	0.206	± 0.014	$^{+0.029}_{-0.025}$
$n_{3,n}$	0.164	± 0.022	$^{+0.009}_{-0.025}$
$n_{3,\gamma}$	0.129	± 0.006	$^{+0.013}_{-0.017}$

(a)

LPmax	mean	σ_{stat}	σ_{syst}
τ_1 [ns]	6.9	$\pm$ 0.1	$^{+0.3}_{-0.2}$
τ_2 [ns]	25.9	$\pm$ 0.4	$^{+1.7}_{-2.0}$
τ_3 [ns]	142.9	$\pm$ 2.9	$^{+12.0}_{-35.0}$
$n_{1,n}$	0.600	± 0.009	$^{+0.035}_{-0.037}$
$n_{1,\gamma}$	0.676	± 0.016	$^{+0.029}_{-0.021}$
$n_{2,n}$	0.235	± 0.006	$^{+0.013}_{-0.013}$
$n_{2,\gamma}$	0.197	± 0.011	$^{+0.023}_{-0.023}$
$n_{3,n}$	0.163	± 0.013	$^{+0.023}_{-0.035}$
$n_{3,\gamma}$	0.126	± 0.005	$^{+0.007}_{-0.011}$

(b)

Table 5.15: Final fit results of the pulse decay constants and amplitudes for (a) LP1d and (b) LPmax.

DCMV	mean	σ_{stat}	σ_{syst}
τ_1 [ns]	8.8	$\pm$ 0.1	$^{+0.3}_{-0.1}$
τ_2 [ns]	34.4	$\pm$ 2.0	$^{+5.0}_{-3.4}$
τ_3 [ns]	224.1	$\pm$ 69.3	$^{+12.8}_{-29.2}$
$n_{1,n}$	0.651	± 0.010	$^{+0.035}_{-0.027}$
$n_{1,\gamma}$	0.715	± 0.011	$^{+0.039}_{-0.041}$
$n_{2,n}$	0.197	± 0.004	$^{+0.029}_{-0.027}$
$n_{2,\gamma}$	0.157	± 0.009	$^{+0.033}_{-0.029}$
$n_{3,n}$	0.149	± 0.010	$^{+0.013}_{-0.023}$
$n_{3,\gamma}$	0.120	± 0.011	$^{+0.021}_{-0.033}$

(a)

L50	mean	σ_{stat}	σ_{syst}
τ_1 [ns]	7.4	$\pm$ 0.1	$^{+0.5}_{-0.4}$
τ_2 [ns]	29.1	$\pm$ 1.2	$^{+3.1}_{-1.8}$
τ_3 [ns]	152.1	$\pm$ 10.0	$^{+9.7}_{-15.2}$
$n_{1,n}$	0.621	± 0.012	$^{+0.021}_{-0.015}$
$n_{1,\gamma}$	0.681	± 0.017	$^{+0.043}_{-0.007}$
$n_{2,n}$	0.225	± 0.004	$^{+0.013}_{-0.013}$
$n_{2,\gamma}$	0.190	± 0.012	$^{+0.031}_{-0.033}$
$n_{3,n}$	0.154	± 0.010	$^{+0.013}_{-0.019}$
$n_{3,\gamma}$	0.125	± 0.007	$^{+0.015}_{-0.025}$

(b)

Table 5.16: Final fit results of the pulse decay constants and amplitudes for (a) DCMV an (b) L50.

LH10: The decay amplitudes for γ and neutron induced recoil events differ greatly for all scintillator mixtures. The difference $n_{3,n} - n_{3,\gamma}$ - linked to the slowest decay time τ_3 - is most prominent for LH10. This is one reason why the γ/n discrimination power for LH10 is best (compare table 5.9). Moreover, the absolute value of the amplitude of the third component is highest. In this case the electronic noise has less impact and the pulse shape discrimination is more stable. Due to the high concentration of PPO, the energy transfer most efficient.

In tab. 5.18, the results are compared to LAB + 10 gℓ PPO + 20 mg/ℓ bisMSB from [70]. The differences are less pronounced when comparing the first component from L10 with the second from [70] and so on. On the other side, the decay amplitudes have a high accordance, especially considering that the amplitude of the fourth component is present in the third component of L10. This means, that the smearing of the pulse is large and that the fit fails to unravel the decay constants. Applying the single photon technique, maybe with an AmBe source, it could be possible to determine the true pulse shape of the neutron induced proton recoil.

LH3 and LP: No significant differences can be observed between the mixtures based on LAB from the two different providers. All decay constants and the differences $n_{i,n} - n_{i,\gamma}$ match nearly perfectly. Hence, there is only little influence of the LAB type on the n/γ discrimination power. In table 5.17, the fit results of the neutron beam experiment are compared to measurements of the pulse shape based on the detection of single photons, for LAB + 2 gℓ PPO + 20 mg/ℓ bisMSB [70] and LAB + 2 gℓ PPO [105]. The fast decay constants derived in this work are significantly higher than the ones from [70] and [105], while the third component τ_3 lies in between. Like for LH10, this is probably due to the bad timing resolution.

LP1d and LPmax: Within error bars, the decay constants of the aged samples match with the values of the mixture LP. However, the amplitudes $n_{3,\gamma}$ and $n_{3,n}$ are significantly smaller (cf. figure 5.43). This is due to oxygen that quenches the slow decay processes. Another major difference is in the amplitude of the third component. As a result, the discrimination between γ and neutron induced recoils is worse than for LP (cf. table 5.9).

In [105], oxygenated and deoxygenated samples of LAB + 2 gℓ PPO were irradiated with αs and electrons. As observed in this thesis, the influence on the decay constants is minimal. Moreover, the decay amplitudes show the same behavior like the samples from LP to LP1d and LPmax: growing $n_{1,\gamma}$ while $n_{3,\gamma}$ decreases and $n_{2,\gamma}$ stays almost constant.

L50 and DCMV: L50 and and especially DCMV exhibit the slowest decay times. This can be explained by the slower intermolecular energy transfer from the excited LAB to the

PPO because of the abundant non-scintillating n-paraffin. Moreover, the smallest n_3 and $n_{3,n} - n_{3,\gamma}$ of all make them less suited for pulse shape particle discrimination. The large value and error for τ_3 for DCMV are due to fits that have essentially only two components. Therefore, also τ_2 and its error are appear to be higher.

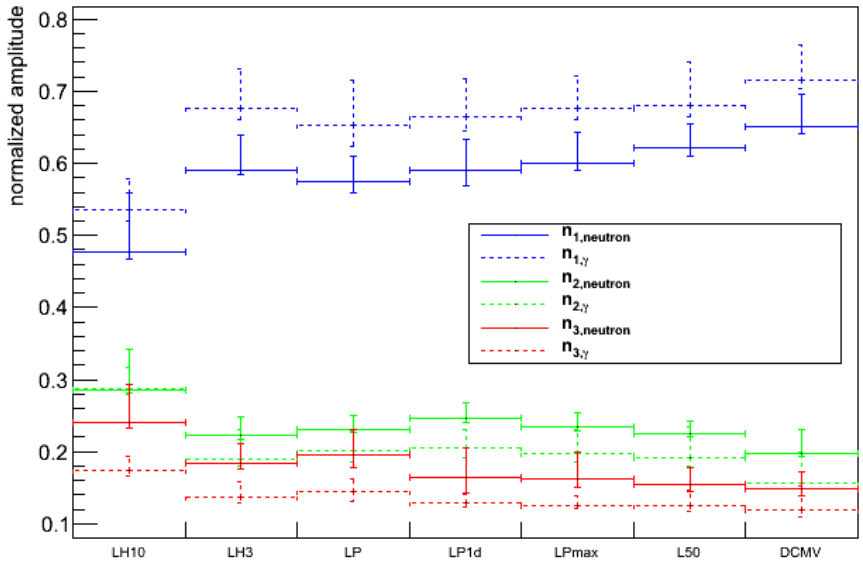

Figure 5.40: Comparison of the final results for the three decay amplitudes n_i for γ and neutron induced recoil events for all scintillator mixtures.

fit parameter	PPO concentration		
	3g/ℓ	2g/ℓ [70]	2g/ℓ [105]
τ_1 [ns]	$6.9 \pm 0.1\ ^{+0.21}_{-0.17}$	$5.21\ ^{+0.04}_{-0.05} \pm 0.03$	4.6 ± 0.3
τ_2 [ns]	$26.4 \pm 0.8\ ^{+2.0}_{-2.2}$	$18.4 \pm 0.6 \pm 0.2$	18 ± 1
τ_3 [ns]	$141.0 \pm 4.3\ ^{+3.6}_{-14.6}$	$118\ ^{+3}_{-2}\ ^{+0}_{-1}$	156 ± 9
n_1	$0.676 \pm 0.016\ ^{+0.039}_{-0.031}$	$0.777 \pm 0.007 \pm 0.003$	0.71
n_2	$0.189 \pm 0.010\ ^{+0.031}_{-0.021}$	$0.170 \pm 0.006\ ^{+0.002}_{-0.003}$	0.22
n_3	$0.136 \pm 0.006\ ^{+0.017}_{-0.025}$	$0.063 \pm 0.009 \pm 0.003$	0.07

Table 5.17: Results of the decay time experiments described in [70, 105] compared to the results in this thesis for LAB from Helm.

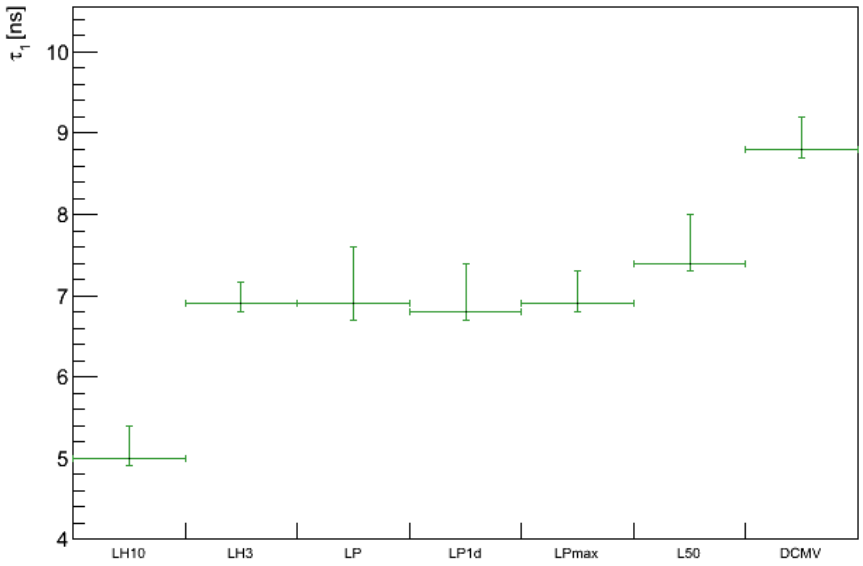

Figure 5.41: Final results for the decay constant τ_1 for combined γ and neutron induced recoil events for all scintillator mixtures.

fit parameter	PPO concentration	
	10g/ℓ	10g/ℓ [70]
τ_1 [ns]	$5.0 \pm 0.1\ ^{+0.3}_{-0.2}$	$1.94\ ^{+0.04}_{-0.05} \pm 0.04$
τ_2 [ns]	$20.4 \pm 0.4\ ^{+1.0}_{-0.8}$	$5.9 \pm 0.3 \pm 0.2$
τ_3 [ns]	$111.1 \pm 1.4\ ^{+2.6}_{-7.2}$	$26.9\ ^{+1}_{-0.9}\ ^{+1}_{-0.3}$
τ_4 [ns]		$137\ ^{+5}_{-4}\ ^{+0}_{-1}$
n_1	$0.536 \pm 0.017\ ^{+0.025}_{-0.021}$	$0.56 \pm 0.02 \pm 0.01$
n_2	$0.288 \pm 0.008\ ^{+0.021}_{-0.023}$	$0.27 \pm 0.01 \pm 0.01$
n_3	$0.175 \pm 0.009\ ^{+0.009}_{-0.013}$	$0.133 \pm 0.004\ ^{+0.01}_{-0.02}$

Table 5.18: Results of the decay time experiment described in [70] compared to the results in this thesis for LAB from Helm.

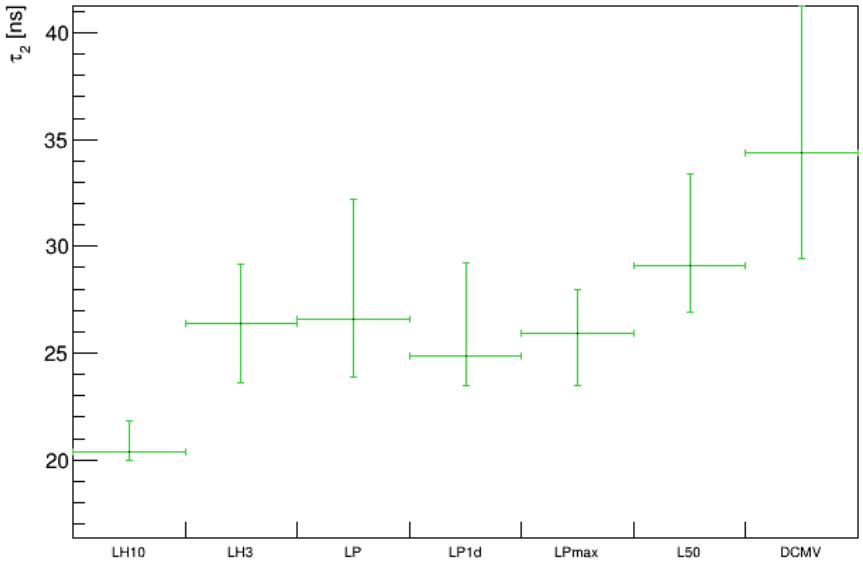

(a) decay constant τ_2

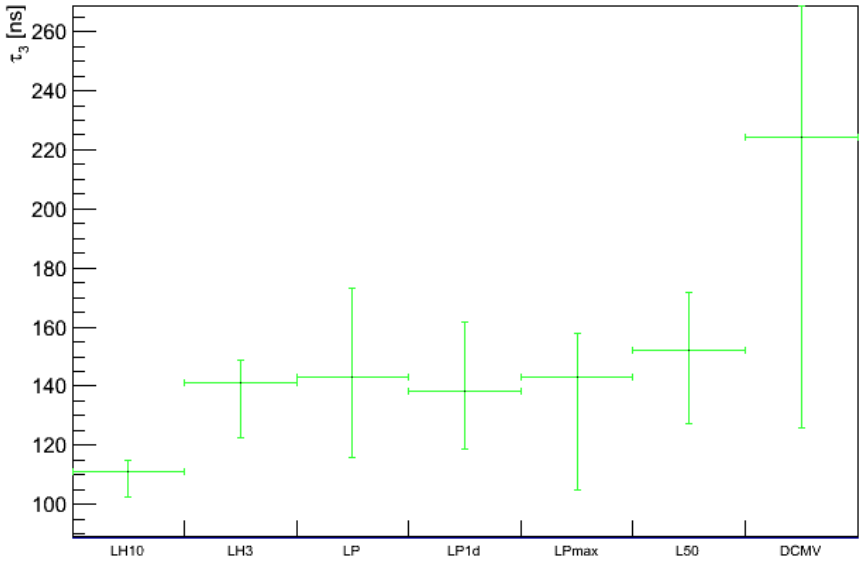

(b) decay constant τ_3

Figure 5.42: Final results for the decay constants τ_2 and τ_3 for combined γ and neutron induced recoil events for all scintillator mixtures.

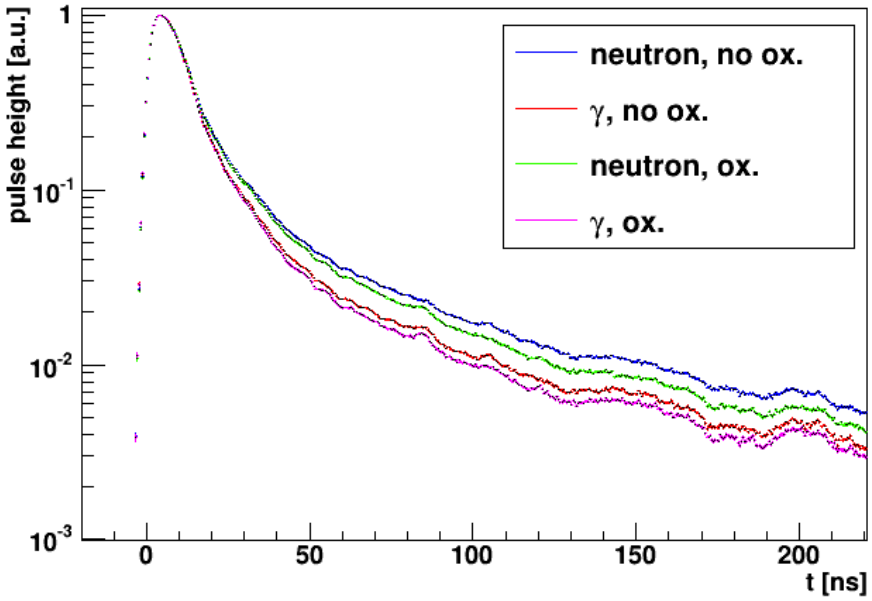

Figure 5.43: Comparison of the standard pulses SP2 for LP and the aged sample LPmax. The oxidation mainly leads to suppression of the slowest decay amplitude n_3.

5.5 Proton Quenching

Taking advantage of the neutron beam setup, the proton quenching factors $Q = \frac{E_{dep}}{E_{vis}}$ have been measured as well for various scintillators [91]. Fitting the edge of the neutron induced recoil spectrum, the maximum visible energy E_{vis} can be reconstructed. The fit function was determined in simulations. In approximation, the neutron transfers all its energy to the recoil proton. Hence the ToF energy of the neutrons is equal to the maximum energy deposit E_{dep}. By variation of the detector positions along different off-axis angles, different maximum neutron ToF energies can be observed. Thus, this method offers the possibility to measure the energy-dependent quenching factor. By a fit to the data using Birks equation [69], the kB value can be calculated for each scintillator as shown in fig. 5.44. Information on the energy deposit per unit length is provided by the PSTAR data base [106]. For LH3, $kB = 0.01869 \pm 0.00799\,\mathrm{cmMeV^{-1}}$ [91]. Within error, this value is compatible with [107].

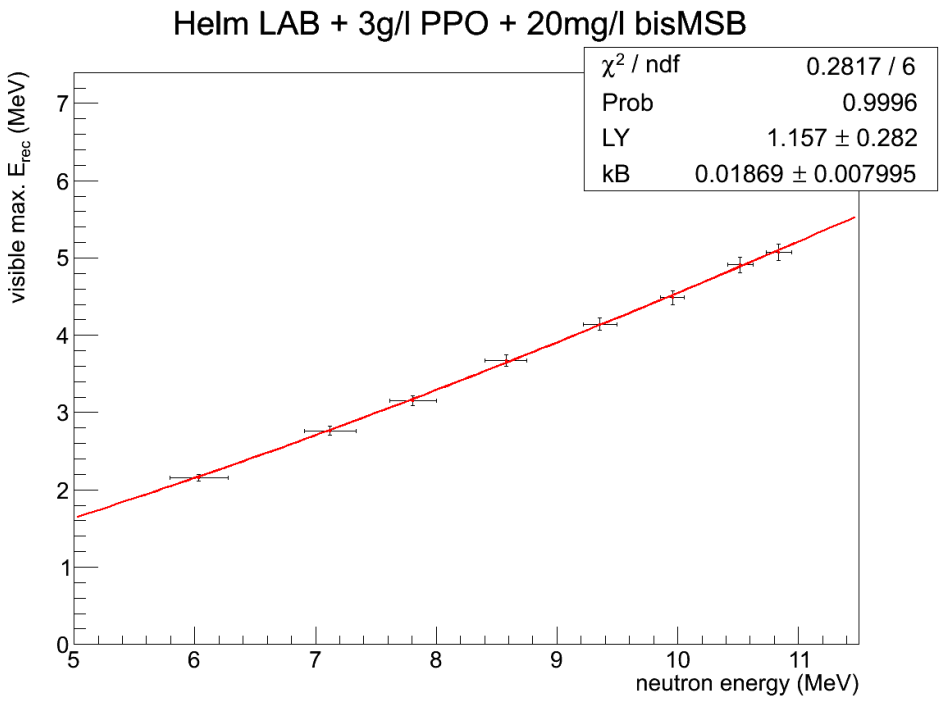

Figure 5.44: Quenched visible energy as a function of the neutron energy for LH3. By a fit using the Birks equation [69], the kB value can be calculated. [91].

Chapter 6

Detection of supernova neutrinos with LENA

Core-collapse supernovae (SNe) are amongst the most energy-rich events in the universe, possibly outshining even entire galaxies. It is the violent fate of massive stars with masses above $8\,M_\odot$[1]. In the collapse, about 99% of the gravitational binding energy is released in the form of neutrinos, leaving back a neutron star or a black hole.

Galactic SN explosions are very rare events. There are several estimates for the galactic core collapse rate. While extragalactic optical observations [108] suggest a higher rate, historical records and remnant counts point to a rate of one to three SNe per century only [109].

A galactic core-collapse SN would trigger an enormous number of events in a large detector like LENA. Both the energy spectra of all neutrino flavors and the temporal variation of the signal intensity convey information about the SN dynamics. Unlike photons, νs are not obstructed by the outer layers of the star or interstellar matter and thus provide a deep look almost into the heart of the explosion. Only gravitational waves have a comparable potential. Moreover, as the the neutrinos propagate through matter with high densities, they might give hints on oscillation parameters such as the sign of Δm^2_{23} or mixing angles in

In the beginning of this chapter, two computational SN simulations are presented that model the SN neutrino emission. First, a model from the Garching group [110, 111], which is used for the event rate calculations, and secondly the Basel group model [112], which is used for comparison. Afterwards, the six detection channels for SN neutrinos with LENA are presented. Finally, the possibility to observe the earth effect and neutrinos from late

[1] solar mass $M_\odot = 1.9 \cdot 10^{30}\,\mathrm{kg}$

burning stages of SN progenitors is discussed.

6.1 SN models

6.1.1 Garching model

For the determination of the SN neutrino event rates, spectra, and their temporal evolution, SN simulation results from the Garching group [110, 111] are used. Their model is based on the VERTEX[2] code. The hydrodynamic evolution of the environment is described using non-relativistic Euler equations, while general relativity effects are modeled by a modified gravitational potential. Redshift and time dilation are implemented as well. A key feature of the model is the exact conservation of mass, energy, and momentum. The transport of the neutrinos, coupled in multi-energy groups, is calculated in a complex Boltzmann solver scheme [113, 114]. In order to solve this integro-differential set of equations, a variable Eddington factor closure relation is implemented. Only $\nu_e, \bar{\nu}_e$ and $\bar{\nu}_x(\nu_\mu, \bar{\nu}_\mu, \nu_\tau, \bar{\nu}_\tau)$ are considered as the temperature is too low to produce μ or even τ in significant quantities. Therefore, CC reactions leading to a spectral and number difference of ν_μ and ν_τ can be safely neglected.

For the equation of state describing the properties of the hot protoneutron star, the model of Shen [115, 116] is chosen. It includes a large set of neutrino interactions and the neutrino-nucleon opacity treatment according to Burrows [117, 118].

While the long-used one-dimensional SN models did not result in a successful explosion, state-of-the-art 2d-simulations have shown to describe the scenario more precisely [119]. However, a long term evolution of the explosion up to 10 s exceeds the processing power of today's super-computers. Therefore, a spherically symmetric model has been used. Fortunately, using a O-Ne-Mg progenitor, also the one-dimensional description results in a successful explosion. Here, a progenitor model from [120, 121] has been used.

Binned neutrino spectra are evaluated in a co-moving frame at a radius of 500 km. At each time step, they have been fitted with a pinched Fermi-Dirac distribution:

$$f_{FD}(E;\eta) = \frac{1}{NT^3}\frac{E^2}{1 + exp\left(\frac{E}{T} - \eta\right)}. \tag{6.1}$$

Here, T denotes the temperature, η is the chemical potential (describing the degeneracy),

[2] **V**ariable **E**ddington factor **R**adiative **T**ransfer for **S**upernova **EX**plosions

and N is the normalization factor

$$\begin{aligned} N &= \int_0^\infty \frac{1}{T^3} \frac{E^2}{1 + exp\left(\frac{E}{T} - \eta\right)} \\ &= -2 \cdot Li_3(-exp(-\eta)) \\ &\overset{\eta=0}{=} \frac{3}{2}\zeta_3 \end{aligned} \tag{6.2}$$

with the polylogarithmic (or Jonquière's) function $Li_n(x) = \sum_{k=1}^{\infty} \frac{x^k}{k^n}$ and the Riemann zeta function $\zeta_n = \sum_{k=1}^{\infty} \frac{1}{k^n}$.

Usually, the distortion of the spectrum from a thermal shape is described by the pinching factor p:

$$\begin{aligned} p &\equiv \frac{\langle E_{\eta=0} \rangle^2}{\langle E^2_{\eta=0} \rangle} \cdot \frac{\langle E^2 \rangle}{\langle E \rangle^2} \\ &\simeq \frac{1}{1.3029} \cdot \frac{\langle E^2 \rangle}{\langle E \rangle^2} \\ &\overset{\eta=0}{=} 1 \end{aligned} \tag{6.3}$$

with the average energy

$$\langle E \rangle = \int_0^\infty \frac{1}{NT^3} \frac{E^3}{1 + exp\left(\frac{E}{T} - \eta\right)} dE \tag{6.4}$$

and the second moment

$$\langle E^2 \rangle = \int_0^\infty \frac{1}{NT^3} \frac{E^4}{1 + exp\left(\frac{E}{T} - \eta\right)} dE. \tag{6.5}$$

$\langle E^n_{\eta=0} \rangle$ stands for the n-th energy moment for a Fermi-Dirac distribution without chemical potential. If $p = 1$, a perfect Fermi-Dirac spectrum is obtained. Otherwise, if the spectrum is pinched ($p < 1$), the high-energy tail is suppressed. For $p > 1$ (anti-pinched), the high-energy tail is enhanced.

A fit to the binned simulation output, for ν_x at $t \approx 2\,\mathrm{s}$ after the bounce is shown in figure 6.1. Clearly, the fit reproduces the data very well.

The evolution of the luminosities, mean neutrino energies and the pinching factors can be seen in figures 6.2, 6.3, and 6.4. For better understanding, the evolution has been split into two time ranges for each parameter: the first spreads from the core bounce ($t = 0\,\mathrm{s}$) to 0.2 s, including the *deleptonization* phase ($t < 20\,\mathrm{ms}$) and the *accretion* phase. The *cooling* phase is shown in the second figure, spreading from 0.2 to 10 s.

Looking at the luminosity evolution (see figure 6.2), the deleptonization burst is visible as a distinct peak as expected. For about 20 ms, the luminosity L_e of the ν_e is about one or

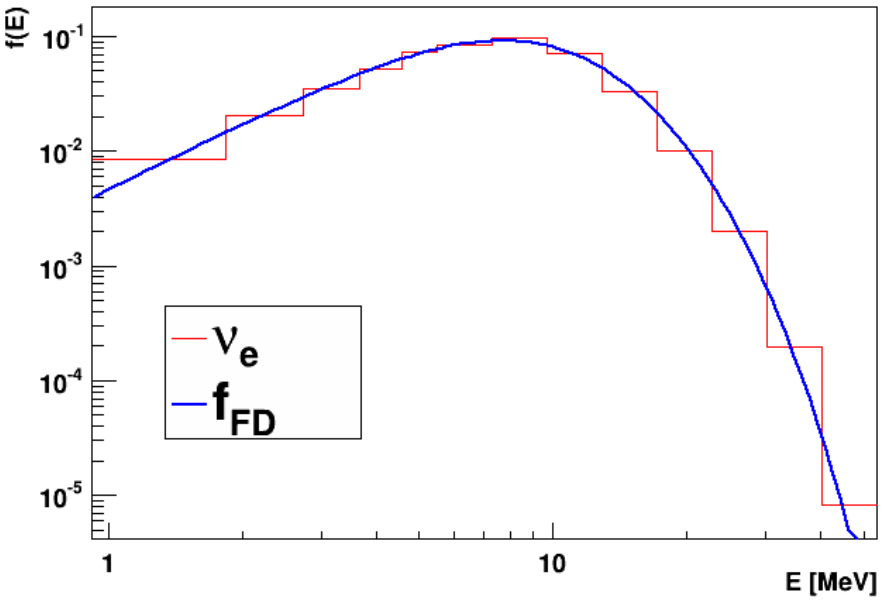

(a) ν_e

Figure 6.1: Comparison of simulation output (red) to the spectral fit for ν_e 2s after the bounce.

two orders of magnitude higher than that of the other flavors. The luminosity of $\bar{\nu}_x$ begins to rise a few ms before $\bar{\nu}_e$. This is due to the high degeneracy of electrons and thus the low abundance of positrons during deleptonization that suppresses the production of $\bar{\nu}_e$. Note that L_x stands for the luminosity of a single flavor ν_μ,ν_τ or the respective antiparticles.

During the accretion phase, the luminosity difference between the flavors is getting less pronounced and vanishes completely in the cooling phase. Towards the end of the cooling phase, the surface cooling fades into volume cooling and the luminosities drop even faster. The total energy release in this model is $\sim 1.7 \cdot 10^{53}$ erg.

As expected, the neutrino energy $\langle E_{\nu_e} \rangle$ peaks as well during the deleptonization burst, which is due to the high degeneracy (see figure 6.3). This energy is rapidly transferred to the thermal production of $\bar{\nu}_e$ and $\bar{\nu}_x$, whose mean energy rise steeply. During the accretion phase, the 'classical' hierarchy holds: $\langle E_x \rangle > \langle E_{\bar{e}} \rangle > \langle E_e \rangle$. However, down-scattering of $\bar{\nu}_x$ in the transport sphere gets more dominant in time until no more difference to $\bar{\nu}_e$ is present. The mean energies of $\bar{\nu}_e$ and $\bar{\nu}_x$ cross around 790 ms. As was shown in [110], nucleon recoils are responsible for this behavior. Neutrino-cooling of the protoneutron star leads to decreasing neutrino energies.

The pinching factor (figure 6.4) shows how similar a spectrum is to a thermal Fermi-Dirac

spectrum, see eqs. (6.1),(6.3). For $p < 1$ the high energy tail is suppressed (*pinched*), while for $p > 1$ it is more pronounced (*anti-pinched*). While the ν_e spectrum is always pinched, the other flavors are antipinched during a short time period in the cooling phase. However, this may be an artificial effect of the simulation.

6.1.2 Basel model

In [112], SN explosion models are presented for an $8.8\,M_\odot$ O-Ne-Mg progenitor ([120, 121], as in [110]), and $10.8\,M_\odot$ and $18\,M_\odot$ progenitors with Fe-cores [31]. The treatment of the neutrinos is comparable to the Garching group, however there are differences in the considered neutrino-nucleus interactions. The evolution of the neutrino luminosities and energies is shown in Figures 6.5 and 6.6. The luminosity curves of both O-Ne-Mg models are largely in agreement for all flavors: except for the deleptonization peak, all L_α ($\alpha = e, \bar{e}, x$) are almost equal and decreasing with time. However, the Garching model predicts higher luminosities by a factor of 1.5-2. Concerning the mean energies $\langle E \rangle$, a large difference can be observed between the two models. While the evolution $\langle E_e \rangle$ is comparable, there are major differences concerning $\langle E_{\bar{e}} \rangle$ and $\langle E_x \rangle$. In the Garching model, the mean energies are in the 'classical' hierarchy $\langle E_e \rangle < \langle E_{\bar{e}} \rangle < \langle E_x \rangle$ only during the first $\sim$200 ms after the bounce. Later the mean energy of the anti-electron neutrinos is in the same order or even higher than $\langle E_x \rangle$. In the Basel model, the 'classical' hierarchy holds throughout the neutrino emission, which would be beneficial for the search of oscillation effects.

The same prominent energy hierarchy along with higher neutrino mean energy is expected according to the Basel calculations for the iron-core progenitors. While the increase is small for ν_e and $\bar{\nu}_e$, the mean energy of $\overset{(-)}{\nu}_x$ shoots up to 16 MeV in the first 400 ms. As before, the hierarchy $\langle E_e \rangle < \langle E_{\bar{e}} \rangle < \langle E_x \rangle$ holds for the entire 10 s of the explosion. The fact that the mean energy difference of $\overset{(-)}{\nu}_x$ and $\bar{\nu}_e$ is significant for at least 2 s can be essential for the observation of the earth effect in the anti-neutrino sector in LENA. The luminosity curves of both iron-core progenitors show a distortion from the O-Ne-Mg core in the first few 100 ms. For both electron and electron anti-neutrinos, there is a plateau around $4 \cdot 10^{52}$erg/s between $\sim 50 - 300$ ms, before the luminosities decrease linearly in both models. At the same time, L_x is higher and decreasing less rapidly. As a result, the event rates of LENA will be significantly higher for an iron-core than an O-Ne-Mg based SN. The numbers given in the next chapter referring to the Garching model can therefore be considered conservative.

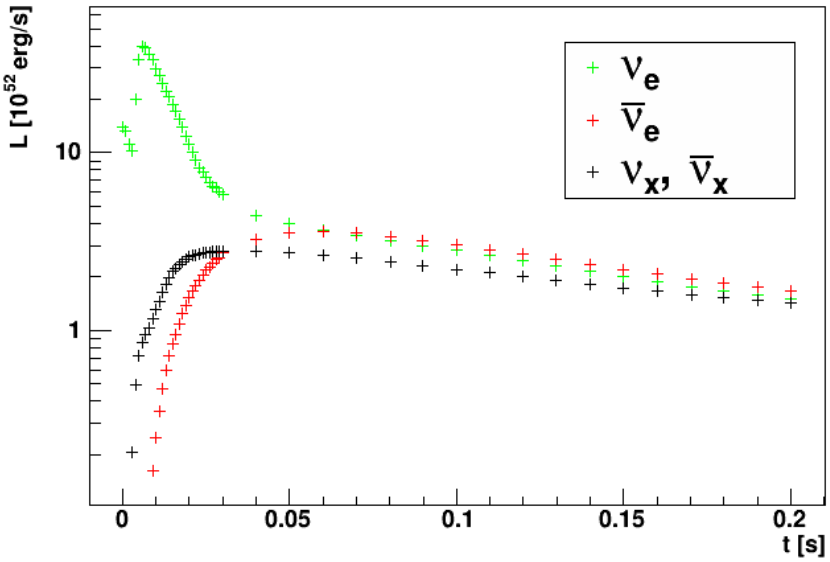

(a) Deleptonization (0-20 ms) and accretion phase (∼20-200 ms).

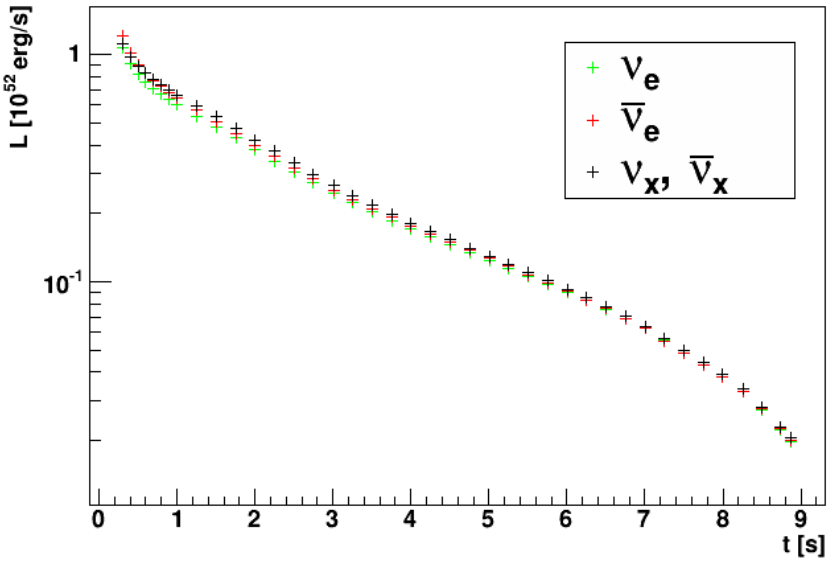

(b) Cooling phase.

Figure 6.2: Time evolution of the luminosities L for ν_e, $\bar{\nu}_e$ and ν_x, where $x = \mu, \tau$, for *deleptonization* and *accretion phase* (a), and the *cooling phase* (b) [110]. During the first tens of milliseconds after the core bounce ($t = 0$), a peak in the luminosity L_e due to deleptonization can be observed. L_x rises faster that $L_{\bar{e}}$, as the low abundance of positrons during deleptonization suppresses the production of $\bar{\nu}_e$. During the accretion phase the luminosity differences get less pronounced and vanish completely during the cooling phase. Around $t = 8\,\mathrm{s}$, the surface cooling fades into volume cooling and the luminosities drop more rapidly.

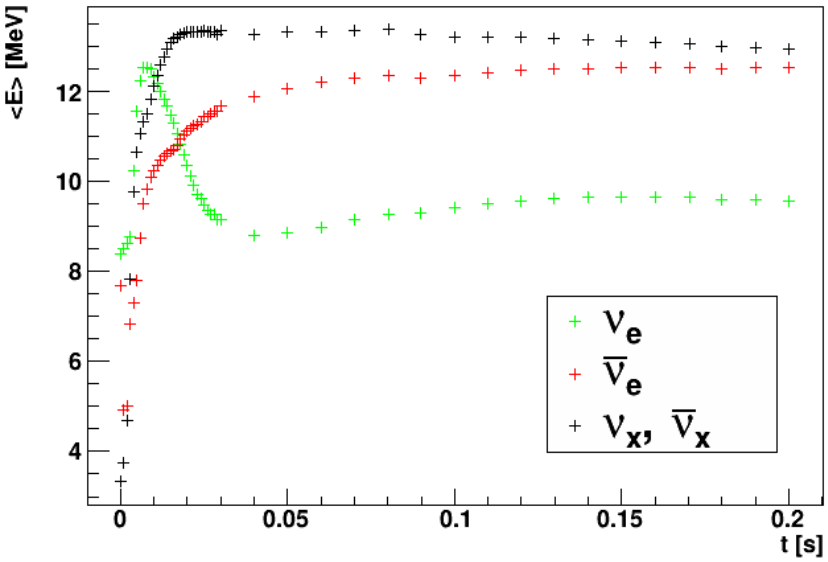

(a) Deleptonization (0-20 ms) and accretion phase (∼20-200 ms).

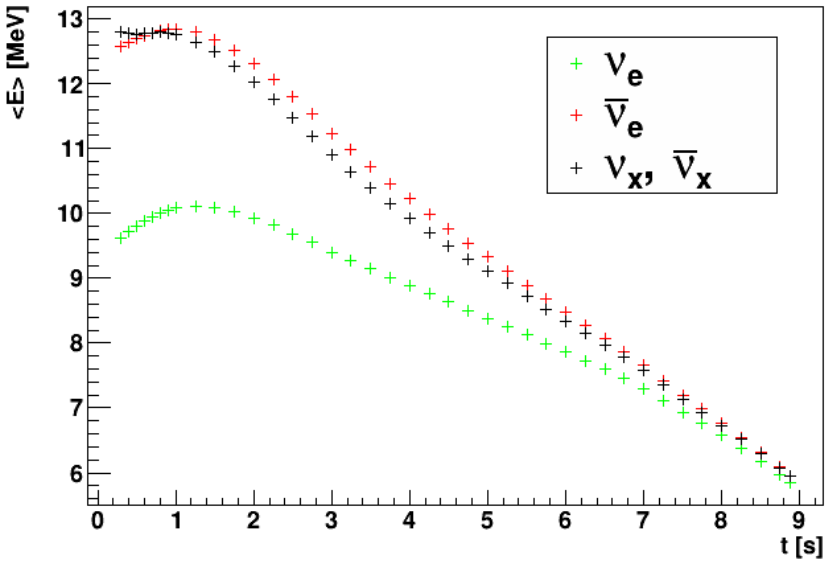

(b) Cooling phase.

Figure 6.3: Time evolution of the mean energies $\langle E \rangle$ for $\nu_e, \bar{\nu}_e$ and ν_x, where $x = \mu, \tau$, for *deleptonization* and *accretion phase* (a), and the *cooling phase* (b) [110]. In the deleptonization phase, $\langle E_e \rangle$ shows a peak due to the high degeneracy of the ν_e produced. As the energy is transferred to the medium, $\langle E_{\bar{e}} \rangle$ and $\langle E_x \rangle$ rise steeply. During the accretion phase, the hierarchy $\langle E_x \rangle > \langle E_{\bar{e}} \rangle > \langle E_e \rangle$ is most prominent. This is to due the differences of the neutrino production processes for each flavor that freeze out at different radii, i.e. $R_x < R_{\bar{e}} < R_e$. Due to multiple scattering processes, the difference between $\langle E_x \rangle$ and $\langle E_{\bar{e}} \rangle$ get less pronounced and even inverted during the cooling phase.

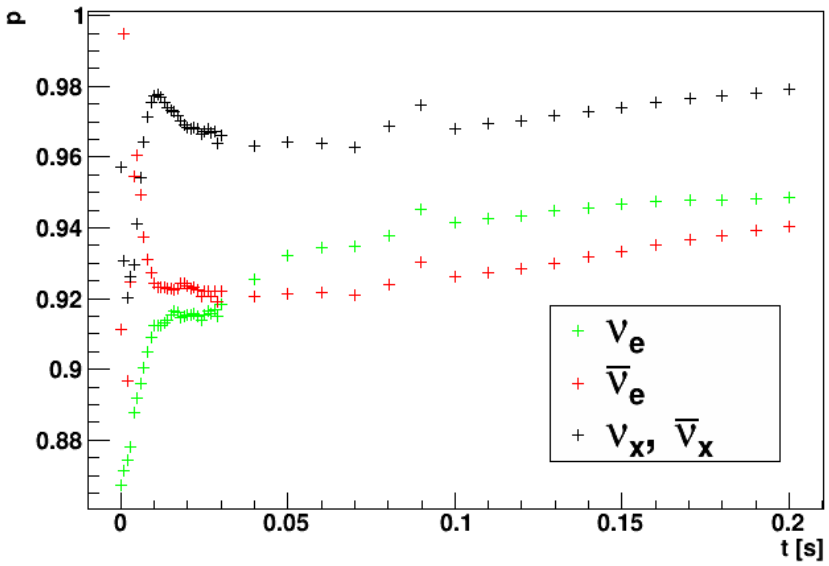

(a) Deleptonization (0-20 ms) and accretion phase (∼20-200 ms).

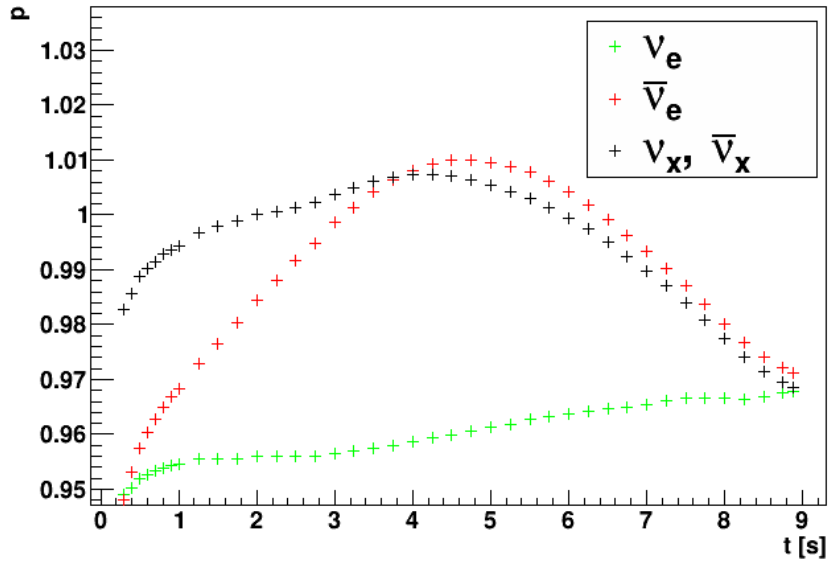

(b) Cooling phase.

Figure 6.4: Time evolution of the pinching factors p for $\nu_e, \bar{\nu}_e$ and ν_x, where $x = \mu, \tau$, for *deleptonization* and *accretion phase* (a), and the *cooling phase* (b) [110]. During almost the whole explosion, the energy spectra can be described with pinched Fermi-Dirac distributions ($p < 1$) with suppressed high-energy tails. Since the neutrino cross-sections increase with energy, this is disadvantageous for the detection of SN neutrinos compared to unpinched spectra.

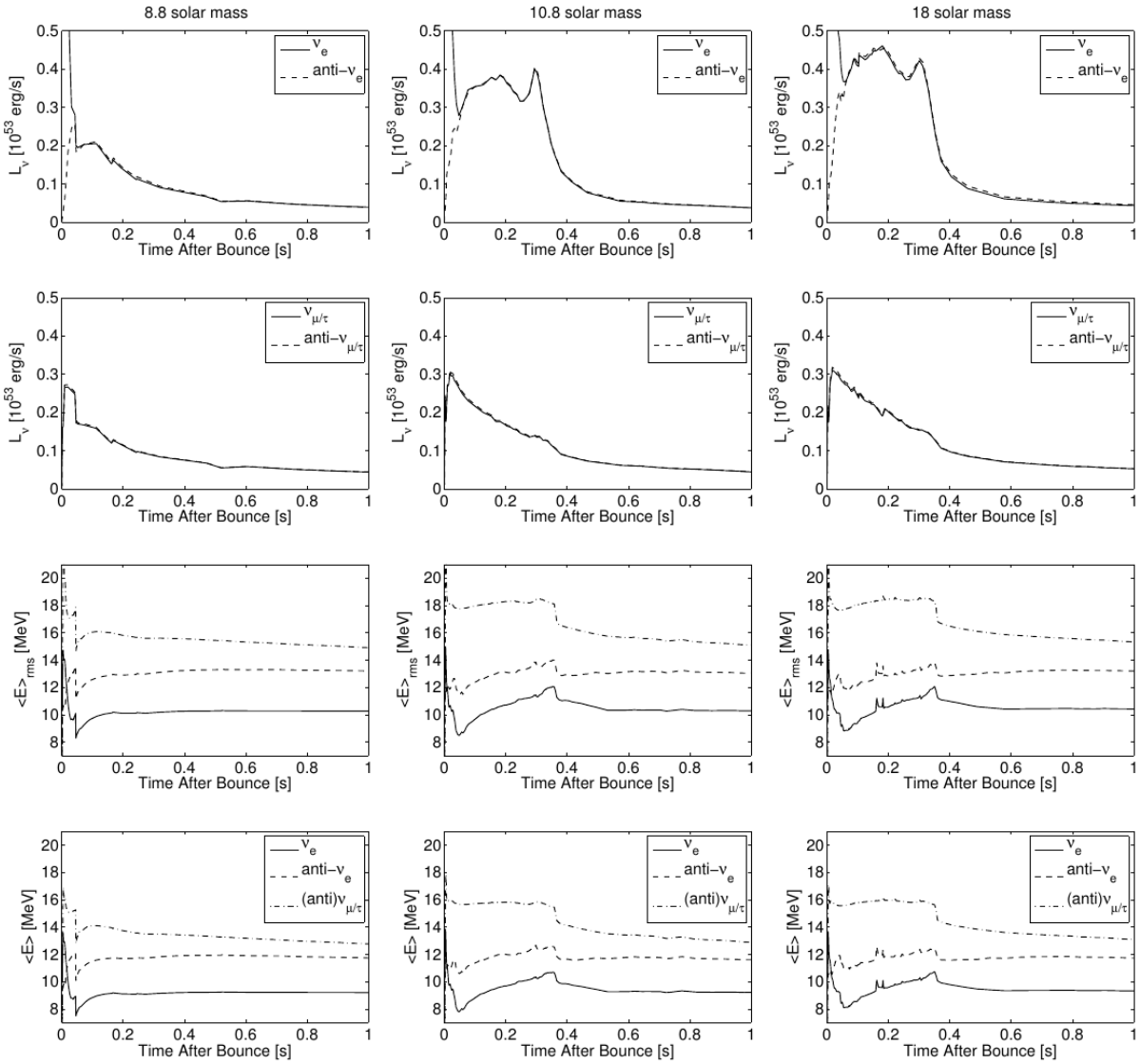

Figure 6.5: Evolution of neutrino luminosities and mean energies for three different SN progenitor in the first second after the bounce for the calculations from the Basel group. From [112].

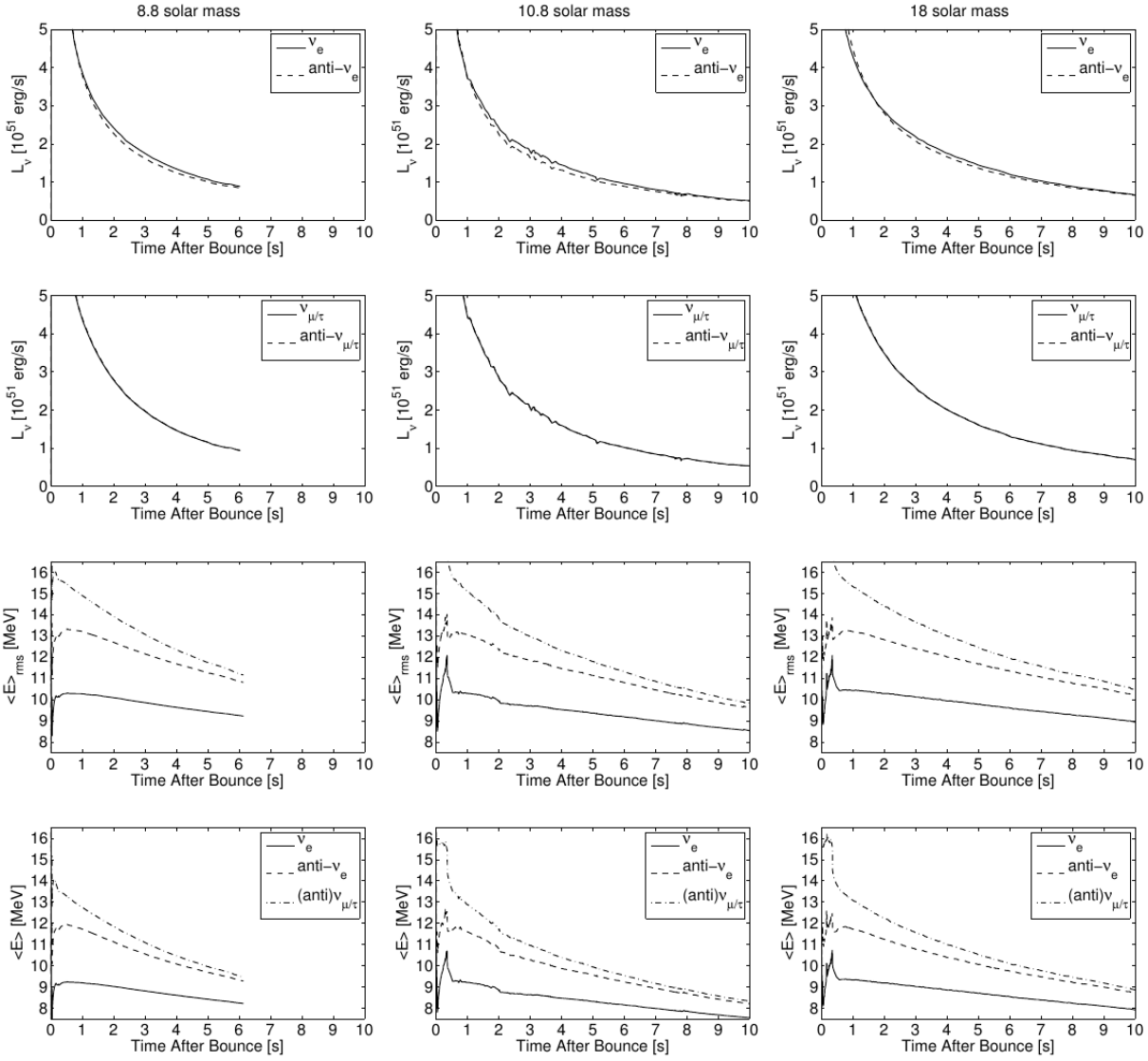

Figure 6.6: Evolution of neutrino luminosities and mean energies for three different SN progenitosup to ∼10 s after the bounce for the calculations from the Basel group. From [112].

6.2 Event rate calculation

Given a differential cross-section $\frac{d\sigma}{dT}(E,T)$ and a spectrum $f_{FD}(E)$ of incident particles, the recoil energy distribution of the final state particles $\frac{df}{dT}(T)$ is

$$\frac{df}{dT}(T) = \int_{E_{min}} \frac{d\sigma}{dT}(E,T) \cdot f_{FD}(E)\, dE \tag{6.6}$$

where the integral lower limit is the minimum required incident particle energy to obtain a kinetic energy T.

In case of proton recoils (or other heavy particles), quenching has to be taken into account. The quenched recoil spectrum is

$$\frac{df}{dE_q}(E_q) = \frac{df}{dT}(T) \cdot \frac{dT}{dE_q}, \tag{6.7}$$

where E_q is the quenched recoil energy in electron equivalent[3] and $\frac{dT}{dE_q}$ accounts for the quenching. For electrons $\frac{dT}{dE_q} \equiv 1$.

As the detector has a finite energy resolution, the quenched recoil spectrum has to be convoluted with the resolution function $D(E_{vis})$ in order to obtain the visible spectrum

$$\frac{df}{dE_{vis}}(E_{vis}) = \frac{df}{dE_q}(E_q) \otimes D(E_q) \tag{6.8}$$

using a Gaussian detector resolution

$$D(E_{vis}) = \frac{1}{\sqrt{2\pi\sigma^2}} \cdot exp\left(-\frac{E_{vis}^2}{2\sigma^2}\right). \tag{6.9}$$

LENA aims for an energy resolution σ of 3% at 5 MeV, i.e. around 10^2 detected photons per MeV. This value includes losses due to attenuation in the scintillator, the photon detection efficiency of the photo multipliers (PMTs), and the PMT coverage of 30%.

For the reactions of SN neutrinos with carbon, the recoil of the nucleus can be neglected. Thus, the recoil energy of the electron T can be approximated by

$$T = E_\nu - E_{thr} \tag{6.10}$$

with the energy threshold E_{thr} for the reaction channel. The recoil spectrum can then be derived to

$$\frac{df}{dT}(T) = \sigma(E - E_{thr}) \cdot f(E - E_{thr}). \tag{6.11}$$

[3]The kinetic energy of an electron that would produce the same visible energy as the quenched particle. In organic liquid scintillator, a proton with a recoil energy of 6 MeV releases about the same amount of photons as a 1.5 MeV electron.

Like before, the visible energy spectrum is calculated taking into account the detector resolution.

The total number of events N for a detection channel with N_p target particles is

$$N = N_p \frac{\dot{N}}{4\pi d^2} \int_{E_{thr,D}}^{\infty} \frac{df}{dE_{vis}}(E_{vis})\, dE_{vis}, \tag{6.12}$$

with the neutrino number flux $\dot{N} = L\langle E \rangle$, the distance d from the SN to earth, and the detector threshold $E_{thr,D}$. For the fiducial volume V, the molar mass of the scintillator M_{mol}, and the density ρ, N_p is given by

$$N_p = \frac{\rho V n_P N_A}{M_{mol}} \tag{6.13}$$

where n_p is the number particles per solvent molecule. Assuming a fiducial volume for LENA with a height of 100 m and a radius of 13 m, the number of respective particles for different solvents is shown in table 6.1. In order to implement time-dependency, the

solvent	fiducial mass	free p $[10^{33}]$	e^- $[10^{34}]$	^{12}C $[10^{33}]$	^{13}C $[10^{31}]$
LAB	45.8 kton	3.37	1.55	2.00	2.21
n-paraffin	39.8 kton	3.67	1.38	1.68	1.84
PXE	52.3 kton	2.70	1.71	2.37	2.61

Table 6.1: Target particles in the LENA fiducial volume, $5.3 \cdot 10^4\, m^3$, for different solvents. LAB is the preferred solvent, an addition of n-paraffin would increase the number of free protons and thus the sensitivity for the inverse β-decay channel and the proton decay search. More information on liquid scintillator in chapter 3.

following substitutions have to be done:

$$f(E) \longrightarrow f(E,t) \tag{6.14}$$

$$\dot{N} \longrightarrow \dot{N}(t) \tag{6.15}$$

The time-dependent number of events $N(t)$ is accordingly given by

$$N(t) = N_p \frac{\dot{N}(t)}{4\pi d^2} \int_{E_{thr,D}}^{\infty} \frac{df}{dE_{vis}}(E_{vis}, t)\, dE_{vis} \tag{6.16}$$

with $\dot{N}(t)$ given by the SN models. Finally, the total number of events per neutrino flavor is

$$N_\nu = \int_{t_0}^{t_1} N(t) dt, \tag{6.17}$$

with the start and the end of the neutrino emission t_0 and t_1, respectively, and the total number of events is

$$N_{tot} = \sum_{\alpha} N_\nu. \tag{6.18}$$

6.3 SN neutrino detection channels in liquid scintillator

The energy spectra and event rates presented in this section all refer to a distance[4] of 10 kPc and LAB as solvent. The fiducial volume with a height of 100 m and a radius of 13 m is assumed, i.e. ∼45.7 kt LAB. The two possible scenarios for the MSW effect are included: the H-resonance in the neutrino sector for the normal mass hierarchy and the H-resonance in the anti-neutrino sector for inverted hierarchy. While the NC reactions only give information on the total neutrino flux, the CC reactions are more sensitive to the electron flavor neutrinos.

There are six major detection channels for SN neutrinos in liquid-scintillator. The cross-sections are shown in fig. 6.7. Throughout the relevant energy range the inverse β-decay dominates. While elastic ν-e and ν-p scattering are only limited by the energy threshold of the detector, the carbon channels are only sensitive to the high-energy tail of the neutrino spectra due to the high energy threshold.

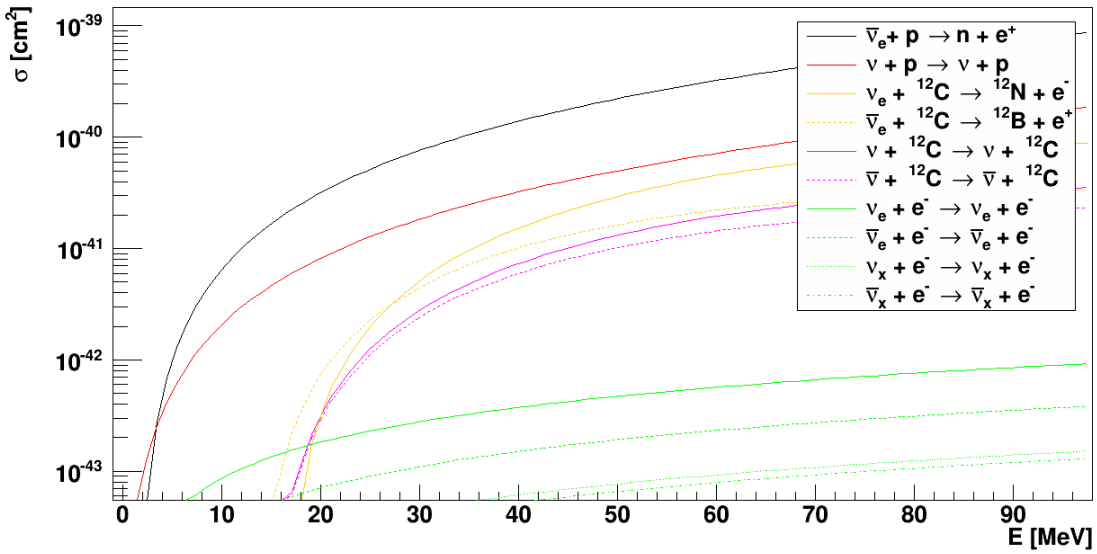

Figure 6.7: Cross sections relevant for the detection of SN neutrinos with liquid-scintillator detectors. In the relevant energy range, the inverse beta decay clearly dominates. Although elastic ν-p scattering provides a large cross-section as well, quenching of the proton recoil significantly reduces the expected signal. Above the energy threshold of ~ 15 MeV, reactions with ^{12}C become important. As ν-e scattering has no energy threshold, it provides information from low neutrino energies.

[4]Parsec: $1\,\mathrm{Pc} = 3.26\,\mathrm{ly} = 3.0857 \cdot 10^{16}\,\mathrm{m}$

6.3.1 Inverse β-decay

Quasi-elastic neutrino-proton scattering, often referred to as *inverse β-decay*, is the so-called *golden channel* in liquid-scintillator experiments. It features the highest cross-section ($E_{thr} = 1.8$) MeV amongst all channels and a distinct signature:

$$\bar{\nu}_e + p \longrightarrow n + e^+. \tag{6.19}$$

While the annihilation of the positron gives a prompt signal above $2m_e = 1.022$ MeV, the neutron thermalizes and is finally captured after a mean lifetime of $\sim 250\,\mu$s on a proton. The binding energy of $E_{thr} = 2.2$ MeV is released in γs. The delayed coincidence between prompt positron signal and delayed neutron capture this channel is used to discriminate background efficiently. The expected background due to reactor neutrinos and geo-neutrino is less than 10 events per days for Pyhäsalmi [19].

The differential cross-section used in this thesis is taken from [122], including radiative corrections and final state interactions. The angular distribution is almost flat, $\frac{d\sigma}{d\theta} \propto 1 - 0.104\,\cos\theta$. The total cross-section evolves with the square of the neutrino energy [123]

$$\sigma \approx 9.52 \cdot 10^{44}\,(E_e - 1.29)^2\ \mathrm{MeV}^{-2}\mathrm{cm}^2 \tag{6.20}$$

with $E_e = E_\nu - E_{thr}$. However, especially at higher energies, this approximation overestimates the cross-section significantly. As single pion production gets only important above 0.34 GeV, when $\Delta(1232)$ is produced, it can be safely neglected for SN neutrinos.

The time-integrated visible spectra of the prompt positrons are shown in fig. 6.8 for normal and inverted hierarchy compared to a scenario without oscillation. For both mass hierarchies, the high-energy tail is enhanced. This is due to the first few seconds after the bounce, as can be seen in fig. 6.9 for IH. The temporal behavior for NH is the same, however the difference is not as distinct. In any case, the enhancement is due to the contribution of the $\bar{\nu}_x$ that have a higher mean energy $\langle E_x \rangle$ than $\langle E_{\bar{e}} \rangle$ in the beginning of the neutrino emission.

In table 6.5, the time- and energy-integrated events rate in LENA for the inverse β-decay for a SN at 10 kPc and assuming the Garching model. More than 5000 events in 10 s can be observed for even such a distant explosion. The time-dependency of the three oscillation scenarios is shown in fig. 6.10. For IH, the event rate rises earlier and has a broader peak due to the large fraction of $\bar{\nu}_x$ produced in the SN.

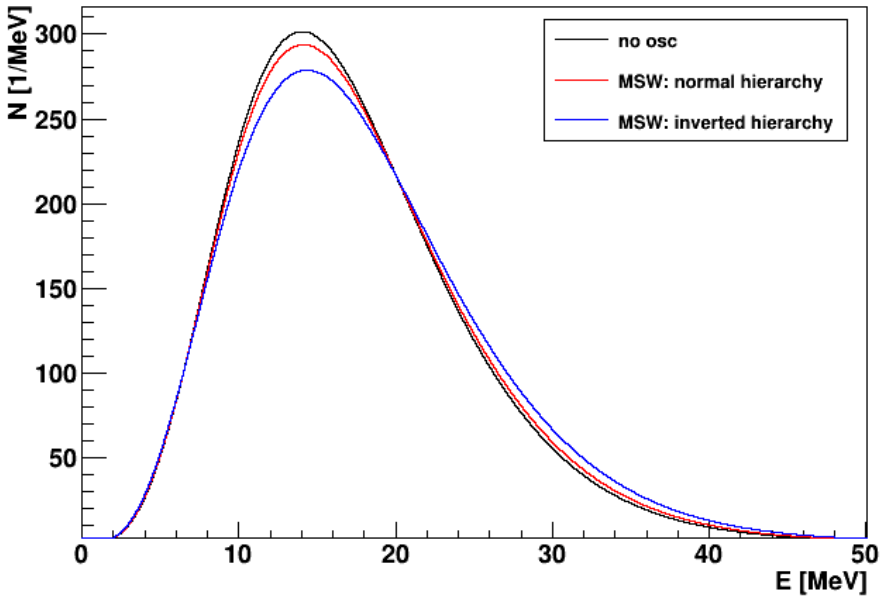

Figure 6.8: Time-integrated visible energy spectrum of the inverse β-decay channel in LENA for NH and IH compared to no oscillations.

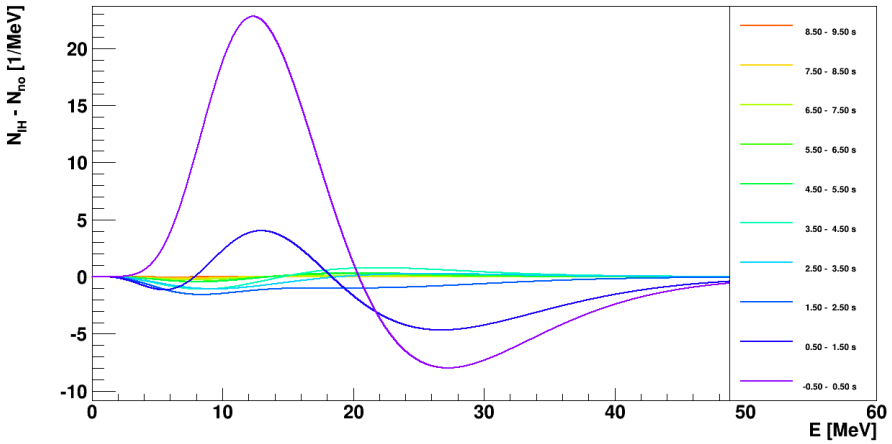

Figure 6.9: Difference of visible energy spectra of IH and no oscillation scenario for the inverse β-decay in LENA at different time. The plot shows well that the enhancement of the high-energy tail is due to the first few seconds after the core bounce.

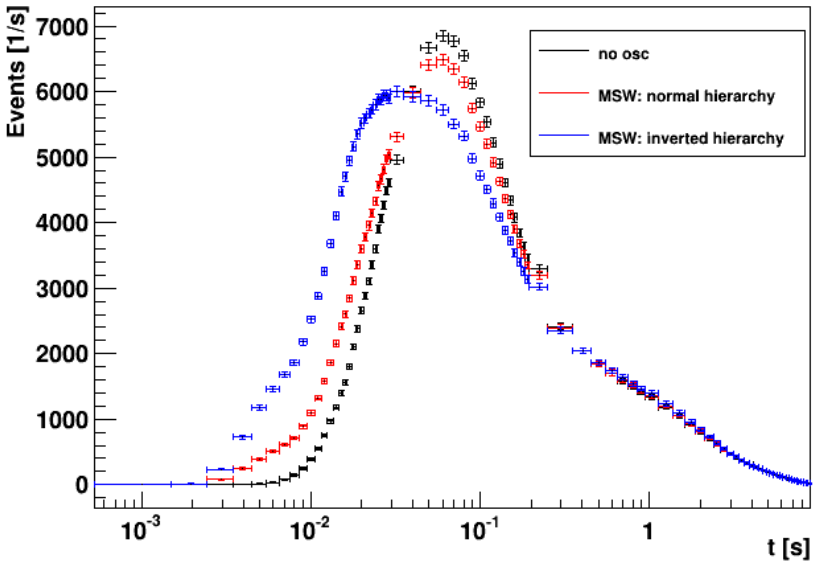

Figure 6.10: Time evolution of the event rates for the inverse β-decay channel in LENA for NH, IH and no oscillations. The event rate for IH rises earlier than for NH, as the $\bar{\nu}_e$-flux $f_{\bar{e}}$ has a large fraction of the original $f^0_{\bar{x}}$ whose emission starts to increase earlier than $f^0_{\bar{e}}$.

6.3.2 Elastic neutrino-proton scattering

The elastic neutrino-protons scattering

$$\nu + p \longrightarrow \nu + p \tag{6.21}$$

is an important detection channel for SN neutrinos in liquid-scintillator detectors due to its large cross-section. It has first been investigated by J.F. Beacom *et al.* [124]. As the reaction is a NC reaction, it is sensitive to all neutrino flavors. However, the neutrino flavor with the highest mean energy dominates, due to the quenching of the proton recoil energy. In a simplification for low energies, the differential cross-section $\frac{d\sigma}{dT}(T, E_\nu)$ is derived from [124, 125, 126] as

$$\begin{aligned}\frac{d\sigma}{dT}(T, E_\nu) = \frac{G_F^2 m_p}{2\pi E_\nu^2} \Big(&(c_V + c_A)^2 E_\nu^2 + (c_V - c_A)^2 (E_\nu - T)^2 \\ &- (c_V^2 - c_A^2) m_p T + \frac{2T}{E_\nu} c_M c_A \Big),\end{aligned} \tag{6.22}$$

with the proton kinetic energy T and the incident neutrino energy E_ν. The proton mass is given as $m_p = 938.272\,\mathrm{MeVc}^{-2}$, $G_F = 2.31 \cdot 10^{-22}\,\mathrm{GeV/cm}^{-1}$ is the Fermi coupling constant and $c_V = 0.04$ and $c_A = 0.635$ denote the vector and axial neutral current

coupling constants for neutrinos. For anti-neutrinos, the substitution $c_A \longrightarrow -c_A$ has to be made. The last term includes weak magnetism corrections of about 10%, with $c_M \simeq 1.4$. As it is shown in [124], the cross-section favors large recoils, which is beneficial for detection. Kinematically, the minimum neutrino energy E_{min} to obtain a recoil energy T for a scattering angle of 180° is

$$E_{min} = \frac{m_p T}{\sqrt{(T^2 + 2m_p T)} - T} \approx \sqrt{\frac{m_p T}{2}} \gg T. \tag{6.23}$$

Hence, the proton recoil energies are small, which makes detection more complicated.

The recoil spectrum then is derived as

$$\frac{df(T)}{dT} = \int_{Emin}^{\infty} \frac{d\sigma(E,T)}{dT} f(E) dE. \tag{6.24}$$

As the ionization density of heavy charged particles is much higher than that of electrons, not all of the recoil energy is visible in the detector. This quenching has to be considered on the way to calculate the visible spectrum from proton recoils (cf. eq. (6.7)). Approximated with the empirical Birks' equation [69], the quenched proton recoil energy is

$$E_q(T) = \int_0^T \frac{A\frac{dT}{dx}}{1 + kB\frac{dT}{dx}} dT \tag{6.25}$$

Here, A is a constant proportional to the light yield, kB a factor describing the amount of quenching, and $\frac{dT}{dx}$ the energy deposit per unit length, which is taken from the PSTAR database [106].

As the cross-sections are identical for all neutrino and anti-neutrino flavors, respectively, the total number of events is the same for all oscillation scenarios. Hence, the neutrino-proton elastic scattering channel offers the possibility for the flux normalization. The energy spectrum considering no oscillations is shown in figure 6.11. As the cross-section favors neutrinos with higher energies and the mean energies $\langle E_{\bar{e}} \rangle$ and $\langle E_x \rangle$ are highest during most part of the explosion, the detection channel is most sensitive to $\bar{\nu}_e$ and $\bar{\nu}_x$. Since the number flux $\dot{N}_x$ includes two neutrino flavors ν_μ and ν_τ, the contribution from $\bar{\nu}_x$ is most prominent for the neutrino-proton scattering channel. For $E_{thr} = 0.2\,\mathrm{MeV}$, the number of events originating from ν_e is almost negligible (cf. table 6.2). Hence, SN neutrino detection via ν-p scattering provides information on the original $\bar{\nu}_x$ spectrum produced during the SN explosion. The time evolution of the events from neutrino-proton elastic scattering is shown in fig. 6.12. The peak in ν_e due to deleptonization totally accounts for ∼10 events, $\geq 30\%$ of the time-integrated total event number N_e.

The statistics of the SN neutrino detection via the neutrino-proton elastic scattering largely depends on the energy threshold of the detector. The total number of expected events for

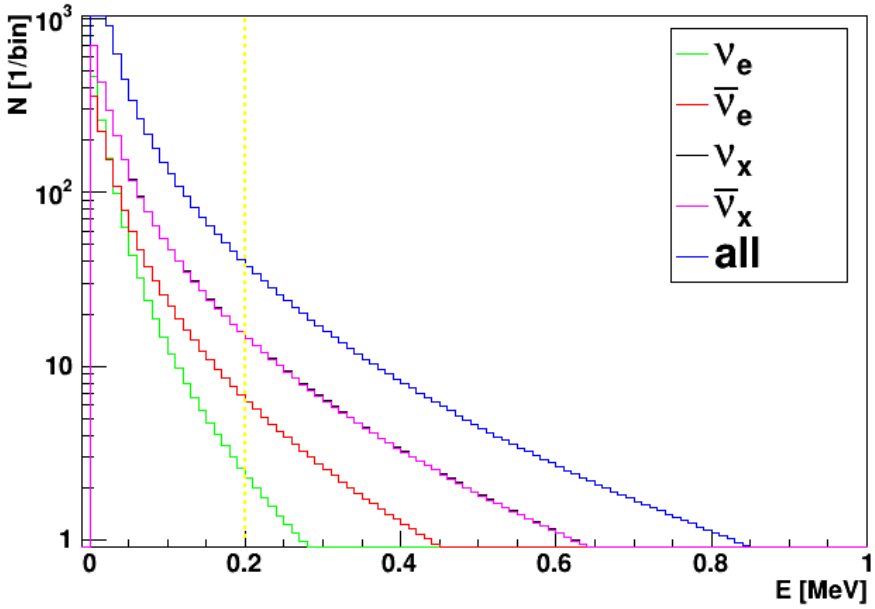

Figure 6.11: Visible Energy spectrum for neutrino-proton scattering in the case of no oscillation, i.e. the neutrino flavors coincide with the originally produced flavors in the SN. Therefore, the recoil spectra induced from ν_x and $\bar{\nu}_x$ coincide and dominate due to their high mean energy and number flux. The energy threshold of $E_{thr} = 0.2\,\mathrm{MeV}$ used for the event rate calculations is depicted by the vertical yellow line.

flavor	no osc.	normal hierarchy	inverted hierarchy
ν_e	26	114	89
ν_x	233	144	169
$\bar{\nu}_e$	99	100	115
$\bar{\nu}_x$	231	224	208
total	582	582	581

Table 6.2: Time- and energy-integrated event rates in LENA for the SN neutrino detection channel $\nu + p \longrightarrow \nu + p$. As the cross-section are equal for all neutrinos and anti-neutrinos, respectively, the total number of expected events does not change for different oscillation scenarios.

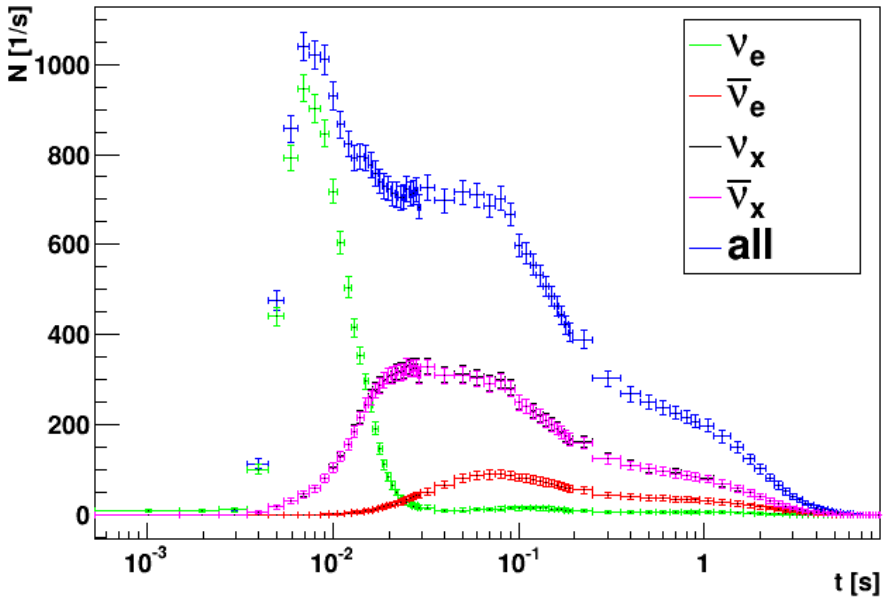

Figure 6.12: Time evolution of neutrino proton scattering in case of no oscillations. Attention has to be paid to the non-linear binning. The deleptonization burst of ν_e accounts for only about ten events.

a SN at 10 kPc and LAB as scintillator as a function of the detector threshold is shown in figure 6.13. For a threshold of $E_{thr} = 0.2$ MeV, totally almost 600 events are expected, making ν-p scattering the second prominent detection channel after the inverse beta decay. However, the number of total events decreases almost exponentially with E_{thr}. For example, for $E_{thr} = 0.25$ MeV, the rate already drops to ∼400 events.

The most dangerous background for the observation of the proton recoils spectrum arises from the β-decay of ^{14}C. As organic liquid-scintillator consists of hydrocarbons, it is an intrinsic background. It has a half-life of 5730 years and its β-spectrum has an endpoint of 156 keV. However, due to the finite energy resolution, the visible spectrum in a detector extends to higher energies. It has been shown in simulations that the signal to background rate is 1:6 between 0.2-0.3 MeV [127]. However, pulse shape analysis can help to disentangle proton recoil from γ-induced events.

Due to quenching, events above 0.5 MeV are only a minor fraction compared to the total event number for an energy threshold of 0.2 MeV (cf. fig. 6.13). Therefore, taking the neutron efficiencies ε_n between 0-0.5 MeV reported in chapter 5.9 gives a good estimate of the effective ν-p event rates. For LH3, about 84% of the ν-p scattering events can be retained while rejecting 99% of the γ-induced events for LH3 in this energy range of $0.2 - 0.5$ MeV. While the addition 50% of non-scintillating n-paraffin increases the number of free protons by a factor of ∼1.05, the discrimination between proton and electron recoils

deteriorates. For L50, $\varepsilon_n \approx 0.65$ for a γ rejection of 90% below 0.5 MeV. Thus, the gain in events due the higher number of protons is by far surpassed by the worse discrimination. Moreover, the proton quenching factor seems to increase with the addition of n-paraffin[5], further decreasing the signal. Hence, for the detection of SN-ν via elastic proton scattering, the addition of n-paraffin to LAB is disadvantageous.

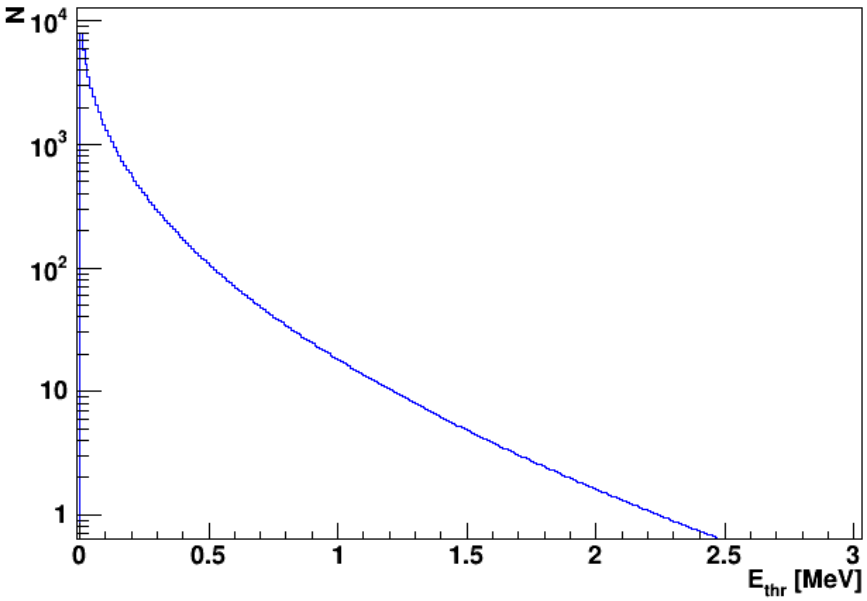

Figure 6.13: Total event number for elastic ν-p scattering in dependency of the detector threshold E_{thr} in LAB for a SN at 10 kPc distance.

The kB values taken for the calculation are determined in [91] (cf. sec. 5.5). The quenching factor for LAB + 3 g/ℓ PPO + 20 mg/ℓ bisMSB (LH3) was determined to $kB = 0.01869 \pm 0.00799\,\mathrm{cmMeV^{-1}}$. The number of proton recoil events detected in LENA largely depends on the quenching factor and the energy threshold. Spectra for different kB, fit values and respective $1\,\sigma$ bounds (cf. table 6.3), are shown in Fig. 6.14. Varying the kB value within one standard deviation already introduces an uncertainty of 40-80% with respect to the best fit value. Unless more precise measurements further reduce this error, the utilization of the ν-p channel for the determination of the total flux seems problematic.

6.3.3 Elastic neutrino-electron scattering

Like ν-p scattering, elastic neutrino-electron scattering is sensitive to all neutrino flavors:

$$\nu + e^- \longrightarrow \nu + e^-. \tag{6.26}$$

[5]DCMV: $kB = 0.02041 \pm 0.0049\,\mathrm{cmMeV^{-1}}$ [91]

fit	$kB\,[\mathrm{cmMeV}^{-1}]$	N_{tot}
best fit-1σ	0.01070	326
best fit	0.01869	516
best fit$+1\sigma$	0.02668	940

Table 6.3: Event rates in LENA for the SN neutrino detection channel $\nu{+}p \longrightarrow \nu{+}p$ for different kB values ($kb, kB \pm 1\sigma$).

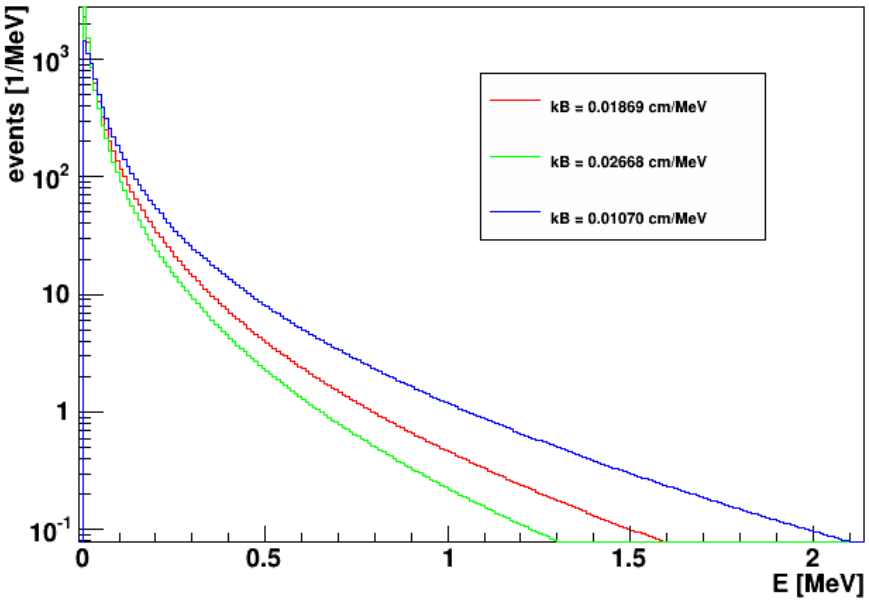

Figure 6.14: Quenched proton recoil spectra assuming different kB factors. Within one standard deviation around the best fit value fit LAB [91], the event rate varies with a factor of three.

As electron quenching gets important well below 1 MeV [128], it can be neglected for SN neutrinos. The differential cross-section is [129, 23]

$$\frac{d\sigma}{dT}(T,E) = \frac{2G_F^2 m_e}{\pi}\left(c_L^2 + c_R^2\left(\frac{E_\nu + T}{E_\nu}\right)^2 - c_L c_R \frac{m_e T}{E_\nu^2}\right) \tag{6.27}$$

with the coupling constants c_L and c_R as shown in table 6.4. The cross-sections for ν_e and

	c_L	c_R
ν_e	$1/2 + sin^2(\theta_W)$	$sin^2(\theta_W)$
$\bar{\nu}_e$	$sin^2(\theta_W)$	$1/2 + sin^2(\theta_W)$
ν_x	$-1/2 + sin^2\theta_W$	$sin^2\theta_W$
$\bar{\nu}_x$	$sin^2\theta_W$	$-1/2 + sin^2\theta_W$

Table 6.4: Coupling constants for neutrino-electron scattering, $sin^2(\theta_W) = 0.231$ [20, 23].

$\bar{\nu}_e$ are larger than for $\bar{\nu}_x$ as CC interactions contribute, too (cf. fig. 6.7. Therefore, the contributions from ν_e induced electron recoils to the visible spectrum is largest as shown in fig. 6.15 for NH. The impact of the detector threshold of this detection channel is very small compared to the ν-p scattering because the spectrum is not quenched and thus extends to higher energies and is less steep. An increase of $E_{thr,D}$ from 0.2 MeV to 0.3 MeV only decreases the event rate in the order of few percent.

The time-integrated event rates for no oscillations, normal and inverted neutrino mass hierarchy are listed in table 6.5. The differences between the scenarios is only few percent due to small differences of the cross-sections. Therefore, elastic ν-e scattering is perfectly suited for the determination of the total SN neutrino flux.

The time evolution of the single flavor and total event rates are shown for NH and IH in fig. 6.16. As for NH most ν_e oscillate into ν_x and the cross-section for ν_x is smaller than for ν_e, the deleptonization burst is less prominent than in case of IH.

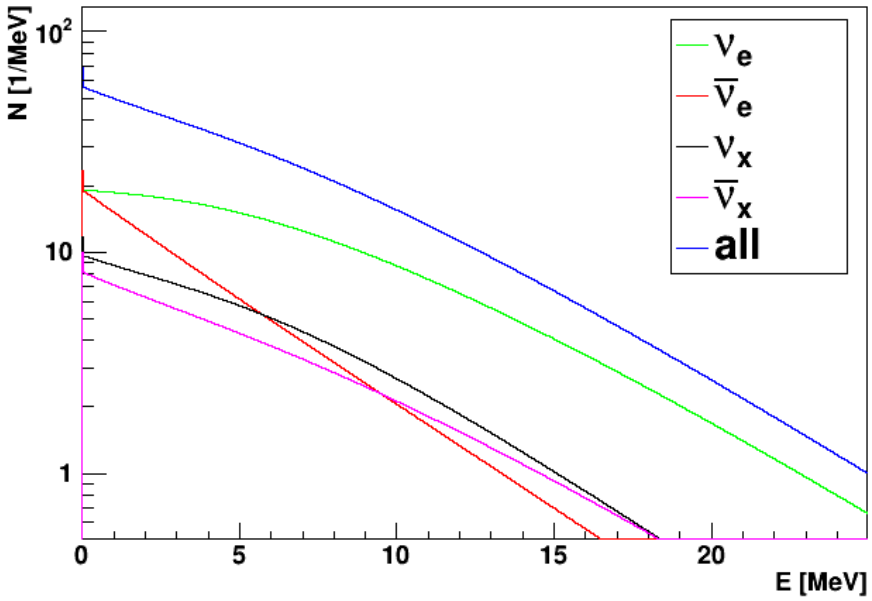

Figure 6.15: Visible energy spectrum of elastic neutrino-electron scattering for NH.

6.3.4 NC scattering on ^{12}C

The flavor-independent detection channel

$$\nu + {}^{12}\mathrm{C} \longrightarrow \nu + {}^{12}\mathrm{C}^* \tag{6.28}$$

allows to measure the total neutrino flux. It features a high energy threshold of $E_{thr} = 15.1\,\mathrm{MeV}$. As the mass of the carbon nucleus is much higher than the neutrino energy, the recoil is small, e.g. $\leq 2\,\mathrm{MeV}$ for $E_\nu = 100\,\mathrm{MeV}$. Moreover, the high quenching factor for carbon recoils [130] reduces the visible energy below the detection threshold of $\sim 0.2\,\mathrm{MeV}$.

The excited carbon atom decays into

$${}^{12}\mathrm{C}^* \longrightarrow {}^{12}\mathrm{C} + \gamma \tag{6.29}$$

The final state γs add up to 15.1 MeV and thus give a distinct signature in the detector. Nevertheless, information on the neutrino spectra is lost. As the decay is electromagnetic and super-allowed, the decay time $\tau \approx 1 \cdot 10^{-16}\,\mathrm{s}$ is significantly higher than the decay constants of the scintillator. The cross-section for neutrinos is higher than for anti-neutrinos, as shown in figure 6.7 [131, 23].

Figure 6.17 shows the expected visible energy signal in LENA for a SN at 10 kPc using the Garching model in case of NH. An energy resolution of 3% at 5 MeV and according to eq. (6.9) is assumed.

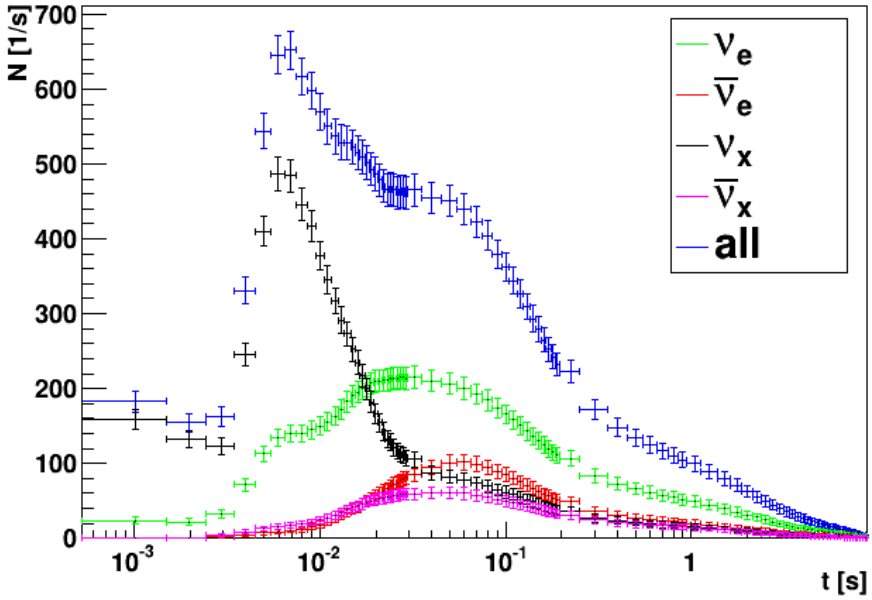

(a) normal hierarchy

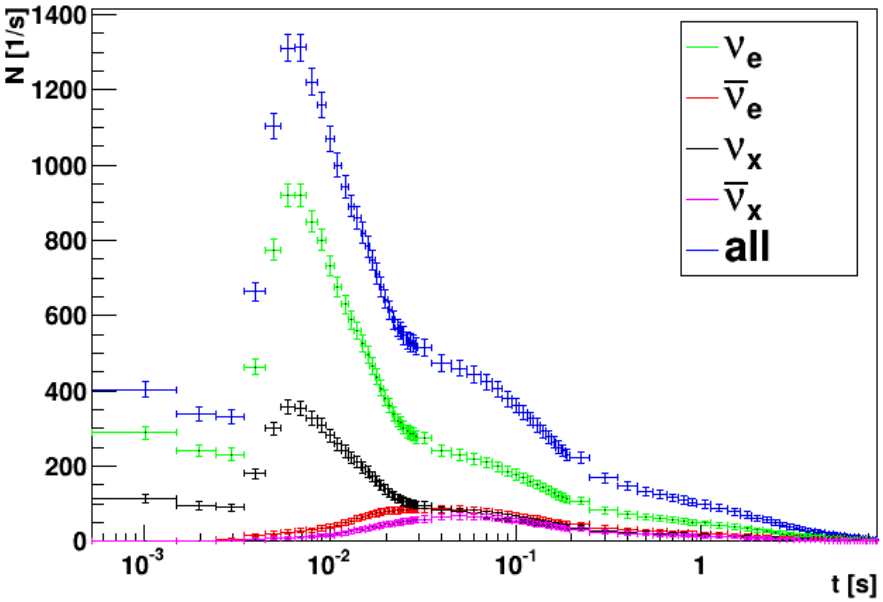

(b) inverted hierarchy

Figure 6.16: Time evolution of event rates for elastic ν-e scattering for (a) normal hierarchy and (b) inverted hierarchy.

In table 6.5, the time- and energy-integrated event numbers for different oscillation scenarios is depicted. As the difference of the cross-sections is small, the time- and energy-integrated event rates are almost identical. Hence, the reaction $^{12}\mathrm{C} \longrightarrow {}^{12}\mathrm{C}^{*} + \nu$ is perfectly suited to measure the total neutrino flux.

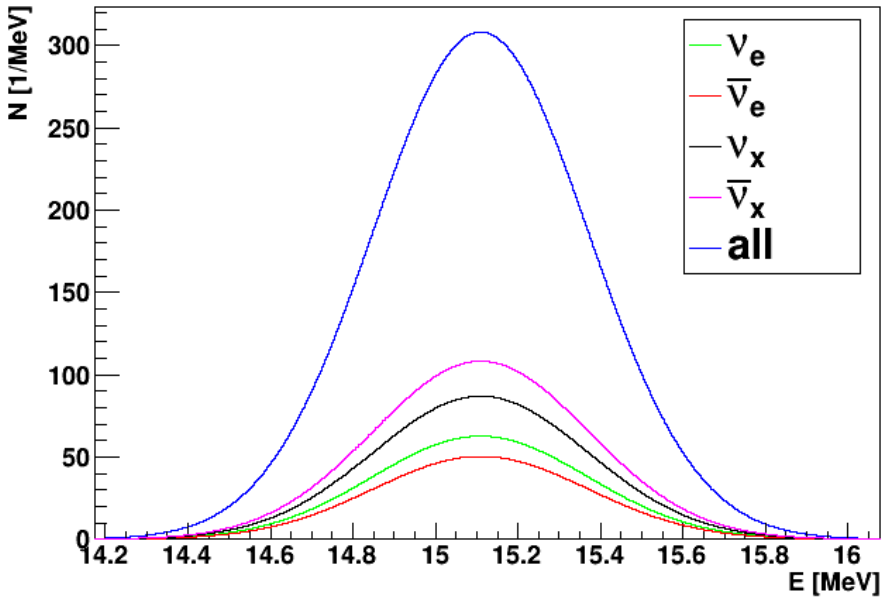

Figure 6.17: Spectrum of the $^{12}\mathrm{C} \longrightarrow {}^{12}\mathrm{C}^{*} + \nu$ reaction, showing the single contributions of each flavor.

6.3.5 $\nu_e + {}^{12}\mathbf{C} \rightarrow e + {}^{12}\mathbf{N}$

The reaction channel

$$\nu_e + {}^{12}\mathrm{C} \longrightarrow e^{-} + {}^{12}\mathrm{N} \tag{6.30}$$

offers the unique possibility to measure the ν_e flux f_e. Its energy threshold is relatively high with $E_{thr} = 17.34\,MeV$. The cross-section is shown in fig. 6.7 is still given with an error of $\geq 12\%$ [131].

With a life-time of $\tau = 11.00\,\mathrm{ms}$, $^{12}\mathrm{N}$ decays into

$$^{12}\mathrm{N} \longrightarrow \bar{\nu}_e + {}^{12}\mathrm{C} + e^{-}, \tag{6.31}$$

giving a delayed signal that can be used to tag this channel. However, the CC reaction channel of $\bar{\nu}_e$ on $^{12}\mathrm{C}$ has a similar signature.

The time-integrated spectrum of the CC capture of ν_e on ^{12}C is shown for NH, IH, an no oscillations in fig. 6.18. The oscillations $\nu_e \longrightarrow \nu_x$ greatly increase the number of events, as $\langle E_x \rangle > \langle E_e \rangle$, as listed in table 6.5.

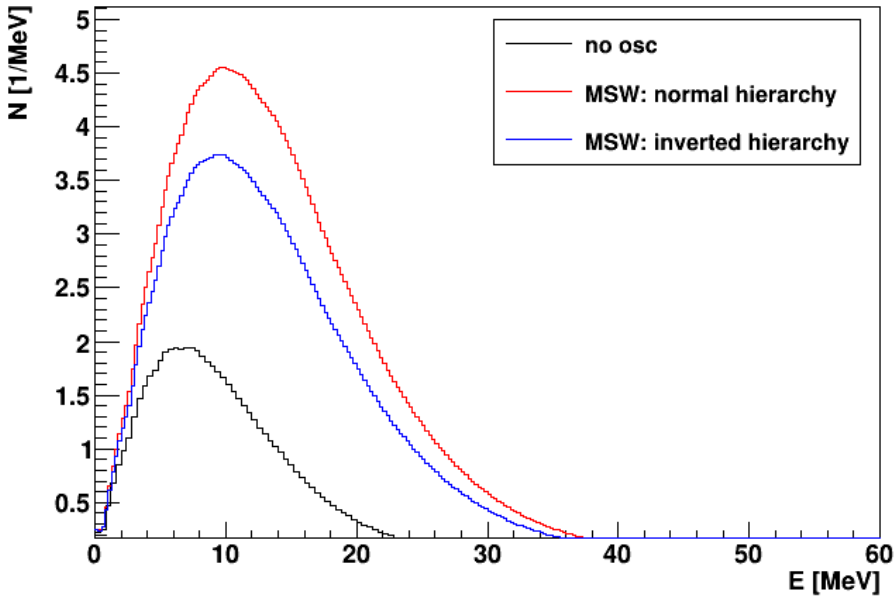

Figure 6.18: Time-integrated energy spectrum of the $\nu_e + {}^{12}\mathrm{C} \longrightarrow e + {}^{12}\mathrm{N}$ reaction channel in LENA.

Fig. 6.19 shows the temporal evolution of the event rate. As most ν_e oscillate into ν_x, the deleptonization burst is largely reduced for IH and even vanishes for NH.

6.3.6 $\overline{\nu}_e + {}^{12}\mathbf{C} \rightarrow e^+ + {}^{12}\mathbf{B}$

The reaction channel $\bar{\nu}_e + {}^{12}\mathrm{C} \longrightarrow e^+ + {}^{12}\mathrm{B}$ has an energy threshold of $E_{thr} = 13.8\,\mathrm{MeV}$. Subsequent decay

$$^{12}\mathrm{B} \longrightarrow {}^{12}\mathrm{C} + e + \bar{\nu}_e \tag{6.32}$$

has a life-time $\tau = 20.2\,\mathrm{ms}$. Both energy and temporal signature are in the region of the reaction $\nu_e + {}^{12}\mathrm{C} \longrightarrow e + {}^{12}\mathrm{N}$. However, spectral fits showed a very good discrimination $\gtrsim 99\%$[127].

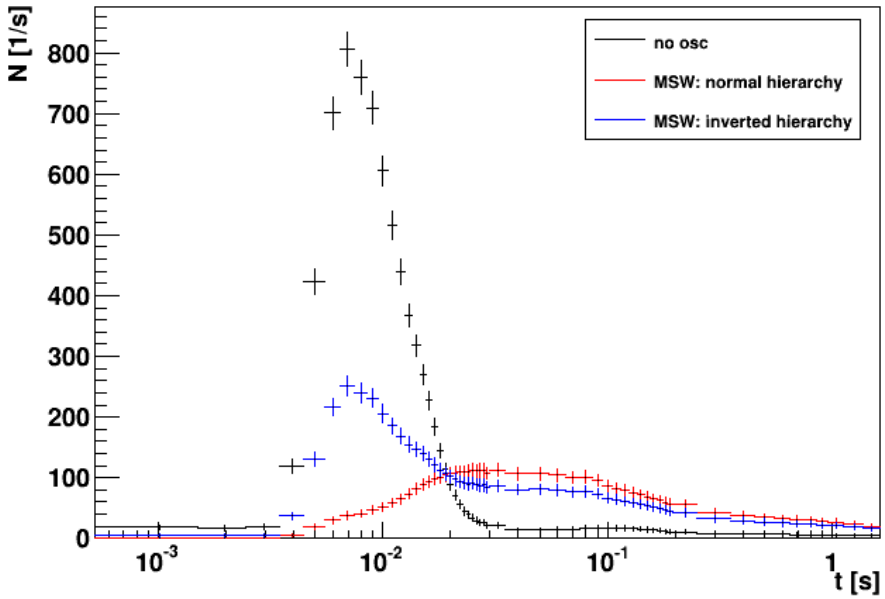

Figure 6.19: Temporal evolution of the $\nu_e + {}^{12}\mathrm{C} \longrightarrow e + {}^{12}\mathrm{N}$ reaction channel in LENA

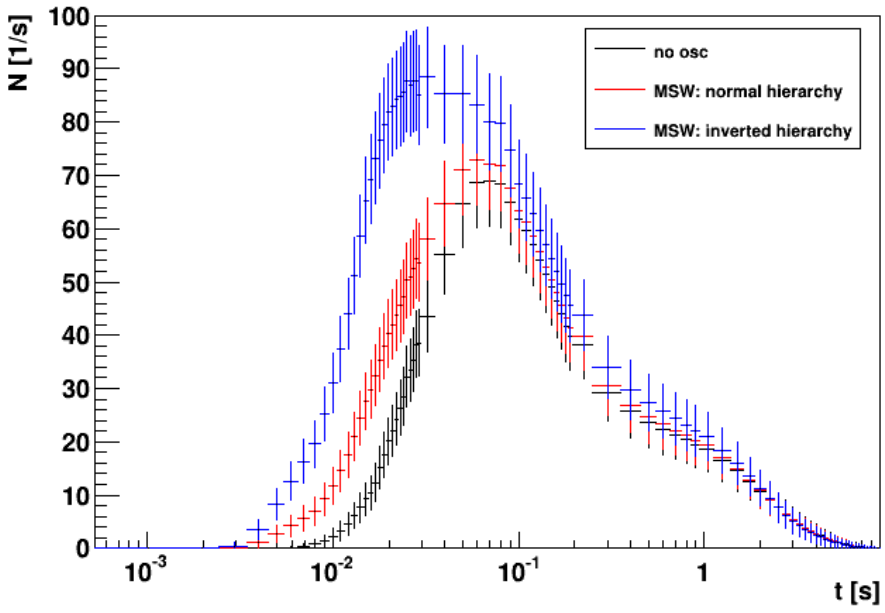

Figure 6.20: Time evolution of $\bar{\nu}_e + {}^{12}\mathrm{C} \longrightarrow e^+ + {}^{12}\mathrm{B}$ channel in LENA.

6.3.7 Summary

The expected event rates for the six channels for neutrinos from a galactic core-collapse SN in LENA are listed in tab. 6.5 for the Garching model and different oscillation scenarios. A distance of 10 kPc is assumed and LAB is taken as scintillator. In total, more than 6000 events can be expected independently from the neutrino mass hierarchy. About 80% of the total rate is from the inverse β-decay channel. In the Garching model, the mean neutrino energies $\langle E_{\bar{e}} \rangle$ and $\langle E_x \rangle$ and the luminosities $L_{\bar{e}}$ and L_x are similar. Thus, the rates for the inverse β-decay channel, which would be suited best for the search of oscillation effects due to its high statistics, do not differ significantly.

The discrimination of the channels has been investigated in a Monte-Carlo study in [127]. Taking advantage of the delayed coincidence signatures, the CC channels can be identified with high efficiencies $\gtrsim 99\%$. Moreover, spectral fits gain comparably high efficiencies for the NC ^{12}C and ν-p channel. However, misidentified ν-p events pose a significant background to the ν-e channel, which can be reduced by pulse shape discrimination.

channel	no oscillations	NH	IH
inverse β-decay	5061	5064	5070
ν-p scattering	582	582	581
ν-e scattering	429	403	410
^{12}C NC	201	202	202
^{12}C CC ν_e	58	61	65
^{12}C CC $\bar{\nu}_e$	25	130	104
total	6265	6351	6341

Table 6.5: Event rates for SN neutrinos in LENA for the Garching model for a SN at 10 kPc distance.

The ^{12}C CC ν_e reaction is the only detection channel sensitive to ν_e only. However, due to the short time scale ($t \leq 30$ ms), the low $\langle E_e \rangle$ and L_e, the deleptonization burst will hardly be visible in this channel at 10 kPc (cf. tab. 6.6). Assuming no background and estimating the error of the cross section to be $\sim 20\%$, a SN at a distance ≤ 0.85 kPc is needed to discriminate between NH and IH on a statistical basis. In this case, the NC channels can be used for normalization and to determine the onset of the ν_e-burst. Analogously, ν-e scattering can be used for a discrimination of the neutrino mass hierarchies. However, like before, the sensitivity largely depends on the distance to the SN.

As can be seen in figs. 6.21 and 6.22, LENA is perfectly suited to monitor the evolution of the neutrino emission,and thus the dynamics, of a SN at 10 kPc. Even for NH, the NC reaction monitor well the deleptonization burst. This is mainly due the peak in the neutrino mean energy $\langle E_e \rangle$, which reflects positively in the ν-p scattering event rate. During the accretion and cooling phase, the high event rate from the inverse β-decay channel allows

channel	no oscillations	NH	IH
ν-p scattering	20	20	20
ν-e scattering	43	14	22
^{12}C NC	8	8	8
^{12}C CC ν_e	7	2	4

Table 6.6: Event rates for SN neutrinos in LENA for the Garching model for a SN at 10 kPc distance during the deleptonization burst ($t \leq 30$ ms).

for a high resolution of the neutrino flux.

Besides the MSW oscillation scenarios, also other effects can cause a flavor conversion. Potential spectral swaps due to collective oscillations could be monitored with the time-resolved spectra of the inverse β-decay. Shock waves passing though the resonance layers can induce dips in the time evolution [26]. Nevertheless, the NC channels guarantee to monitor the total flux and thus give a measure for these unknown effects.

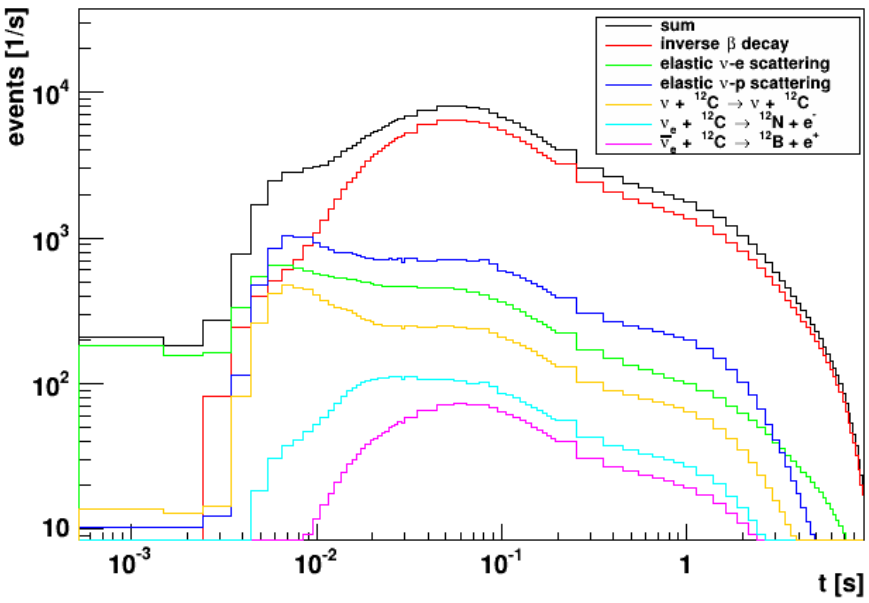

Figure 6.21: Time evolution for NH for the Garching model for the six detection channels discussed. While the NC channels monitor the deleptonization burst, the inverse β-decay dominates during accretion and cooling phase.

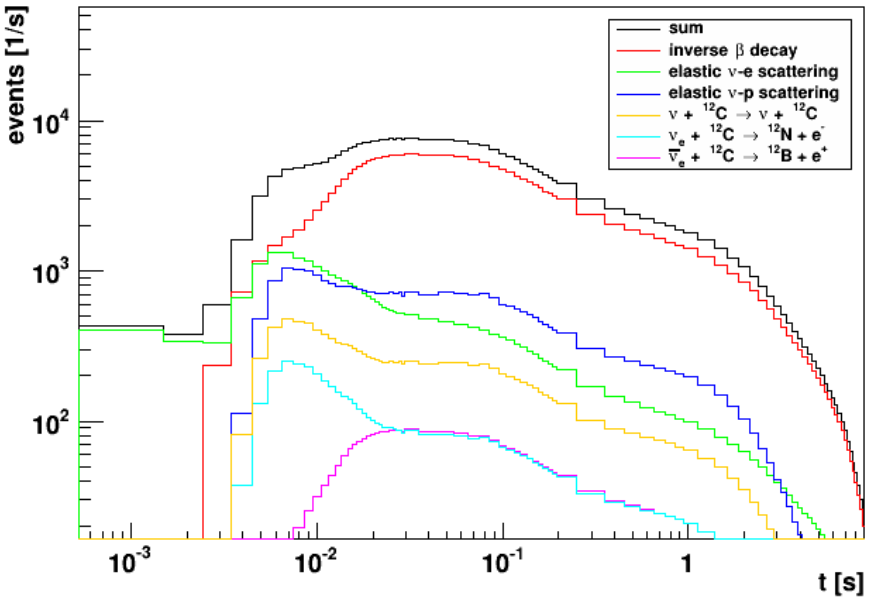

Figure 6.22: Time evolution for IH for the Garching model for the six detection channels discussed. The deleptonization burst can be resolved by the NC channels and the CC reaction of ν_e on carbon.

6.4 Earth effect

The earth effect can appear if the neutrinos coming from the SN pass through the earth's mantle and core before reaching the detector. As explained in chapter 1, this effect only occurs in certain circumstances. First, the spectra of the ν_e and ν_x produced in the SN have to be different. For the Garching model, this is true during the first seconds after the core bounce (cf. figure 6.3). At later time, however, the spectra gradually become more similar. Moreover, the luminosity is already is the same order after the accretion phase. As the mixing angle θ_{13} is relatively large, the H-resonance is perfectly adiabatic. Thus the earth effect can only appear for neutrinos in the inverted hierarchy and for anti-neutrinos in the normal hierarchy. The observation of a distortion of the spectrum in the neutrino or anti-neutrino sector might reveal this puzzle. In order to disentangle the effect, it would be beneficial to have observations by two detectors. However, a single detector could suffice if it has a sufficient energy resolution [132].

In figure 6.23, the spectrum of $\bar{\nu}_e$ passing through 10,000 km of constant density is shown for the Garching model. Every spectrum at every 0.5 ms time interval between 0 and 9 s, is added to the previous one. Hence, the last line shows the time-integrated spectrum. As one can see, the spectrum shows modulations, so called *wiggles*. Only events within the first second after the bounce contribute to this distinct structure, as the difference

between $\langle E_{\bar{e}} \rangle$ and $\langle E_{\bar{x}} \rangle$ vanishes at later times. The fact that this behavior is common in the Garching and Basel model make it clear that the observation of the Earth effect is possibly limited to the first second after the bounce.

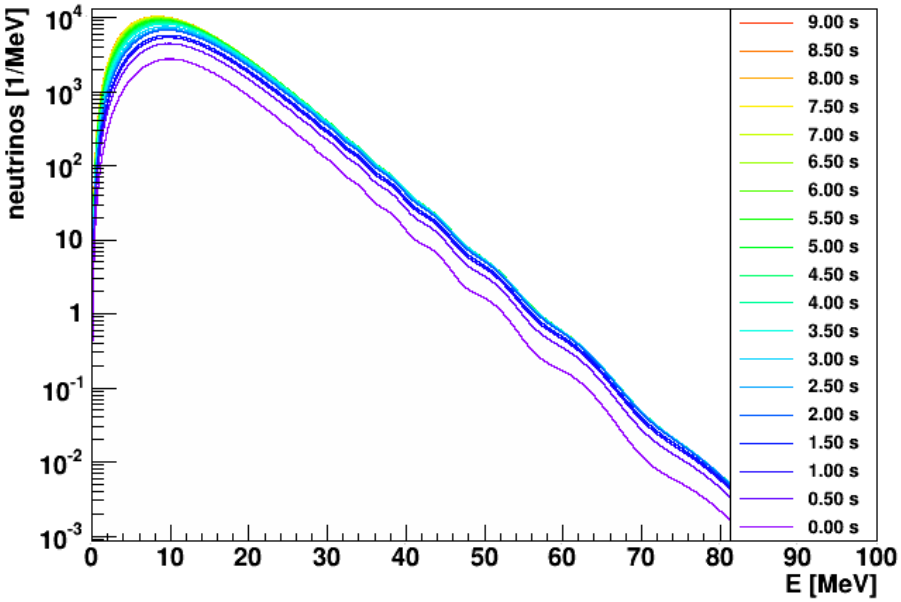

Figure 6.23: Spectrum of $\bar{\nu}_e$ after passing though 10,000 m of earth matter ($\rho = 5.5\,\mathrm{gcm}^{-3}$) according to the Garching model for NH. Every spectra of every 0.5 MeV time step is added atop of the others.

Figure 6.24 shows the energy deposit of the positron of the inverse β-decay channel for a SN at a distance of 10 kPc. The earth effect is more prominent, if the difference between the mean energies is large. Hence, in order to estimate the potential of LENA, the mean energies and (average) luminosities of the Basel group within the first second after the bounce are assumed. The mean neutrino energies are $\langle E_{\bar{e}} \rangle$=12 MeV and $\langle E_x \rangle$=16 MeV, the luminosities $L_{\bar{e}} = 3 \cdot 10^{52}\,\mathrm{ergs}^{-1}$ and $L_x = 2 \cdot 10^{52}\,\mathrm{erg\,s}^{-1}$ and the inverted neutrino mass hierarchy holds. Assuming an optimal case, the neutrinos travel 10,000km through the earth before reaching the detector. As the hierarchy is only this pronounced in the beginning, the luminosity of the first second is integrated. Obviously, even in the optimistic cast of almost maximum propagation though Earth, the signal is faint. Only above ~25 MeV, the wiggles appear, yet on a level of a few events only. In order to have a higher event rate, the ratio of luminosity to distance square has to increase. This means, that explosion has to be more energetic, or the SN has to be closer. Both criteria drastically limit the potential of LENA to observe the earth effect intrinsically. A less pronounced energy hierarchy would make the observation of the earth effect in a single detector and thus the determination of the neutrino mass hierarchy improbable.

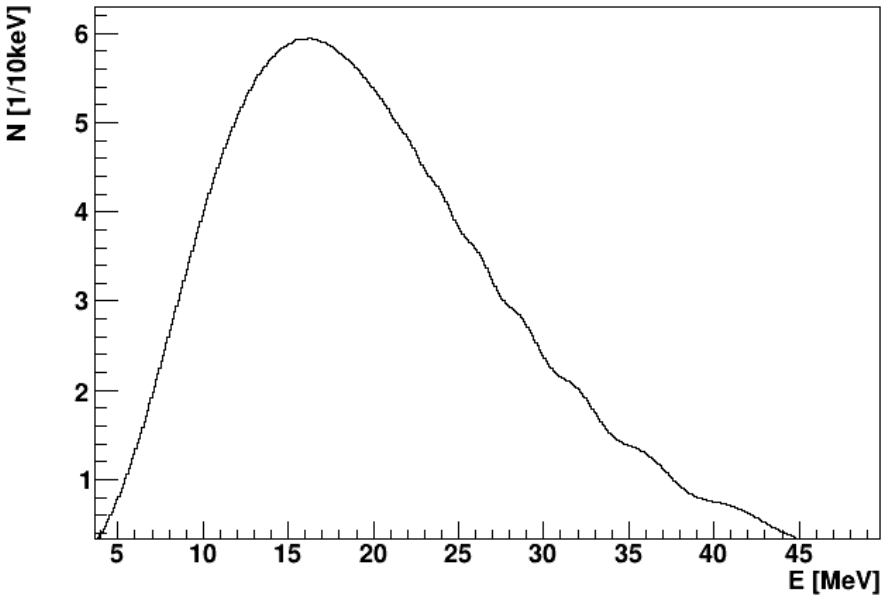

Figure 6.24: Earth matter effect in the spectrum of the inverse β-decay for NH assuming the energy hierarchy: $\langle E_{\bar{e}} \rangle$=12 MeV, $\langle E_x \rangle$=16 MeV and luminosities $L_{\bar{e}} = 3 \cdot 10^{52}\text{ergs}^{-1}$, $L_x = 2 \cdot 10^{52}\,\text{erg s}^{-1}$.

6.5 Late burning stages

As discussed thoroughly in section 1.5, the last nuclear burning stages of a massive star are accompanied by a large emission of thermally produced neutrinos. Hence, these neutrinos could act as a messenger from these phases and give an early warning signal for a SN explosion in the vicinity of the earth. For the calculation of the expected event rates of ν from late fusion stages in LENA, the average neutrino energies and spectrum-averaged cross-sections and flavor fractions calculated in [33] are used (see table 1.3). The evolution of the neutrino luminosities are taken from [133] and the abundance of the respective fuel from [31]. Carbon and neon burning are not considered, as the luminosities are too low to observe the processes at larger distances. In liquid scintillator, the neutrinos from O and Si burning can be detected best via the inverse β-decay or elastic ν-e scattering. The threshold of all ^{12}C channels is too high and the quenching of the proton recoil shifts the visible spectrum below the detection threshold of 0.2 MeV. Two possible candidates for a galactic SN are Betelgeuse ($\beta\,Orionis$) and $\eta\,Carinae$ at distances of 0.2 and 2.3 kPc, respectively. Their expected event rates per day in LENA can be seen in table 6.7. Core masses of 2 $M_\odot$, 1.6 $M_\odot$, and 1.4 $M_\odot$ are estimated for C/Ne, O, and Si burning, respectively [134]. According to [31], the time span of a 20 $M_\odot$ star like Betelgeuse for O burning is 1.25 y, for Si 11.5 d. For a 75 $M_\odot$ star, it is 0.9 y and 2 d, respectively. For larger masses, it will be even shorter.

Table 6.7 shows the event rates for the single burning phases in LENA for the ν-e scattering and the inverse β-decay channel. The fiducial volume with a height of 100 m and a radius of 13 m is assumed and LAB as scintillator mixture. For ν-e scattering, [33] assumes an energy threshold of 0 MeV. The effect of a threshold of 0.2 MeV is estimated assuming Fermi-Dirac distributions with the respective mean energies and the cross-section given in section 6.3.1. This reduces the expected event rates by a factor of 0.65 to 0.8.

The start and end rates for each fusion stage refer to the luminosities given in the first columns. They are derived from the luminosity per gram of fusion material from [31] for the core masses given above. Also, the abundance of each fuel in the core at each burning stage (20%, 20%, 70%, and 50% from C to Si) is considered [31]. The event rates are calculated for a star at a distance of 1 kPc. While the luminosity of the carbon fusion is too low, already the Ne burning phase induces > 10 cpd at the end of the stage at the distance of Betelgeuse. However, only events from ν-e scattering are detectable. A better chance for an observation is given during the O and Si burning stages. Figure 6.25 and 6.26 show the distance dependency of the event rates for both channels at the beginning and the end of the oxygen and silicon stages. Clearly, enough statistics in the inverse β-decay channel is gathered in order to determine the burning phase of Betelgeuse. From start to the end of the O burning, the reach of LENA can extend from 0.1 to 1 kPc using only this channel. For silicon, LENA is sensitive even up to 5 kPc, even beyond $\eta\,Carinae$.

	L [erg/s]		rate [cpd]: $\nu e \longrightarrow \nu e$		rate [cpd]: $\bar{\nu}_e e \longrightarrow n e^+$	
fusion stage	start	end	start	end	start	end
C	$9.5 \cdot 10^{38}$	$2.8 \cdot 10^{42}$	$2.3 \cdot 10^{-5}$	0.07	$4.2 \cdot 10^{-10}$	$1.2 \cdot 10^{-6}$
Ne	$2.8 \cdot 10^{42}$	$2.9 \cdot 10^{43}$	0.08	0.79	$1.5 \cdot 10^{-3}$	$1.6 \cdot 10^{-2}$
O	$8.0 \cdot 10^{43}$	$5.6 \cdot 10^{45}$	2.3	160	0.16	11
Si	$3.5 \cdot 10^{45}$	$9.8 \cdot 10^{45}$	108	301	71	199

Table 6.7: Luminosities and expected event rates in counts per day (cpd) in LENA for a star at 1 kPc at the beginning and the end of each late burning stage. As solvent, LAB is assumed.

As shown in table 1.3, the mean energy of the neutrinos at late burning stages is only few MeV oder even below. The spectra are quasi-thermal and are thus a in the region of solar neutrinos. Therefore, there is a large background from solar ν_e that makes the detection of neutrinos from neutrino-electron scattering challenging. Event rates from ^{7}Be are several thousand per day and even pep and pp neutrinos will largely obscure the neutrinos from late burning stages from distant stars. Moreover, the ^{14}C background will partially hide the signal. As the luminosity is increasing within each burning phase, the solar neutrino background might be determined at early stages and subtracted later in order to measure the O or Si neutrinos. For $\bar{\nu}_e$, the detection seems more promising. First, the delayed coincidence signal of the inverse β-decay allows to discriminate background

	rate [cpd]: $\nu e \longrightarrow \nu e$		rate [cpd]: $\bar{\nu}_e e \longrightarrow n e^+$	
fusion stage	start	end	start	end
C	$6 \cdot 10^{-4}$	1.7	$1 \cdot 10^{-8}$	$3 \cdot 10^{-5}$
Ne	2	20	0.04	0.4
O	58	4003	4	275
Si	2697	7522	1779	4963

Table 6.8: Expected event rates for Betelgeuse in LENA at the beginning and the end of each the late burning stages. As solvent, LAB is assumed.

	rate [cpd]: $\nu e \longrightarrow \nu e$		rate [cpd]: $\bar{\nu}_e e \longrightarrow n e^+$	
fusion stage	start	end	start	end
O	0.2	16	0.02	1
Si	11	29	7	19

Table 6.9: Expected event rates for $\eta\,Carinae$ in LENA at the beginning and the end of oxygen and silicon burning. As solvent, LAB is assumed.

very effectively. However, irreducible background arises from geo and reactor neutrinos in the energy regime of interest. Below ∼2.6 MeV, the geo neutrino rate is dominant, around $\sim 1000\,\mathrm{y}^{-1}$. Hence the detection limit for late burning stage neutrinos is at around 5-10 cpd, conservatively. Spectral analysis disentangling between the single contributions may help to extend the detection probability even further into space.

Spatial interferometry measurements in the infrared show that the diameter of Betelgeuse decreased ∼ 15% over the last decade [135]. This observed contraction might be a sign that the star entered the late burning stages and a core-collapse could be imminent. Although the time scale is small compared to cosmology, the process can take up to 10^6 years. Nevertheless, thanks its low energy threshold, LENA could provide an early warning signal for an upcoming explosion.

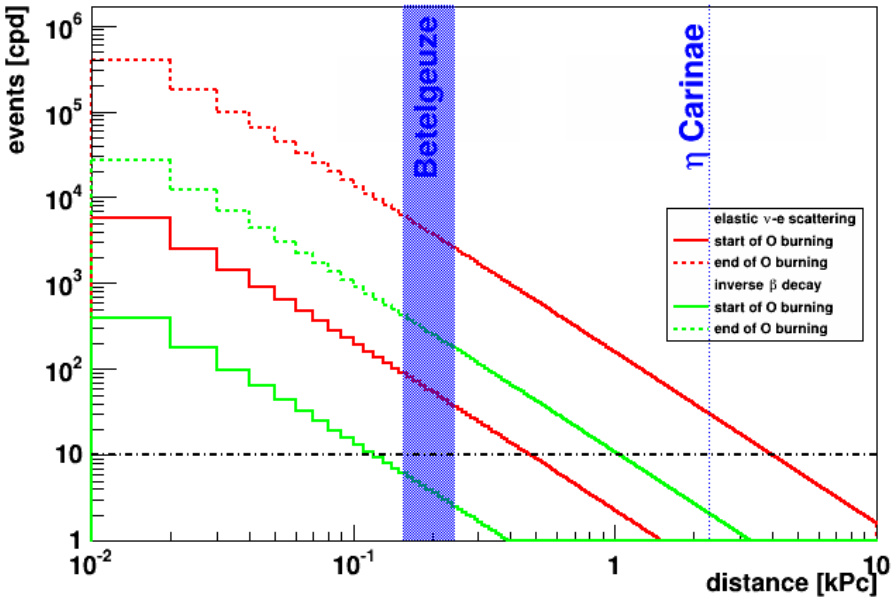

Figure 6.25: Events rates as a function of the distance from earth for the ν-e scattering and inverse β-decay channel in LENA for oxygen burning. For Betelgeuse, already the O burning stage can be observed.

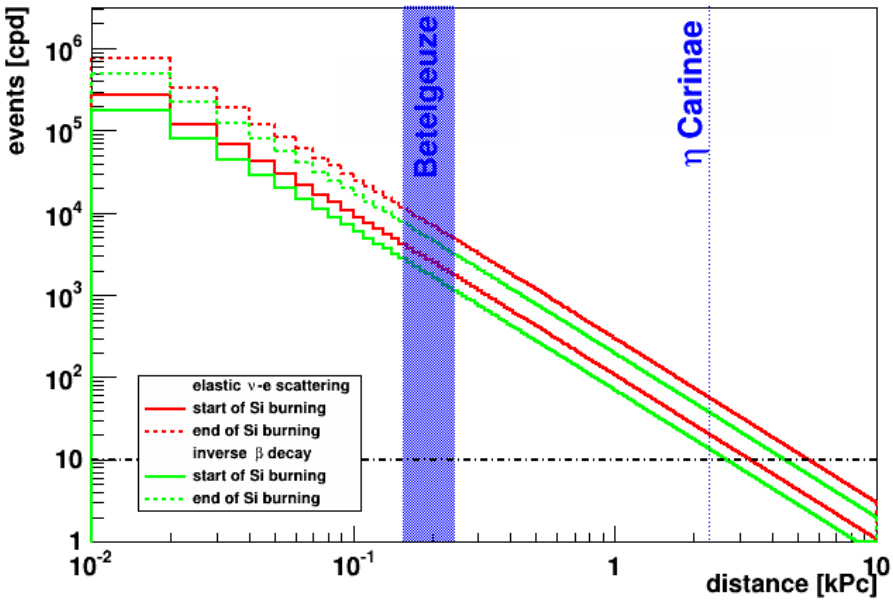

Figure 6.26: Events rates as a function of the distance from earth for the ν-e scattering and inverse β-decay channel in LENA for silicon burning. SN progenitors up to several kPc are in reach.

Chapter 7

Conclusions

In the past decade, the potential of liquid-scintillator detectors has been successfully demonstrated by Borexino [68] and KamLAND [44]. With about 50 kt of liquid scintillator, LENA (**L**ow-**E**nergy **N**eutrino **A**stronomy) will significantly excel their mass. Therefore, neutrinos from already known sources e.g. solar or geo-neutrinos, can be observed with an unprecedented accuracy. In addition, LENA has a high sensitivity for the observation of the yet unobserved diffuse supernova neutrino background. Moreover, the search for proton decay is a major goal of the LENA experiment.

The major part of this thesis is dedicated to the study of pulse shape discrimination in organic liquid scintillator. It is a powerful tool used in liquid-scintillator experiments to distinguish between interactions of different particles. For example, the reduction of the neutral current atmospheric neutrino background, and thus the potential to observe the diffuse supernova neutrino background in LENA, largely depends on the identification of one or more knock-out neutrons [55]. Information on the pulse shape is also used to discriminate the elastic neutrino-proton scattering channel for supernova neutrinos.

At the Maier-Leibnitz-Laboratorium in Garching, an experiment was set up to study the response of various liquid scintillator mixtures under neutron irradiation. A pulsed $^{11}B^{5+}$-ion beam with $E_B = 61.5\,\mathrm{MeV}$ is guided onto a gaseous hydrogen target to produce neutrons via the reaction $^{11}\mathrm{B(p,n)}^{11}\mathrm{C}$. Simultaneously, γs are produced by the Bremsstrahlung of the ion in the target material. In forward scattering direction, the neutrons have an energy of $\sim 11\,\mathrm{MeV}$. Changing the position of the detector, neutron energies down to 6 MeV can be investigated, which is especially useful for the determination of proton quenching.

Elaborate calibration of the scintillator samples with several γ sources is necessary in order to reconstruct the proton recoil energy. The effect of multiple scattering has been investigated in Monte-Carlo simulation studies of the detector along with coincidence measurements with a high-purity germanium detector [82]. In the energy range of interest, a

linear dependency of the photomultiplier output voltage with the energy deposit in the detector is well-given.

A coincidence measurement between the liquid-scintillator detector signal and the pulsing of the ion beam allows for a time-of-flight analysis and thus an efficient identification of the neutrons and γs produced in the hydrogen cell. This provides already background-reduced data samples of neutron-induced proton recoil and γ-induced electron recoils that can be used for later discrimination studies. In addition to the neutron beam, also an americium-beryllium source was used to investigate the γ/n discrimination efficiency.

Several liquid-scintillators were investigated (cf. table B.1). *Linear alkylbenzene* (LAB) + 3 g/ℓ *2,5-diphenyloxazole* (PPO) + 20 mg/ℓ *1,4-bis-(o-methylstyryl)-benzole* (bisMSB) as it is the most promising liquid-scintillator mixture candidate for the LENA detector. Mixtures with LAB from two different suppliers, Helm and Petresa, were used. Moreover, two samples (using LAB from Petresa) were investigated in order to determine the effect of oxidation. Liquid-scintillator mixtures with non-scintillating solvents and a higher concentration of PPO were also measured under neutron irradiation.

After the application of several cuts to reduce background, the γ/n discrimination power is determined in two ways: the so-called Gatti and the tail-to-total (T2T) method. Both show a comparable discrimination power. For the LENA standard solution, the neutron identification efficiency with a γ rejection of 99% is (99.70 ± 0.05)% for a combination of the Gatti and T2T method for the neutron beam data between 1-1.5 MeV. No significant difference can be observed between the liquid-scintillator mixtures based on LAB from the two different suppliers. While the neutron efficiency increases with higher PPO concentration, it decreases for oxidized samples and for those with the addition of non-scintillating solvents.

The Gatti method requires the knowledge of the standard pulse shape of both γ and neutron interactions. In a first step, γ and neutron pulse shapes are reconstructed using events in the respective peak in the ToF spectrum. In a second iteration, these events are further filtered with cuts on the Gatti and T2T probabilities. For the derivation of standard pulses from the AmBe source data, γ and neutron induced events are separated using the T2T criterion. The standard pulses have been determined in intervals with a width of 0.5 MeV in order to guarantee sufficient statistics.

For the standard pulses derived from the neutron beam and AmBe data a maximum likelihood fit is performed with a sum of three exponential decays convoluted with a Gaussian for each scintillator. The fit model reflects the deexcitation processes in the solvent and solute and the time resolution of the detector and ion beam. The decay amplitudes $n_{i,j}$ and times $\tau_{i,j}$ $(i = 1, 2, 3; j = \gamma, n)$ are evaluated in 0.5 MeV intervals. While the decay times do not depend on the type of excitation, $\tau_{i,\gamma} \approx \tau_{i,n} = \tau_i$, a significant difference between the decay amplitudes $n_{i,\gamma}$ and $n_{i,n}$ is observed over the whole energy range from

0-6 MeV. While for γs the fastest component $n_{1,\gamma}$ dominates, the slow components are more important for neutron events as recoil protons have a higher ionization density than recoil electrons. This fact is exploited in the T2T method for particle discrimination. For the decay times, no energy dependence can be observed. Moreover, the two fastest decay times for both γ and neutron induced events agree well within error bars. However, $\tau_{3,\gamma}$ is systematically higher than $\tau_{3,n}$.

Two samples of the LENA-favored liquid scintillator were made from LAB from two different suppliers, HELM (LH3) [74] and Petresa (LP) [73]. Both the decay amplitudes and the constants match within the error bars and no influence of the different LAB provided can be observed. The energy-averaged fit parameters LH3, including statistical and systematical 1σ errors, are $\tau_1 = (6.9 \pm 0.1^{+0.21}_{-0.17})$ ns, $\tau_2 = (26.4 \pm 0.8^{+2.0}_{-2.2})$ ns, $\tau_3 = (141.0 \pm 4.3^{+3.6}_{-14.6})$ ns, $n_{1,\gamma} = 0.676 \pm 0.016^{+0.039}_{-0.031}$, $n_{1,n} = 0.591 \pm 0.006^{+0.043}_{-0.027}$, $n_{2,\gamma} = 0.189 \pm 0.010^{+0.031}_{-0.021}$, $n_{2,n} = 0.222 \pm 0.004^{+0.070}_{-0.019}$, $n_{3,\gamma} = 0.136 \pm 0.006^{+0.017}_{-0.025}$, and $n_{3,n} = 0.183 \pm 0.007^{+0.021}_{-0.025}$.

While the decay constants of the aged samples LP1d and LPmax agree to those of LP, they have a less prominent slow decay amplitude n_3 due to oxygen quenching. The addition of a non-scintillating solvent further reduces n_3.

The detection of proton recoils largely depends on the characteristics of the liquid scintillator. In order to make more precise predictions, both the proton quenching factor and the neutron identification efficiency have to be known with a higher accuracy. A higher luminosity of the pulsed neutron beam can help to acquire more statistics and thus reveal possible subleading effects that appear around the shoulder of the proton recoil spectrum. On the other side, a single photon detection coincidence experiment might be the best way to determine the pulse shape of a recoil proton as it would be less influenced by the photomultiplier an the cross-play of electronics and wiring.

A major goal of LENA is the detection of neutrinos from galactic core-collapse supernovae. As neutrinos - unlike photons - are undisturbed by the outer layers of the remnant star, they offer the unique possibility to take a look inside a supernova explosion. Moreover, in case the supernova cannot be observed optically due to interstellar matter, neutrinos provide the sole information on a supernova explosion in the galaxy.

In LENA, supernova neutrinos can be detected via six major channels that allow to measure the total flux, single neutrino flavor fluxes, and spectra. The dominating reaction is the $\bar{\nu}_e$-sensitive inverse β decay. Due to quenching, neutrino-proton scattering is most sensitive to the neutrinos with the highest mean energy. While neutrino-electron scattering and neutral interactions on ^{12}C give information on the total flux, charged current reactions on ^{12}C are sensitive to ν_e and $\bar{\nu}_e$.

The event rates strongly depend on the mean neutrino energies $\langle E \rangle$ and luminosities L. Due to the inclusion of neutrino-nucleus interactions, recent supernova models from the Garching group [110] and the Basel group [112] predict lower $\langle E \rangle$ than older models [136,

35, 137]. Moreover, the difference between the mean energies of the neutrino flavors is shown to be smaller. This limits the sensitivity to neutrino oscillations significantly. The time-dependent signals were calculated for all six channels using the Garching model. H- and L-resonance occurrence due to the varying matter density are considered as well. In total, about 6,000 events can be expected for a supernova explosion at 10 kPc distance

As galactic core-collapse supernovae are rare events not to miss, it is vital to have the detector online at all times. Due to its low energy threshold, LENA can provide a supernova explosion warning signal by the observation of the thermal neutrinos emitted in the late burning stages of the supernova progenitor. During the silicon burning phase - the last fusion stage before the collapse - the neutrino luminosity $L_{Si} = 9.8{\cdot}10^{45}\,\mathrm{ergs}^{-1}$ and the mean neutrino energy of $\langle E_{Si}\rangle = 1.85\,\mathrm{MeV}$ are highest [31, 33]. Via neutrino-electron scattering and inverse β decay, up to $\sim$300 and 200 counts per day, respectively, could be observed for a progenitor at 1 kPc, respectively. For the inverse β decay, possible background due to reactor and geo-$\bar{\nu}_e$ is in the order of a few events per day. Hence, LENA offers the possibility to observe silicon neutrinos up to several kPc.

Already to this day, there are several detector running that could observe a galactic supernova. Although Čerenkov-detectors like Super-Kamiokande [8] gather high statistics, they are limited to neutrinos with energies above $\sim$5 MeV. However, state-of-the-art supernova models predict mean neutrino energies around or below 10 MeV and thus a large part of the spectrum is hidden for this kind of detector. Compared to LENA, current liquid-scintillator experiments like Borexino [68] have only little mass and thus only little statistics. For a supernova at 10 kPc and according to the Garching model, Borexino will measure less than 100 events, yet mostly via inverse β-decay. The elastic ν-p channel, providing information on the mean neutrino energy $\langle E_x\rangle$, will only be significant in a detector with the size of LENA.

Abbreviations

ADC	analog-to-digita converter
bisMSB	1,4-bis-(o-methylstyryl)-benzole
CC	charged current
C.L.	confidence level
CO	carbon-oxygen core
DAQ	data acquisition
DM	dark matter
DSNB	diffuse supernova neutrino background
FV	fiducial volume
IH	inverted neutrino mass hierarchy
LAB	linear alkylbenzene
LAGUNA	large apparatus for grand unification and neutrino astrophysics
LAGUNA- LBNO	LAGUNA - long baseline neutrino oscillations
LSM	Laboratoire Souterrain de Modane
MC	Monte Carlo
MSW	Mikheyev-Smirnov-Wolfenstein
NC	neutral current
NH	normal neutrino mass hierarchy
OM	optical modules
PDF	probability density function
pe	photo electrons
PMNS	Pontecorvo-Maki-Nakagawa-Sakata
PMT	photomultiplier tube
PPO	2,5-Diphenyloxazole
PTFE	polytetrafluoethylene
SN	supernova
SM	standard model
SP1	standard pulse derived from neutron beam data with cut on ToF peaks
SP2	standard pulse, derived as SP1 with additional Gatti and T2T cuts
SPA	standard pulse derived from AmBe source data with T2T cut
T2T	tail-to-tot
ToF	time-of-flight

Appendices

Appendix A

Kinematics

In this chapter, the kinematics of the neutron production in the hydrogen cell is discussed.

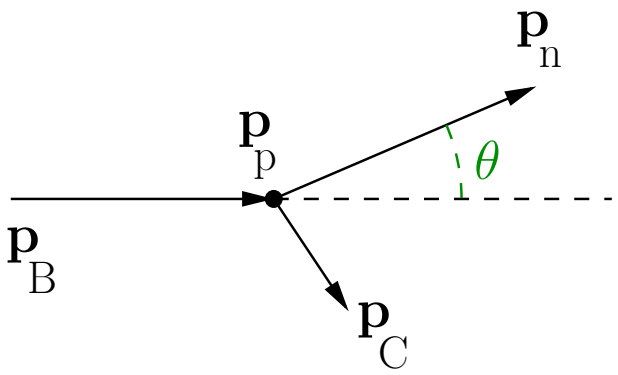

Figure A.1: Vector diagram of the reaction in the hydrogen cell in the laboratory system.

In the laboratory system, the four vectors of the reaction shown in figure A.1 are

$$p_B = \begin{pmatrix} E_B \\ \vec{p}_B \end{pmatrix}, p_p = \begin{pmatrix} m_p \\ \vec{0} \end{pmatrix}, p_n = \begin{pmatrix} E_n \\ \vec{p}_n \end{pmatrix}, p_C = \begin{pmatrix} E_C \\ \vec{p}_C \end{pmatrix}, \tag{A.1}$$

whereas natural units are uses, i.e. $c = 1$. Starting from the 4-vector equation for energy and momentum conservation

$$p_B + p_p = p_C + p_n, \tag{A.2}$$

rearrangement and squaring yields

$$(p_B - p_n)^2 = (p_C - p_p)^2. \tag{A.3}$$

Finally, eliminating p_C

$$\begin{aligned} p_B^2 + p_n^2 - 2p_B p_n &= p_C^2 + p_p^2 - p_p(p_B - p_n + p_p) \\ \frac{1}{2}\left(m_B^2 + m_n^2 - m_C^2 + m_p^2\right) &= -E_B E_p + E_n E_p + E_B E_p \\ &\quad - \sqrt{E_B^2 - m_B^2}\ \sqrt{E_n^2 - m_n^2}\ cos(\theta) \end{aligned} \tag{A.4}$$

one obtains the energy dependence of the kinetic energy of the neutron. Here, θ denotes the angle between the incident boron ion and the neutron. Solving this quadratic equation yields

$$\begin{aligned} E_{kin,n} &= E_n - m_n \\ &= \Bigg(-2(m_p + E_B)(m_p E_B + M) \\ &\quad \pm \Bigg(\left(2(m_p + E_B)(m_p E_B + M)\right)^2 \\ &\quad - 4\left(-(m_p + E_B)^2 + (E_B^2 - m_B^2)cos^2\theta\right) \\ &\quad \cdot \left(-(m_p E_B + M)^2 - m_n^2(E_B^2 - m_B^2)cos^2\theta\right) \Bigg)^{\frac{1}{2}} \Bigg) \\ &\quad \Big/ \Bigg(-2(m_p + E_B)^2 + 2(E_B^2 - m_B^2)cos^2\theta \Bigg) - m_n. \end{aligned} \tag{A.5}$$

Here, m_p, m_n, m_B, and m_C denote the rest mass of proton, neutron, ^{11}B and ^{11}C, respectively. Moreover,

$$M = \frac{1}{2}(m_B^2 + m_n^2 - m_C^2 + m_p^2). \tag{A.6}$$

The incident kinetic energy $E_{kin,B} = E_B - m_B$ is the only free fit parameter shown in Figure 4.5.

Experimentally, the information of the incident neutron kinetic energy $E_{kin,n}$ is derived from the ToF spectrum. A relativistic calculation shows

$$\begin{aligned} E_{kin,n} &= (\gamma - 1)m_n \\ &= \left(\sqrt{\frac{1}{1-\beta^2}} - 1\right) m_n \\ &= \left(\left(1 - \left(\frac{d}{ct_{n,calib}}\right)^2\right)^{-\frac{1}{2}} - 1\right) m_n \\ &= E_{tof}. \end{aligned} \tag{A.7}$$

Here, d is the distance of the hydrogen cell to the center of the scintillator probe. $t_{n,calib} = t_n - t_\gamma + d/c$ is the calibrated ToF of the neutrons, whereas t_n and t_γ denote the respective peak maxima in the ToF spectrum.

Appendix B

Scintillator property tables

In this appendix,the results for all cut efficiencies and fit parameters from chapter 5 are presented.

B.1 Scintillator mixtures

short	solvent 1 (provider)	solvent 2 (provider)	PPO	bis-MSB
LH3	LAB (Helm)		3 g/ℓ	20 mg/ℓ
LH3*	LAB (Helm)		3 g/ℓ	20 mg/ℓ
LH10	LAB (Helm)		10 g/ℓ	20 mg/ℓ
LP	LAB (Petresa)		3 g/ℓ	20 mg/ℓ
LP1d	LAB (Petresa)		3 g/ℓ	20 mg/ℓ
LPmax	LAB (Petresa)		3 g/ℓ	20 mg/ℓ
DCMV	51.6% LAB (Helm/Petresa)	48.4% n-paraffin (CBR)	2 m/ℓ	20 mg/ℓ
L50	50 % LAB (Helm)	50% n-paraffin (CBR)	3 g/ℓ	20 mg/ℓ

Table B.1: Liquid-scintillator mixtures inverstigated in this thises and their abbreviations.

B.2 Cut efficiencies

pulse cuts	**LH3**	**LPmax**	**DCMV**	**LP**	**L50**	**L10**	**average**
rise time	0.985 ± 0.002	0.978 ± 0.003	0.978 ± 0.003	0.984 ± 0.002	0.977 ± 0.002	0.943 ± 0.002	0.974 ± 0.002
charge/height	0.986 ± 0.002	0.980 ± 0.003	0.980 ± 0.003	0.987 ± 0.002	0.980 ± 0.002	0.982 ± 0.002	0.983 ± 0.002
pre pulses	0.999 ± 0.002	0.997 ± 0.003	0.997 ± 0.003	0.999 ± 0.002	0.997 ± 0.002	0.999 ± 0.002	0.998 ± 0.002
double pulses	0.982 ± 0.002	0.979 ± 0.003	0.979 ± 0.003	0.974 ± 0.002	0.975 ± 0.002	0.970 ± 0.002	0.976 ± 0.002
baseline	0.987 ± 0.002	0.986 ± 0.003	0.986 ± 0.003	0.990 ± 0.002	0.985 ± 0.002	0.992 ± 0.002	0.988 ± 0.002
Gatti + T2T 90% C.L.							
neutron type	0.440 ± 0.0009	0.329 ± 0.001	0.329 ± 0.001	0.344 ± 0.001	0.345 ± 0.001	0.435 ± 0.001	0.370 ± 0.001
γ type	0.336 ± 0.0007	0.342 ± 0.001	0.342 ± 0.001	0.393 ± 0.001	0.261 ± 0.001	0.364 ± 0.001	0.340 ± 0.001
other cuts							
beam	0.938 ± 0.001	0.916 ± 0.003	0.916 ± 0.003	0.724 ± 0.002	0.803 ± 0.001	0.951 ± 0.002	0.875 ± 0.002
γ peak	0.146 ± 0.0004	0.146 ± 0.001	0.146 ± 0.001	0.123 ± 0.001	0.127 ± 0.0004	0.146 ± 0.001	0.139 ± 0.001
neutron peak	0.181 ± 0.0005	0.172 ± 0.001	0.172 ± 0.001	0.157 ± 0.001	0.170 ± 0.0005	0.182 ± 0.001	0.172 ± 0.001
total (without Gatti + T2T cut)							
γ	0.171 ± 0.0005	0.165 ± 0.001	0.165 ± 0.001	0.112 ± 0.001	0.153 ± 0.0005	0.168 ± 0.001	0.156 ± 0.001
neutron	0.137 ± 0.0004	0.139 ± 0.001	0.139 ± 0.001	0.099 ± 0.001	0.112 ± 0.0004	0.131 ± 0.001	0.126 ± 0.001
total with Gatti + T2T cut							
γ	0.137 ± 0.0004	0.098 ± 0.001	0.098 ± 0.001	0.070 ± 0.0004	0.101 ± 0.0004	0.136 ± 0.001	0.107 ± 0.001
neutron	0.102 ± 0.0004	0.096 ± 0.001	0.096 ± 0.001	0.081 ± 0.0005	0.073 ± 0.0003	0.102 ± 0.001	0.092 ± 0.0005

Table B.3: Cut efficiencies for different LS mixtures summed over all neutron beam runs.

B.3 Fit parameter tables

In this section, the results of the standard pulse fits for different LS mixtures is shown. Details on the fit function and routine are presented in section 5.4. The parameter uncertainties are derived from the fit. Systematical errors are shown in table B.12.

LS	standard pulse	σ_γ [ns]	σ_n [ns]	$t_{0,\gamma}$ [ns]	$t_{0,n}$ [ns]
LH3	SP1	2.23 ± 0.12	1.92 ± 0.58	1.79 ± 0.11	1.70 ± 0.14
	SP2	2.10 ± 0.26	2.09 ± 0.08	1.79 ± 0.09	1.76 ± 0.05
	SPA	2.00 ± 0.61	2.09 ± 0.11	1.62 ± 0.45	1.71 ± 0.04
LH3*	SPA	1.98 ± 0.61	1.92 ± 0.59	1.78 ± 0.11	1.70 ± 0.17
LH10	SP1	1.98 ± 0.14	1.85 ± 0.10	1.49 ± 0.06	1.43 ± 0.09
	SP2	1.93 ± 0.14	1.84 ± 0.10	1.48 ± 0.07	1.43 ± 0.10
	SPA	2.97 ± 1.44	2.92 ± 1.47	1.00 ± 0.71	0.95 ± 0.67
LP	SP1	2.25 ± 0.15	2.10 ± 0.07	1.82 ± 0.10	1.77 ± 0.04
	SP2	2.16 ± 0.12	2.03 ± 0.17	1.81 ± 0.07	1.69 ± 0.28
LP1d	SPA	2.11 ± 0.09	2.05 ± 0.11	1.77 ± 0.07	1.71 ± 0.08
LPmax	SP1	2.25 ± 0.14	2.08 ± 0.08	1.83 ± 0.09	1.74 ± 0.05
	SP2	2.41 ± 0.79	2.06 ± 0.08	1.63 ± 0.50	1.74 ± 0.07
	SPA	2.12 ± 0.12	2.05 ± 0.08	1.76 ± 0.08	1.71 ± 0.07
L50	SP1	2.28 ± 0.15	2.11 ± 0.10	1.87 ± 0.07	1.79 ± 0.07
	SP2	2.24 ± 0.26	2.09 ± 0.10	1.95 ± 0.38	1.84 ± 0.17
	SPA	2.17 ± 0.09	2.03 ± 0.21	1.89 ± 0.07	1.83 ± 0.10
DCMV	SP1	2.39 ± 0.14	2.20 ± 0.08	2.02 ± 0.15	1.91 ± 0.05
	SP2	2.37 ± 0.12	2.38 ± 0.20	2.04 ± 0.07	2.00 ± 0.05
	SPA	2.68 ± 1.04	2.25 ± 0.19	1.60 ± 0.72	1.83 ± 0.06

Table B.4: Energy-averaged fit results of σ and t_0 according to Eq.(5.13) for differently constructed standard pulses.

parameter	recoil type	SP1	SP2	SPA	3d fit	Total
τ_1 [ns]	n	7.0 ± 0.3	7.0 ± 0.3	6.9 ± 0.2	7.0 ± 0.4	6.9 ± 0.1
	γ	6.8 ± 0.3	6.9 ± 0.2	6.8 ± 0.2		
τ_2 [ns]	n	27.6 ± 1.6	26.9 ± 2.0	25.5 ± 2.0	23.4 ± 3.0	26.4 ± 0.8
	γ	26.7 ± 2.7	27.4 ± 2.5	26.8 ± 1.2		
τ_3 [ns]	n	141.6 ± 12.0	139.1 ± 9.2	126.0 ± 15.0	111.1 ± 12.6	141.0 ± 4.3
	γ	156.5 ± 25.7	160.4 ± 26.6	146.1 ± 5.9		
n_1	n	0.611 ± 0.014	0.606 ± 0.011	0.586 ± 0.007	0.608 ± 0.088	0.590 ± 0.008
	γ	0.674 ± 0.026	0.682 ± 0.022	0.669 ± 0.022	0.670 ± 0.066	0.586 ± 0.213
n_2	n	0.219 ± 0.006	0.219 ± 0.005	0.227 ± 0.006	0.193 ± 0.040	0.232 ± 0.005
	γ	0.189 ± 0.015	0.184 ± 0.016	0.193 ± 0.014	0.164 ± 0.051	0.256 ± 0.155
n_3	n	0.170 ± 0.013	0.176 ± 0.012	0.187 ± 0.009	0.198 ± 0.032	0.179 ± 0.008
	γ	0.137 ± 0.014	0.134 ± 0.008	0.138 ± 0.009	0.165 ± 0.026	0.157 ± 0.058

Table B.5: Scintillation decay constants τ_i and amplitudes n_i for LH3, derived from the fit described in section 5.4. The total result is a combination of the pulse shape fits of the three independent standard pulses SP2 (LH3), SPA (LH3) and SPA (LH3*). Since the decay times for γ and neutron induced recoil events are assumed to be identical, they are combined.

parameter	recoil type	SP1	SP2	SPA	3d fit	Total
τ_1 [ns]	n	5.4 ± 0.4	5.4 ± 0.4	5.0 ± 0.2	2.9 ± 5.0	5.0± 0.1
	γ	5.3 ± 0.3	5.3 ± 0.3	4.9 ± 0.2		
τ_2 [ns]	n	22.4 ± 1.4	22.4 ± 1.7	20.7 ± 1.4	11.5 ± 99.9	20.4 ± 0.4
	γ	20.0 ± 0.6	20.4 ± 0.5	19.3 ± 1.1		
τ_3 [ns]	n	114.8 ± 4.6	116.2 ± 5.6	114.0 ± 9.4	201.0 ± 63.6	111.1 ± 1.4
	γ	114.1 ± 2.1	112.3 ± 2.4	109.7 ± 1.8		
n_1	n	0.487 ± 0.015	0.483 ± 0.014	0.470 ± 0.015	0.487 ± 0.077	0.477 ± 0.010
	γ	0.545 ± 0.030	0.554 ± 0.025	0.519 ± 0.024	0.541 ± 0.140	0.536 ± 0.017
n_2	n	0.285 ± 0.006	0.286 ± 0.005	0.284 ± 0.008	0.265 ± 0.037	0.285 ± 0.004
	γ	0.279 ± 0.014	0.280 ± 0.015	0.291 ± 0.010	0.262 ± 0.047	0.288 ± 0.008
n_3	n	0.228 ± 0.020	0.231 ± 0.017	0.246 ± 0.011	0.248 ± 0.036	0.241 ± 0.009
	γ	0.175 ± 0.020	0.166 ± 0.012	0.189 ± 0.015	0.197 ± 0.032	0.175 ± 0.009

Table B.6: Scintillation decay constants τ_i and amplitudes n_i for LH10, derived from the fit described in section 5.4. The total result is a combination of the pulse shape fits to the two independent standard pulses SP2 and SPA (column 4 and 5). Since the decay times for γ and neutron induced recoil events are assumed to be identical, they are combined.

parameter	recoil type	SP1	SP2	3d fit	Total
τ_1 [ns]	n	7.0 ± 0.3	7.1 ± 0.4	6.9 ± 0.5	6.9 ± 0.2
	γ	6.8 ± 0.3	6.8 ± 0.3		
τ_2 [ns]	n	26.4 ± 1.3	27.2 ± 2.4	22.5 ± 3.7	26.6 ± 1.7
	γ	25.8 ± 2.5	26.1 ± 2.3		
τ_3 [ns]	n	137.4 ± 6.3	142.1 ± 13.5	120.0 ± 16.4	142.9 ± 9.8
	γ	145.4 ± 12.1	143.7 ± 14.4		
n_1	n	0.573 ± 0.016	0.574 ± 0.015	0.558 ± 0.126	0.574 ± 0.015
	γ	0.646 ± 0.035	0.653 ± 0.029	0.630 ± 0.115	0.653 ± 0.029
n_2	n	0.231 ± 0.006	0.231 ± 0.004	0.213 ± 0.036	0.231 ± 0.004
	γ	0.199 ± 0.014	0.202 ± 0.016	0.189 ± 0.039	0.202 ± 0.016
n_3	n	0.197 ± 0.016	0.195 ± 0.017	0.229 ± 0.036	0.195 ± 0.017
	γ	0.155 ± 0.022	0.145 ± 0.013	0.181 ± 0.049	0.145 ± 0.013

Table B.7: Scintillation decay constants τ_i and amplitudes n_i for LP, derived from the fit described in section 5.4. Since the decay times for γ and neutron induced recoil events are assumed to be identical they are combined.

parameter	recoil type	SPA	Total
τ_1 [ns]	n	6.9 ± 0.3	6.8 ± 0.1
	γ	6.7 ± 0.1	
τ_2 [ns]	n	25.6 ± 2.9	24.9 ± 0.4
	γ	24.9 ± 0.4	
τ_3 [ns]	n	127.7 ± 17.5	138.5 ± 2.7
	γ	138.8 ± 2.7	
n_1	n	0.590 ± 0.022	0.590 ± 0.022
	γ	0.665 ± 0.020	0.665 ± 0.020
n_2	n	0.246 ± 0.006	0.246 ± 0.006
	γ	0.206 ± 0.014	0.206 ± 0.014
n_3	n	0.164 ± 0.022	0.164 ± 0.022
	γ	0.129 ± 0.006	0.129 ± 0.006

Table B.8: Scintillation decay constants τ_i and amplitudes n_i for LP1d, derived from the fit described in section 5.4. Since the decay times for γ and neutron induced recoil events are assumed to be identical they are combined.

parameter	recoil type	SP1	SP2	SPA	3d fit	Total
τ_1 [ns]	n	7.1 ± 0.3	7.1 ± 0.4	7.5 ± 1.1	6.9 ± 0.4	6.9 ± 0.1
	γ	6.8 ± 0.3	6.9 ± 0.3	6.9 ± 0.1		
τ_2 [ns]	n	27.6 ± 2.5	27.4 ± 2.2	25.6 ± 2.4	21.1 ± 3.2	25.9 ± 0.4
	γ	25.8 ± 3.1	27.1 ± 3.1	25.9 ± 0.4		
τ_3 [ns]	n	145.0 ± 23.9	140.9 ± 13.6	116.1 ± 24.0	99.4 ± 0.3	142.9 ± 2.9
	γ	149.7 ± 24.9	161.3 ± 36.8	143.3 ± 3.0		
n_1	n	0.604 ± 0.019	0.603 ± 0.016	0.598 ± 0.010	0.550 ± 4e-05	0.600 ± 0.009
	γ	0.666 ± 0.035	0.678 ± 0.026	0.675 ± 0.020		0.676 ± 0.016
n_2	n	0.236 ± 0.007	0.236 ± 0.006	0.231 ± 0.020	0.210 ± 0.030	0.235 ± 0.006
	γ	0.197 ± 0.019	0.196 ± 0.018	0.198 ± 0.013		0.197 ± 0.011
n_3	n	0.160 ± 0.016	0.161 ± 0.014	0.171 ± 0.027	0.240 ± 0.030	0.163 ± 0.013
	γ	0.137 ± 0.018	0.127 ± 0.008	0.126 ± 0.007		0.126 ± 0.005

Table B.9: Scintillation decay constants τ_i and amplitudes n_i for LPmax, derived from the fit described in section 5.4. The total result is a combination of the pulse shape fits to the two independent standard pulses SP2 and SPA (column 4 and 5). Since the decay times for γ and neutron induced recoil events are assumed to be identical they are combined. The 3-d fit of the single γ induced pulses did not converge.

parameter	recoil type	SP1	SP2	SPA	3d fit	Total
τ_1 [ns]	n	9.0 ± 0.2	8.8 ± 0.3	8.8 ± 0.3	8.9 ± 0.5	8.8 ± 0.1
	γ	9.1 ± 0.8	8.8 ± 0.2	8.7 ± 0.2		
τ_2 [ns]	n	37.3 ± 2.1	34.1 ± 3.4	32.8 ± 3.6	27.0 ± 4.5	34.4 ± 2.0
	γ	34.6 ± 10.0	37.5 ± 5.2	35.6 ± 5.1		
τ_3 [ns]	n	254.8 ± 92.9	221.0 ± 98.7	182.1 ± 114.8	108.4 ± 14.0	224.1 ± 69.3
	γ	410.8 ± 346.5	435.8 ± 335.2	303.2 ± 220.3		
n_1	n	0.666 ± 0.007	0.649 ± 0.011	0.665 ± 0.028	0.653 ± 0.074	0.651 ± 0.010
	γ	0.680 ± 0.058	0.701 ± 0.022	0.720 ± 0.013		0.715 ± 0.011
n_2	n	0.201 ± 0.007	0.196 ± 0.005	0.203 ± 0.014	0.171 ± 0.051	0.197 ± 0.004
	γ	0.174 ± 0.047	0.153 ± 0.012	0.164 ± 0.014		0.157 ± 0.009
n_3	n	0.133 ± 0.004	0.154 ± 0.011	0.132 ± 0.019	0.175 ± 0.035	0.149 ± 0.010
	γ	0.146 ± 0.031	0.147 ± 0.032	0.116 ± 0.012		0.120 ± 0.011

Table B.10: Scintillation decay constants τ_i and amplitudes n_i for DCMV, derived from the fit described in section 5.4. The total result is a combination of the pulse shape fits to the two independent standard pulses SP2 and SPA (column 4 and 5). Since the decay times for γ and neutron induced recoil events are assumed to be identical, they are combined. The 3-d fit of the single γ induced pulses did not converge.

parameter	recoil type	SP1	SP2	SPA	Total
τ_1 [ns]	n	7.5 ± 0.3	7.4 ± 0.4	7.5 ± 0.2	7.4 ± 0.1
	γ	7.3 ± 0.3	7.2 ± 0.5	7.4 ± 0.2	
τ_2 [ns]	n	29.9 ± 2.1	28.9 ± 3.4	29.1 ± 1.5	29.1 ± 1.2
	γ	28.7 ± 3.3	28.2 ± 7.3	29.3 ± 2.3	
τ_3 [ns]	n	165.6 ± 26.6	167.0 ± 28.0	146.4 ± 11.4	152.1 ± 10.0
	γ	177.3 ± 40.0	259.1 ± 281.0	176.0 ± 31.8	
n_1	n	0.635 ± 0.018	0.621 ± 0.027	0.621 ± 0.013	0.621 ± 0.012
	γ	0.690 ± 0.027	0.669 ± 0.029	0.688 ± 0.021	0.681 ± 0.017
n_2	n	0.223 ± 0.008	0.225 ± 0.014	0.225 ± 0.004	0.225 ± 0.004
	γ	0.185 ± 0.016	0.191 ± 0.025	0.189 ± 0.014	0.190 ± 0.012
n_3	n	0.142 ± 0.011	0.154 ± 0.016	0.155 ± 0.013	0.154 ± 0.010
	γ	0.125 ± 0.013	0.140 ± 0.023	0.123 ± 0.007	0.125 ± 0.007

Table B.11: Scintillation decay constants τ_i and amplitudes n_i for L50, derived from the fit described in section 5.4. The total result is a combination of the pulse shape fits to the two independent standard pulses SP2 and SPA (column 4 and 5). Since the decay times for γ and neutron induced recoil events are assumed to be identical, they are combined.

B.4 Systematical errors

LS	recoil type	σ_{syst}					
		$\tau_1[ns]$	$\tau_2[ns]$	$\tau_3[ns]$	n_1	n_2	n_3
LH10	n	$^{+0.29}_{-0.21}$	$^{+0.98}_{-0.83}$	$^{+2.56}_{-6.31}$	$^{+0.073}_{-0.070}$	$^{+0.053}_{-0.009}$	$^{+0.043}_{0.005}$
	γ	$^{+0.17}_{-0.11}$	$^{+0.83}_{-0.68}$	$^{+1.63}_{-7.24}$	$^{+0.025}_{-0.021}$	$^{+0.021}_{-0.023}$	$^{+0.009}_{-0.013}$
LH3	n	$^{+0.17}_{-0.17}$	$^{+1.98}_{-2.08}$	$^{+3.61}_{-11.68}$	$^{+0.025}_{-0.023}$	$^{+0.070}_{-0.013}$	$^{+0.019}_{-0.025}$
	γ	$^{+0.17}_{-0.17}$	$^{+1.58}_{-2.23}$	$^{+3.61}_{-14.59}$	$^{+0.039}_{-0.029}$	$^{+0.031}_{-0.021}$	$^{+0.017}_{-0.021}$
LH3*	n	$^{+0.21}_{-0.13}$	$^{+1.33}_{-1.28}$	$^{+2.79}_{-9.11}$	$^{+0.043}_{-0.027}$	$^{+0.023}_{-0.019}$	$^{+0.021}_{-0.023}$
	γ	$^{+0.17}_{-0.11}$	$^{+1.73}_{-1.78}$	$^{+1.98}_{-12.03}$	$^{+0.033}_{-0.031}$	$^{+0.019}_{-0.019}$	$^{+0.017}_{-0.025}$
LP	n	$^{+0.35}_{-0.35}$	$^{+1.73}_{-1.63}$	$^{+4.66}_{-11.68}$	$^{+0.021}_{-0.07}$	$^{+0.070}_{-0.07}$	$^{+0.019}_{-0.027}$
	γ	$^{+0.49}_{-0.09}$	$^{+3.88}_{-0.23}$	$^{+20.41}_{-17.16}$	$^{+0.033}_{-0.005}$	$^{+0.011}_{-0.043}$	$^{+0.005}_{-0.099}$
LP1d	n	$^{+0.23}_{-0.23}$	$^{+1.03}_{-1.53}$	$^{+2.56}_{-8.29}$	$^{+0.011}_{-0.045}$	$^{+0.011}_{-0.027}$	$^{+0.009}_{-0.025}$
	γ	$^{+0.21}_{-0.21}$	$^{+1.33}_{-1.73}$	$^{+4.43}_{-11.44}$	$^{+0.029}_{-0.031}$	$^{+0.029}_{-0.025}$	$^{+0.013}_{-0.017}$
LPmax	n	$^{+0.17}_{-0.13}$	$^{+1.68}_{-2.03}$	$^{+2.68}_{-12.14}$	$^{+0.035}_{-0.037}$	$^{+0.013}_{-0.013}$	$^{+0.023}_{-0.035}$
	γ	$^{+0.29}_{-0.19}$	$^{+1.58}_{-1.13}$	$^{+12.01}_{-35.01}$	$^{+0.029}_{-0.021}$	$^{+0.023}_{-0.023}$	$^{+0.007}_{-0.011}$
L50	n	$^{+0.35}_{-0.37}$	$^{+2.08}_{-1.83}$	$^{+3.49}_{-15.18}$	$^{+0.021}_{-0.07}$	$^{+0.013}_{-0.013}$	$^{+0.013}_{-0.019}$
	γ	$^{+0.47}_{-0.19}$	$^{+3.13}_{-1.08}$	$^{+9.68}_{-14.59}$	$^{+0.043}_{-0.007}$	$^{+0.031}_{-0.033}$	$^{+0.070}_{-0.025}$
DCMV	n	$^{+0.29}_{-0.13}$	$^{+3.58}_{-3.23}$	$^{+12.01}_{-29.18}$	$^{+0.035}_{-0.027}$	$^{+0.029}_{-0.027}$	$^{+0.013}_{-0.023}$
	γ	$^{+0.29}_{-0.11}$	$^{+4.98}_{-3.43}$	$^{+12.83}_{-23.11}$	$^{+0.039}_{-0.041}$	$^{+0.033}_{-0.029}$	$^{+0.021}_{-0.033}$

Table B.12: List of systematic errors for all decay times and amplitudes for different scintillator mixtures.

List of Figures

List of Tables

Bibliography

[1] *Wolfgang Pauli - Wissenschaftlicher Briefwechsel mit Bohr, Einstein, Heisenberg u.a. Band II: 1930–1939* (Springer, 1985).

[2] F. Reines and C. L. Cowan, Nature **178**, 446 (1956).

[3] B. T. Cleveland, Astrophys. J. **496**, 505 (1998).

[4] SNO Collaboration, B. Aharmim *et al.*, Phys. Rev. **C81**, 055504 (2010), arXiv:0910.2984 [nucl-ex].

[5] GALLEX Collaboration, W. Hampel *et al.*, Phys. Lett. **B447**, 127 (1999).

[6] GNO COLLABORATION, M. Altmann *et al.*, Phys. Lett. **B616**, 174 (2005), hep-ex/0504037.

[7] SAGE Collaboration, J. Abdurashitov *et al.*, Phys. Rev. Lett. **83**, 4686 (1999), astro-ph/9907131.

[8] Super-Kamiokande Collaboration, J. Cravens *et al.*, Phys. Rev. **D78**, 032002 (2008), arXiv:0803.4312 [hep-ex].

[9] Super-Kamiokande Collaboration, R. Wendell *et al.*, Phys. Rev. **D81**, 092004 (2010), arXiv:1002.3471 [hep-ex].

[10] K2K Collaboration, M. Ahn *et al.*, Phys. Rev. **D74**, 072003 (2006), arXiv:hep-ex/0606032 [hep-ex].

[11] MINOS Collaboration, P. Adamson *et al.*, Phys. Rev. Lett. **110**, 251801 (2013), arXiv:1304.6335 [hep-ex].

[12] DAYA-BAY Collaboration, F. An *et al.*, Phys. Rev. Lett. **108**, 171803 (2012), arXiv:1203.1669 [hep-ex].

[13] RENO collaboration, J. Ahn *et al.*, Phys. Rev. Lett. **108**, 191802 (2012), arXiv:1204.0626 [hep-ex].

[14] DOUBLE-CHOOZ Collaboration, Y. Abe *et al.*, Phys. Rev. Lett. **108**, 131801 (2012), arXiv:1112.6353 [hep-ex].

[15] GERDA Collaboration, M. Agostini *et al.*, Phys. Rev. Lett. **111**, 122503 (2013).

[16] C. Arnaboldi *et al.*, Phys. Rev. C **78**, 035502 (2008).

[17] G. Drexlin, V. Hannen, S. Mertens, and C. Weinheimer, Adv. High Energy Phys. **2013**, 293986 (2013), arXiv:1307.0101 [physics.ins-det].

[18] T. Patzak and the LAGUNA-LBNO collaboration, Journal of Physics: Conference Series **375**, 042056 (2012).

[19] LENA Collaboration, M. Wurm *et al.*, Astropart. Phys. **35**, 685 (2012), arXiv:1104.5620 [astro-ph.IM].

[20] Particle Data Group, J. Beringer *et al.*, Phys. Rev. **D86**, 010001 (2012).

[21] B. Povh, *Teilchen und Kerne* (Springer-Verlag Berlin Heidelberg, 2004).

[22] G. Mention *et al.*, Phys. Rev. **D83**, 073006 (2011), arXiv:1101.2755 [hep-ex].

[23] M. Fukugita and T. Yanagida, *Physics of Neutrinos* (Springer-Verlag Berlin Heidelberg New York, 2003).

[24] L. Wolfenstein, Phys. Rev. **D17**, 2369 (1978).

[25] S. Mikheyev and A. Y. Smirnov, Prog. Part. Nucl. Phys. **23**, 41 (1989).

[26] K. Kotake, K. Sato, and K. Takahashi, Rept. Prog. Phys. **69**, 971 (2006), arXiv:astro-ph/0509456 [astro-ph].

[27] S. Woosley and T. Weaver, Astrophys. J.Suppl. **101**, 181 (1995).

[28] W. Haxton, Phys. Rev. Lett. **57**, 1271 (1986).

[29] H. Duan, G. M. Fuller, and Y.-Z. Qian, Ann.Rev.Nucl.Part.Sci. **60**, 569 (2010), arXiv:1001.2799 [hep-ph].

[30] B. Dasgupta, A. Dighe, G. G. Raffelt, and A. Y. Smirnov, Phys.Rev.Lett. **103**, 051105 (2009), arXiv:0904.3542 [hep-ph].

[31] S. Woosley, A. Heger, and T. Weaver, Rev. Mod. Phys. **74**, 1015 (2002).

[32] J. N. Bahcall, M. Gonzalez-Garcia, and C. Pena-Garay, Phys. Rev. Lett. **90**, 131301 (2003), arXiv:astro-ph/0212331 [astro-ph].

[33] A. Odrzywolek, M. Misiaszek, and M. Kutschera, Astropart. Phys. **21**, 303 (2004), arXiv:astro-ph/0311012 [astro-ph].

[34] G. G. Raffelt, Astrophys. J. **561**, 890 (2001), arXiv:astro-ph/0105250 [astro-ph].

[35] M. T. Keil, G. G. Raffelt, and H.-T. Janka, Astrophys. J. **590**, 971 (2003), arXiv:astro-ph/0208035 [astro-ph].

[36] K. Takahashi, J. Witti, and H.-T. Janka, Astron. Astrophys. **286**, 857 (1994).

[37] L. Oberauer, F. von Feilitzsch, and W. Potzel, Nucl. Phys. Proc. Suppl. **138**, 108 (2005).

[38] K. A. Hochmuth *et al.*, Earth Moon Planets **99**, 253 (2006), arXiv:hep-ph/0610048 [hep-ph].

[39] T. Marrodan Undagoitia *et al.*, Prog. Part. Nucl. Phys. **57**, 290 (2006).

[40] M. Wurm *et al.*, Phys. Rev. **D75**, 023007 (2007), astro-ph/0701305.

[41] D. Hellgartner *et al.*, Liquid scintillator specification document.

[42] V. Kudryavtsev, N. Spooner, and J. McMillan, Nucl. Instrum. Meth. **A505**, 688 (2003), arXiv:hep-ex/0303007 [hep-ex].

[43] LAGUNA Collaboration, D. Angus *et al.*, (2010), arXiv:1001.0077 [physics.ins-det].

[44] KamLAND Collaboration, S. Abe *et al.*, Phys. Rev. Lett. **100**, 221803 (2008), arXiv:0801.4589 [hep-ex].

[45] J. Brack *et al.*, Nuclear Instruments and Methods in Physics Research A **712**, 162 (2013), arXiv:1210.2765 [physics.ins-det].

[46] Hamamatsu Photonics K.K., Photomultiplier tubes - basics and applications, 2007, http://www.hamamatsu.com/resources/pdf/etd/PMT˙handbook˙v3aE.pdf.

[47] M. Tippmann, *Development of an Optical Module for the LENA detector*, PhD thesis.

[48] G. Beischler, *Development and construction of a prototype of the optical module for the LENA project*, Master's thesis, Technische Universität München, 2013.

[49] KAMIOKANDE-II Collaboration, K. Hirata *et al.*, Phys. Rev. Lett. **63**, 16 (1989).

[50] Super-Kamiokande Collaboration, J. Hosaka *et al.*, Phys. Rev. **D73**, 112001 (2006), hep-ex/0508053.

[51] Borexino Collaboration, C. Arpesella *et al.*, Phys. Rev. Lett. **101**, 091302 (2008), arXiv:0805.3843 [astro-ph].

[52] Borexino Collaboration, G. Bellini *et al.*, Phys. Rev. **D82**, 033006 (2010), arXiv:0808.2868 [astro-ph].

[53] Borexino Collaboration, G. Bellini *et al.*, Phys. Rev. Lett. **108**, 051302 (2012).

[54] C. Kraus, Progress in Particle and Nuclear Physics **57**, 150 (2006), International Workshop of Nuclear Physics 27th course: Neutrinos in Cosmology, in Astro, Particle and Nuclear Physics Ettore Majorana Center for Scientific Culture.

[55] R. Möllenberg, *Monte Carlo Study of the Fast Neutron Background in LENA*, Diplomarbeit, Technische Universität München, 2009.

[56] M. Wurm *et al.*, Phys. Rev. **D83**, 032010 (2011), arXiv:1012.3021 [astro-ph.IM].

[57] R. Möllenberg, *Monte Carlo Study of the Solar ^8B Neutrinos and the Diffuse Supernova Neutrino Background in LENA*, PhD thesis, Technische Universität München, 2013.

[58] T. Lyubetskaya and J. Korenaga, J. Geophys. Res. **112**, B03212 (2007).

[59] Borexino Collaboration, G. Bellini *et al.*, Phys. Lett. **B687**, 299 (2010), arXiv:1003.0284 [hep-ex].

[60] Borexino Collaboration, G. Bellini *et al.*, Phys. Lett. **B722**, 295 (2013), arXiv:1303.2571 [hep-ex].

[61] M. Wurm, *Untersuchungen zu den optischen Eigenschaften eines Fluessigszintilators und zum Nachweis von Supernova Relic Neutrinos*, Diplomarbeit, Technische Universität München, 2005.

[62] Super-Kamiokande Collaboration, M. Malek *et al.*, Phys. Rev. Lett. **90**, 061101 (2003), hep-ex/0209028.

[63] P. Fileviez Perez, H. Iminniyaz, and G. Rodrigo, Phys. Rev. **D78**, 015013 (2008), arXiv:0803.4156 [hep-ph].

[64] N. Shaban and W. J. Stirling, Phys. Lett. **B291**, 281 (1992).

[65] P. Nath and P. Fileviez Perez, Phys. Rept. **441**, 191 (2007), arXiv:hep-ph/0601023 [hep-ph].

[66] T. M. Undagoitia *et al.*, Phys. Rev. **D72**, 075014 (2005), arXiv:hep-ph/0511230 [hep-ph].

[67] D. Autiero *et al.*, Nucl. Phys.Proc.Suppl. **188**, 188 (2009).

[68] Borexino Collaboration, G. Alimonti *et al.*, Astropart. Phys. **16**, 205 (2002), arXiv:hep-ex/0012030 [hep-ex].

[69] J. B. Birks, *The Theory and Practice of Scintillation Counting* (Pergamon Press London, 1964).

[70] T. Marrodan Undagoitia, *Measurement of light emission in organic liquid scintillators and studies towards the search for proton decay in the future large-scale detector LENA*, PhD thesis, Technische Universität München, 2008.

[71] C. Buck, F. X. Hartmann, D. Motta, and D. Schoenert, Chem. Phys. Lett. **435**, 452 (2007).

[72] S. Quirk, *Purification of Liquid Scintillator abd Monte Carlo Simulations of Relevant Internal Background in SNO+*, PhD thesis.

[73] CEPSA Química Bécancour Inc., `www.cepsa.ca`.

[74] HELM AG, `www.helmag.com`.

[75] PerkinElmer, `www.perkinelmer.de`.

[76] Dräger Safety AG & Co. KGaA, `www.draeger.com`.

[77] S. Prummer, *Bestimmung optischer Parameter und der Stabilität des Flüssigszintillators für den LENA - Detektor*, Bachelor's thesis, Technische Universität München, 2012.

[78] J. Meyer, *Realization and Characterization of the Muon Veto Scintillator and the Buffer Liquid of the Double Chooz Experiment*, Diplomarbeit, Technische Universität München, 2010.

[79] Cölner Benzin Raffinerie Karl A. Kroseberg GmbH & Co. KG, `www.cbr-online.de`.

[80] Wurm *et al.*, Astroparticle Physics **35**, 685 (2012).

[81] B. Krosigk, L. Neumann, R. Nolte, S. Röttger, and K. Zuber, The European Physical Journal C **73**, 1 (2013).

[82] L. Prade, *Precise determination of Quenching factors and of the energy response function of liquid scintillators for future neutrino-astroparticle physics experiments*, Diplomarbeit, Technische Universität München, 2013.

[83] G. Angloher *et al.*, EUR PHYS J C **72** (2012).

[84] T. Jagemann *et al.*, Nucl. Instr. Meth. A **551** (2005).

[85] C. Ciemniak, *Setup of a Neutron Scattering Facility for the Measurement of Scintillation Light Quenching Factors of Low-Temperature Detectors Used in the Direct Dark Matter Search Experiments CRESST and EURECA*, PhD thesis, Technische Universität München, 2011.

[86] R. Strauß, *Quenching Factor Measurements of CaWO4 at mK Temperatures by Neutron Scattering for the Dark Matter Experiments CRESST and EURECA, Diploma Thesis, Technische Universität München*, Diplomarbeit, Technische Universität München, 2009.

[87] P. Hartung, `http://homepages.physik.uni-muenchen.de/~Ludwig.Beck/index-Dateien/Page1564.htm`.

[88] L. Rohrer, K. Jakob, and S. Skorka, NIM **220** (1984).

[89] M. Drosg, NIM A **254** (1987).

[90] W. v. Witsch and J. Willaschek, NIM **138** (1979).

[91] V. Zimmer, *Quenching in liquid scintillators in Double Chooz*, PhD thesis, Technische Universität München, in preparation.

[92] H. Kellermann, *Präzise Vermessung der fokussierten Reflektivität der MAGIC-Teleskopspiegel und Charakterisierung des hierfür verwendeten diffusen Reflektors*, Master's thesis, Munich University for Applied Sciences, 2011.

[93] ET Enterprises, `http://my.et-enterprises.com/pdf/9822B.pdf`, Accessed: 2013-09-17.

[94] Vacuumschmelze GmbH Co. KG, `http://www.vacuumschmelze.de`.

[95] item Industrietechnik GmbH, `www.item24.de/`.

[96] LEICA Geosystems, `http://www.leica-geosystems.com`.

[97] CAEN S.p.A., `http://www.caen.it`.

[98] R. Brun and F. Rademakers, Nucl. Inst. & Meth. in Phys. Res. A **389**, 81 (1997), http://root.cern.ch/.

[99] Ferd. Wiesenhahn GmbH, `www.wiesenhahn.com`.

[100] M. v. Sivers, priv.comm.

[101] GEANT4, S. Agostinelli *et al.*, Nucl. Instrum. Meth. **A506**, 250 (2003).

[102] R. Brun and F. Rademakers, Nucl. Instrum. Meth. **A389**, 81 (1997).

[103] E. Gatti and F. de Martini, Nuclear Electronics **2**, 265 (1962).

[104] Borexino Collaboration, H. Back *et al.*, Nucl. Instrum. Meth. **A584**, 98 (2008), arXiv:0705.0239 [physics.ins-det].

[105] H. O'Keeffe, E. O'Sullivan, and M. Chen, Nucl.Instrum.Meth. **A640**, 119 (2011), arXiv:1102.0797 [physics.ins-det].

[106] M. Berger, J. Coursey, M. Zucker, and J. Chang, Estar, pstar, and astar: Computer programs for calculating stopping-power and range tables for electrons, protons, and helium ions, 2005, (version 1.2.3). [Online] Available: http://physics.nist.gov/Star [June 2013]. National Institute of Standards and Technology, Gaithersburg, MD.

[107] B. von Krosigk, L. Neumann, R. Nolte, S. Rottger, and K. Zuber, Eur.Phys.J. **C73**, 2390 (2013), arXiv:1301.6403 [astro-ph.IM].

[108] E. Cappellaro and M. Turatto, (2000), arXiv:astro-ph/0012455 [astro-ph].

[109] S. Bergh and G. Tammann, Ann.Rev.Astron. Astrophys. **29**, 363 (1991).

[110] L. Hüdepohl, *Neutrino cooling evolution of the newly formed neutron stars from electron capture supernova*, Diplomarbeit, Technische Universität München, 2009.

[111] L. Hudepohl, B. Muller, H.-T. Janka, A. Marek, and G. Raffelt, Phys. Rev. Lett. **104**, 251101 (2010), arXiv:0912.0260 [astro-ph.SR].

[112] T. Fischer, S. Whitehouse, A. Mezzacappa, F.-K. Thielemann, and M. Liebendorfer, Astron. Astrophys. **517**, A80 (2010), arXiv:0908.1871 [astro-ph.HE].

[113] M. Rampp and H. T. Janka, Astron. Astrophys. **396**, 361 (2002), arXiv:astro-ph/0203101 [astro-ph].

[114] R. Buras, M. Rampp, H.-T. Janka, and K. Kifonidis, Astron. Astrophys. **447**, 1049 (2006), arXiv:astro-ph/0507135 [astro-ph].

[115] H. Shen, H. Toki, K. Oyamatsu, and K. Sumiyoshi, Prog.Theor.Phys. **100**, 1013 (1998), arXiv:nucl-th/9806095 [nucl-th].

[116] H. Shen, H. Toki, K. Oyamatsu, and K. Sumiyoshi, Nucl. Phys. **A637**, 435 (1998), arXiv:nucl-th/9805035 [nucl-th].

[117] A. Burrows and R. Sawyer, Phys. Rev. **C58**, 554 (1998), arXiv:astro-ph/9801082 [astro-ph].

[118] A. Burrows and R. Sawyer, Phys. Rev. **C59**, 510 (1999), arXiv:astro-ph/9804264 [astro-ph].

[119] A. Marek and H.-T. Janka, Astrophys. J. **694**, 664 (2009), arXiv:0708.3372 [astro-ph].

[120] K. Nomoto, Astrophys. J. **277**, 791 (1984).

[121] K. Nomoto, Astrophys. J. **322**, 206 (1987).

[122] A. Strumia and F. Vissani, Phys. Lett. **B564**, 42 (2003), arXiv:astro-ph/0302055 [astro-ph].

[123] L. Cadonati, F. Calaprice, and M. Chen, Astropart. Phys. **16**, 361 (2002), arXiv:hep-ph/0012082 [hep-ph].

[124] J. F. Beacom, W. M. Farr, and P. Vogel, Phys. Rev. **D66**, 033001 (2002), arXiv:hep-ph/0205220 [hep-ph].

[125] S. Weinberg, Phys. Rev. D **5**, 1412 (1972).

[126] L. A. Ahrens *et al.*, Phys. Rev. D **35**, 785 (1987).

[127] M. Kaiser, *Supernova Neutrinos in LENA*, Master's thesis, Universität Hamburg.

[128] T. Lewke, *Studies of Scintillator Optical Properties, Electronics Simulation and Data Analysis for the BOREXINO Neutrino Experiment*, PhD thesis, Technische Universität München, 2013.

[129] G. 't Hooft, Phys. Lett. **B37**, 195 (1971).

[130] S. Yoshida *et al.*, Nucl. Instrum. Meth. **A622**, 574 (2010).

[131] M. Fukugita, Y. Kohyama, and K. Kubodera, Phys. Lett. **B212**, 139 (1988).

[132] A. S. Dighe, M. T. Keil, and G. G. Raffelt, JCAP **0306**, 006 (2003), arXiv:hep-ph/0304150 [hep-ph].

[133] Y. K. Munakata, H. and N. Itoh, Astrophys. J. **296** (1985).

[134] M. Limongi, O. Straniero, and A. Chieffi, Astrophys. J.Suppl. **129**, 625 (2000), arXiv:astro-ph/0003401 [astro-ph].

[135] C. H. Townes, E. H. Wishnow, D. D. S. Hale, and B. Walp, The Astrophysical Journal Letters **697**, L127 (2009).

[136] T. Totani, K. Sato, H. Dalhed, and J. Wilson, Astrophys. J. **496**, 216 (1998), arXiv:astro-ph/9710203 [astro-ph].

[137] T. A. Thompson, A. Burrows, and P. A. Pinto, Astrophys. J. **592**, 434 (2003), arXiv:astro-ph/0211194 [astro-ph].

Danksagung

Zuallererst möchte ich mich bei Prof. Stefan Schönert und bei Prof. Franz von Feilitzch bedanken für die freundliche Aufnahme am Lehrstuhl E15 sowie die Möglichkeit, diese Arbeit anzufertigen. Ein riesengroßes Dankeschön gilt meinem Doktorvater, Prof. Lothar Oberauer, für die Betreuung und die beständige Motivation zu dieser Arbeit.
Des Weiteren bedanke ich mich bei Vincenz Zimmer für die wunderbare Zusammenarbeit am Beschleunigerexperiment sowie das Korrekturlesen der Arbeit. Des Weiteren gebührt Raimund Strauß und Stephan Wawoczny ein großes Dankeschön für die Möglichkeit, an ihren Strahlzeiten zu partizipieren. Allen Mitarbeitern am MLL danke ich für dir freundliche Aufnahme am Beschleuniger.
Quirin Meindl, Timo Lewke, Marc Tippmann, German Beischler und Ludwig Prade danke ich für die höchst unterhaltsame geimeinsame Stunden innerhalb und außerhalb der Büros. Ein Dankeschön gebührt auch allen anderen Mitarbeitern am Lehrstuhl für interessante Unterhaltungen bei Kaffee und der schönen gemeinsamen Zeit auf diversen Reisen und Konferenzen.
Des Weiteren danke ich unserer Sekretärin Maria Bremberger und ihren Vorgängerinnen für die Hilfe bei zahlreichen bürokratischen Dingen und ihre stets zuvorkommende Art. Der E15 Werkstatt danke ich für das stets schnelle Anfertigen von diversen Bauteilen zu meiner vollsten Zufriedenheit.
Mein größter Dank gilt meiner Familie für die stetige Unterstützung für alle meine Vorhaben und das Vertrauen in meine Person. Barbara danke ich für unendlich viel Geduld und Verständnis.